Harnessing the Power of Boronic Acids: Unique Biocompatible Reactivity Enables Development of Synthetic Probes for Specific Bacterial Pathogens

Author: Samantha Elizabeth Cambray

Harnessing the Power of Boronic Acids: Unique Biocompatible Reactivity Enables Development of Synthetic Probes for Specific Bacterial Pathogens

Samantha E. Cambray

A dissertation

submitted to the Faculty of

the department of Chemistry

in partial fulfillment

of the requirements for the degree of

Doctor of Philosophy

Boston College
Morrissey College of Arts and Sciences
Graduate School

March 2019

Harnessing the Power of Boronic Acids: Unique Biocompatible Reactivity Enables Development of Synthetic Probes for Specific Bacterial Pathogens

Samantha E. Cambray

Advisor: Professor Jianmin Gao, Ph.D.

The imminent threat of antibiotic resistant pathogens that have emerged in clinical settings over the past several decades demands novel solutions in the form of both species- and/or strain-specific diagnostic technologies and treatments. Such new developments would aid in the improved management of bacterial infections by accurate diagnosis and targeted bacterial killing, which would mitigate the continued spread of antibiotic resistance as a result of broad-spectrum antibiotic application The cell surface of bacteria presents a unique opportunity towards development of these modalities, as bacterial cell walls possess both universal and unique features that can be targeted by chemical functionalities without the requirement of cell penetration. This work has sought to take advantage of naturally existing and non-natively installed bacterial cell wall chemical functionalities for which we can develop novel chemoselective chemistries and unique peptides that incorporate those chemical functionalities to enable targeted, biocompatible methods of bacterial labeling and targeting.

We initially began these endeavors with the goal of improving upon existing readily reversible iminoboronate chemistry with acetylphenyl boronic acid (APBA), which selectively labels bacteria that contain amine-presenting cell wall lipids (e.g. PE and Lys-PG). In our efforts to improve upon the binding potency of this chemical motif, we synthesized a panel of APBA analogues with varying substituents to modulate amine-binding affinity. We additionally characterized these analogues capacity to form thiazolidinoboronates with free and N-terminal cysteine.

Furthermore, we applied an APBA dimer presenting phage library towards identification of potent and selective APBA-presenting peptide binders of 1) a cationic antimicrobial peptide (CAMP) implicated in cancer, human beta defensin 3 (hBD3), and 2) colistin-resistant strains of bacteria that attain their resistance through a variety of different mechanisms. This high-throughput technology afforded identification of peptides that are indeed protein or species/strain selective binders, thus enabling targeted labeling of these important biomolecules.

In our continued efforts to identify highly potent and selective bacterial targeting chemistries, we also developed an irreversible chemistry that enables the incorporation of chemical motifs, APBA and semicarbazide, into the cell walls of bacteria through cell wall remodeling mechanisms, which then undergo rapid conjugation with fluorescent and turn-on fluorescent reactive partners. While this alternative approach to bacterial detection requires a primary cell-wall incorporation step, the incorporation and subsequent labeling of these chemical motifs are both highly efficient, which enhances the potency of this bacterial labeling approach

The chemical approaches to targeted bacterial labeling herein highlight our ability to develop several species- and strain-selective bioorthogonal chemical probes towards the goal of discovering targeted bacteria binding modalities. Beyond identification of such targeted bacterial binding molecules, we hope to translate these findings into effective, narrow-spectrum antibiotics, which is an endeavor currently being pursued in our laboratory.

TABLE OF CONTENTS

LIST OF TABLES

LIST OF FIGURES

LIST OF SCHEMES

LIST OF ABBREVIATIONS

A. baumannii	*Acinetobacter baumannii*
Ala, A	Alanine
Alloc	Allyloxycarbonyl
APBA	Acetylphenyl boronic acid
Ara4N	4-Amino-4-deoxy-arabinose
Arg, R	Arginine
Asn, N	Asparagine
Asp, D	Aspartic Acid
B_2pin_2	Bis(pinacolato)diboron
Boc	*Tert*-butyloxycarbonyl
Bpin	Pinacol ester
BSA	Bovine serum albumin
CAMP	Cationic antimicrobial peptide
CD4	Cluster of differentiation 4
CCR2	C-C chemokine receptor 2
cfu	Colony Forming Units
CuAAC	Copper (I) Azide-Alkyne Click Chemistry
Cys, C	Cysteine
DAB1	Diazaborine conjugate of 2-FPBA and semicarbazide
DAB2	Diazaborine conjugate of 2-APBA and semicarbazide
Dap	Diaminopropionic acid
D-Dap-Scz	D-Diaminopropionic acid-semicarbazide
Dbz	Diaminobenzoic acid
DCM	Dichloromethane
DIPEA	*N,N'*-Diisopropylethylamine

DMF	Dimethylformamide
DMSO	Dimethylsulfoxide
E. coli	*Eschericia coli*
EGFR	Epidermal growth factor
ESI	Electrospray ionization
Et_3N	Triethylamine
FAM	Carboxyfluorescein
4-F-2-APBA	4-Fluorine-2-acetylphenyl boronic acid
4,6-F-2-APBA	4,6-Fluorine-2-acetylphenyl boronic acid
FBS	Fetal bovine serum
FDA	Food and Drug Administration
FITC	Fluorescein isothiocyanate
Fmoc	Fluorenylmetholoxycarbonyl
FPBA	Formylphenyl boronic acid
GlcNAc	*N*-Acetylglucosamine
Gln, Q	Glutamine
Glu, E	Glutamic acid
Gly, G	Glycine
hBD2	Human beta defensin 2
hBD3	Human beta defensin 3
HBTU	Hexafluorophosphate Benzotriazole Tetramethyl Uronium
HCl	Hydrochloride
His, H	Histidine
HS	Human serum
IA	Iodoacetamide
IFN-γ	Interferon gamma
IL1-α/β/6/8	Interleukin 1 alpha/beta/6/8
Ile, I	Isoleucine
IPTG	Isopropyl β-D-1-thioglactopyranoside
iTCEP	Immobilized TCEP

K_2CO_3	Potassium carbonate
K_d	Equilibrium dissociation constant
KOAc	Potassium acetate
K. pneumoniae	*Klebsiella pneumoniae*
LC-MS	Liquid chromatography-mass spectrometry
Leu, L	Leucine
LOS	Lipooligosaccharide
LPS	Lipopolysaccharide
Lys, K	Lysine
Lys-PG	Lysyl phosphatidylglycerol
MCP-1	Monocyte chemoattractant protein 1
mcr	Mobilized colisitin resistance determinant
MeOH	Methanol
Met, M	Methionine
MRSA	Methicillin resistant *Staphylococcus aureus*
MS	Mass spectrometry
MSSA	Methicillin sensitive *Staphylococcus aureus*
MTT	3-(4,5-dimethylthiazol-2-yl)-2,5-diphenyltetrazolium bromide
MurNAc	*N*-Acetylmuramic acid
NaCl	Sodium chloride
NBD	Nitrobenzoxadiazole
Nbz	*N*-acyl-benzimidazolinone
NEB	New England Biolabs
NF-κB	Nuclear factor kappa-light-chain-enhancer of activated B cells
NMM	*N*-Methylmorpholine
NMR	Nuclear Magnetic Resonance spectroscopy
6-NO_2-2-APBA	6-Nitro-2-acetylphenylboronic acid
OD_{600}	Optical density measured at 600 nm
4-OMe-2-APBA	4-Methoxy-2-acetylphenyl boronic acid

5-OMe-2-APBA	5-Methoxy-2-acetylphenyl boronic acid
p53	Tumor protein p53
PAGE	Polyacrylamide gel electrophoresis
PBP	Penicillin binding protein
PBS	Phosphate-buffered saline
PBST	Phosphate-buffered saline with Tween
Pd(dppf)Cl2•DCM	1,1′-Bis(diphenylphosphino)ferrocene]dichloropalladium(II) complex with dichloromethane
PE	Phosphatidylethanolamine
PEG	Polyethylene glycol
pfu	Plaque-forming units
PG	Peptidoglycan
Phe, F	Phenylalanine
D-Phe-Scz	D-Phenylalanine semicarbazide
Phzn	Phenylhydrazine
PLP	Pyridoxal phosphate
PMA	Phorbol 12-myristate 13-acetate
Pro, P	Proline
P. aeruginosa	*Pseudomonas aeruginosa*
RP-HPLC	Reversed-phage high-performance liquid chromatography
S. aureus	*Staphylococcus aureus*
Scz	Semicarbazide
S. enteritiditis	*Salmonella enteritiditis*
Ser, S	Serine
SPAAC	Strain-Promoted Azide-Alkyne Click Chemistry
SPPS	Solid-phase peptide synthesis
TAMRA	Carboxytetramethylrhodamine
TBS	Tris buffered saline
TBST	Tris-buffered saline with Tween
TCEP	Tris(2-carboxyethyl)phosphine
TFA	Trifluoroacetic acid

THF	Tetrahydrofuran
Thr, T	Threonine
TIS	Triisopropylsilane
TLC	Thin layer chromatography
TLR	Toll-like receptor
TNF-α	Tumor necrosis factor alpha
3-CF_3-2-APBA	3-Trifluoroacetyl-2-acetylphenyl boronic acid
Trp, W	Tryptophan
Tyr, Y	Tyrosine
TzB	Thiazolidinoboronate
UV-Vis	Ultraviolet-visible
Val, V	Valine
WT	Wild type
Xgal	5-bromo-4-chloro-2-indolyl-β-D-galactopyranoside

ACKNOWLEDGEMENTS

Firstly, I would like to thank Dr. Jianmin Gao for being a fantastic research advisor throughout my time in graduate school. His commitment to and passion for science inspired me to keep pushing for results and maintain a high level of curiosity throughout my thesis work. Not only has he helped me to become a better critical thinker, but he has also taught me how to be a mentor, friend and steward of science. I would also like to thank Dr. Eranthie Weerapana, Dr. Abhishek Chatterjee and Dr. Jia Niu for all of their helpful feedback along this journey and for always taking an interest in my science.

My time spend in lab would have been a far different experience if not for the friendship of my co-workers. Firstly, I must thank my mentor Dr. Anupam Bandyopadhyay who showed me how to be a great chemist and thinker, and pushed me through some tough days in my early graduate school career. Kaicheng Li, Mike Kelly, Wenjian Wang and Chelsea Weidman were also not only great motivators for my science, but have made the lab a fun and collaborative environment. Although I do love science, Dr. Breanna Zerfas and Dr. Kelly McCarthy are the real reason I enjoyed coming to lab everyday. Their commitment to both helping me learn how to do and think about science, as well as to being great friends are undoubtedly the reason I was able to write most of this thesis. I will always be thankful that by coming to BC and joining the Gao lab I was able to meet two such great people and friends. Several of the projects herein were also contributed to by two wonderful undergraduate mentees, Ik Joo Kim and Claire

Ferguson, who not only provided me the opportunity to learn how to mentor, but also deeply shaped the way I think and talk about my own projects and science in general. I would also like to thank all of my friends and colleagues in the Weerapana, Chatterjee and Liu labs who helped me frequently with both science and sanity.

Much of the work in this thesis would have gone unaccomplished had it not been for the encouragement and support of my family and friends. First and foremost, I would like to thank my Mom and Dad who have always pushed me to be the best version of myself. Because of them, I have learned to always give my best effort, to never back down from a challenge, and to try to see the best in any situation. This work is a testament to the countless ways they have helped me to pursue my dreams, no matter how big or small. I will be forever grateful for the example they have set for me that nothing good comes without hard work and determination. My sister, Danielle, has also been by my side and pushed me to be my best in countless ways, and I am thankful for all of her love and friendship. My extended family and friends have given me shoulders to lean on throughout the ups and downs of life as well, especially during these past five years, and I sincerely appreciate all of their love and support.

I would also not be here without one of my biggest cheerleaders, Mike, who has lent a listening ear and lots of helpful advice throughout my long days in the lab. I cannot express how thankful I am to have someone who sees the best in me and amplifies it on a daily basis. I am looking forward to our next big adventures, and especially to searching for all the world's best food together. Finally, I would also like to thank my fur child, Brady the cat, who only sometimes yelled at me when I got home from the lab later than his dinnertime.

CHAPTER 1

Introduction

1.1 The Challenge Posed by Antibiotic Resistance

Over the past several decades, antibiotic resistance has emerged as one of the most significant threats to worldwide human health. In the US alone, cases of bacterial infections reach upwards of 2 million each year, resulting in ~30,000 deaths per year as a direct result of the emergence of antibiotic resistance.[1,2] To combat this pressing issue, scientists aim to tackle the eradication of bacterial infections via several approaches, including prevention of infections, observing resistance patterns, improving appropriate antibiotic use, and most importantly, developing novel antibiotics and diagnostics.

Importantly, despite the significant need for the development of new antibiotics, the actual number of new FDA approved antibiotics has been steadily decreasing over the past several decades (**Figure 1-1**). This deficiency in antibiotic development is due to a wide number of factors including increasingly complicated bacterial targets due to multifaceted resistance mechanisms, as well as the challenge of targeting a specific species of bacteria while bypassing all others towards efforts to maintain commensal bacterial populations. Given these many challenges, our group has sought to develop chemistries that would aid in the development of targeted molecular tools that would allow us to differentiate between not only different species of bacteria, but also between antibiotic resistant and sensitive bacteria. In order to do so, we must first understand the emergence of antimicrobial resistance, including which species and strains of bacteria are hardest to tackle, in addition to how antibiotics have traditionally been discovered and what new methods of antibiotic discovery are available in the modern era.

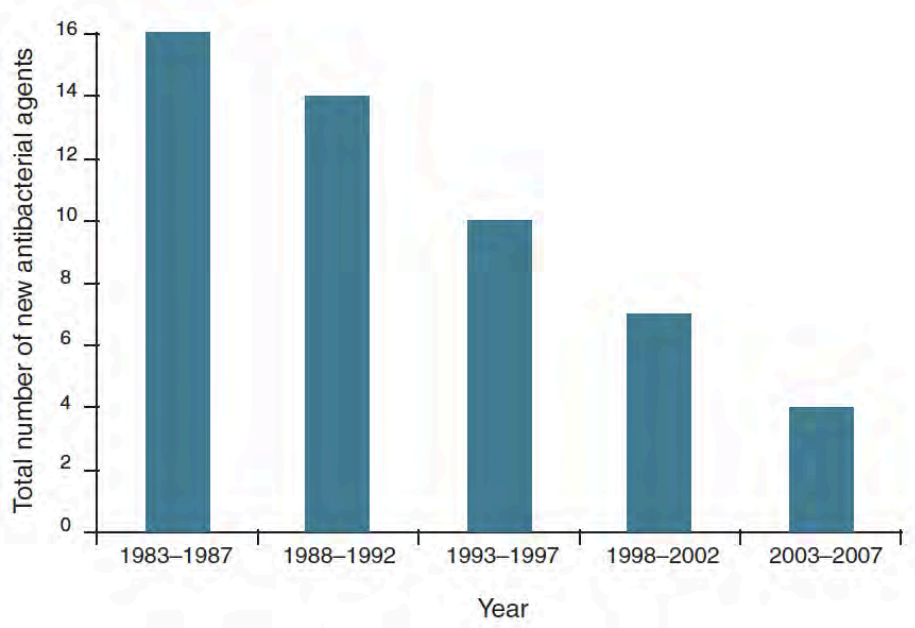

Figure 1-1. Declining antibiotic approvals from 1983 – 2007 (Image from Ref. 3).[3]

1.1.1 Discovery of Antibiotics: Past and Present

In the "Golden Age" of antibiotic innovation antibiotics were discovered through screening of natural sources, such as soil and plants. While the widely renowned antibiotic penicillin was identified through a more serendipitous discovery methodology, the Waksman platform, a method that was so revolutionary it won a Nobel Prize in 1952, provided a systematic screening approach, which eventually led to the discovery of streptomycin.[4] The Waksman platform, which was the first "high throughput" antibiotic discovery methodology, essentially screened for compounds in soil that would inhibit the growth of lab-cultured bacteria. When growth inhibition was observed, the soil compound was isolated and tested in its pure form.[5]

Over the proceeding several decades, this method produced upward of ten new major classes of antibiotics, including beta lactams, macrolides, tetracyclines, in addition to several others (**Table 1-1**); however, over time the platform's production dropped off,

leading to a decline in new antibiotic/antibiotic class discoveries. Concurrent with this drop off in new discoveries, microbe resistance to available antibiotics emerged. For a period of time, synthesis of novel antibacterial analogues was able to temporarily quell the major antibiotic resistance uprising.

The last major class of antibiotics to be discovered since this "Golden Age" of antibiotic discovery were the lipopetides, a class that includes the important drug daptomycin, which was discovered in 1986, but not approved for clinical use until 2003.[6] During this significant innovation gap, the spread of antimicrobial resistance has greatly outpaced the discovery of new and effective drugs. This in turn has led scientists to invent and execute new discovery methodologies – if we can no longer rely on natural sources or rational design manipulation of existing scaffolds to find new drugs, the question is how do we challenge these bad bugs, and more importantly, which bacterial targets are worthy of pursuit.

Table 1-1. Discovery and resistance timeline for important classes of antibiotics (adapted from Ref. 7).[7]

Antibiotic Class	Year Discovered	Resistance Observed	Species Activity
β-lactams	1928	1945	Broad spectrum
Sulfadrugs	1932	1942	Gram positive
Aminoglycosides	1943	1946	Broad spectrum
Tetracyclines	1944	1950	Broad spectrum
Chloramphenicols	1946	1950	Broad spectrum
Macrolides	1948	1955	Broad spectrum
Glycopeptides	1953	1960	Gram positive
Oxazolidinones	1955	2001	Gram positive
Rifamycins	1957	1962	Gram positive
Quinolines	1961	1968	Broad spectrum
Streptogramins	1963	1964	Gram positive
Lipopeptides	1986	1987	Gram positive

1.1.2 Mechanisms of Antibiotic Activity and Acquired Bacterial Resistance

Although they are quite simple organisms, bacteria contain a wide variety of distinct targets for the development of novel antibiotics, which are well conserved across different species of bacteria. Due to this high level of conservation between the varying bacterial species, antibiotics are oftentimes effective for all species of bacteria (broad spectrum), while some select antibiotics are effective only against Gram-positive species. In the latter case, the antibiotic typically cannot permeate the thick outer cell wall of Gram-negative bacteria, making the drug ineffective towards this class of bacteria (**Figure 1-2**).

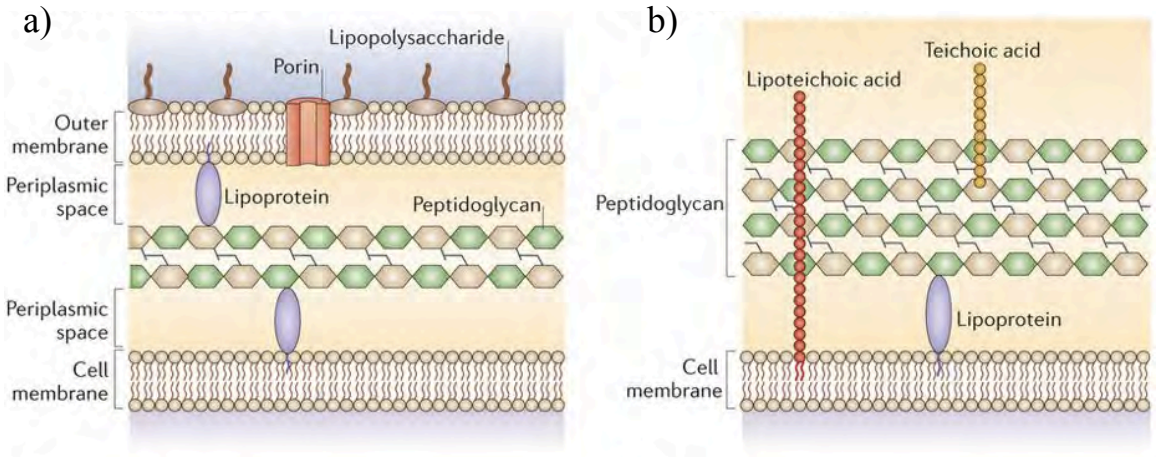

Figure 1-2. Structure of (a) Gram-negative and (b) Gram-positive bacterial cell walls (image from Ref. 8).[8]

There are a wide variety of intracellular bacterial targets, which are accessed by antibiotics that are capable of bypassing the inner cell membrane. These targets include nucleic acid synthesis, RNA polymerase, protein synthesis and folate synthesis (**Figure 1-3**).[9] These intracellularly active drugs including aminoglycosides, sulfonamides, and quinolones, all function to disrupt the metabolic activity of the bacterial cell, eventually leading to cell death. In order to evade killing by such antibiotics, bacteria generally evolve mechanisms to keep the drugs from entering the cell by either altering the permeability of their membranes, or by up-regulating drug efflux pumps that will quickly remove the antibiotic upon its entry into the cell.[10] Alternatively, if the antibiotic is successfully taken up into the cells without up-regulation of efflux, bacteria are capable of modifying the antibiotic target.[11] For example, in the case of aminoglycosides, the subunits of the ribosome can be modified (eg. methylation of specific nucleotide bases) to achieve resistance to aminoglycoside antibiotics by inhibiting binding of the antibiotic and maintaining the unwanted activity of the target.[12,13]

Extracellularly active antibiotics alternatively function by compromising the cell wall to prohibit its synthesis, or by directly disrupting the membrane, causing leakage of the cellular contents.[14] Some of the most well known antibiotics, such as the beta lactam class, are inhibitors of cell wall synthesis; notably, these types of antibiotics are greatly susceptible to development of resistance due to the up-regulation of inhibited or inactivated enzymes, such as the beta lactamases.[15] Another common mechanism of resistance to extracellularly active antibiotics is modification of the extracellular antibiotic target.[11] One important example of target modification leading to antibiotic inactivation is that of vancomycin, which targets the D-Ala-D-Ala dipeptide of membrane anchored Lipid II. By mutating the terminal D-Ala to a D-Lac residue, bacteria are able to evade vancomycin binding, thus leading to the rise of vancomycin resistant bacterial strains of *S. aureus* and *Enterococcus*.[16,17]

Overall, while there are many mechanisms of antibiotic activity, there are similarly a wide array of antibiotic resistance mechanisms that bacteria have evolved in response to these drugs. Looking towards the future, it is important to not only develop targeted antibiotics for specific strains and species of bacteria to minimize the chance of resistance development, but it is also important to identify novel targets and mechanisms of action that are minimally susceptible to future resistance development.

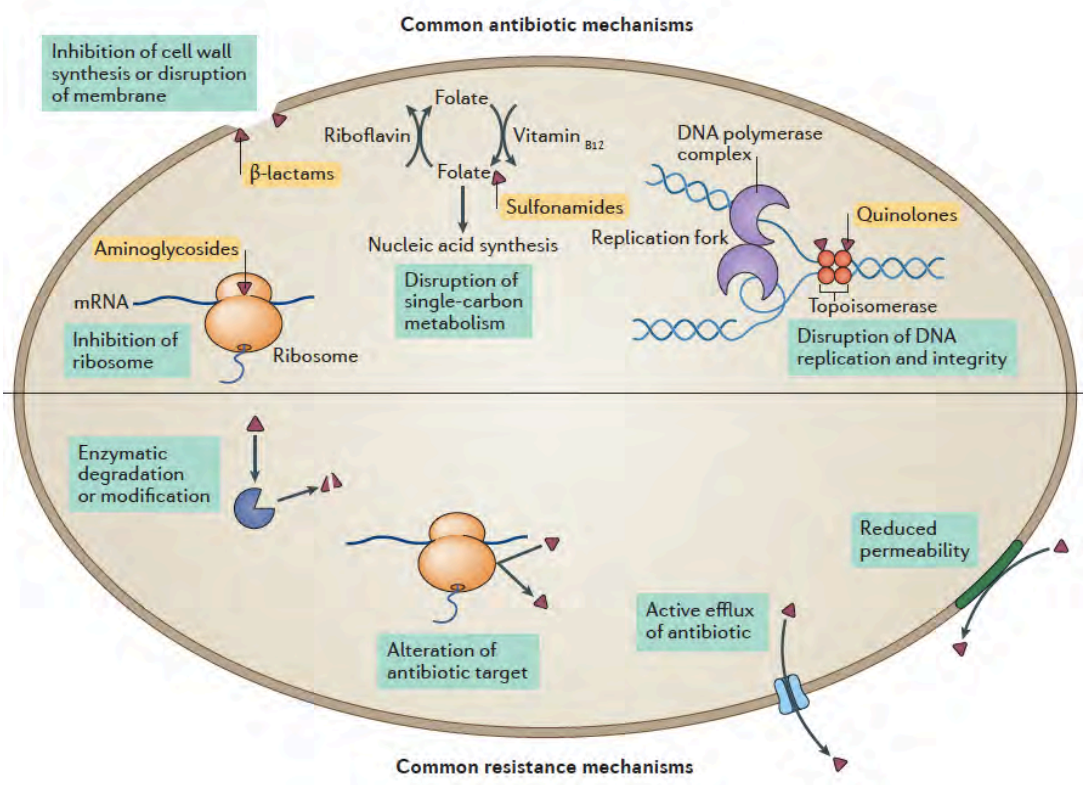

Figure 1-3. Mechanisms of antibiotic action and resistance (image from Ref. 9).[9]

1.1.3 Emergence of Antibiotic Resistant Bacterial Infections and Multidrug Resistance

Antibiotic resistance was first documented for the antibiotic sulfadrugs in 1942, shortly after their introduction to the clinic, and other classes of antibiotics have followed suit by displaying resistance shortly after, or even before, initial clinical use.[7] The main source of widespread resistance across hundreds of bacterial species and strains is the ability of closely related bacteria to undergo horizontal gene transfer. Recent functional metagenome screens have identified that environmental antibiotic resistance genes have >99% nucleotide identity to those in pathogenic isolates, thus supporting the role of gene transfer in the dissemination of antibiotic resistance.[18] Most notably, the combination of

the transfer of multiple resistance genes to the same organism can lead to the formation of dangerous multidrug resistant bacterial species.[19]

The antibiotic resistant "ESKAPE" pathogens (*Enterococcus* species, *Staphylococcus aureus*, *Klebsiella* species, *Acinetobacter baumannii*, *Pseudomonas aeruginosa* and *Enterobacter* species) have experienced rapid spread in recent years, and are notoriously resistant to several or in some cases, such as certain species of *A. baumannii*, all clinically available antibiotics.[20] This widespread antibiotic resistance problem has generated a significant number of infections each year, and ultimately leads to several thousand deaths per year (**Table 1-2**). As the problem of antibiotic resistant bacterial strains grows, we are challenged to find inventive solutions to a vastly complicated problem.

Table 1-2. Infection and mortality data on antibiotic resistance across various strains (data obtained from Ref. 2).

Bacterial Species	Antibiotic Resistance	Infections per Year	Deaths per Year
Clostridioides difficile	MDR	500,000	15,000
*Enterobacteriaceae**	Carbapenem	9,000	600
*Acinetobacter**	MDR	7,300	500
Enterococcus	Vancomycin	20,000	1,300
*Pseudomonas aeruginosa**	MDR	6,700	440
Staphylococcus aureus	Methicillin	80,500	11,300
Streptococcus pneumoniae	MDR	19,000	7,000

*: Gram negative strain of bacteria; MDR: multidrug resistant

1.1.4 Novel Mechanisms of Targeted Antibiotic Discovery

A wide array of new approaches for discovering novel antibiotics and antibiotic classes have been pursued in the past several years. For the former case, novel antibiotics generally originate from previously applied antibiotics that are reformulated in combination with another drug that works to mitigate the resistance pathway observed for the antibiotic. For example, the new drug Avycaz combines the cephalosporin ceftazidime with a β-lactamase inhibitor in order to maximize the activity of the drug with minimal interference via resistance mechanisms.[21]

Alternatively, researchers have also opted to continue mining natural resources in search of new antibiotic scaffolds that may provide the key to the resistance problem. Recently, revival of arylomycins, a class of bacterially secreted macrocyclic lipopeptide antibiotics originally discovered in 2002, has transformed these once believed ineffective narrow-spectrum compounds into highly potent drugs for treating the most challenging gram-negative ESKAPE pathogens.[22] Structurally arylomycins contain a macrocyclic tripeptide core (with two phenols on the aromatic rings of the core), an N-terminal lipopeptide tail and a C-terminal carboxylic acid. To improve upon their activity, arylomycin was modified at the lipopeptide tail to successfully improve binding affinity and thus activity towards gram-negative bacterial species. Indeed, in contrast to FDA approved, commercially available antibiotics, including the aforementioned drug Avycaz, the optimized arylomycin maintained potent activity against an array of MDR isolates of *K. pneumoniae*, *A. baumannii*, *P. aeruginosa* and *E. coli*. Thus, improving previously mined unsuccessful natural products can lead to new, potent compounds for treating challenging MDR infections.

Expanding natural source screenings with new technologies has also been successful in the discovery of new, potent compounds. New approaches to growing uncultured organisms via cultivation of the species in their natural environment has led to an increase in bacterial recovery from 1% to 50%; through this method, the novel antibiotic texiobactin was discovered.[23] This natural product antibiotic displays excellent activity towards MDR gram-positive bacteria, including *Mycobacterium tuberculosis* and *Clostridium difficile*. Moreover, texiobactin showed superior *S. aureus* killing to the highly potent drug vancomycin. Importantly, texiobactin did not induce any detectable resistance in a variety of bacterial species.

While natural sources can continue to be mined for bacterially active compounds, we also need to invent novel approaches to specifically detect and target various species and strains of bacteria in order to mitigate the challenges posed by antibiotic resistance. To develop novel antibiotics that are specific for one species or strain of bacteria versus another, we envisioned applying chemistry that enables chemoselective reactivity towards our distinct target of interest; however, in order to develop such chemistries, we first needed to define a specified target. Given the complications of intracellular delivery in drug discovery, we have focused our efforts on targeting the natural or unnaturally installed unique chemical motifs that are displayed on the surface of bacteria, including lipid composition, lipid modifications, and surface protein or sugar modifications in the former case, or installed bioorthogonal handles in the latter, which can be specifically targeted by our chemoselective biocompatible chemistries.

1.2 Development of Boronic Acid-Mediated Chemoselective Chemistries for Selective Bacterial Detection

In order to improve our ability to produce target-specific features of antibiotic resistant bacteria, we need chemistry that can specifically go after the unique chemical markers that define certain species of bacteria. In the past few decades, bioorthogonal chemistry innovation has come to the forefront of biochemical discovery, as it enables the study and understanding of a wide variety of biomolecules and biochemical processes in their native environments.[24] Indeed, such innovations have promoted the study of proteins, sugars, lipids, metabolites and post-translational modifications; however, over time these widely lauded biocompatible chemistries have been found to exhibit a variety of drawbacks to achieving true biocompatibility[25], thus prompting our continued search for better bioorthogonal chemistries through the exploration of boronic acid-mediated biocompatible conjugation reactions.

1.2.1 Origins and Principles of Biocompatible Chemoselective Reactivity

Bioorthogonal chemistry can be traced back to the model protein GFP and tetracysteine motifs, both of which were discovered and applied for the study of proteins; however, more recent searches have focused on chemistries that can be applied as bioothogonal tools for the study of a wider array of biomolecules (e.g. sugars, lipids). There are a number of key principles for the development of bioorthogonal chemistries: 1) the chemistry should be selective for its reactive partner and exhibit no cross-reactivity; 2) the products of the reaction should be relatively stable; 3) the reagents should be non-toxic, and produce non-toxic products; 4) the chemistry should yield a fast reaction rate in biological conditions (37 ^{o}C, physiological buffer) at low concentrations

(nM-μM); and 5) the reagents should be stable in these same biological conditions.[26]

Towards the development of such chemoselective reactions, two distinct approaches have been taken: application of bioorthogonal reactions that afford conjugation to natural chemical moieties, and installation of unnatural chemical moieties through various mechanisms (e.g. chemical, genetic, metabolic) to which a biocompatible chemoselective reaction partner can conjugate (**Figure 1-4**).[24] In the former case, intrinsically reactive functional groups, such as amines, alcohols and thiols presented on biomolecules are used as handles for chemoselective labeling by an orthogonal reactive partner. Some key examples include reductive amination, transamination and isothiocyanate chemistry; however, these methods are often applied in protein labeling, where selectivity for a single residue is challenging given that there are often several copies of amino acids in a protein sequence. In the latter case, unnatural chemical functionalities can be selectively incorporated into biomolecules, and subsequently labeled chemoselectively with a complementary probe containing a bioorthgonal functionality. Widely used examples of these types of bioorthogonal reactions include the Staudinger ligation and the array of azide-alkyne chemistries (eg. CuAAC, SPAAC). While this class of bioorthogonal chemistries enables higher selectivity for the desired conjugation reaction, the reagents required for these chemistries often fall short of true bioorthogonality.

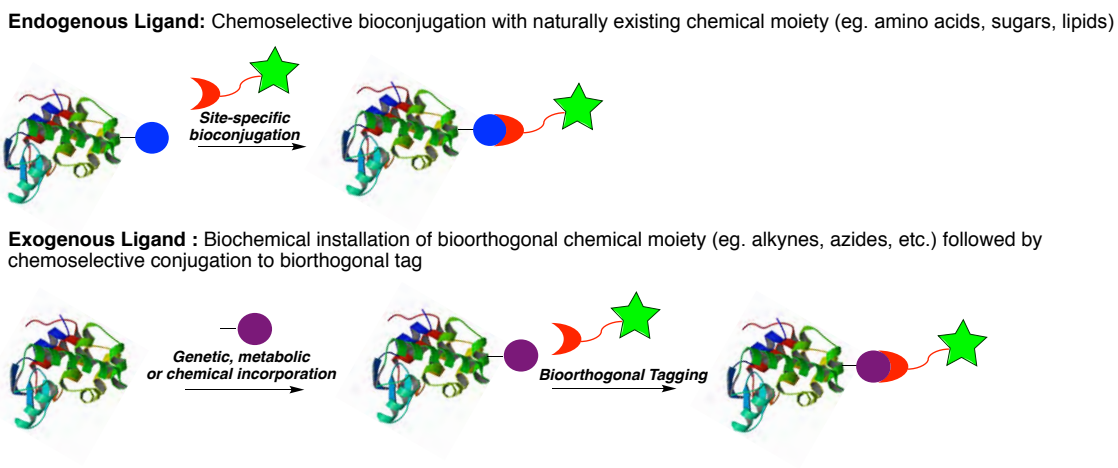

Figure 1-4. Comparison of bioorthogonal chemistries involving selective labeling of endogenous and exogenously installed ligands.

1.2.2 Drawbacks of "Traditional" Bioorthogonal Chemistries

There are a variety of drawbacks associated with these outlined bioorthogonal chemistries, which prohibit their application as truly biocompatible chemical functionalities in certain biological contexts (**Scheme 1-1**).[25] Some examples include the necessity of high concentrations of copper (I) in applications of CuACC, which may create toxicity issues, or the slow reaction rates of certain SPAAC chemistries. Indeed, most "bioorthogonal" chemistries actually struggle to achieve true biocompatibility due to toxicity at the concentrations necessary to produce fast reaction rates, or conversely the reagents are non-toxic, but the reaction rate is quite slow. Ultimately, we strive to achieve optimization of both bioorthogonality parameters to ensure maximal effectiveness and biocompatibility of the chemistries.

Scheme 1-1. Drawbacks of common bioorthogonal chemistries (modified from Ref. 16).

Hydrazone/Oxime Condensation

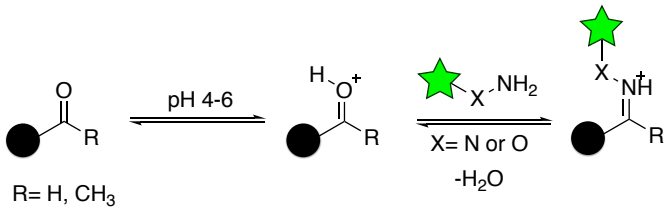

- Moderately acidic pH required (4-6)
- Slow reaction rates (10^{-4}-20 $M^{-1}s^{-1}$)
- Aniline catalyst required to improve reaction rate
- Adducts prone to hydrolysis

Staudinger Ligation

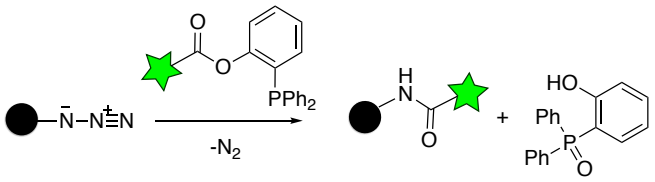

- Slow reaction rates (10^{-3} $M^{-1}s^{-1}$)
- Phosphines susceptible to hydrolysis

Cu(I) Catalyzed Azide-Alkyne Click Chemistry

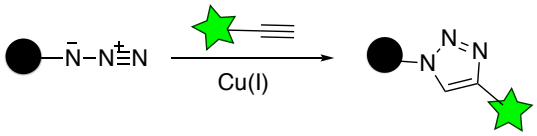

- Copper catalysts and ligands required to achieve fast reaction rates (10-200 $M^{-1}s^{-1}$)

Strain-Promoted Azide-Alkyne Click Chemistry

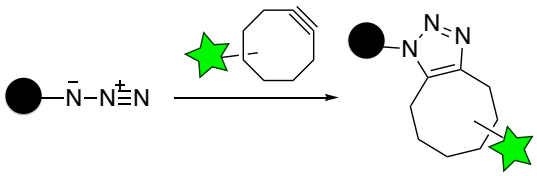

- Slow to moderate reaction rates (10^{-2}-2 $M^{-1}s^{-1}$)

Inverse Electron Demand Diels Alder

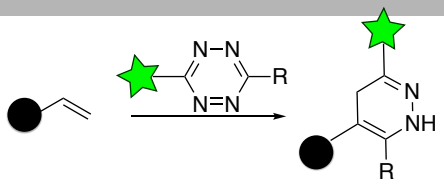

- Tetrazines may be susceptible to hydrolysis
- Trans-cyclooctene prone to isomerization/side reaction with thiols

1.2.3 Emergence of Boronic Acid Chemistries For Chemoselective Bioorthogonal Conjugation

With a continued interest in the discovery of novel biocompatible conjugation reactions, our research has focused on exploration of a new class of such reactions, which exploits the unique reactivity of aryl ketones and aldehydes with an *ortho*-boronyl substituent (**Figure 1-5**). For these boronic acid-mediated bioorthogonal reactions, 2-formyl and 2-acetyl phenylboronic acid (2-FPBA and 2-APBA) have been found to conjugate with a variety of amines and α-nucleophiles with rate constants $>10^3$ $M^{-1}s^{-1}$, which is orders of magnitude greater than that of the aforementioned azide-alkyne click chemistry.[27]

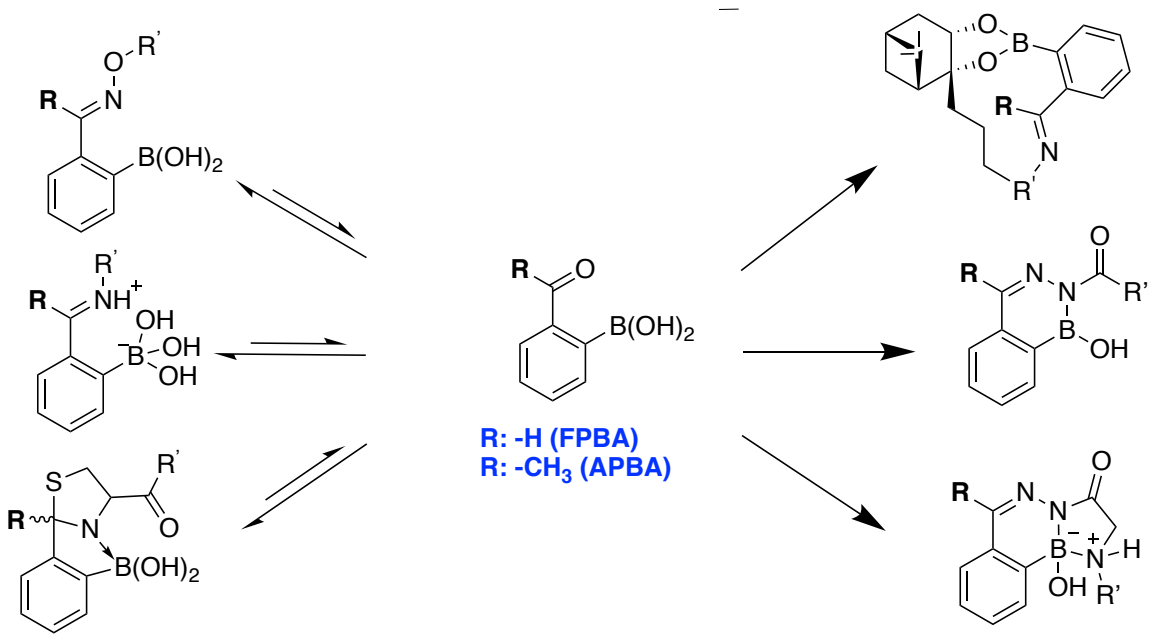

Figure 1-5. Diverse conjugation chemistries of 2-FPBA/2-APBA display varied product stability and reaction reversibility. The conjugation partners include functional groups of biomolecules, as well as non-natural nucleophiles designed for bioorthogonal conjugation (figure modified from Ref. 27).[27]

In addition to the fast reaction rates, these boronic acid accelerated reactions conjugate to a variety of reactive partners, which affords diverse product structures with distinct thermodynamic and kinetic stabilities. Both covalent and reversible covalent approaches have been taken in the discovery of boronic acid accelerated bioorthogonal chemistries, with each having their own advantages. While irreversible, covalent chemistries afford higher binding potency, they often induce high toxicity as a result of off-target labeling and subsequent immunogenicity. Conversely, reversible covalent chemistries suffer diminished potency, yet do not exhibit significant biological toxicity due the transient and reversible nature of binding. This ability to tune reaction profiles affords the boronic acid accelerated bioorthogonal chemistries a unique capability to be applied for a wide array of different biocompatible applications in accordance with the designated biological target (e.g. amines, N-terminal cysteines, exogenously installed α-nucleophile)[25], as well as the desired kinetic and thermodynamic properties.[27]

One example of a bioorthogonal boronic acid-accelerated reaction that will be further explored and applied throughout this manuscript is that of simple iminoboronate formation.[28] Iminoboronate chemistry was derived from simple imine formation of amines and ketones, which has a K_d of ~300 M, indicating that even with millimolar concentrations of reagents, the conjugate is formed in minimal amounts. However, by installing an *ortho* boronic acid, the reaction is accelerated and the K_d is reduced to low millimolar concentrations as a result of the formation of an ion-pair interaction between boron and nitrogen (**Figure 1-6**).[29] This increased thermodynamic stability allows for facile conjugation of 2-APBA and 2-FPBA to a variety of amine-presenting biological targets, including lysines in proteins[30], and in our case, amines on the surface of bacterial

cell walls via lipids (e.g. PE, Lys-PG)[28] and bacterial cell surface sugar modifications (e.g. phosphoethanolamine modification of Lipid A). In terms of biocompatibility, iminoboronate formation harnesses fast and dynamic conjugation capabilities in biological settings. While the iminoboronate chemistry itself is less than desirable in terms of target specificity considering the abundance of amines in cellular contexts, we have been able to incorporate these 2-APBA motifs into high throughput screening platforms to enhance target selectivity by direct target-based screening methodologies.[31] Through these applications, we have been able to transform the boronic acid warheads into key chemical motifs for binding to an array of distinct biological targets, including proteins and whole bacterial cells.

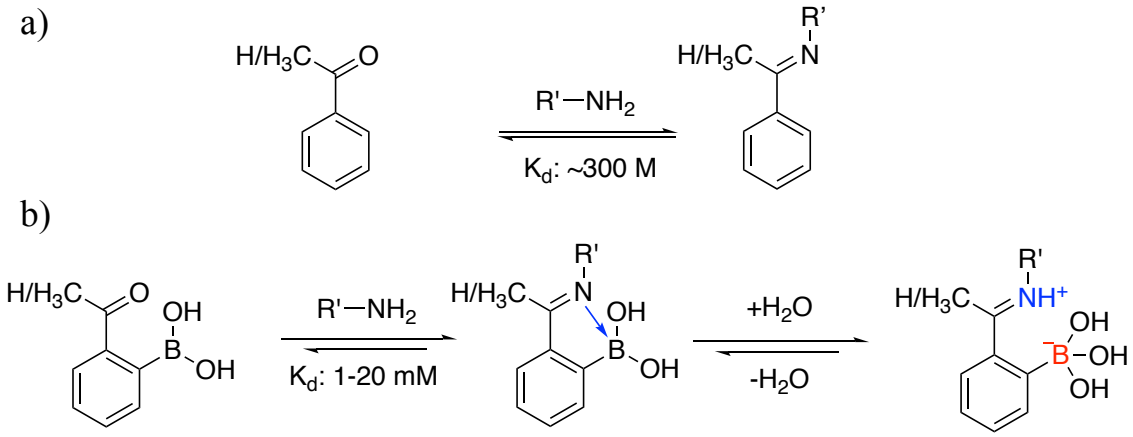

Figure 1-6. Amine conjugation by (a) simple aryl ketones/aldehydes and (b) *ortho* boronic acid ketones and aldehydes displays the improvement of the thermodynamics of conjugation by boronic acid incorporation.

Beyond iminoboronate chemistry, we have also explored applications of bioorthogonal boronic acid-mediated chemoselective chemistries towards reversible conjugation of free and N-terminal cysteines[32], as well as irreversible conjugation to unnatural α-nucleophiles, such as semicarbazide.[33,34] This toolbox of bioorthogonal

boronic acid accelerated reactions has afforded us an arsenal of weapons with which we have investigated the selective labeling of bacteria to develop solutions for the current urgent state of the antibiotic resistant threat.

1.3 Conclusions

The aims of the research described throughout this manuscript exist at the intersection of biocompatible chemoselective chemistries and bacterial targeting, with the former informing our capabilities in tackling in the latter. While our application of amine-targeting chemistries via iminoboronate formation toward bacterial targeting was inspired by the chemoselective targeting of amines in proteins (e.g. lysine side chains) in biologically relevant contexts[30], we have sought to apply this reversible covalent approach towards selective identification of bacterial species. Through this pursuit, we have been able to exploit both amine-modified lipids in the cell wall of bacteria[28], as well as amine presentation differences in bacterial cell wall composition in non-resistant and resistant strains of bacteria via a high throughput peptide screening approach.[31] Similarly, this APBA assisted high throughput screening approach has been applied to the discovery of potent protein (e.g. human beta defensin 3) binding peptides. Moreover, we have been able to transform and expand our boronic acid chemistry toolbox beyond simple amines to selectively target naturally (e.g. cysteine)[32] and exogenously installed unnatural chemical moieties (e.g. semicarbazide)[33,34], with varying degrees of kinetic and thermodynamic stability.

Thus, the research outlined herein summarizes our efforts to both 1) discover novel bioorthogonal chemistries to enhance our development of both protein and bacterial targeting molecules via conjugation to either naturally presented or

metabolically incorporated chemical functionalities, as well as 2) the application of those new chemoselective biocompatible technologies to achieve potent and selective binding to bacterial strains and proteins of interest, towards completion of the following aims:

1. Modulating the reversible amine and cysteine conjugation properties of APBA/FPBA via synthetic analogues (**Chapter 2**)
2. Detection of bacterial pathogens via stable diazaborine formation of APBA and semicarbazide (**Chapter 3**)
3. Discovery of APBA dimer CX_7C peptides selective for detection of various mechanisms of colistin resistance in Gram-negative bacteria (**Chapter 4**)
4. Development of targeted APBA dimer CX_7C peptides towards the bacterial-related protein human beta defensin 3 (**Chapter 5**)

1.4 References

1. Hampton, T. Report Reveals Scope of US Antibiotic Resistance Threat. *JAMA* **310,** 1661–1663 (2013).
2. CDC. Antibiotic Resistance Threats. 1–114 (2013). Available at: https://www.cdc.gov/drugresistance/pdf/ar-threats-2013-508.pdf.
3. Fox, J. L. The business of developing antibacterials. *Nat. Biotechnol.* **24,** 1521–1528 (2006).
4. Waksman, S. A. Streptomycin: Background, Isolation Properties, and Utilization. *Science* **118,** 259–266 (1953).
5. Lyddiard, D., Jones, G. L. & Greatrex, B. W. Keeping it simple : lessons from the golden era of antibiotic discovery. *FEMS Microbiol. Lett.* **363,** 1–3 (2016).
6. Beiras-Fernandez, A., Vogt, F., Sodian, R. & Weis, F. Daptomycin : a novel lipopeptide antibiotic against Gram-positive pathogens. *Infect. Drug Resist.* 95–101 (2010). doi:10.2147/IDR.S6961
7. Lewis, K. Platforms for antibiotic discovery. *Nat. Rev.* **12,** 371–387 (2013).
8. Brown, L., Wolf, J. M., Prados-Rosales, R. & Casadevall, A. Through the wall : extracellular vesicles in Gram-positive bacteria, mycobacteria and fungi. *Nat. Rev. Microbiol.* **13,** 620–630 (2015).
9. Crofts, T. S., Gasparrini, A. J. & Dantas, G. Next-generation approaches to understand and combat the antibiotic resistome. *Nat. Rev. Microbiol.* **15,** 422–434 (2017).
10. Poole, K. Efflux-mediated antimicrobial resistance. *J. Antimicrob. Chemother.* **56,** 20–51 (2005).

11. Lambert, P. A. Bacterial resistance to antibiotics: Modified target sites. *Adv. Drug Deliv. Rev.* **57,** 1471–1485 (2005).

12. Beauclerk, A. A. D., Cundliffet, E. & Lel, L. Sites of Action of Two Ribosomal RNA Methylases Responsible for Resistance to Aminoglycosides. *J. Mol. Biol.* **193,** 661–671 (1987).

13. Alper, P. B. *et al.* Probing the Specificity of Aminoglycoside Ribosomal RNA Interactions with Designed Synthetic Analogs. *J. Am. Chem. Soc.* **120,** 1965–1978 (1998).

14. Epand, R. M., Walker, C., Epand, R. F. & Magarvey, N. A. Molecular mechanisms of membrane targeting antibiotics. *Biochim. Biophys. Acta* **1858,** 980–987 (2016).

15. Wright, G. D. Bacterial resistance to antibiotics: Enzymatic degradation and modification. *Adv. Drug Deliv. Rev.* **57,** 1451–1470 (2005).

16. Gardete, S. & Tomasz, A. Mechanisms of vancomycin resistance in Staphylococcus aureus. *J. Clin. Invest.* **124,** 2836–2840 (2014).

17. Gold, H. S. Vancomycin-Resistant Enterococci: Mechanisms and Clinical Observations. *Antimicrob. Resist.* **33,** 210–219 (2001).

18. van Hoek, A. H. A. M. *et al.* Acquired antibiotic resistance genes: an overview. *Front. Microbiol.* **2,** 1–27 (2011).

19. Wright, G. D. The antibiotic resistome: the nexus of chemical and genetic diversity. *Nat. Rev. Microbiol.* **5,** 175–186 (2007).

20. Lee, C., Lee, J. H., Park, M., Park, K. S. & Bae, I. K. Biology of Acinetobacter baumannii: Pathogenesis, Antibiotic Resistance Mechanisms, and Prospective Treatment Options. *Front. Cell. Infect. Microbiol.* **7,** 1–35 (2017).

21. Garber, K. A β-lactamase inhibitor revival provides new hope for old antibiotics. *Nat. Rev. Drug Discov.* **14,** 445–447 (2015).

22. Smith, P. A. *et al.* Optimized arylomycins are a new class of Gram-negative antibiotics. *Nature* **561,** 189–194 (2018).

23. Ling, L. L. *et al.* A new antibiotic kills pathogens without detectable resistance. *Nature* **517,** 455–459 (2015).

24. Sletten, E. M. & Bertozzi, C. R. Bioorthogonal Chemistry: Fishing for Selectivity in a Sea of Functionality. *Angew. Chemie Int. Ed.* **48,** 6974–6998 (2009).

25. Akgun, B. & Hall, D. G. Boronic Acids as Bioorthogonal Probes for Site-Selective Labeling of Proteins. *Angew. Chemie Int. Ed.* **57,** 13028–13044 (2018).

26. Mckay, C. S. & Finn, M. G. Review Click Chemistry in Complex Mixtures: Bioorthogonal Bioconjugation. *Chem. Biol.* **21,** 1075–1101 (2014).

27. Cambray, S. & Gao, J. Versatile Bioconjugation Chemistries of ortho-Boronyl Aryl Ketones and Aldehydes. *Acc. Chem. Res.* **51,** 2198–2206 (2018).

28. Bandyopadhyay, A., McCarthy, K. A., Kelly, M. A. & Gao, J. Targeting bacteria via iminoboronate chemistry of amine-presenting lipids. *Nat. Commun.* **6,** 6561–6569 (2015).

29. Collins, B. E. *et al.* Probing Intramolecular B-N Interactions in Ortho-Aminomethyl Arylboronic Acids. *J. Org. Chem.* **74,** 4055–4060 (2009).

30. Cal, P. M. S. D. *et al.* Iminoboronates : A New Strategy for Reversible Protein Modi fi cation. *J. Am. Chem. Soc.* **134,** 10299–10305 (2012).

31. McCarthy, K. A. *et al.* Phage Display of Dynamic Covalent Binding Motifs Enables Facile Development of Targeted Antibiotics. *J. Am. Chem. Soc.* **140,**

6137–6145 (2018).

32. Bandyopadhyay, A., Cambray, S. & Gao, J. Fast and selective labeling of N-terminal cysteines at neutral pH via thiazolidino boronate formation. *Chem. Sci.* **7,** 4589–4593 (2016).

33. Bandyopadhyay, A., Cambray, S. & Gao, J. Fast Diazaborine Formation of Semicarbazide Enables Facile Labeling of Bacterial Pathogens. *J. Am. Chem. Soc.* **139,** 871–878 (2017).

34. Cambray, S., Bandyopadhyay, A. & Gao, J. Fluorogenic diazaborine formation of semicarbazide with designed coumarin derivatives. *Chem. Comm.* **53,** 12532–12535 (2017).

CHAPTER 2

Modulating the Reversible Amine and Cysteine Conjugation Properties of 2-Acetylphenylboronic Acid (2-APBA) and 2-Formylphenylboronic Acid (2-FPBA) via Synthetic Analogues

2.1 Introduction

2.1.1 Reversible Conjugation of Amines via Iminoboronate Formation with 2-Formyl/Acetylphenyl Boronic Acid

Schiff base, or imine, formation plays an important catalytic role in enzymes throughout nature via reversible conjugation to amines. A well-known application of imine formation in enzyme catalysis is that of the pyridoxal phosphate (PLP) co-enzyme, whose aldehyde forms an imine linkage with a lysine side chain on the related enzyme; notably, this interaction is stabilized via several hydrogen bond linkages between the enzyme and *ortho*-phenoxide moiety in the cofactor to yield an association constant of $1x10^3$ M^{-1} (K_d~1 mM).[1,2]

Without such assistance from additional bonding interactions, simple Schiff base formation is thermodynamically unfavorable under physiologic conditions. For example, the imine forming reaction of glycine with acetone yields a dissociation constant of nearly 300 M (K_a~$3x10^{-3}M^{-1}$), indicating that the imine conjugate is formed only at parts per million levels, even with millimolar concentrations of reactants.[2] Yet, as observed with PLP, the thermodynamic stability of imine formation can be tuned by modifying the chemical functionalities adjacent to the reactive aldehyde/ketone (**Figure 2-1**).

In order to improve the kinetic reactivity and thermodynamic stability of the imine conjugation reaction, chemists have sought methods to improve the thermodynamic stability of imine formation via incorporation of *ortho* boronic acids into the molecular scaffold with 2-formyl/acetylphenyl boronic acid (2-FPBA/2-APBA). Both molecules undergo iminoboronate formation with primary amines at low millimolar concentrations of reactants in neutral aqueous media (**Figure 2-1**).[3–8] While 2-APBA is

selective for unhindered amines, such as lysine side chains[7], 2-FPBA is amenable to conjugation of more sterically hindered amines (e.g. α-amines of peptides).[4] The thermodynamic stabilization provided by the boronic acid could potentially be rationalized by formation of an N-B dative bond; indeed, an ^{11}B NMR study[9] has shown that iminoboronate formation of 2-FPBA in methanol predominantly gives a solvent-inserted zwitterionic structure.[10,11] Thus, an ion-pair interaction is likely the source of the greater thermodynamic stability of iminoboronates in comparison to imines.

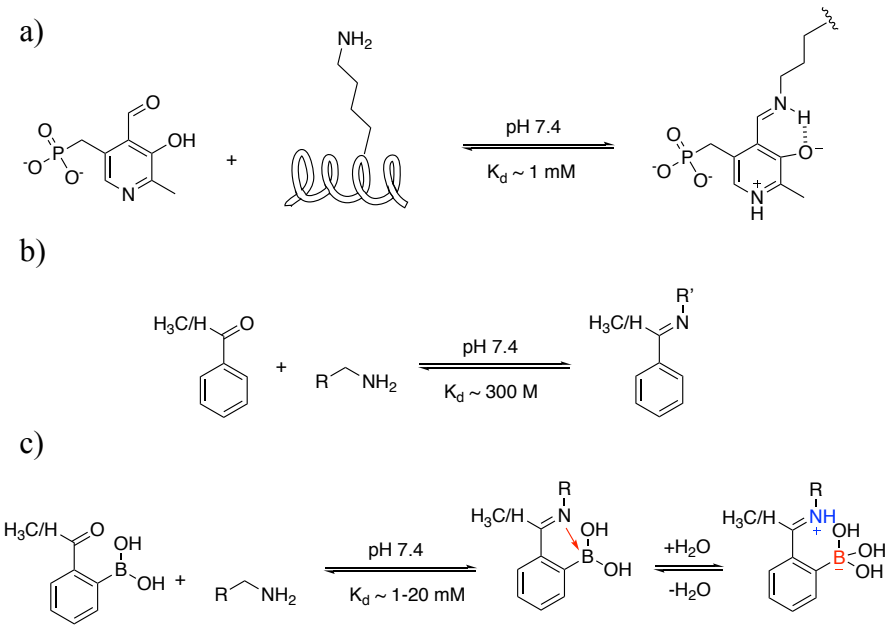

Figure 2-1. Evolution of thermodynamically unfavorable imine formation into the more stable iminoboronate conjugate. (a) PLP coenzyme catalysis employs imine formation with enzyme lysine residues, which are thermodynamically stabilized by hydrogen bonds. (b) Simple imine formation forms unstable amine conjugates only at ≥ molar concentrations. (c) Iminoboronate formation employs an *ortho* boronic acid on a benzaldehyde or acetophenone scaffold to achieve improved thermodynamic stability via an ion pair interaction.

While iminoboronates experience greater thermodynamic stability than their imine counterparts, they maintain rapid reversibility (i.e. accelerated forward and backward reactions) under physiologic conditions, which can be rationalized by the N-B

coordination or imine protonation resulting from solvent insertion.[7] Both the thermodynamic stability and rapid reversibility make iminoboronates analogous to hydrogen bonds; however, iminoboronate formation is specific for primary amines and yields stronger transient bonds (3-4 kcal/mol energy gain versus 1-2 kcal/mol for hydrogen bonds).[7,12,13]

It is feasible that incorporation of the iminoboronate dynamic covalent binding motif in ligand design could lead to reversible covalent probes and inhibitors that bind to a desired target in complex biological systems. In one such instance, 2-APBA incorporation into a cationic peptide (H-Lys-AB1) yielded selective labeling of *Staphylococcus aureus* bacterial cells in complex mixtures of mammalian cells and blood serum.[7] This targeted binding phenomenon is facilitated by the host defense evasion mechanism of *S. aureus*, that induces the overexpression of lysyl phosphatidylglycerol (Lys-PG), which can undergo facile iminoboronate formation with the APBA motifs in H-Lys-AB1 (**Figure 2-2**). Furthermore, APBA motifs can be incorporated into peptide libraries on phage, enabling facile selection of reversible covalent peptide probes that are selective binders to a wide array of bacterial species by whole cell screening, as will be later discussed.[14]

Other recent biological applications of iminoboronate chemistry beyond bacterial labeling have focused on the development of reversible covalent protein inhibitors. Protein modification via lysine-directed iminoboronate chemistry was first introduced by Gois and co-workers towards labeling of purified proteins, which was not intended to be site-specific.[5,15] Alternatively, Su and co-workers have reported targeted covalent inhibition of Mcl-1 via incorporation of 2-APBA into a previously identified non-

covalent ligand (**Figure 2-2**).[6,16] These iminoboronate capable inhibtors displayed 20-50 times better binding affinity in comparison to their non-covalent counterparts (IC_{50}~3 nM). Notably, only the protein-iminoboronate capable inhibitor adduct was observed by LC-MS analysis, whereas no protein-APBA adduct was detectable due to the rapid reversibility of iminoboronate formation, thus highlighting the importance of the non-covalent interactions in adduct stabilization. While reversible covalent inhibitors bearing boronic acids have been previously reported for targeting alcohols and thiols (eg. Velcade and PRN1008)[17–19], this contribution by Su *et al.* is the first report of an iminoboronate-capable reversible covalent protein inhibitor.

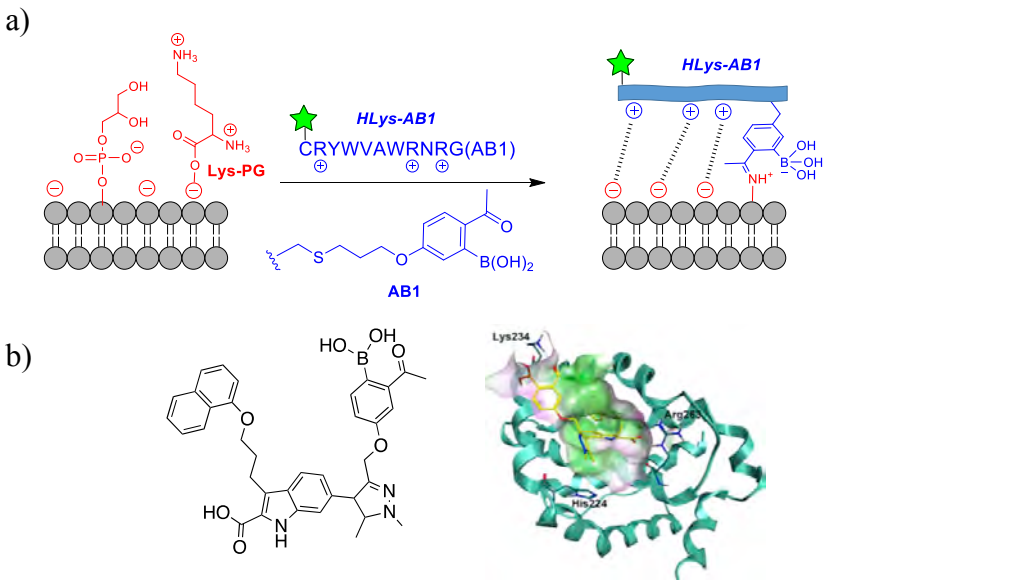

Figure 2-2. Biological applications of iminoboronate formation towards conjugation of biological amines. (a) APBA iminoboronate formation with Lys-PG synergizes with electrostatic interactions of cationic peptides (H-Lys) to enable facile targeted labeling of bacterial cells. (b) Iminoboronate mediated inhibition of Mcl-1 via 2-APBA incorporation into a non-covalent ligand of Mcl-1, with ligand structure (left) and protein-inhibitor complex (right) shown (figure adapted from Ref. 6).

2.1.2 Discovery of N-Terminal Cysteine Conjugation Capabilities of 2-Formyl/Acetylphenyl Boronic Acid

While iminoboronate formation favors unhindered amines (e.g. lysine side chains) over more hindered amines, such as the α-amine of alanine, 2-APBA has interestingly been shown to reversibly conjugate to free or N-terminal cysteine at sub-millimolar concentrations.[20] The distinct reactivity of cysteine results from the side-chain thiol attacking the iminoboronate to form a thiazolidino boronate (TzB) complex. TzB formation with cysteine has been reported for both 2-APBA and 2-FPBA, with the former displaying low millimolar binding affinity, whereas the latter experiences facile conjugation at low micromolar concentrations (**Figure 2-3**).[21,22] The kinetics of conjugation showed rates $>10^3$ $M^{-1}s^{-1}$ in comparison to cysteine conjugation with unsubstituted benzaldehyde, which requires several days to achieve conjugation, even under conjugation-favorable acidic conditions.[23] The fast kinetics of TzB formation can be attributed to boronic acid activation of the imine intermediate, as supported by the observation of rapid conjugation of 2-FPBA and 2-aminophenol.[24]

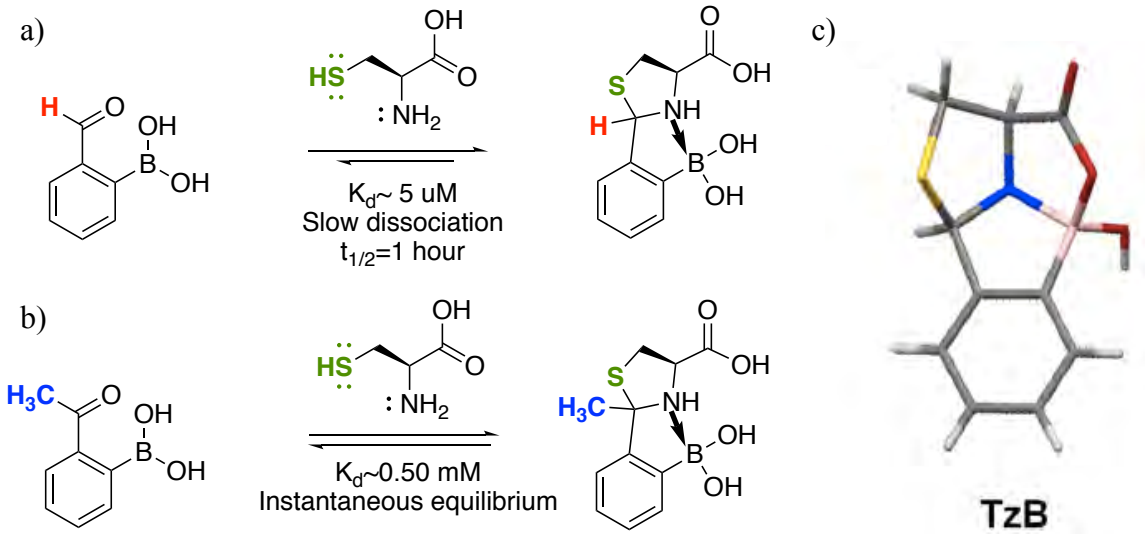

Figure 2-3. Conjugation of 2-FPBA and 2-APBA to cysteine forms thiazolidinoboronates (TzBs). (a) 2-FPBA conjugates with cysteine at low micromolar concentrations, yielding a more stabilized TzB. (b) 2-APBA conjugates with cysteine at low millimolar concentrations to form a rapidly reversible TzB. (c) X-ray crystal structure (obtained by Dr. Anupam Bandyopadhyay) of the TzB complex formed with cysteine and 2-FPBA in 1:1 MeOH/H_2O (gray=C, yellow=S, red=O, blue=N, pink=B).

In addition to their vastly different binding affinities, 2-FPBA and 2-APBA also display distinct reaction profiles of TzB formation. While 2-APBA conjugates with cysteine at sub-millimolar concentrations in a rapidly reversible manner, 2-FPBA forms a more stable TzB conjugate that dissociates over the course of several hours. Importantly, the TzB formation of 2-FPBA has shown to be highly chemoselective, as little interference in N-terminal cysteine conjugation was observed from glutathione, cysteine, serine or lysine. Additionally, the thermodynamic stability of 2-FPBA conjugates with cysteine has been shown to be pH-dependent, whereby the TzB complex rapidly dissociates at acidic pH (**Figure 2-4**). These properties afford 2-FPBA with a unique N-terminal cysteine protein labeling capacity in physiologic conditions, at low micromolar concentrations in as little as a few minutes, that can be manipulated by environmental

conditions.[21] While cysteine residue-specificity cannot afford protein or site-specific labeling capabilities in complex biological mixtures, the N-terminal cysteine specificity provided by APBA/FPBA conjugation may prove advantageous for more site-selective labeling. Conversely, 2-APBA conjugates dynamically with cysteine, which similar to iminoboronate formation, is appealing for the development of reversible covalent protein inhibitors. Given the wide thermodynamic range in forming TzB conjugates by 2-FPBA and 2-FPBA, it is feasible that the thermodynamic and kinetic properties of TzB conjugation should be further tunable via construction of synthetic analogues of these molecules.

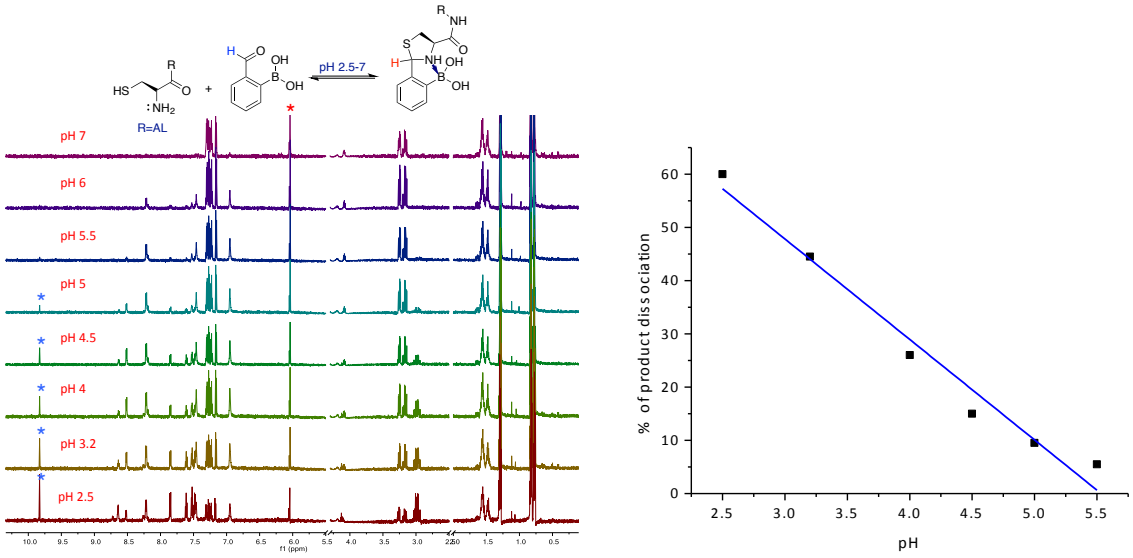

Figure 2-4. pH-triggered reversibility of the TzB conjugate of 2-FPBA and an N-terminal cysteine-containing peptide, CAL, as shown by (a) ^{1}H NMR analysis and (b) a plot of the percentage of TzB dissociated at each pH point, as determined by integration of the 2-FPBA (*) and TzB (*) formyl chemical shifts (data collected by Dr. Anupam Bandyopadhyay).

2.1.3 Synthesis of Analogues for Modulating the Conjugate Properties of 2-APBA

With our knowledge of the power of simple 2-FPBA/2-APBA towards binding of amines and cysteines, we questioned if the binding properties of these powerful chemical

motifs could be altered to enhance binding affinity. Thus, we pursued optimization of the structure of 2-APBA, which was amenable to alterations at several positions on the phenyl ring, through a drug discovery inspired route. The process of drug discovery has traditionally followed the pathway of: 1) target discovery, 2) target validation, 3) screening and identification of hits, 3) lead optimization and drug development, and 5) clinical trials and FDA approval.[25] A highly important step in this process is lead optimization, where potential drugs' properties are altered to maximize their potential as therapeutic compounds. While synthetic compounds may display pharmacological activity, their other important drug properties, such as drug interactions or ADME (absorption, distribution, metabolism and excretion), may prohibit their transition to the clinic. One notable example in medicinal chemistry of the importance of lead optimization is that of Glivec, a notable chemotherapeutic agent.[26] While a lead compound was initially identified by screening for inhibitors of protein kinase C, different alterations to the core structure enabled enhancement of activity, abolished undesired interaction with non-target proteins, and improved the solubility and oral bioavailability properties of the drug (**Figure 2-5**). Thus, structural optimization is a key step in the transformation of a candidate molecule for biological applications into its final structural composition.

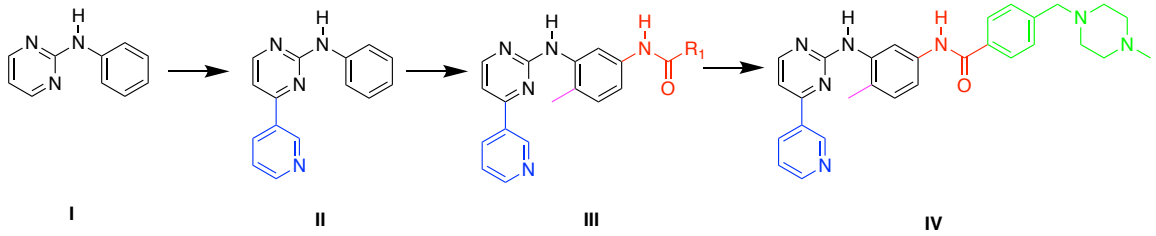

Figure 2-5. Hit to lead compound development (I-IV) of the chemotherapeutic agent Glivec underscores the utility of structural optimization in the generation of potent, biocompatible compounds.

Inspired by the transformation of good compounds into great compounds, we ventured to determine if structural analogues of 2-APBA could improve the binding properties (eg. thermodynamic stability, kinetics) of 2-formyl/acetylphenyl boronic acids towards amine and cysteine conjugation.

2.2 Modulating the Readily Reversible Amine Conjugation of 2-APBA with Synthetic Analogues

2.2.1 Design of Panel of Synthetic 2-APBA Analogues

Towards this goal of generating more thermodynamically and kinetically superior amine and cysteine conjugating APBA warheads, we designed a set of compounds with altered electronic properties to enable varied binding capabilities (**Scheme 2-1**). For some compounds, the 2-APBA scaffold was manipulated to include electron withdrawing functional group(s), such as fluorine (-F) or nitrogen dioxide ($-NO_2$). In other cases, the scaffold was altered to incorporate an electron donating group, such as methoxy ($-OCH_3$).[27] We hypothesized that the electron withdrawing groups would promote greater Lewis acidity at the electron poor boron atom to enable greater conjugate stability, and that electron donating analogues would have the opposite effect. Indeed, a similar approach was recently reported to enhance protein-ligand affinity by reversible covalent modification of lysine residues with a library of benzaldehyde derivatives.[28] Through lysine binding studies, it was determined that a 2-hydroxybenzaldehyde analogue with a fluorine in the *meta* position afforded the most efficient imine formation with a binding dissociation constant (K_d) of about 20 mM. In comparison, simple 2-hydroxybenzaldehyde showed no detectable imine formation at 20 mM lysine; therefore,

it is feasible that alteration of the substituents on 2-APBA could similarly produce analogues with improved binding properties to both amines and cysteines.

Scheme 2-1. Panel of 2-APBA analogues for analysis of altered amine and cysteine kinetic and thermodynamic binding properties, with parent compounds (2-APBA and 2-FPBA) shown for reference. Numbering of the core structure is shown on 2-APBA.

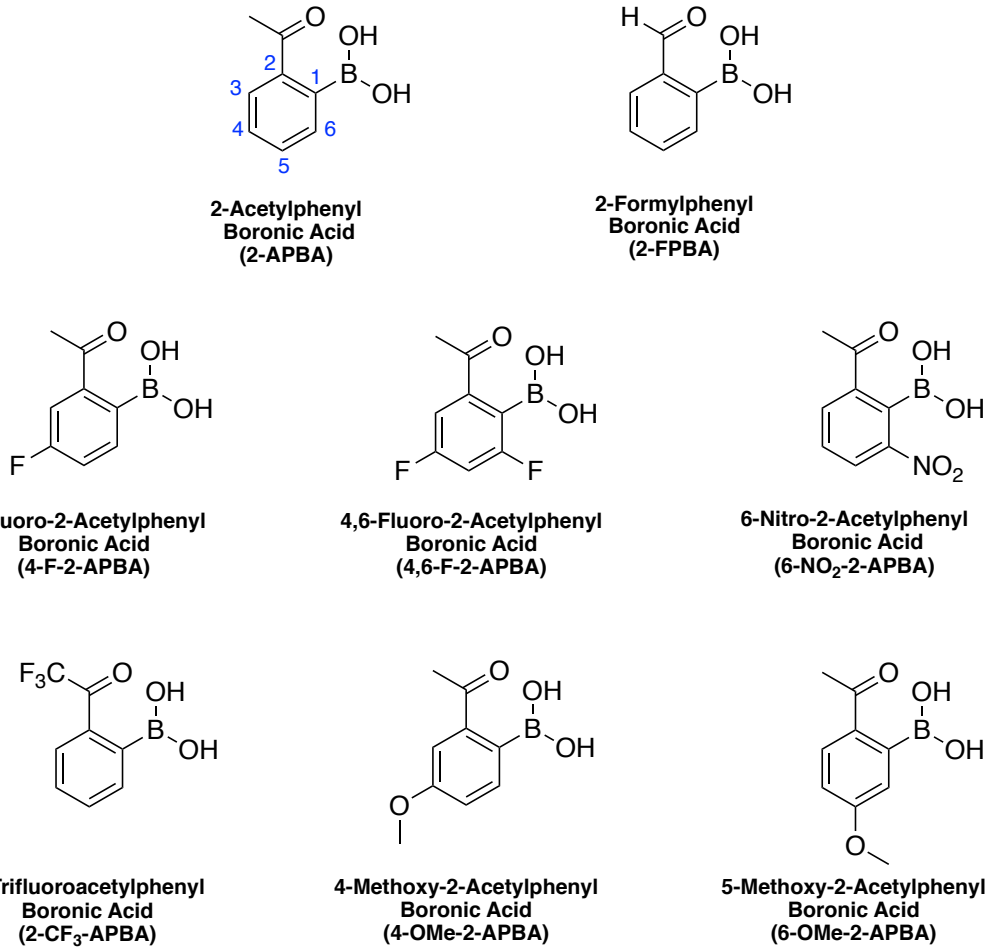

2.2.2 Synthesis of 2-APBA Analogues

In order to synthesize the 2-APBA analogues, two different synthetic approaches were taken. In the first two-step route, a bromine substituted starting material was directly subjected to Miyaura borylation, then the purified pinacol substituted product was pinacol deprotected and again purified to yield the final product (**Scheme 2-2**).

Scheme 2-2. Two-step synthetic route to desired 2-APA analogues. Synthesis requires 1) Suzuki-Miyaura borylation, and 2) pinacol deprotection to yield the desired boronic acid substituted 2-APBA analogues.

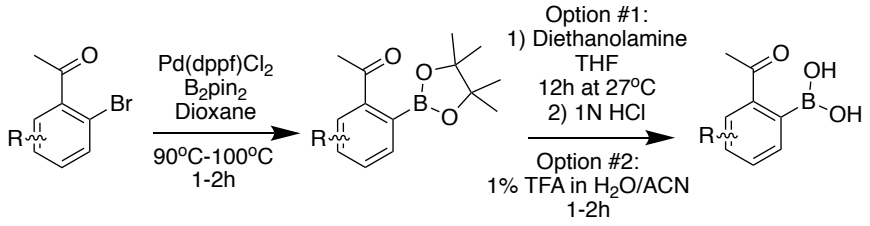

The secondary synthetic route was accessed upon initial synthesis of the majority of 2-APBA analogues using the first route given the high cost of the bromine substituted starting material in comparison to hydroxyl substituted. For the alternative route, the hydroxyl substituted starting material first underwent triflate protection to enable Suzuki-Miyaura borylation of the purified triflate protected product. The purified pinacol substituted product was again subjected to pinacol deprotection and purified to yield the desired boronic acid (**Scheme 2-3**).

Scheme 2-3. Three-step synthetic route to desired 2-APBA analogues. Synthesis requires 1) triflate protection, 2) Suzuki-Miyaura borylation, and 3) pinacol deprotection to yield the desired boronic acid substituted 2-APBA analogues.

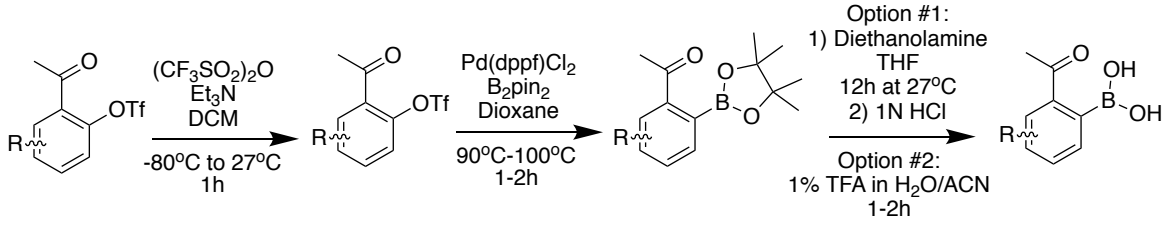

One challenge in the synthesis of these analogues was determining the optimal reaction duration and temperature to achieve minimal protodeboronated side product during the Suzuki-Miyaura borylation step. In general, the approach taken was to start with a low temperature (~80°C) and allow the reaction to proceed for a short period of time (~0.5 hour), and monitor the reaction by TLC with a p-anisaldehyde stain. The

starting material, desired borylated product, and undesired protodeboronated product all stained distinctly (yellow vs. blue-green vs. orange) to afford clear reaction progress monitoring. After these conditions were applied, the reaction was checked and if no reaction was observed, the temperature was increased by 5^{o}C and continued while monitoring in ~15 minute increments. The process was continued until the majority of starting material was consumed, or protodeboronated product was observed.

Another challenge encountered during the synthesis of these APBA analogues was in determining the optimal pinacol deprotection conditions. In some cases, simple acidic hydrolysis with trifluoroacetic acid in a water/acetonitrile mixture was sufficient for deprotection of the analogues within a few hours. In other cases, an alternative strategy involving transesterification with diethanolamine in tetrahydrofuran stirred overnight, then acidified with HCl was necessary to achieve deprotection of the pinacol group. However, between these two methodologies, we were able to achieve efficient deprotection of all analogues to enable purification of the boronic acid substituted products.

2.2.3 UV-Vis Analysis of 2-Methoxyethylamine (MEA) Binding Profiles of 2-APBA Analogues

To assess the iminoboronate formation of the 2-APBA analogues with amines, we titrated in (0-60 mM) a model primary amine, 2-methoxyethylamine (MEA), to a fixed concentration of the 2-APBA analogue (50 μM). Throughout the titration, we monitored the shift in maximal UV-Vis absorption from ~254 nm for the boronic acid to ~280 nm for the iminoboronate. Simple 2-APBA and 2-FPBA were first titrated to determine the dissociation constants for the parent compounds, which were 15 mM and 20 mM,

respectively. We then carried out titrations of the synthesized 2-APBA analogues. The UV-Vis spectra (**Figure 2-6**), fitted plots (**Figure 2-7**), and compiled dissociation constants (**Table 2-1**) are shown.

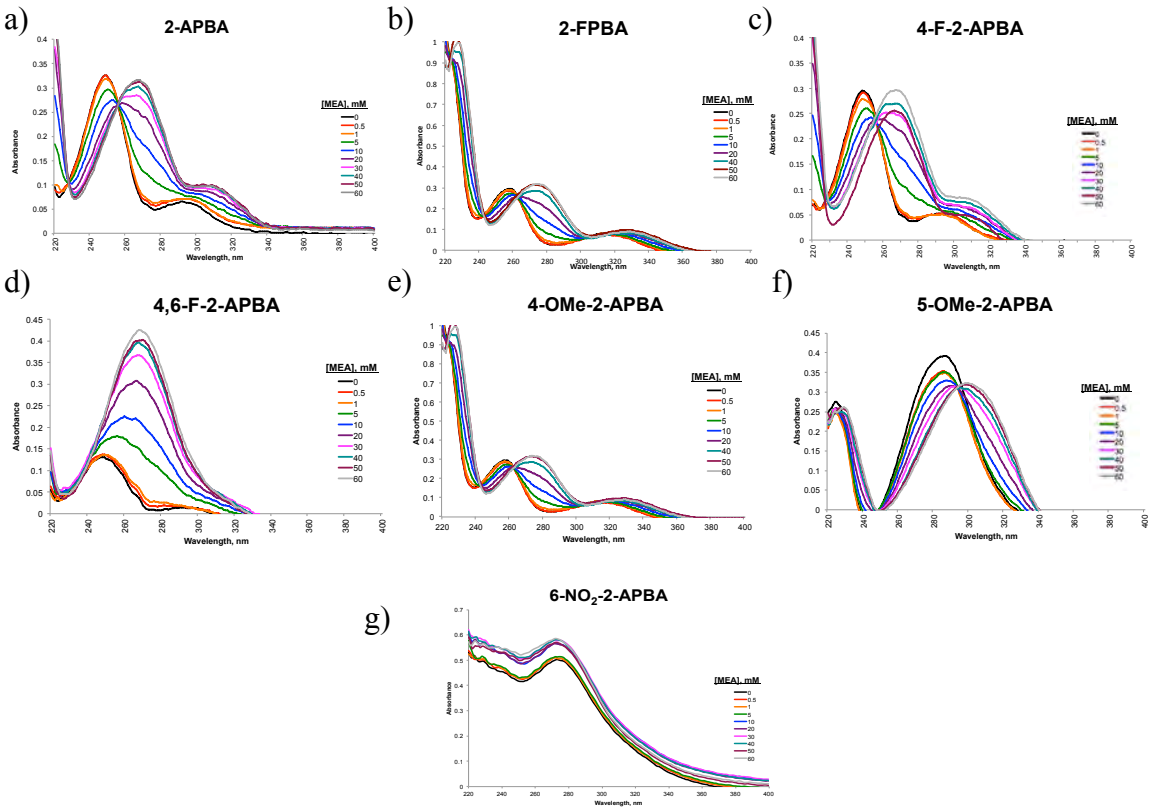

Figure 2-6. UV-Vis titration of (a) 2-APBA, (b) 2-FPBA, (c) 4-F-2-APBA, (d) 4,6-F-2-APBA, (e) 4-OMe-2-APBA (f) 5-OMe-2-APBA and (g) 6-NO_2-2-APHA with MEA displays the shift in maximal absorption wavelength from ~254 nm to ~280 nm. The absorbance ~280 nm at each MEA concentration point were used to determine the binding dissociation constants.

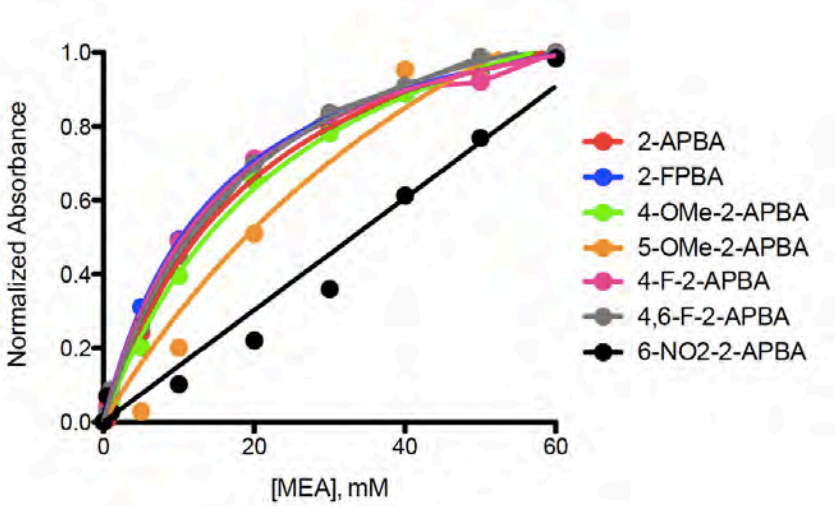

Figure 2-7. Compiled normalized MEA titration plots for 2-APBA, 2-FPBA and associated analogues, which were fit to determine dissociation constants (K_d).

Table 2-1. Dissociation constants (K_d) determined from the fit of the MEA titration of 2-APBA, 2-FPBA and association analogues.

	K_d, mM
2-APBA	20
2-FPBA	15
4-F-2-APBA	13
4,6-F-2-APBA	14
4-OMe-2-APBA	21
5-OMe-2-APBA	28
6-NO_2-2-APBA	>60

From these results, we observe that while the fluorine-containing 2-APBA analogues display a slight improvement in binding affinity, an alternative electron withdrawing group containing 2-APBA analogue (6-NO_2) shows a significant decrease in

binding affinity. Additionally, the 2-APBA analogues that present an electron-donating group also show a decrease in binding affinity. Thus, while minor improvements in the thermodynamics of iminoboronate formation were made with the 4-F-2-APBA and 4,6-F-2-APBA analogues, the improvements were not as significant as anticipated.

2.2.4 ^{1}H NMR Analysis of Boroxole Formation of 2-APBA Analogues

To assess a possible cause for the lack of improvement in binding affinity of the 2-APBA analogues, ^{1}H NMR analysis of the iminoboronate conjugates was carried out. For this experiment, 7.5 mM of each 2-APBA analogue was mixed with 60 mM 2-methoxyethylamine in PBS pH 7.4 with 10% D_2O, and was allowed to incubate for ~15 minutes. This analysis revealed that a significant portion of several of the 2-APBA analogues (4,6-F-2-APBA, 6-NO_2-2-APBA, 2CF_3-APBA), as well as simple 2-FPBA, exist in the boroxole form in aqueous pH 7.4 buffer conditions (**Table 2-2**), which has previously been documented as a competing tautomeric structure by Gois and co-workers, as well as Yatsimirsky and co-workers.[3,15] The formation of boroxole is indicated by the significant upfield shift in the formyl/acetyl peak signal (**Figure 2-8**). As observed through the addition of MEA to these analogues (sample shown is 4,6-F-2-APBA), the equilibrium can be shifted for some boroxole-forming APBA analogues towards iminoboronate formation; however, iminoboronate formation is not 100% complete, even with a large excess of MEA. Notably, ^{11}B NMR analysis of 2-CF_3-APBA in PBS Buffer pH 7.4 displays 100% boroxole formation (**Figure 2-9**).

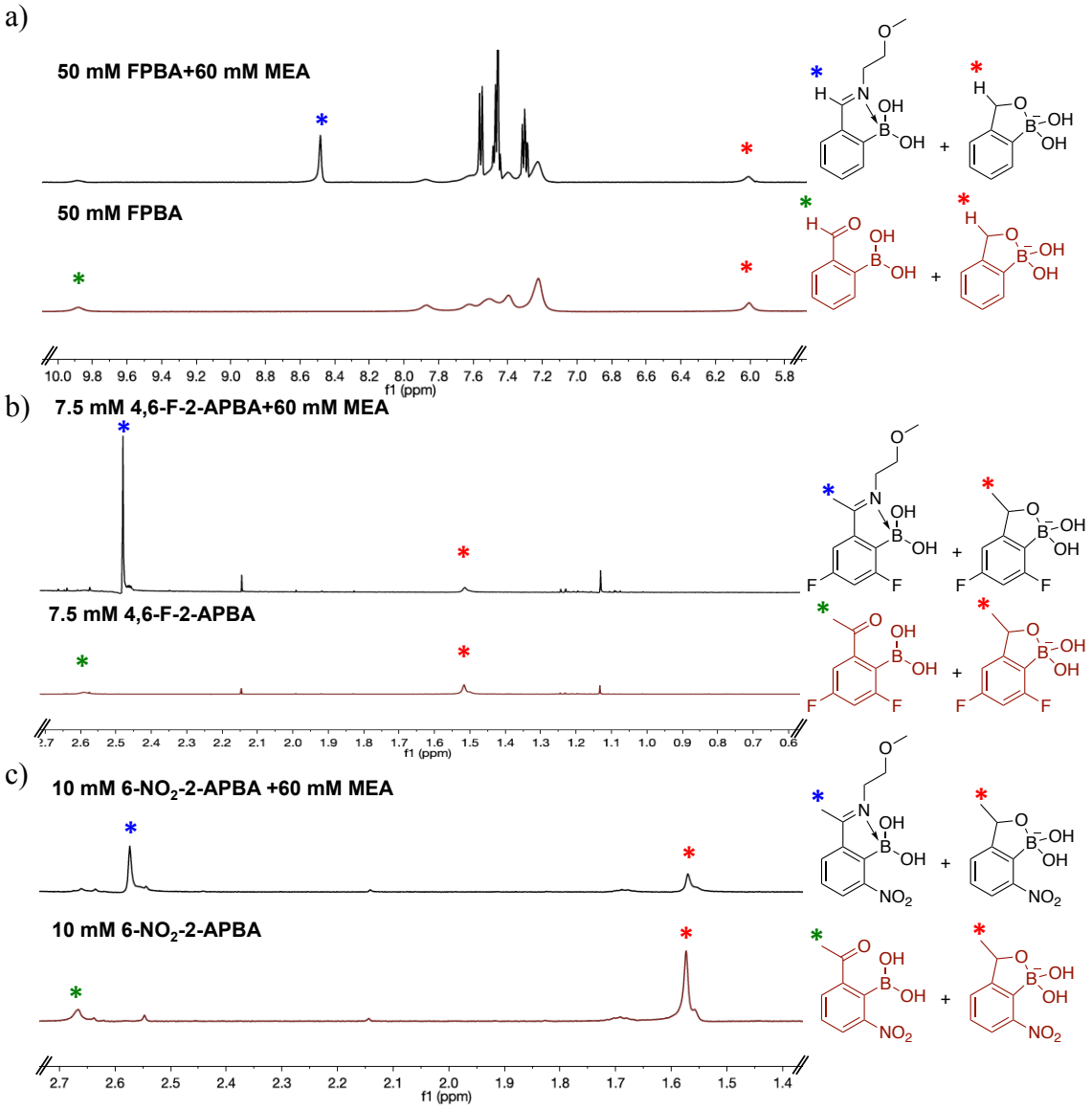

Figure 2-8. Boroxole formation of (a) 2-FPBA (b) 4,6-F-2-APBA analogue and (c) 6-NO_2-2-APBA, as depicted by the upfield shift of the formyl/acetyl peak (*), which is observed even upon MEA conjugation. The acetyl shifts of the parent compound (*) and iminoboronate product (*) are shown for reference.

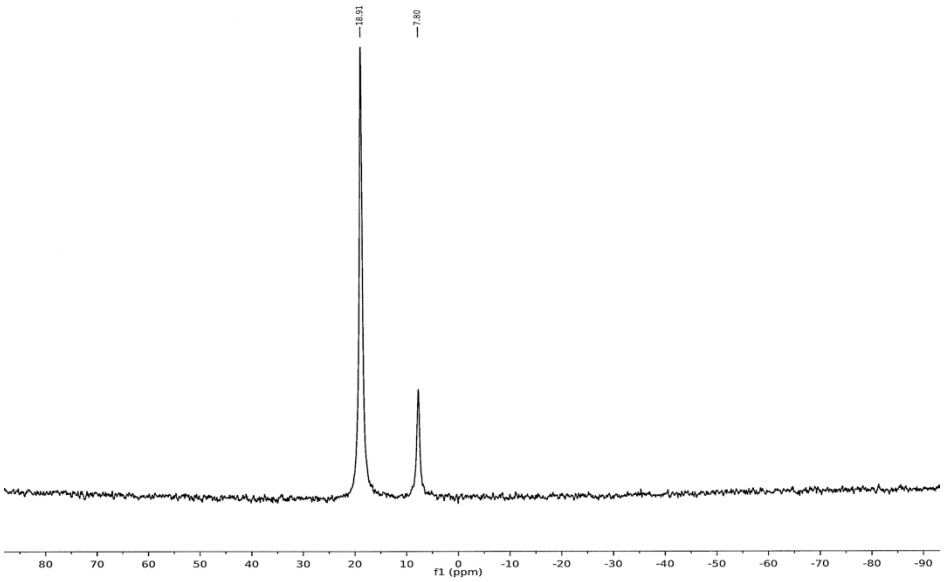

Figure 2-9. ^{11}B NMR of the 2-CF_3-APBA analogue in PBS Buffer pH 7.4 exhibits 100% boroxole formation (chemical shift ~20 ppm corresponds to boric acid).

Table 2-2. Summary of boroxole formation of 2-FPBA, 2-APBA, and related analogues in PBS pH 7.4 at 7.5 mM.

	% Boroxole formed in PBS pH 7.4
2-FPBA	75
2-APBA	0
4-OMe-2-APBA	0
5-OMe-2-APBA	0
4-F-2-APBA	0
4,6-F-2-APBA	80
5-NO_2-2-APBA	95
2-CF_3-APBA	100

Boroxole formation is described as either 1) a nucleophilic addition of hydroxide anion to the carbonyl group, or 2) the shift of the equilibrium of boroxole formation by addition of hydroxide to the trigonal boron atom to convert the boron to a tetrahedral stabilized state, similar to the stabilization of boronate diol esters (**Scheme 2-4**). The second case of forming a trigonal boron atom for stabilization has been observed for halogen substituted 2-FPBA derivatives in organic solvents; however, such a mechanism has not been reported in aqueous conditions. Given the aqueous conditions of our experiments, it is likely that boroxoles of the 2-APBA analogues are being formed through the mechanism shown in Scheme 2-4a as a result of hydroxide ion in the aqueous buffer environment.

Scheme 2-4. Mechanisms of 2-FPBA boroxole formation. Boroxole formation is hypothesized to proceed via either (a) the nucleophilic addition of hydroxide anion or (b) reversible intramolecular cyclization to form a benzoboroxole (figure modified from Ref. 3).

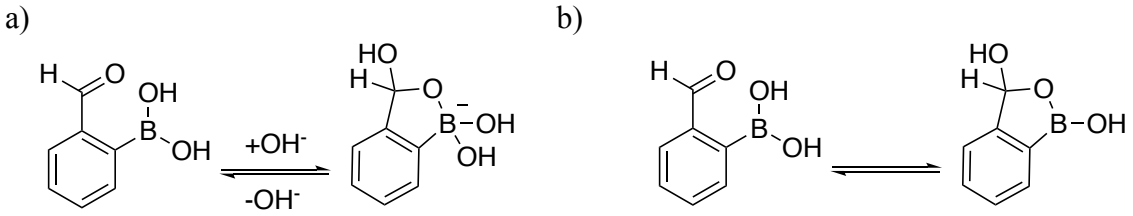

Thus, it appears that the iminoboronate forming capacity of several 2-APBA analogues that display electron withdrawing groups is diminished as a result of the competing boroxole formation mechanism (**Scheme 2-5**). It is likely the case that the increased electronegativity imparted on the electron deficient boron atom promotes a shift in equilibrium of the 2-APBA analogues towards the tetrahedral stabilized boroxole. This is highlighted by the 2-CF_3-2-APBA analogue, which displays 100% boroxole

formation in PBS pH 7.4, and whose equilibrium cannot be shifted to favor iminoboronate formation (**Figure 2-8**). Therefore, through these efforts to induce greater thermodynamic stability to iminoboronate conjugates of 2-APBA and 2-FPBA via synthetic analogues, the analogues instead favored stabilization of the non-iminoboronate conjugated starting material through forming a more stabilized tautomeric boroxole structure.

Scheme 2-5. Schematic of acid-base equilibria involved in the condensation of 2-FPBA with primary amines to form iminoboronates (figure modified from Ref. 3).

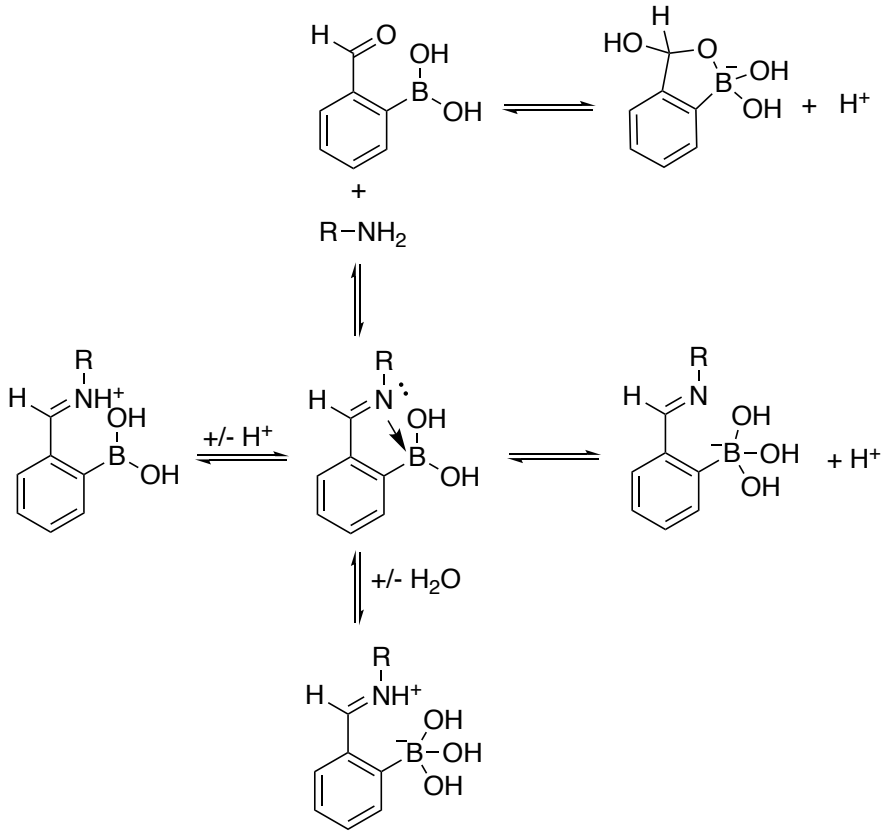

2.3 Application of 2-FPBA and 2-APBA and Their Analogues for Dynamic N-Terminal Cysteine Conjugation

2.3.1 Cysteine Binding Analysis of 2-APBA via ^{1}H NMR

Given the aforementioned unique cysteine conjugation properties of 2-FPBA, we set out to determine if 2-APBA and its analogues would be able to provide different TzB formation capabilities to enable a range of different applications in biology. First, we explored the conjugation of simple 2-APBA to cysteine. For this experiment, we carried out both a 2-APBA titration with cysteine to determine the dissociation constant, as well as a reversibility dilution test, both of which were studied by ^{1}H NMR (**Figure 2-10**). From these experiments, we observed that 2-APBA has a dissociation constant of 0.5 mM, which is two orders of magnitude greater than that of 2-FPBA (5 μM). Additionally, from the dilution experiment, we observed that the TzB conjugate formed with 2-APBA is rapidly reversible, similar to iminoboronate formation.

With these studies of 2-APBA, we aimed to determine if the 2-APBA analogues, shown in Scheme 2-1, would be capable of improving the thermodynamic stability of APBA-Cysteine TzB conjugates, thus decreasing the 2-APBA binding dissociation constant of 2-APBA through their altered electronic properties.

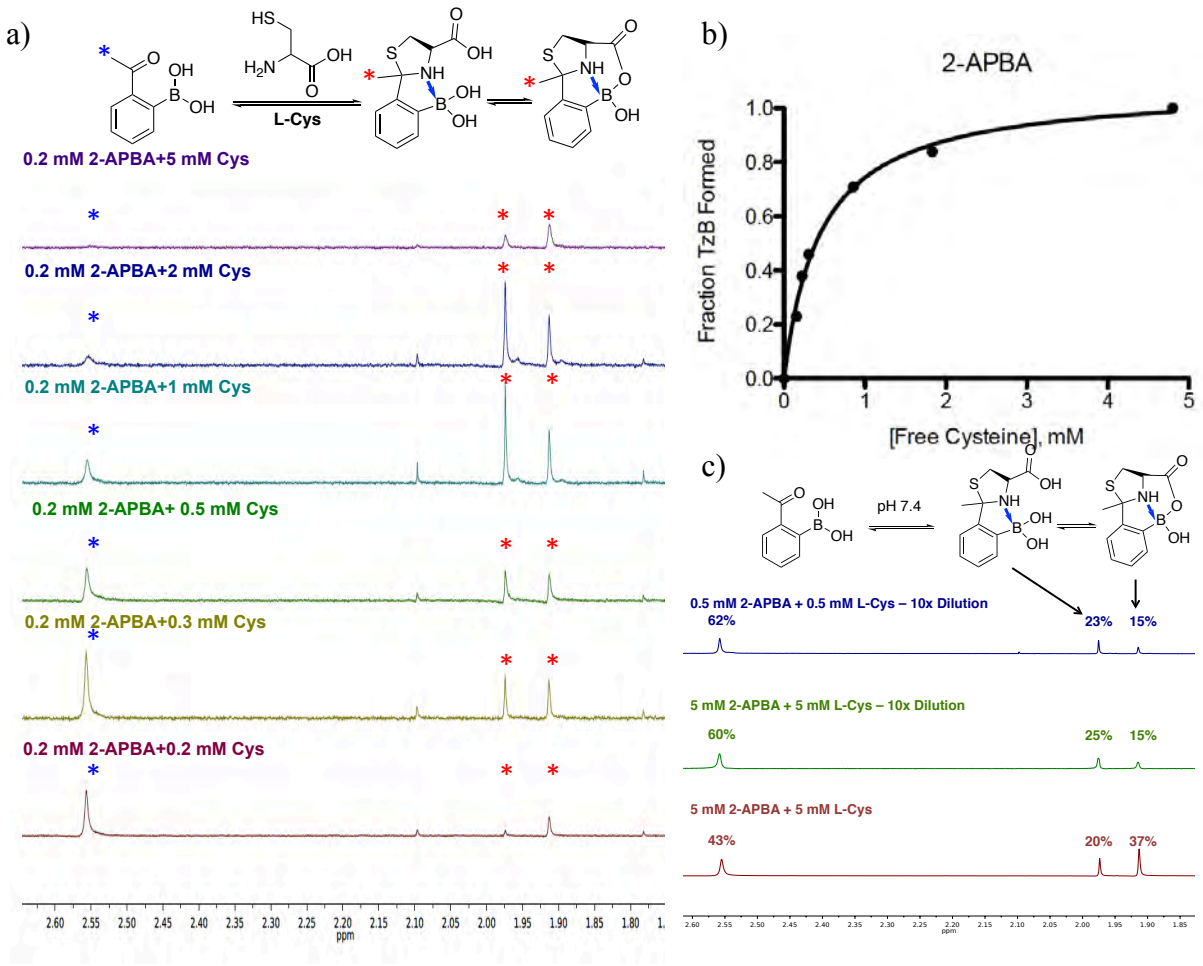

Figure 2-10. Cysteine conjugation studies of 2-APBA. (a) ^{1}H NMR TzB formation titration of 2-APBA and L-cysteine. (b) Fitting the plot of fraction of TzB formed versus free cysteine concentration enables determination of K_d. (c) Reversibility studies of 2-APBA by 10x dilution displays that TzB conjugates of 2-APBA are instantaneously reversible.

2.3.2 Cysteine Binding Titration of 2-APBA Analogues via ^{1}H NMR Analysis

Given the greater thermodynamic reversibility afforded by the 2-APBA scaffold, we next sought to determine whether our 2-APBA analogues with altered electronic properties would modulate the binding dissociation constant towards cysteine binding. To do so, we mixed 200 μM of each 2-APBA analogue with increasing concentrations of L-cysteine until TzB formation was complete (**Figure 2-11**). We tested the 4-F, 4,6-F, 4-OMe and 5-OMe analogues, but not the 6-NO_2 analogue, given the high concentration of

boroxole that 6-NO_2 forms in aqueous conditions. TzB formation proceeds to form two species, a mixed anhydride and a hydrolyzed product. While the mixed anhydride is favored in acidic conditions, the hydrolyzed product predominates in basic conditions; however, as pH 7.4, both species exist, and thus are observed by ^{1}H NMR. Integration of the TzB chemical shifts and acetyl chemical shift allowed us to quantitate the fraction of TzB formed at each cysteine concentration (**Figure 2-12**, **Table 2-3**).

From this data, it appears that the two electron-withdrawing group-containing 2-APBA analogues (4-F and 4,6-F) both lower the binding dissociation constant by ~4x. The methoxy electron-donating group, however, appears to have different K_d modulating behavior depending on whether it is *para* (4-OMe) or *meta* (5-OMe) to the boronic acid functionality. This could possibly be due to the 4-OMe-2-APBA resonance structures that may promote cysteine binding; however, this is in contrast to the results with iminoboronate formation, for which both the 4-OMe and 5-OMe analogues increased the binding dissociation constant towards MEA. Thus, while we can slightly improve the thermodynamic stability of simple 2-APBA cysteine conjugates via APBA analogues with alterations to the core phenyl structure, these improvements are somewhat minimal.

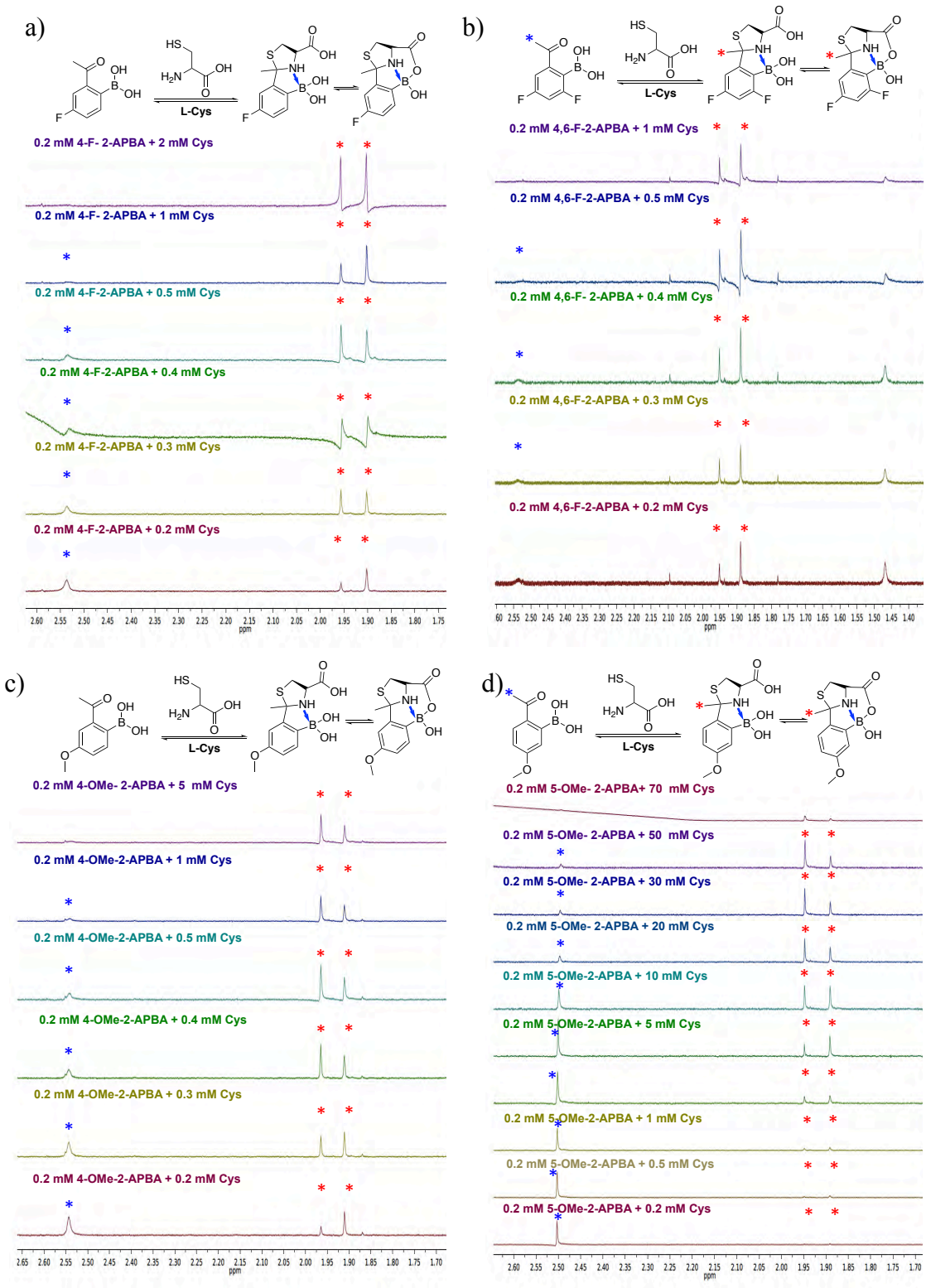

Figure 2-11. ^{1}H NMR cysteine titration assays of (a) 4-F-2-APBA, (b) 4,6-F-2-APBA, (c) 4-OMe-2-APBA and (d) 5-OMe-2-APBA in PBS pH 7.4 (10% D_2O) with increasing concentrations of cysteine to assess TzB formation (data collected in collaboration with Ik Joo Kim).

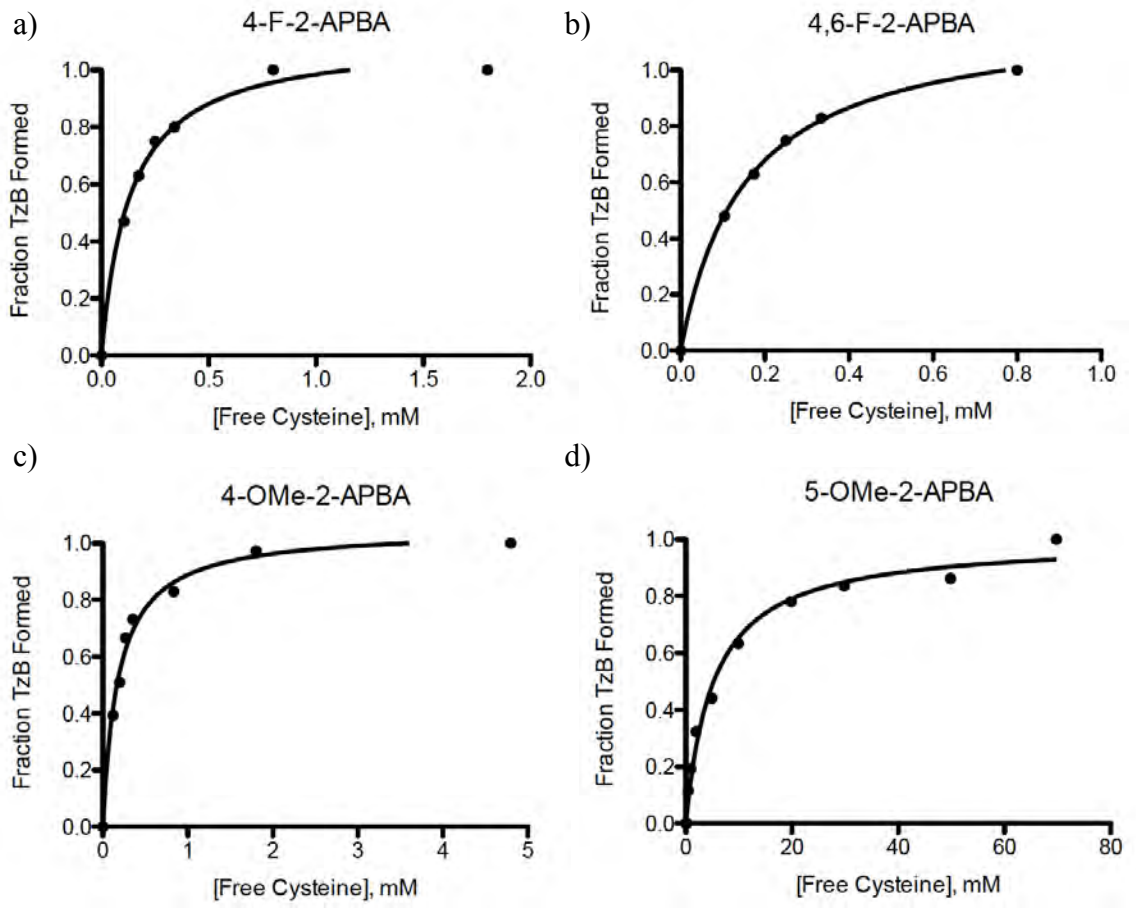

Figure 2-12. Plots of the fraction of TzB formed versus concentration of free cysteine of (a) 4-F-2-APBA, (b) 4,6-F-2-APBA, (c) 4-OMe-2-APBA and (d) 5-OMe-2-APBA from the ^{1}H NMR titration assays to determine dissociation constants (K_d) of cysteine binding for the 2-APBA analogues.

Table 2-3. Summary of dissociation constants (K_d) for cysteine binding of 2-APBA analogues.

Analogue	K_d, mM
2-APBA	0.45
4-F-2-APBA	0.13
4,6-F-2-APBA	0.15
4-OMe-2-APBA	0.18
5-OMe-2-APBA	5.23

2.3.3 2-APBA Coumarin Cysteine Sensing

With our knowledge of the rapid reversibility of thiazolidinoboronate conjugates of 2-APBA, we sought to determine if the TzB forming reaction could be transformed into a cysteine-sensing platform. Using APBA coumarin analogues AB21/22 (described in Chapter 3), we carried out a fluorescence titration experiment to assess the conjugation of cysteine to these molecules. While AB21 and AB22 are minimally fluorescent molecules, once they form conjugates, such as thiazolidinoboronates, their fluorescence significantly increases (**Figure 2-13**). From this experiment, it is clear that the fluorescence of AB21/22 dramatically increases when conjugated with cysteine, and the K_d of binding for both coumarin analogues was ~1 mM. Thus, TzB formation can be used as a fluorogenic method to sense cysteine at low mM concentrations.

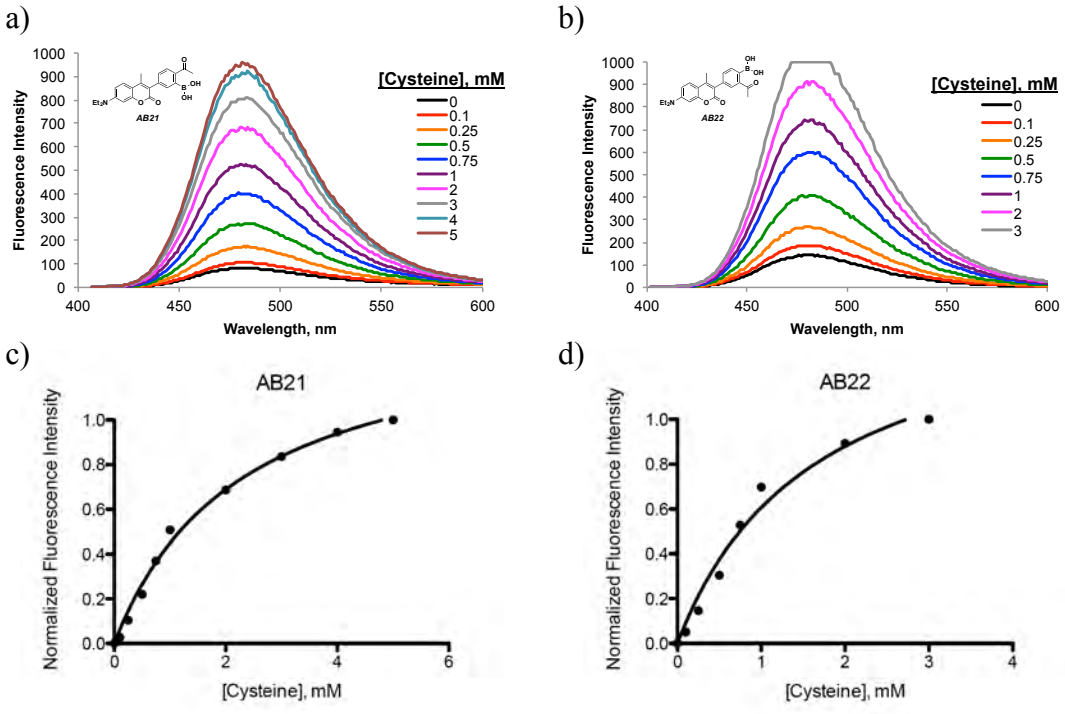

Figure 2-13. Fluorescence increase of APBA-containing coumarin analogues, AB21 (a) and 22 (b), upon conjugation with L-cysteine and (c,d) associated dissociation constant fits (AB21/22 synthesized by Dr. Anupam Bandyopadhyay).

2.4 Conclusions

While none of the 2-APBA analogues displayed significantly superior thermodynamic stability towards forming iminoboronate or cysteine conjugates compared to simple 2-APBA, the analogues did show the ability to provide greater exchange of TzB formation with free or N-terminal cysteine in comparison to 2-FPBA. This opens up the opportunities for this type of TzB forming bioorthogonal reaction for a wider array of applications, including the development of reversible covalent protein inhibitors. Indeed, the reversibility imparted by the APBA molecules makes it an excellent pharmacophore for these types of endeavors.[17]

Recent research has explored the application of salicaldehyde coumarin compounds towards labeling of N-terminal cysteines, which have shown the capacity to form more stable conjugates with cysteine that persist even after an hour of incubation in PBS/acetic acid/pyridine (4:1:1).[29] Considering the vast kinetic improvement on the simple salicaldehyde molecule afforded by our incorporation of an *ortho*-boronic acid in amine and cysteine conjugation, it may be interesting to explore the stability of iminoboronate and cysteine conjugates formed with our coumarin APBA analogues to better understand the potential thermodynamic stability of these APBA-containing molecules with a larger core structure.

Indeed, similar to Su *et al.*'s development of a reversible covalent inhibitor for Mcl-1[6], the forging of additional interactions by a core ligand structure with a distinct target molecule may enable development of more stable APBA-containing binding and inhibiting molecules. In this case, we would be generating APBA-containing ligands for defined targets that experience greater target residence than either the APBA or larger

ligand structure alone. This is quite different from the more general APBA analogues pursued herein, yet the data collected thus far on simple APBA molecules shows that their binding dissociation constants stay in the low millimolar range despite incorporation of different chemical modalities. Therefore, larger structural modifications in more specific contexts will likely be necessary to achieve greater thermodynamic stability.

Overall, boroxole formation, as well as oxidative deboronation[30], are significant challenges with the application of boronic acids to biological systems. However, by making structural modifications to these molecules, their application in biology may be significantly improved towards the generation of new probes and pharmaceutical agents of important biological targets.

2.5 Experimental Procedures

2.5.1 General Methods

2-Acetylphenyl boronic acid (2-APBA), 2-Formylphenyl boronic acid (2-FPBA), trifluoromethane sulfonic anhydride, triethylamine, phenol, aluminum chloride, N-methylmorpholine and potassium acetate were purchased from Sigma Aldrich. 1-(5-Fluoro-2-hydroxyphenl)ethan-1-one and 1-(3,5-Difluoro-2-hydroxyphenyl)ethan-1-one were purchased from Maybridge. Dry dioxane, dry dichloromethane, diethanolamine and methoxyethylamine were purchased from Acros Organics. Bispinacolato diboron (B_2pin_2) was purchased from Matrix Scientific. 1,1'-Bis(Diphenylphosphino)ferrocenepalladium(II) dichloride and 2-hydroxy-3-nitroacetophenone were purchased from Oakwood chemical. 2'Bromo-4' Methoxyacetophenone was purchased from Combi Blocks. Trifluoroacetic anhydride and 2'-hydroxy-4'-methoxyacetophenone were purchased from Alfa Aessar. Trifluoroacetic

acid was purchased from Protein Technologies. Deuterated chloroform, deuterated DMSO, and D_2O were purchased from Cambridge Isotopes. ^{1}H, ^{13}C and ^{11}B NMR data were collected on a VNMRS 600MHz NMR spectrometer. Mass spectrometry data was generated using an Agilent 6230 LC TOF mass spectrometer with a 1.8 μm Agilent Extend C18 column. All RP-HPLC purifications were carried out on a Waters Prep LC with a Jupiter 10 μm C4 300A column with water/acetonitrile/0.1% TFA as eluent (Buffer A= 95% water, 5% acetonitrile, 0.1% TFA, Buffer B= 95% acetonitrile, 5% water, 0.1% TFA) with a gradient from 100% Buffer A to 60% Buffer B. UV-Vis data was collected on a Nanodrop 2000c UV/Vis spectrometer by cuvette. Fluorescence data were collected on a Cary Eclipse fluorescence spectrophotometer with slit width set to 5 nm.

2.5.2 Synthesis of 2-APBA Analogues

The nomenclature for labeling 2-APBA analogues throughout the synthetic methods is shown in **Scheme 2-6**. Methods are described for each individual analogue below with associated ^{1}H NMR, ^{13}C NMR and mass spectrometry analysis.

Scheme 2-6. Structures and labeling nomenclature of 2-APBA analogues.

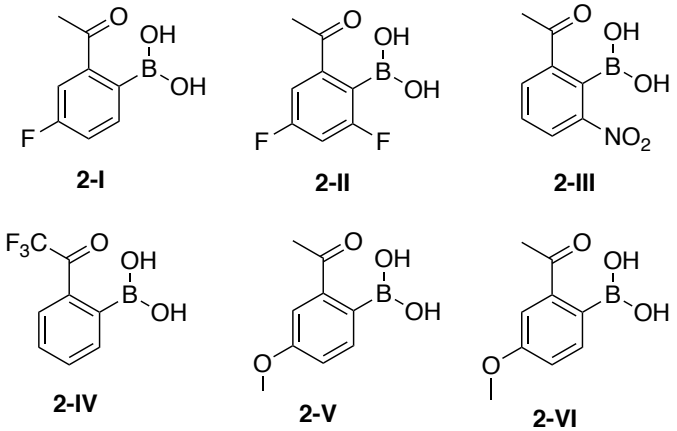

2.5.2.1 Synthesis of 4-F-2-APBA (2-I)

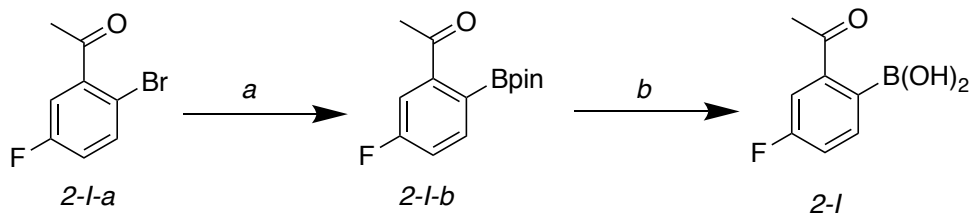

2-I-a *2-I-b* *2-I*

(a) Synthesis of **2-I-b**: **2-I-a** (1.00 mmol) was combined in a dry round bottom flask with 8 mol % $Pd(dppf)Cl_2$•DCM (0.08 mmol), 2.5 equivalents bis(pinacolato)diboron (2.5 mmol), 3 equivalents KOAc (3.0 mmol) and 4.5 mL dry dioxane. The solution was flushed with argon for 15 minutes, and stirred at 95°C for 30 minutes under argon. Upon completion, the reaction mixture was cooled to room temperature and diluted in 100 mL ethyl acetate. The solution was washed with water (3x100mL) and brine (1x100mL) before being dried over sodium sulfate and evaporated. The dried product was purified by silica gel chromatography with a hexane/diethyl ether mixture to yield the pure produce, which was dried to a yellow oil (190 mg, 65%).

^{1}H NMR (CDCl3): δ 1.43 (s, 12H), 2.59 (s, 3H), 7.25 (d, J=2.5 Hz, 1H), 7.49 (ddd, J=11.6, 8.7, 4.2 Hz, 2H).

^{13}C NMR (CDCl3): δ 21.34, 28.61, 92.42, 110.29, 122.41, 133.66, 136.78, 141.02, 172.41, 201.41.

MS-ESI$^+$ (m/z): Calculated for $C_{14}H_{18}BFO_3$ $[M-H_2O+H]^+$ 247.21, observed 247.10.

(b) Synthesis of **2-I**: **2-I-b** (0.1 mmol) was stirred with 10 equivalents (1 mmol) diethanolamine in 1 mL THF for 10 hours. The mixture was treated with 1N HCl

for 30 minutes, then evaporated and dissolved in 4 mL 2:1 water/acetonitrile mixture. The crude material was purified by RP-HPLC with a water/acetonitrile mixture to yield a white powder after lyophilization (7 mg, 38%).

^{1}H NMR (10% D_2O in 1X PBS pH 7.4): δ 2.58 (s, 3H), 7.35 (d, J=8.8 Hz, 1H), 7.43 (t, J=6.9 Hz, 1H), 7.70 (d, J=9.8 Hz, 1H).

^{13}C NMR (10% D_2O in 1X PBS pH 7.4): δ 23.72, 24.83, 113.74, 121.40, 132.75, 141.44, 161.87, 203.25.

MS-ESI^{+} (m/z): Calculated for $C_8H_8BFO_3$ $[M-H_2O+H]^{+}$ 165.10, observed 165.06.

2.5.2.2 Synthesis of 4,6-F-2-APBA (2-II)

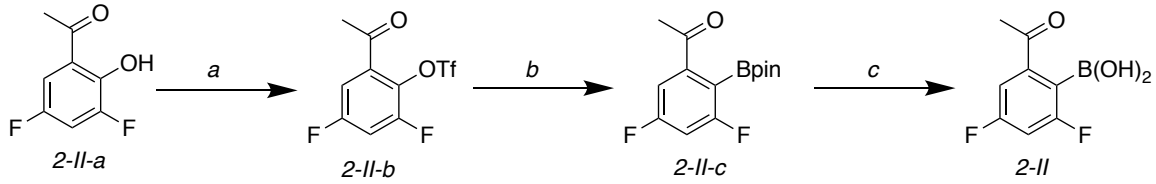

(a) Synthesis of **2-II-b**: **2-II-a** (2.9 mmol) was combined with 4 equivalents (11.6 mmol) triethylamine and 10 mL dry dichloromethane, and cooled to -80^{o}C under argon. To this stirring cooled mixture, 2.2 equivalents (6.40 mmol) trifluoromethanesulfonic anhydride was added dropwise. The mixture was stirred for 5 minutes at -80^{o}C, then brought to room temperature, and stirred 30 minutes. 100 mL sodium bicarbonate was added to the stirring mixture, and allowed to mix for 30 minutes. The organic layer was extracted with dichloromethane (3x100 mL), and the combined organic layers were washed with brine and dried over sodium sulfate. The mixture was then evaporated and purified via silica gel chromatography with a hexane/ethyl acetate mixture. The pure product was dried to a yellow oil (792 mg, 90% yield).

^{1}H NMR (CDCl3): δ 2.63 (s, 3H), 7.15 (s, 1H), 7.28 (s, 1H).

^{13}C NMR (CDCl3): δ 29.44, 108.59, 109.28, 112.28, 117.21, 153.33, 155.50, 161.74, 194.02.

MS-ESI^{+} (m/z): Calculated for $C_9H_5F_5O_4S$ $[M+H]^{+}$ 305.19, observed 304.99.

(b) Synthesis of **2-II-c**: **2-II-b** (1.32 mmol) was combined in a dry round bottom flask with 8 mol % Pd(dppf)Cl_2•DCM (0.11 mmol), 2.5 equivalents bis(pinacolato)diboron (3.3 mmol), 3 equivalents KOAc (4.95 mmol) and 6.0 mL dry dioxane. The solution was flushed with argon for 15 minutes, and stirred at 80^{o}C for 30 minutes under argon. Upon completion, the reaction mixture was cooled to room temperature and diluted in 100 mL ethyl acetate. The solution was washed with water (3x100 mL) and brine (1x100mL) before being dried over sodium sulfate and evaporated to yield. The dried product was purified by silica gel chromatography with a hexane/diethyl ether mixture to yield the pure product, which was dried to a yellow oil (169 mg, 46%).

^{1}H NMR (CDCl3): δ 1.43 (d, J=1.9 Hz, 12H), 2.57 (s, 3H), 6.96 (s, 1H), 7.34 (s, 1H).

^{13}C NMR (CDCl3): δ 22.31, 92.86, 114.73, 117.42, 125.45, 141.13, 164.54, 167.61, 189.76, 204.55.

MS-ESI^{+} (m/z): Calculated for $C_{14}H_{17}BF_2O_3$ $[M+H]^{+}$ 283.09, observed 283.16.

(c) Synthesis of **2-II**: **2-II-c** (0.35 mmol) was stirred in 1 mL of 2:1 acetonitrile/water with 1% TFA for 1 hour. The mixture was evaporated and dissolved in 4 mL 2:1 water/acetonitrile mixture. The crude material was purified by RP-HPLC with a water/acetonitrile mixture to yield a white powder after lyophilization (5 mg, 7%).

^{1}H NMR (10% D_2O in 1X PBS pH 7.4): δ 1.52 (s, 3H), 2.58 (s, 3H), 6.65 (s, 1H), 6.80 (s, 1H), 7.16 (s, 1H), 7.61 (s, 1H). (*Boroxole and boronic acid structures co-exist).

^{13}C NMR (DMSO-d_6): δ 27.91, 113.23, 115.35, 117.28, 119.22, 162.78, 163.02, 200.09.

MS-ESI$^+$ (m/z): Calculated for $C_8H_8BF_2O_3$ $[M-H_2O+H]^+$ 182.95, observed 183.04.

2.5.2.3 Synthesis of 6-NO_2-2-APBA (2-III)

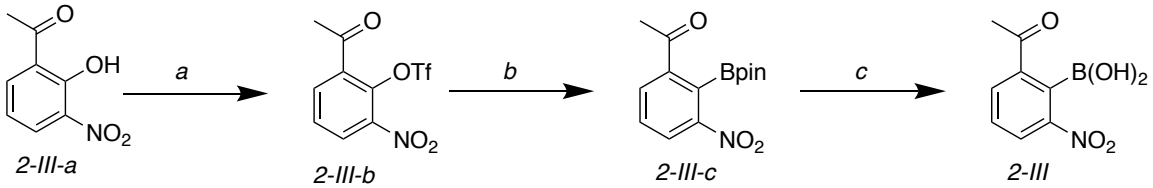

2-III-a *2-III-b* *2-III-c* *2-III*

(a) Synthesis of **2-III-b**: **2-III-a** (2.76 mmol) was combined with 4 equivalents (11.1 mmol) triethylamine and 10 mL dry dichloromethane, and cooled to -80^{o}C under argon. To this stirring cooled mixture, 2.2 equivalents (5.5 mmol) trifluoromethanesulfonic anhydride was added dropwise. The mixture was stirred for 5 minutes at -80^{o}C, then brought to room temperature, and stirred 30 minutes. 100 mL sodium bicarbonate was added to the stirring mixture, and allowed to mix for 30 minutes. The organic layer was extracted with dichloromethane (3x100 mL), and the combined organic layers were washed with brine and dried over sodium sulfate. The mixture was then evaporated and purified via silica gel chromatography with a hexane/ethyl acetate mixture. The pure product was dried to a yellow oil (500 mg, 60% yield).

^{1}H NMR (CDCl3): δ 2.68 (s, 3H), 7.75-7.61 (m, 1H), 7.98 (dd, J=1.8, 1.3 Hz, 1H), 8.20 (d, J=8.2 Hz, 1H).

^{13}C NMR (CDCl3): δ 29.73, 114.48, 117.04, 119.59, 129.01, 134.36, 135.75, 138.02, 195.13.

MS-ESI^{+} (m/z): Calculated for $C_9H_6F_3NO_6S$ $[M+H]^{+}$ 314.20, observed 313.98.

(b) Synthesis of **2-III-c**: **2-III-b** (0.639 mmol) was combined in a dry round bottom flask with 8 mol % Pd(dppf)Cl_2•DCM (0.051 mmol), 2.5 equivalents bis(pinacolato)diboron (1.60 mmol), 3 equivalents KOAc (1.92 mmol) and 4.0 mL dry dioxane. The solution was flushed with argon for 15 minutes, and stirred at 97^{o}C for 30 minutes under argon. Upon completion, the reaction mixture was cooled to room temperature and diluted in 100 mL ethyl acetate. The solution was washed with water (3x100 mL) and brine (1x100mL) before being dried over sodium sulfate and evaporated to yield. The dried product was directly used in step c without purification (171 mg, 92%).

(c) Synthesis of **2-III**: **2-III-c** (0.34 mmol) was stirred in 2 mL of 2:1 acetonitrile/water with 1% TFA for 2 hours at room temperature. The mixture was evaporated and dissolved in 4 mL 2:1 water/acetonitrile mixture. The crude material was purified by RP-HPLC with a water/acetonitrile mixture to yield a white powder after lyophilization (5 mg, 7% over 2 steps).

^{1}H NMR (10% D_2O in 1X PBS pH 7.4): δ 1.53 (s, 3H), 2.62 (s, 3H), 7.34-7.40 (m, 1H), 7.54 (d, J=7.4 Hz, 1H), 7.69 (t, J=7.9 Hz, 1H), 7.97 (d, J=7.81 Hz, 1H), 8.40, (d, J=8.3 Hz, 1H). (*Boroxole and boronic acid structures co-exist).

^{13}C NMR (DMSO-d_6): δ 28.17, 123.21, 128.26, 130.81, 136.27, 140.50, 150.63, 202.41.

MS-ESI$^+$ (m/z): Calculated for $C_8H_8NO_5$ $[M\text{-}H_2O+H]^+$ 191.96, observed 192.04.

2.5.2.4 Synthesis of 2-CF_3-APBA (2-IV)

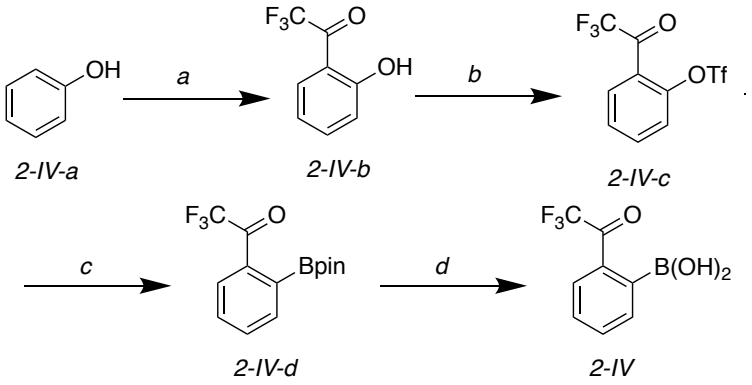

(a) Synthesis of **2-IV-b**: **2-IV-a** (21.25 mmol) was stirred with 3 equivalents aluminum chloride (63.76 mmol) and 25 mL 1,2-Dichloroethane for 30 minutes. To this stirring mixture, 2 equivalents (42.5 mmol) of trifluoroacetic anhydride was added drop-wise over 30 minutes. The reaction mixture was stirred for 4 hours at room temperature. The mixture was slowly poured over 10 grams of ice, after which the organic layer was extracted with DCM (3x250 mL). The combined organic layers were washed with brine and dried over sodium sulfate and evaporated. The dried product was purified by silica gel chromatography with a hexane/diethyl ether mixture to yield the pure product, which was dried to a yellow oil (526 mg, 13%).

^{1}H NMR (CDCl3): δ 7.00 (ddd, J=8.3 Hz, 7.2 Hz, 1.2 Hz, 1H), 7.09 (ddd, J=8.5 Hz, 1.2 Hz, 0.5 Hz, 1H), 7.63 (dddd, J=8.7 Hz, 7.2 Hz, 1.6 Hz, 0.5 Hz, 1H), 7.78-7.88 (m, 1H), 11.06 (d, J=0.5 Hz, 1H).

^{13}C NMR (CDCl3): δ 115.22, 117.52, 119.30, 120.14, 130.65, 138.79, 164.58, 184.25.

MS-ESI$^+$ (m/z): Calculated for $C_8H_5F_3O_2$ $[M+H]^+$ 191.12, observed 191.03.

(b) Synthesis of **2-IV-c**: **2-IV-b** (2.77 mmol) was combined with 4 equivalents (11.1 mmol) N-methylmorpholine and 10 mL dry dichloromethane, and cooled to -80^{o}C under argon. To this stirring cooled mixture, 2.2 equivalents (6.10 mmol) trifluoromethanesulfonic anhydride was added dropwise. The mixture was stirred for 5 minutes at -80^{o}C, then brought to room temperature, and stirred 30 minutes. 100 mL sodium bicarbonate was added to the stirring mixture, and allowed to mix for 30 minutes. The organic layer was extracted with dichloromethane (3x100 mL), and the combined organic layers were washed with brine and dried over sodium sulfate. The mixture was then evaporated and purified via silica gel chromatography with a hexane/ethyl acetate mixture. The pure product was dried to a yellow oil (300 mg, 34% yield).

^{1}H NMR (CDCl3): δ 7.48 (dd, J=8.3, 1.0 Hz, 1H), 7.60 (td, J=7.7 Hz, 1.0 Hz, 1H), 7.79 (ddd, J=8.4 Hz, 7.5 Hz, 1.7 Hz, 1H), 7.98 (dt, J=7.9 Hz, 1.6 Hz, 1H).

^{13}C NMR (CDCl3): δ 109.81, 114.28, 119.84, 123.72, 128.60, 131.23, 136.10, 148.10, 178.82.

MS-ESI$^+$ (m/z): Calculated for $C_9H_5F_6O_4S$ $[M+H]^+$ 323.18, observed 322.98.

(c) Synthesis of **2-IV-d**: 2-**III-c** (0.93 mmol) was combined in a dry round bottom flask with 8 mol % Pd(dppf)Cl_2•DCM (0.075 mmol), 2.5 equivalents bis(pinacolato)diboron (2.33 mmol), 3 equivalents KOAc (2.79 mmol) and 8.0 mL dry dioxane. The solution was flushed with argon for 15 minutes, and stirred

at 97°C for 30 minutes under argon. Upon completion, the reaction mixture was cooled to room temperature and diluted in 100 mL ethyl acetate. The solution was washed with water (3x100 mL) and brine (1x100mL) before being dried over sodium sulfate and evaporated to yield a yellow oil, which was directly used for step d.

(d) Synthesis of **2-IV-e**: **2-IV-d** (0.13 mmol) was stirred with 10 equivalents (1.33 mmol) diethanolamine in 1 mL THF for 3 hours. The mixture was treated with 1N HCl for 30 minutes, then evaporated and dissolved in 4 mL 2:1 water/acetonitrile mixture. The crude material was purified by RP-HPLC with a water/acetonitrile mixture to yield a white powder after lyophilization (3 mg, 10% over 2 steps).

^{1}H NMR (CDCl3): δ 7.25 (td, J=7.4 Hz, 1.3 Hz, 1H), 7.32 (dd, J=7.2 Hz, 1.1 Hz, 1H), 7.34-7.37 (m, 1H), 7.41 (dt, J=7.2 Hz, 1.1 Hz, 1H).

^{13}C NMR (DMSO-d_6): δ 115.37, 117.30, 122.63, 127.22, 128.49, 129.53, 143.01, 163.01.

MS-ESI^{+} (m/z): Calculated for $C_8H_6BF_3O_3$ $[M+H]^{+}$ 200.94, observed 201.03.

2.5.2.5 Synthesis of 4-OMe-2-APBA (2-V)

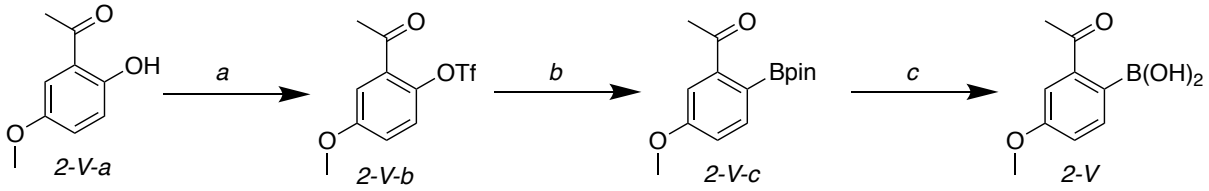

(a) Synthesis of **2-V-b**: **2-V-a** (3 mmol) was combined with 4 equivalents (12 mmol) triethylamine and 10 mL dry dichloromethane, and cooled to -80°C under argon. To this stirring cooled mixture, 2.2 equivalents (6.6 mmol) trifluoromethanesulfonic anhydride was added dropwise. The mixture was

continued to stir for 5 minutes at -80°C, then brought to room temperature, and stirred 30 minutes. 100 mL sodium bicarbonate was added to the stirring mixture, and allowed to mix for 30 minutes. The organic layer was extracted with dichloromethane (3 x 100 mL), and the combined organic layers were washed with brine and dried over sodium sulfate. The mixture was then evaporated and purified via silica gel chromatography with a hexane/ethyl acetate mixture. The pure product was dried to a yellow oil (890 mg, 99% yield).

^{1}H NMR (CDCl3): δ 2.61 (s, 3H), 3.86 (s, 3H), 7.05 (dd, J=9.0 Hz, 3.2 Hz, 1H), 7.22-7.27 (m, 2H).

^{13}C NMR (CDCl3): δ 27.45, 48.76, 98.75, 99.19, 101.32, 119.22, 122.81, 147.66, 165.34, 210.86.

MS-ESI^{+} (m/z): Calculated for $C_{10}H_9F_3O_5S$ $[M+H]^{+}$ 299.23, observed 299.02.

(b) Synthesis of **2-V-c**: **2-V-b** (1.34 mmol) was combined in a dry round bottom flask with 8 mol % Pd(dppf)Cl_2•DCM (0.107 mmol), 2.5 equivalents bis(pinacolato)diboron (3.36 mmol), 3 equivalents KOAc (4.03 mmol) and 6.0 mL dry dioxane. The solution was flushed with argon for 15 minutes, and stirred at 97°C for 30 minutes under argon. Upon completion, the reaction mixture was cooled to room temperature and diluted in 100 mL ethyl acetate. The solution was washed with water (3x100 mL) and brine (1x100mL) before being dried over sodium sulfate and evaporated to yield. The dried product was purified by silica gel chromatography with a hexane/diethyl ether mixture to yield the pure product, which was dried to a yellow oil (169 mg, 46%).

^{1}H NMR (CDCl3): δ 1.41 (s, 12H), 2.57 (s, 3H), 7.04 (dd, J=8,1 Hz, 2.4 Hz, 1H), 7.28 (d, J=2.4 Hz, 1H), 7.44 (d, J=7.91 Hz, 1H).

^{13}C NMR (CDCl3): δ 22.47, 27.91, 56.58, 91.88, 114.56, 121.86, 129.76, 138.22, 146.02, 210.08.

MS-ESI^{+} (m/z): Calculated for $C_{15}H_{21}BO_4$ $[M+H]^{+}$ 277.14, observed 277.08.

(c) Synthesis of **2-V**: **2-V-c** (0.18 mmol) was stirred with 10 equivalents (1.8 mmol) diethanolamine in 0.3 mL THF for 10 hours. The mixture was treated with 1N HCl for 30 minutes, then evaporated and dissolved in 4 mL 2:1 water/acetonitrile mixture. The crude material was purified by RP-HPLC with a water/acetonitrile mixture to yield a yellow powder after lyophilization (10.5 mg, 30%).

^{1}H NMR (10% D_2O in 1X PBS pH 7.4): δ 2.57 (s, 3H), 3.84 (s, 3H), 7.05 (ddd, J=8.1 Hz, 2.4 Hz, 0.9 Hz, 1H), 7.28 (dd, J=2.4 Hz, 0.8 Hz, 1H), 7.45 (dd, J=8.1 Hz, 0.8 Hz, 1H).

^{13}C NMR (10% D_2O in 1X PBS pH 7.4): δ 25.10, 55.70, 113.21, 115.34, 119.31, 132.10, 140.50, 159.23, 204.40.

MS-ESI^{+} (m/z): Calculated for $C_9H_{11}BO_4$ $[M-H_2O+H]^{+}$ 176.99, observed 177.08.

2.5.2.6 Synthesis of 5-OMe-2-APBA (2-VI)

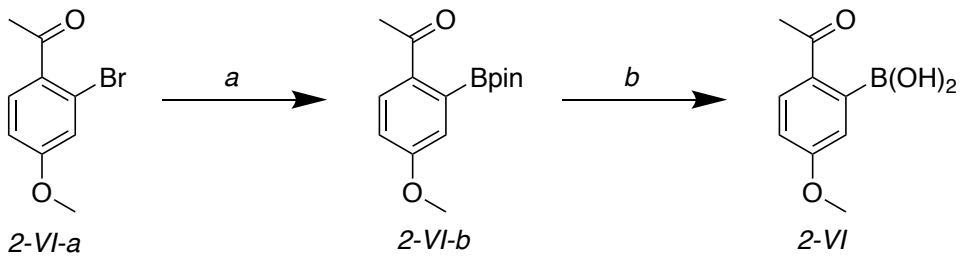

(a) Synthesis of **2-VI-b**: **2-VI-a** (0.90 mmol) was combined in a dry round bottom flask with 3 mol % $Pd(dppf)Cl_2$•DCM (0.0027 mmol), 2 equivalents bis(pinacolato)diboron (1.8 mmol), 3 equivalents KOAc (2.7 mmol) and 4.5 mL dry dioxane. The solution was flushed with argon for 15 minutes, and stirred at 75°C for 75 minutes under argon. Upon completion, the reaction mixture was cooled to room temperature and diluted in 100 mL ethyl acetate. The solution was washed with water (3x100 mL) and brine (1x100mL) before being dried over sodium sulfate and evaporated to yield. The dried product was purified by silica gel chromatography with a hexane/diethyl ether mixture to yield the pure produce, which was dried to a yellow oil (177 mg, 71%).

^{1}H NMR (CD_3Cl3): δ 1.97 (s, 12H), 2.55 (s, 3H), 3.86 (s, 3H), 6.85-6.88 (dd, J=7.8 Hz, 1.8 Hz, 1H), 6.97 (d, J=7.4 Hz, 1H), 7.76-7.78 (d, J=8.2 Hz, 1H).

^{13}C NMR (CDCl3): δ 21.34, 28.61, 92.42, 110.29, 122.41, 133.66, 136.78, 141.02, 172.41, 201.41.

MS-ESI$^+$ (m/z): Calculated for $C_{15}H_{21}BO_4$ $[M+H]^+$ 277.14, observed 277.15.

(b) Synthesis of **2-I**: **2-I-b** (0.1 mmol) was stirred with 10 equivalents (1 mmol) diethanolamine in 1 mL THF for 10 hours. The mixture was treated with 1N HCl

for 30 minutes, then evaporated and dissolved in 4 mL 2:1 water/acetonitrile mixture. The crude material was purified by RP-HPLC with a water/acetonitrile mixture to yield a white powder after lyophilization (3 mg, 15%).

^{1}H NMR (10% D_2O in 1X PBS pH 7.4): δ 1.42 (s, 12H), 2.58 (s, 3H), 3.85 (s, 3H), 7.05 (dd, J=8.1 Hz, 2.4 Hz, 1H), 7.29 (d, J=2.3 Hz, 1H), 7.45 (d, J=8.1 Hz, 1H).

^{13}C NMR (CDCl3): δ 22.73, 29.68, 55.65, 114.64, 114.91, 129.62, 132.40, 165.34, 204.51.

MS-ESI^{+} (m/z): Calculated for $C_9H_{11}BO_4$ $[M-H_2O+H]^{+}$ 176.99, observed 177.07.

2.5.3 UV-Vis Binding Titration Studies with 2-Methoxyethylamine

50 μM of each APBA analogue (1X PBS pH 7.4 stock) was mixed in 1X PBS pH 7.4 with increasing concentrations of 2- methoxyethylamine (1X PBS pH 7.4 stock, 0-60 mM) in a UV-Vis cuvette. After each addition of MEA, the cuvette was inverted several times before an absorbance reading was taken. The titration was determined to be complete when the absorbance at the shifted absorbance maximum wavelength no longer increased.

2.5.4 ^{1}H NMR Iminoboronate Conjugate Analysis

Each APBA analogue was diluted to 7.5 mM in 1X PBS pH 7.4 with 10% D_2O. ^{1}H NMR was obtained with water suppression and 64 scans. To this mixture, 60 mM methoxyethylamine in 1X PBS pH 7.4 was added. The mixture was incubated for 10 minutes at room temperature, before a ^{1}H NMR was again obtained with water suppression and 64 scans.

2.5.5 ^{1}H NMR Cysteine Titration to Determine Dissociation Constants (K_d)

Each APBA analogue was diluted to 0.2 mM in 1X PBS pH 7.4, to which increasing concentrations of L-cysteine was added in 1X PBS pH 7.4. 10% D_2O was added to the mixture, and ^{1}H NMR spectra were immediately obtained with water suppression and 64 scans. The titration cysteine concentration increased until complete disappearance of the acetyl APBA chemical shift.

2.5.6 Reversibility of TzB Formation

2-APBA in 1X PBS pH 7.4 was diluted to 5 mM in 1X PBS pH 7.4, and 5 mM L-cysteine in 1X PBS pH 7.4 was added. An aliquot of this mixture was taken, to which 10% D_2O was added. The mixture was directly analyzed by ^{1}H NMR with water suppression and 64 scans. Another aliquot of same mixture was then diluted 10x in 1X PBS pH 7.4, to which 10% D_2O was added, and another ^{1}H NMR with water suppression and 64 scans was obtained. Additionally, a mixture of 0.5 mM 2-APBA and 0.5 mM L-cysteine was made in 1X PBS pH 7.4 with 10% D_2O, and a ^{1}H NMR was directly obtained with water suppression and 64 scans.

2.5.7 Fluorogenic Cysteine Sensing by 2-APBA Coumarin Analogues

The syntheses of AB21 and AB22 are summarized in *3.6.15*. 50 μM of each analogue (from DMSO stock) was combined in a fluorescence cuvette with increasing concentrations of L-cysteine (1X PBS stock) in 1X PBS pH 7.4. The fluorescence cuvette was inverted several times to mix after each cysteine addition, and the fluorescence readings were obtained at a voltage of 700. The titration was complete when the fluorescence no longer increased.

2.6 References

1. Vàzquez, M. A., Exhevarría, G., Muñoz, F., Donso, J. & Blanco, F. G. Kinetic Study of the Schiff-base Formation between Glycine and Pyridoxal 5'- Phosphate (PLP), Pyridoxal (PL), and 5'-Deoxypyridoxal (DPL). *J. Chem. Soc.* **2,** 1617–1622 (1989).
2. Crugeiras, J., Rios, A., Riveiros, E., Amyes, T. L. & Richard, J. P. Glycine Enolates: The Effect of Formation of Iminium Ions to Simple Ketones on α-Amino Carbon Acidity and a Comparison with Pyridoxal Iminium Ions. *J. Am. Chem. Soc.* **130,** 2041–2050 (2009).
3. Gutierrez-Moreno, N. J., Medrano, F. & Yatsimirsky, A. K. Schiff base formation and recognition of amino sugars, aminoglycosides and biological polymaines by 2-formyl phenylboronic acid in aqueous solution. *Org. Biomol. Chem.* **10,** 6960–6972 (2012).
4. Veiros, F. *et al.* Iminoboronates: A New Strategy for Reversible Protein Modification. *J. Am* **134,** 10299–10305 (2012).
5. Cal, P. M. S. D., Frade, R. F. M., Cordeiro, C. & Gois, P. M. P. Reversible Lysine Modification on Proteins by Using Functionalized Boronic Acids. *Chem. Eur. J.* **21,** 8182–8187 (2015).
6. Akçay, G. *et al.* Inhibition of Mcl-1 through covalent modification of a noncatalytic lysine side chain. *Nat. Chem. Biol.* **12,** 931–938 (2016).
7. Bandyopadhyay, A., McCarthy, K. A., Kelly, M. A. & Gao, J. Targeting bacteria via iminoboronate chemistry of amine-presenting lipids. *Nat. Commun.* **6,** 6561–6569 (2015).

8. Bandyopadhyay, A. & Gao, J. Iminoboronate-Based Peptide Cyclization That Responds to pH, Oxidation, and Small Molecule Modulators. *J. Am. Chem. Soc.* **138,** 2098–2101 (2016).

9. Chapin, B. M. *et al.* Structural and Thermodynamic Analysis of a Three-Component Assembly Forming ortho -Iminophenylboronate Esters. *Hournal Org. Chem.* **81,** 8319–8330 (2016).

10. Ni, W., Kaur, G., Springsteen, G., Wang, B. & Franzen, S. Regulating the fluorescence intensity of an anthracene boronic acid system : a B – N bond or a hydrolysis mechanism? *Bioorg. Chem.* **32,** 571–581 (2004).

11. Collins, B. E. *et al.* Probing Intramolecular B-N Interactions in Ortho-Aminomethyl Arylboronic Acids. *J. Org. Chem.* **74,** 4055–4060 (2009).

12. Bandyopadhyay, A. & Gao, J. Iminoboronate Formation Leads to Fast and Reversible Conjugation Chemistry of α-Nucleophiles at Neutral pH. *Chem. Eur. J.* **21,** 14748–14752 (2015).

13. Myers, J. K. & Pace, C. N. Hydrogen Bonding Stabilizes Globular Proteins. *Biophys. J.* **71,** 2033–2039 (1996).

14. McCarthy, K. A. *et al.* Phage Display of Dynamic Covalent Binding Motifs Enables Facile Development of Targeted Antibiotics. *J. Am. Chem. Soc.* **140,** 6137–6145 (2018).

15. Cal, P. M. S. D. *et al.* Iminoboronates : A New Strategy for Reversible Protein Modi fi cation. *J. Am. Chem. Soc.* **134,** 10299–10305 (2012).

16. Cambray, S. & Gao, J. Versatile Bioconjugation Chemistries of ortho-Boronyl Aryl Ketones and Aldehydes. *Acc. Chem. Res.* **51,** 2198–2206 (2018).

17. Bradshaw, J. M. *et al.* Prolonged and tunable residence time using reversible covalent kinase inhibitors. *Nat. Chem. Biol.* **11,** 525–531 (2015).

18. Groll, M., Berkers, C. R., Ploegh, H. L. & Ovaa, H. Crystal Structure of the Boronic Acid-Based Proteasome Inhibitor Bortezomib in Complex with the Yeast 20S Proteasome. *Structure* 451–456 (2006).

19. Smith, P. *et al.* A phase I trial of PRN1008, a novel reversible covalent inhibitor of Bruton's tyrosine kinase, in healthy volunteers. *Br. J. Clin. Pharmacol.* **83,** 2367–2376 (2017).

20. Bandyopadhyay, A., Cambray, S. & Gao, J. Fast Diazaborine Formation of Semicarbazide Enables Facile Labeling of Bacterial Pathogens. *J. Am. Chem. Soc.* **139,** 871–878 (2017).

21. Bandyopadhyay, A., Cambray, S. & Gao, J. Fast and selective labeling of N-terminal cysteines at neutral pH via thiazolidino boronate formation. *Chem. Sci.* **7,** 4589–4593 (2016).

22. Faustino, H., Silva, M. J., Veiros, L. F., Bernardes, G. J. & Gois, P. M. Iminoboronates are efficient intermediates for selective, rapid and reversible N-terminal cysteine functionalisation. *Chem. Sci.* **7,** 5052–5058 (2016).

23. Bernardes, G. J. L., Steiner, M., Hartmann, I., Neri, D. & Casi, G. Site-specific chemical modification of antibody fragments using traceless cleavable linkers. *Nat. Protoc.* **8,** 2079–2089 (2013).

24. Draganov, A. B. *et al.* Click with a boronic acid handle : a neighboring secondary functionalization †. *Chem. Comun.* **51,** 15180–15183 (2015).

25. Collins, I. & Workman, P. New approaches to molecular cancer therapeutics. **2,**

689–700 (2006).

26. Capdeville, R., Buchdunger, E., Zimmermann, J., Matter, A. & Oncology, N. Glivec (STI571, Imatinib), a rationally developed, targeted anticancer drug. **1,** 493–502 (2002).

27. Harrold, M. W. & Zavod, R. M. *Basic Concepts in Medicinal Chemistry*. (2013).

28. Corso, A. D., Catalano, M., Schmid, A., Scheuermann, J. & Neri, D. Medicinal Chemistry Affinity Enhancement of Protein Ligands by Reversible Covalent Modification of Neighboring Lysine Residues. *Angew. Chemie Int. Ed.* **57,** 17178–17182 (2018).

29. Murale, D. P., Hong, C., Jang, S. & Lee, J. Reinvestigation of an O -Salicylaldehyde Ester Functional Group in Aqueous Buffer and Discovery of a Coumarin Scaffold Probe for Selective N-Terminal Cysteine Labeling. *ChemBioChem* **19,** 2545–2549 (2018).

30. Labutti, J. *et al.* Oxidative Deboronation of the Peptide Boronic Acid Proteasome Inhibitor Bortezomib: Contributions from Reactive Oxygen Species in This Novel Cytochrome P450 Reaction. *Chem. Res. Toxicol.* **19,** 539–546 (2006).

CHAPTER 3

Stable Diazaborine Formation of APBA and Semicarbazide Enables Facile Detection of Bacterial Pathogens

**The work in this chapter was carried out in collaboration with Dr. Anupam Bandyopadhyay*

3.1 Introduction

In our continued search for bioorthogonal reactions that would enable our discovery of solutions to the antibiotic resistance crisis, we turned our attention to a series of published chemistries involving α-nucleophiles that enable reactivity between non-natural chemical moieties. Similar to the discovery of iminoboronate formation, the addition of *ortho*-boronic acids to these chemistries has improved their bioothogonality (eg. fast kinetics in physiologic conditions), which has enabled their application to bacterial labeling via metabolic unnatural amino acid incorporation into the bacterial peptidoglycan component of the cell wall.

3.1.1 Bioorthogonal Conjugation of APBA with Non-Natural Nucleophiles

Mechanistically similar to imine formation, α-nucleophiles are known to conjugate with carbonyls, yielding oximes and hydrazones, which are among the earliest documented bioorthogonal reactions. Also similar to imine formation, oxime and hydrazone formation with carbonyls suffers from slow kinetics, even with high concentrations of aniline catalysts or acidic conditions.[1,2] Incorporation of an *ortho*-boronyl substituent, however, greatly accelerates the conjugation of 2-APBA/2-FPBA to α-nucleophiles through carbonyl activation and assisted dehydration to yield the carbon nitrogen double bond (**Figure 3-1**). These conjugation reactions give second order rate constants of ~10^3-10^4 $M^{-1}s^{-1}$, making them some of the fastest documented bioorthogonal reactions. Notably, the fast conjugation enabled by the reactions affords the use of α-nucleophiles at low concentrations, thus minimizing their potential cytotoxicity and enhancing their bioorthogonality.[3]

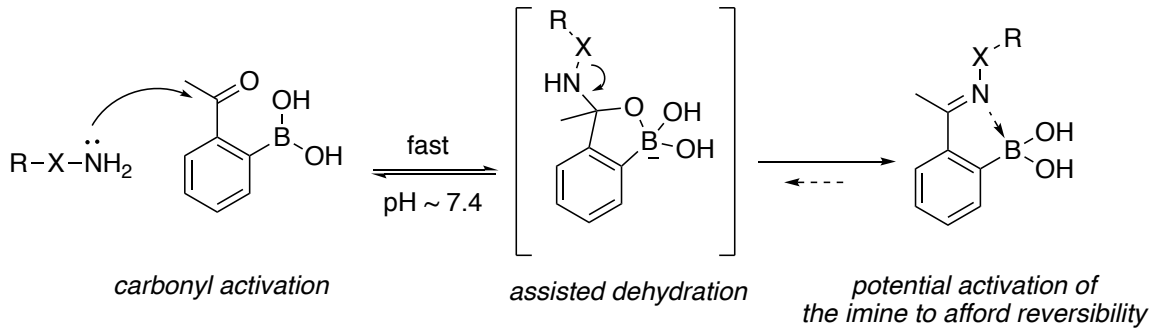

Figure 3-1. Mechanistic illustration of the boronic acid-accelerated conjugation of 2-FPBA/APBA with α-nucleophiles.

Although both 2-APBA and 2-FPBA conjugate with alkoxyamines and hydrazines with fast kinetics, the reaction profiles of these two molecules conjugating to α-nucleophiles can vary dramatically in terms of reversibility and product stability. The conjugation of 2-FPBA to benzylhydroxylamine (**Figure 3-2**) gives fast kinetics (~$1x10^4$ $M^{-1}s^{-1}$), and proceeds with minimal yield reduction in blood serum, indicating high bioorthogonality.[4] Moreover, this conjugation reaction gives a dissociation rate constant of ~$1x10^{-5}$ s^{-1}, indicating a half-life of ~6.6 hours. 2-APBA conjugation to alkoxyamines, however, is instantaneously reversible, with a K_d of $1.4x10^{-5}$ M, which is 3 orders of magnitude larger than that of 2-FPBA (K_d~10^{-8} M).[5] The distinct reactivity profiles of 2-FPBA and 2-APBA towards oxyamines enable different applications given the stabilities of the conjugates formed, with the former finding utility in biomolecular labeling, while the latter may be useful for combinatorial chemistry applications that require facile reversibility for exchange.

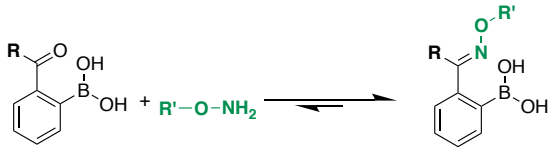

R	K_d (μM)	Dissociation ($t_{1/2}$)	Exchange ($t_{1/2}$)
H	0.004	ND	Yes (6.6 hours)
CH_3	10	Yes (<10 seconds)	NA

Figure 3-2. Oxime formation of 2-FPBA and 2-APBA yields conjugates with varying stabilities. ND= not determined; NA= not applicable.

2-APBA and 2-FPBA have also been shown to readily conjugate with hydrazines, such as phenylhydrazine, at rate constants $>10^3$ $M^{-1}s^{-1}$, yielding highly stable products that do not exhibit dissociation.[5] Kinetic stability experiments have confirmed the slow, minimal dissociation of 2-APBA-Phz conjugates ($k_{-1}<10^{-4}$ s^{-1}). The conjugation of 2-FPBA and phenylhydrazine has also been reported, and these contributions have elucidated a diazaborine structure of these conjugates (**Figure 3-3**).[6,7] The capacity to form diazaborines likely underlies the stability of APBA-phenylhydrazine conjugates; however, structural confirmation of this conjugate has been elusive due to both a lack of crystal structure, as well as the water loss problem of boronic acid analysis by mass spectrometry.[8]

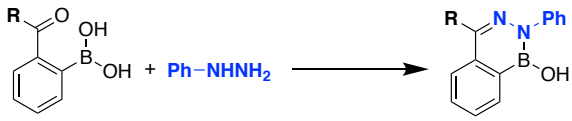

R	K_d (μM)	Dissociation ($t_{1/2}$)	Exchange ($t_{1/2}$)
H	ND	ND	ND
CH_3	ND	ND	Yes (4-6 hours)

Figure 3-3. Stable diazaborine formation of 2-FPBA/APBA upon conjugation with phenylhydrazine. ND= not determined

Phenylhydrazine conjugation with 2-FPBA/APBA has been applied for the labeling of proteins under physiological conditions.[5,6] While this conjugation chemistry readily proceeds without interference by endogenous small molecules or serum proteins, phenylhydrazine is less than ideal for biological applications due to its poor stability and

cytotoxicity, as described herein. Therefore, we investigated the structurally similar molecule, semicarbazide, which enables the same fast formation of stable diazaborine conjugates in complex biological conditions, but with minimal cellular toxicity.[9,10]

3.1.2 Bacterial Metabolic Incorporation of Unnatural Amino Acids into Peptidoglycan

Recently, a series of manuscripts have shown that bacterial peptidoglycan (PG) undergoes dynamic remodeling, which enables the incorporation of synthetic amino acids/dipeptides into the cell wall network (**Figure 3-4**). Peptidoglycan is an essential component of the bacterial cell wall that is highly conserved across bacterial species. This mesh-like polymer consists of linear glycan strands of repeating N-acetylglucosamine (GlcNAc) and N-acetylmuramic acid (MurNAc) dissacharides that are cross-linked by short peptides.[11] While the general structure is conserved, the composition of the cross-linking peptide, as well as the thickness of PG, varies slightly between bacterial species.[12] A key contribution on PG structure and remodeling from the Waldor group described the importance of D-amino acids in the modulation of bacterial cell walls, which are produced at millimolar concentrations and assist in the morphology of cell walls throughout bacterial growth.[13]

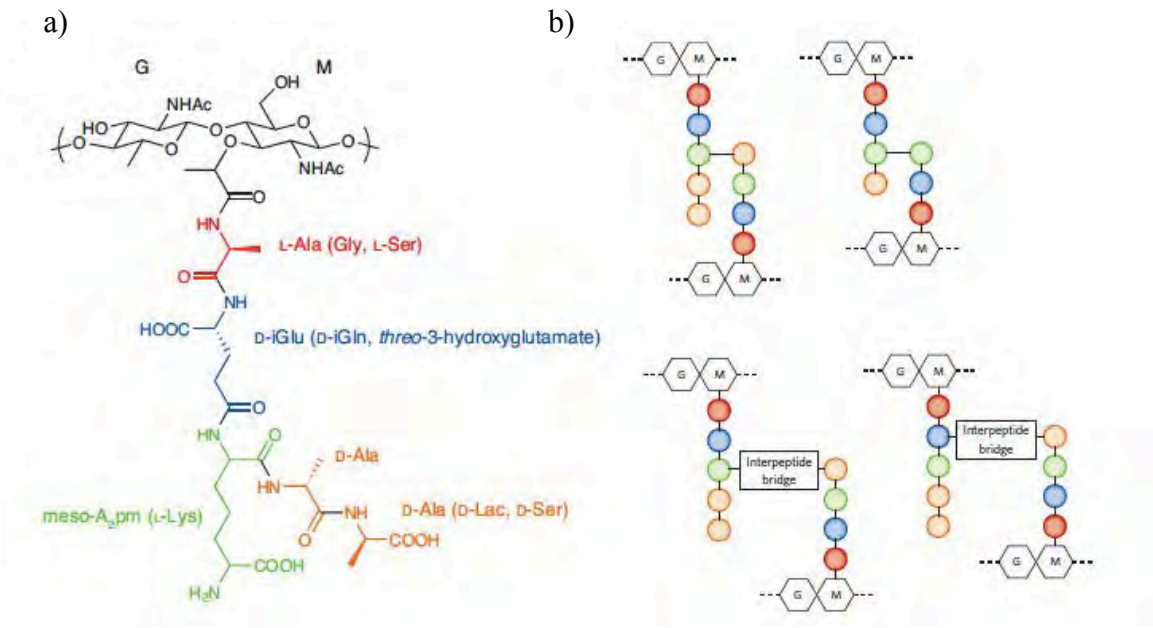

Figure 3-4. Structure of the bacterial peptidoglycan component of the cell wall showing the (a) disaccharide/peptide cross-link as well as (b) possible crosslinking structures (image from Ref. 12).

Many groups have taken advantage of the importance of D-amino acids to bacterial cell morphology throughout cell growth to incorporate a wide array of unnatural D-amino acids into the peptidoglycan.[14–22] The mechanism by which these unnatural amino acids incorporate into the cell wall is through the transpeptidase activity of penicillin binding proteins (PBPs), which is responsible for cross-linking PG (**Figure 3-5**).[14] Transpeptidases activate the donor PG cross-linking peptide via formation of an acyl-enzyme intermediate, which releases the terminal D-Ala. The activated donor then reacts with an amino group on an acceptor peptide or D-amino acid residue. While the donor peptide must be a polymeric fragment of PG, the acceptor molecule can be a single amino acid so long as the α-amino nucleophile is in the D-configuration.

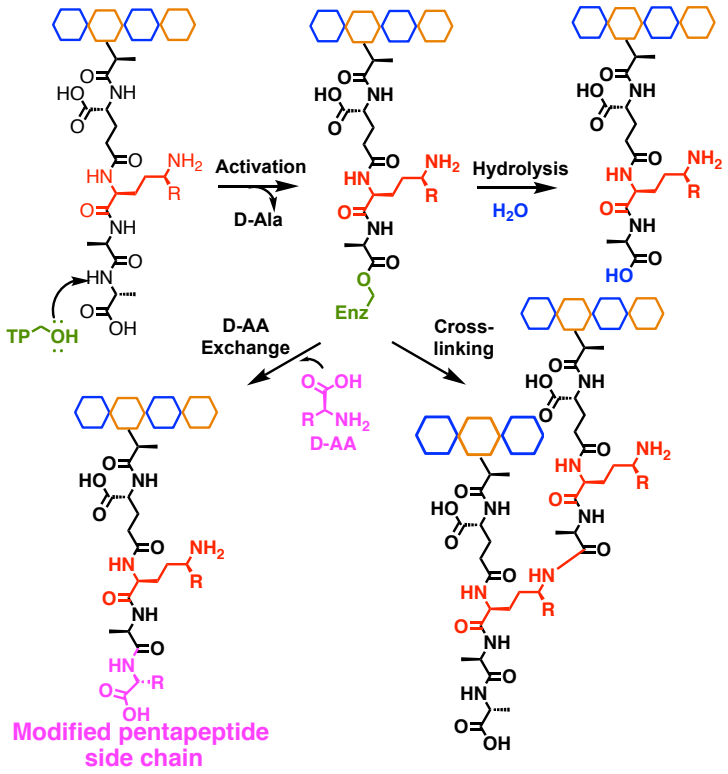

Figure 3-5. Transpeptidase activity of PBPs enables incorporation of unnatural D-amino acids into bacterial peptidoglycan (adapted from Ref. 14).

Through this promiscuous transpeptidase mechanism, several groups have achieved incorporation of a wide array of unnatural amino acids (**Figure 3-6**). These amino acids, which generally fall into either the clickable or fluorescent derivatives categories, often lack one or more ideal criterion for achieving bioorthogonality towards labeling of bacterial cells. The clickable derivatives incorporate CuAAC or SPAAC clickable handles, which suffer from slow kinetics or high toxicity of catalysts required to make the reactions faster. The fluorescent derivatives, on the other hand, are quite large, which makes them challenging to both penetrate through the cell wall, as well as to achieve efficient cell wall incorporation via the transpeptidase enzyme. Therefore, we postulated that the highly bioorthogonal diazaborine chemistry described herein would

provide a better substitute to these aforementioned unnatural D-amino acids given the superior biocompatiblity qualities of semicarbazides and 2-FPBA/APBA towards the labeling of bacterial cells.

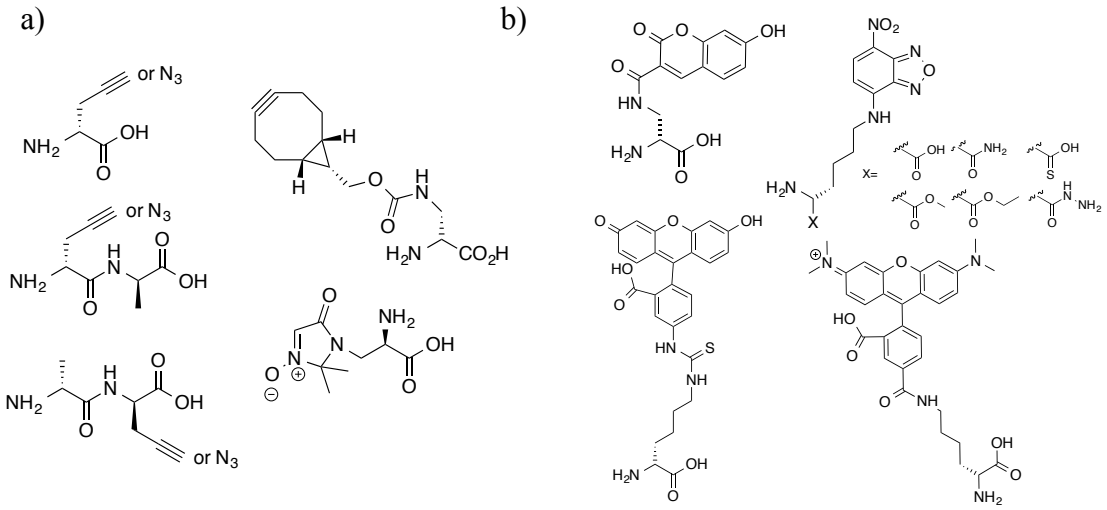

Figure 3-6. Published unnatural D-amino acids for bacterial peptidoglycan labeling. These unnatural amino acids fall into either (a) clickable or (b) fluorescent derivative categories.

3.1.3 Fluorogenic Reactions Enable No Wash Labeling of Bacteria

While fluorescent reactive handles are useful tools for assessing the incorporation of our unnatural amino acids, molecular probes that turn on fluorescence in response to a target are of great utility for biological applications.[23–28] Probes belonging to this category have been successfully developed for a variety of metal ions and small molecule messengers, which function by eliciting a fluorescence increase through coordination or conjugation with a reactive partner probe. Additionally, fluorogenic substrates have been used to study enzymes that can catalyze the formation of fluorescent products.[29]

Alternatively, development of fluorogenic probes for biomolecules with no catalytic function has been challenging until recent advancements in bioorthogonal

chemistry. As previously mentioned, bioorthogonal conjugation chemistry enables the fluorescent labeling of non-enzymatic biomolecules through conjugation of a reactive handle to a reactive partner labeled fluorophore.[30–33] These types of chemistries have been applied for the labeling of proteins, as well as for tracing carbohydrate metabolism in live cells; however, these applications are limited by the need for excess labeling reagents, which often result in high background fluorescence. Thus, bioorthogonal conjugation reactions that are fluorogenic, would help us to overcome this limitation.[34] Towards this end, we envisioned that by generating a non-fluorescent APBA-coumarin analogue, we would be able to elicit turn-on fluorescence via conjugation to semicarbazide (**Figure 3-7**). The capacity for biological applications of this fluorogenic reaction is highlighted by the fast and targeted visualization of semicarbazide-presenting bacterial cells generated through metabolic PG incorporation of a D-Dap-semicarbazide unnatural amino acid.

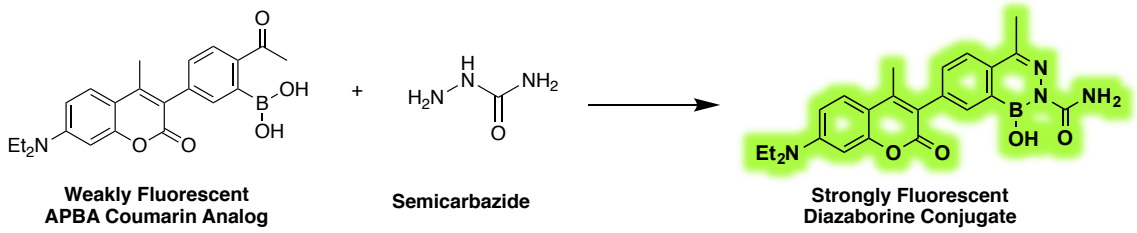

Figure 3-7. Conjugation of a non-fluorescent APBA coumarin derivative with semicarbazide generates a highly fluorescent stable diazaborine conjugate.

3.2 Fast Diazaborine Formation of Semicarbazide Yields Stable Conjugates of 2-FPBA/APBA

Although the rapid conjugation of phenylhydrazine to form stable diazaborines is attractive as a bioorthogonal reaction, we determined that phenylhydrazine is prone to oxidation, which results in a short half life of only a few hours in physiologically relevant aqueous buffer (**Figure 3-8a**). Moreover, phenylhydrazine that is subjected to neutral aqueous conditions for several hours no longer forms diazaborines with 2-APBA (**Figure 3-8b**). Other possible α-nucleophile surrogates that are stable in aqueous physiologic conditions, including acethydrazide and benzhydrazide, have previously been shown to reversibly conjugate with 2-APBA to form iminoboronates instead of stable diazaborines.[35] In search of alternatives to phenylhydrazine that generate stable diazaborine conjugates, we turned to the α-nucleophile semicarbazide.

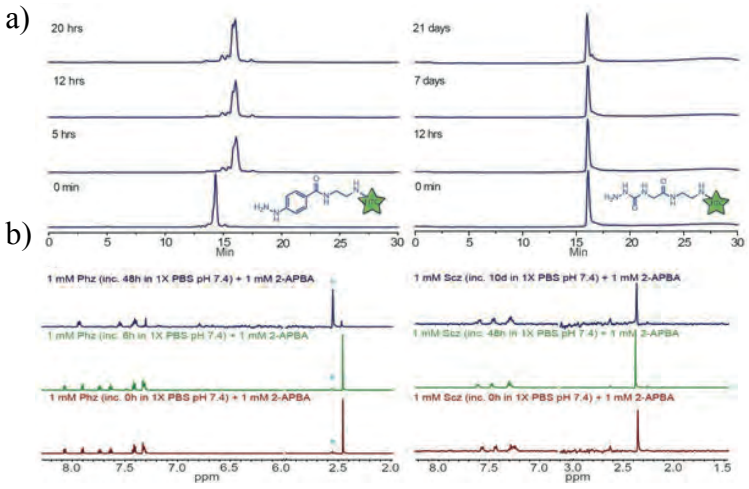

Figure 3-8. Stability test of semicarbazide and phenylhydrazine in 1X PBS buffer (pH 7.4). (a) Stacked HPLC chromatograms over time are shown for 100 μM Phzn-FITC (left) and 100 μM Scz-FITC (right). (b) ^{1}H NMR analysis of non-fluorescently labeled phenylhydrazine and semicarbazide (both 1 mM) incubated in 1× PBS buffer (pH 7.4) over time, then subjected to diazaborine formation with 2-APBA (1 mM) in 1X PBS buffer (pH 7.4) (* denotes 2-APBA CH3 chemical shift).

3.2.1 Semicarbazide Conjugates with 2-FPBA and 2-APBA to Form Diazaborines

The α-nucleophile semicarbazide is superior to phenylhydrazine in terms of its stability in aqueous physiologic buffer, which remains intact even after several weeks of incubation (**Figure 3-8a, right**). Importantly, semicarbazide conjugates with 2-FPBA/APBA to form stable diazaborines (2-FPBA conjugate = DAB1, 2-APBA conjugate = DAB2, **Figure 3-9a**). Mixing semicarbazide with 2-FPBA in neutral buffer resulted in a clean ^{1}H NMR spectrum corresponding to a single conjugation product (**Figure 3-9b**). The crystal structures of the diazaborine conjugate of 2-FPBA and semicarbazide (**Figure 3-9c**), as well as that of a 2-APBA bearing amino acid, L-AB3, and semicarbazide (**Figure 3-9d**) were obtained. These X-ray structures confirmed that the diazaborine heterocycle is indeed formed with semicarbazide conjugation to 2-FPBA/APBA.

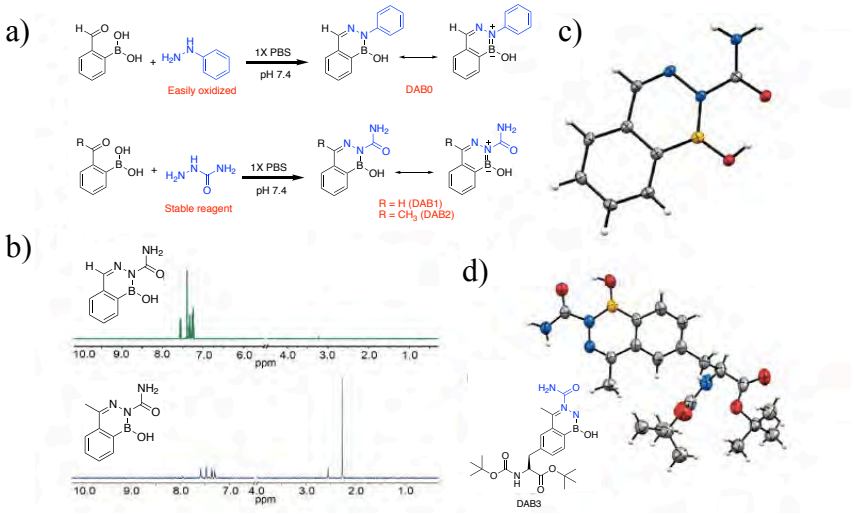

Figure 3-9. Diazaborine formation of semicarbazide. (a) Schematic illustration of diazaborine formation of semicarbazide in comparison to that of phenylhydrazine. (b) ^{1}H NMR spectra of semicarbazide mixed with equimolar 2-FPBA (top) and 2-APBA (bottom). (c) Crystal structure of DAB1, the diazaborine conjugate of semicarbazide and 2-FPBA. (d) Crystal structure of DAB3, a diazaborine conjugate of semicarbazide and the synthetic APBA-presenting amino acid L-AB3. (^{1}H NMR and X-Ray crystal data were collected by Dr. Anupam Bandyopadhyay)

3.2.2 Diazaborine Formation of Semicarbazide is Fast and Irreversible

Similar to phenylhydrazine, semicarbazide conjugation with 2-FPBA/APBA yields stable diazaborine conjugates in aqueous physiologic buffer, as observed by LC-MS and ^{1}H NMR analysis. In the former case, DAB1 and DAB2 remained intact during LC analysis and purification performed with acidic eluents (**Figure 3-10**). Conversely, the 2-APBA conjugates of acethydrazide previously could not be identified in LC-MS analysis due to complete hydrolysis.[35]

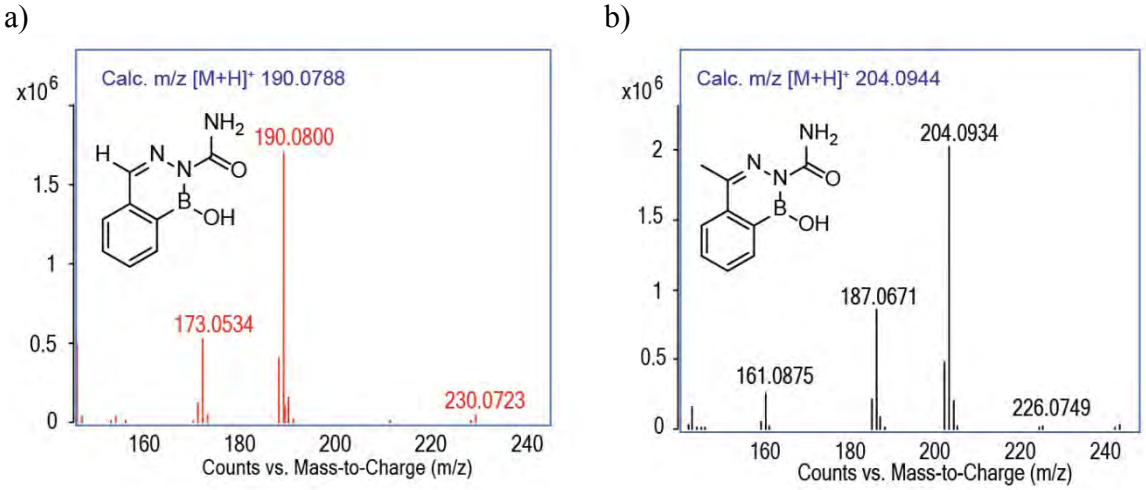

Figure 3-10. ESI-MS analysis of diazaborine conjugates. Diazaborine conjugates (a) DAB1 and (b) DAB2 were identified by MS. (Data collected by Dr. Anupam Bandyopadhyay)

In the case of ^{1}H NMR analysis, 100 μM samples of DAB1 and DAB2 exhibited no degradation over 3 days at room temperature (**Figure 3-11**). To assess whether the stability was a result of kinetic or thermodynamic origin, control samples of 100 μM semicarbazide with equimolar 2-FPBA/APBA were prepared. While 2-FPBA conjugated completely with semicarbazide, 2-APBA reached a maximum yield of 80% with 20% of reactants remaining, as shown by LC-MS analysis (**Figure 3-12**). This incomplete

conjugation of 2-APBA is in contrast to the lack of degradation of DAB2, which indicates that the diazaborines of semicarbazide are kinetically stable, which is highly desirable for bioorthogonal reactions.

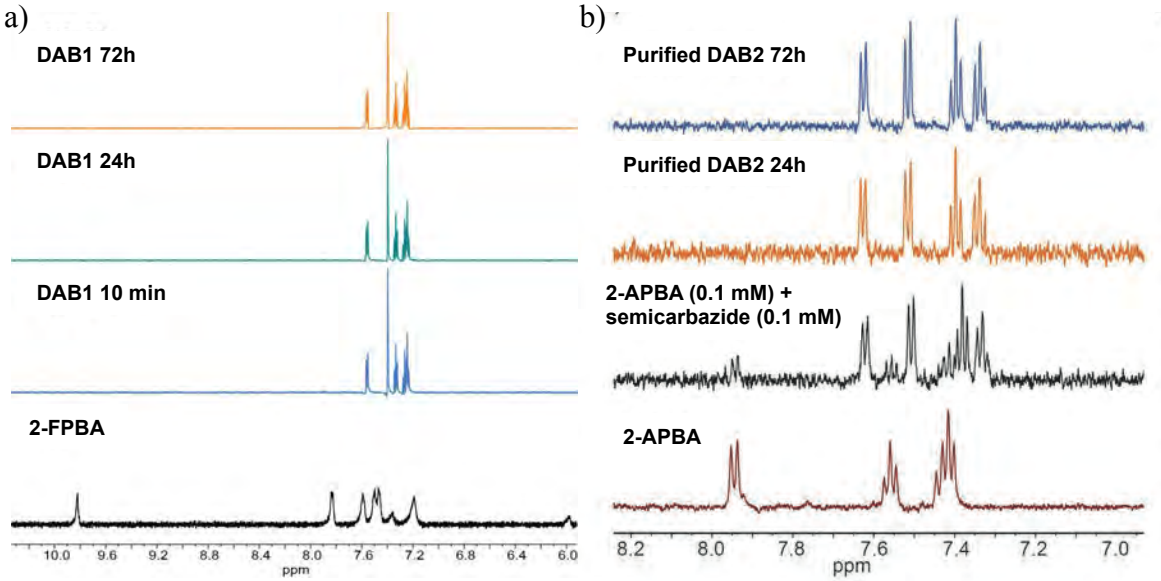

Figure 3-11. ^{1}H NMR analysis of the stability of diazaborine conjugates. Diazaborine conjugates (a) DAB1 and (b) DAB2 were prepared with 100 µM 2-APBA/FPBA and 100 µM semicarbazide in 1X PBS pH 7.4. (Data collected by Dr. Anupam Bandyopadhyay)

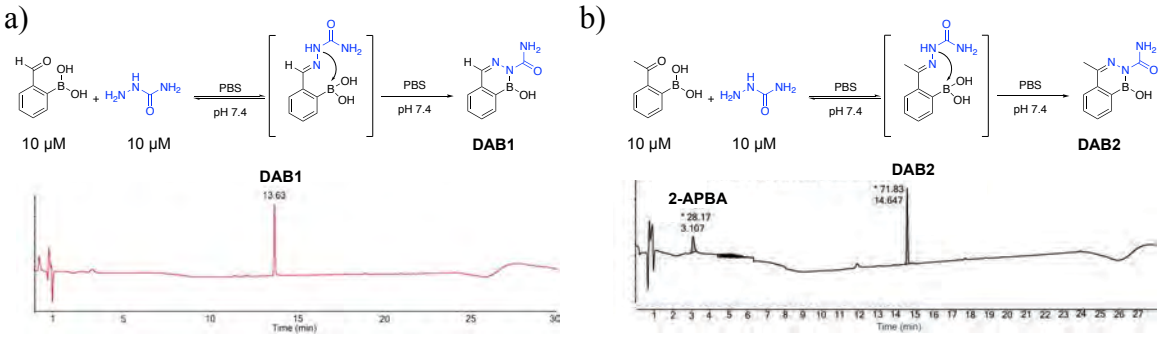

Figure 3-12. LC-MS analysis of the conjugation of 10 µM 2-FPBA/APBA conjugating to 10 µM semicarbazide to generate (a) DAB1 or (b) DAB2. (Data collected by Dr. Anupam Bandyopadhyay)

The conjugation efficiency of semicarbazide was examined by both ^{1}H NMR and LC-MS analysis (**Table 3-1**). ^{1}H NMR results show that while DAB1 formation proceeds quantitatively, even with reactants at low micromolar concentrations, DAB2 formation only yields 60% diazaborine conjugate at 50 μM 2-APBA and semicarbazide (**Figure 3-13b**). The LC-MS analysis yielded consistent results.

Table 3-1. Yields of diazaborine formation for various combinations of 2-FPBA/APBA and semicarbazide as determined by ^{1}H NMR.

Electrophile	Semicarbazide (μM)	Yield
2-FPBA (10 μM)	10	>95%
2-APBA (50 μM)	50	60%
	100	80%
	150	86%
	200	90%
	400	95%

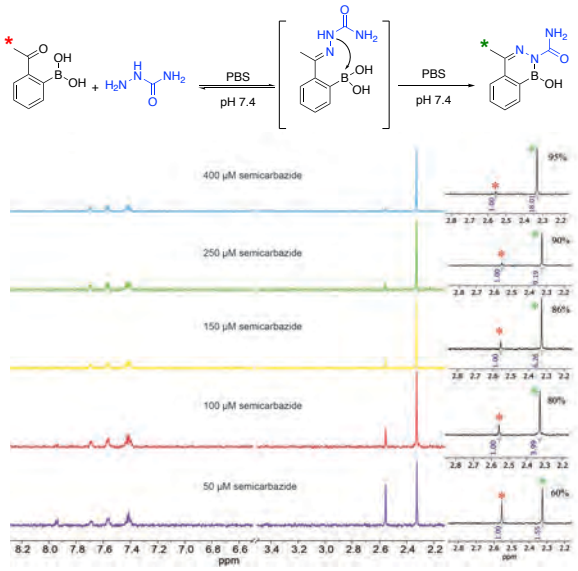

Figure 3-13. Assessing the efficiency of semicarbazide conjugation to APBA by ^{1}H NMR. Yields are calculated by integrating the 2-APBA (*) and diazaborine (*) CH_3 chemical shifts. (Data collected by Dr. Anupam Bandyopadhyay)

To investigate the source of the lack of completion observed for DAB2 formation despite no evidence of side product formation, we probed the possibility of product inhibition by analyzing the ^{1}H NMR spectra of a DAB2 derivative mixed with each reactant at equimolar concentrations (**Figure 3-14**). As a result of low water solubility of DAB2, the diazaborine conjugate of semicarbazide and the unnatural amino acid L-AB3 was used for the experiment. The NMR spectrum revealed a distinct shift of the aromatic peaks of the diazaborine conjugate when mixed with either reactant. This peak is believed to originate from interactions of the product with the reactants, which indicates a probable source of stalled reaction.

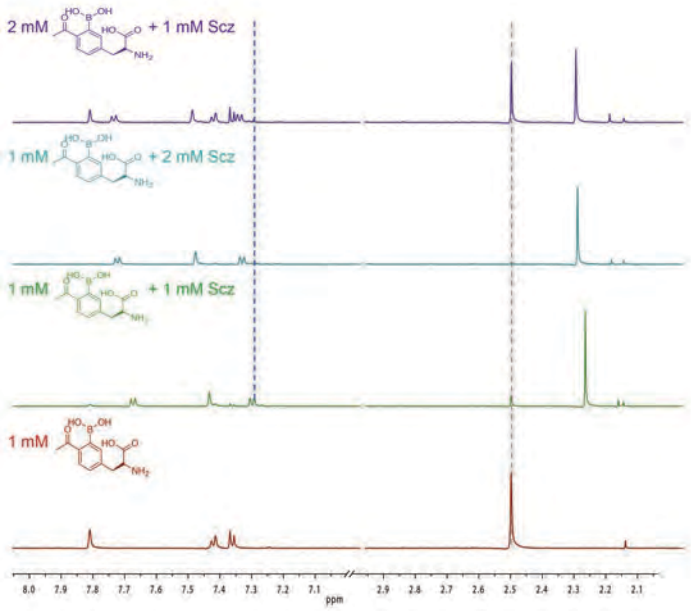

Figure 3-14. ^{1}H NMR analysis of potential sequestration of the reactants by the diazaborine product. Equimolar excess L-AB3 or semicarbazide (1 mM excess each) was added to the pre-formed diazaborine (1 mM) in 1X PBS pH 7.4, and the ^{1}H NMR spectra were obtained in 10% D_2O. The spectra were aligned on by the acetyl peak of free L-AB2 (gray dashed line) and observed shifts in the diazaborine peaks (blue dashed line) indicate interactions between the diazaborine products and reactants.

The kinetics of diazaborine formation of DAB1 and DAB2 were determined via a UV-Vis experiment, which enabled the reaction to be monitored at low concentrations (**Figure 3-15**). Both 2-FPBA and 2-APBA exhibit an absorption maximum at ~254 nm, which shifts to ~290 nm upon diazaborine formation. The kinetics of DAB1 formation was determined upon mixing 10 μM 2-FPBA and semicarbazide by monitoring the absorption increase at 290 nm, which afforded a kinetic plot of the reaction that was fit to a second order reaction mechanism, yielding a rate constant of $>10^3$ $M^{-1}s^{-1}$ (**Figure 3-16**). A similar rate constant was obtained for the conjugation of 2-APBA and semicarbazide, which shows that the diazaborine formation of semicarbazide is equally fast to that of phenylhydrazine, and is also comparable to the fastest conjugation reactions documented in literature.

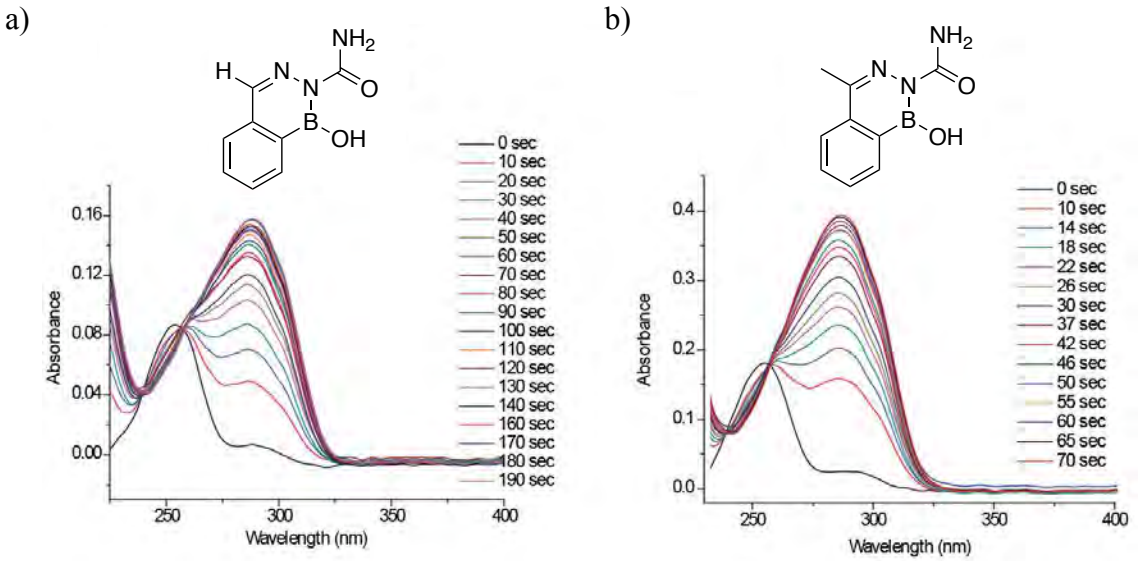

Figure 3-15. UV-Vis assessment of the kinetics of diazaborine formation. Kinetic rate constants of (a) DAB1 and (b) DAB2 were determined by UV-Vis absorption. (Data collected by Dr. Anupam Bandyopadhyay)

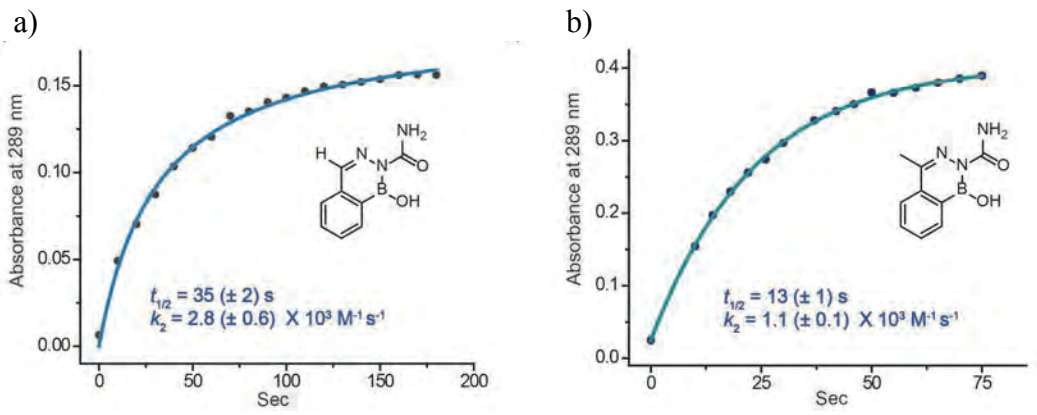

Figure 3-16. Kinetic profiles of diazaborine formation. Kinetic fits of (a) DAB1 and (b) DAB2 formation as monitored by UV-Vis absorption. Measurements were carried out in triplicate to generate error values. (Data collected by Dr. Anupam Bandyopadhyay)

3.3 Diazaborine Formation of Semicarbazide Enables Facile Labeling of Bacterial Pathogens via D-AB3 Peptidoglycan Incorporation

With the knowledge that diazaborine formation of semicarbazide with 2-FPBA/APBA yields stable conjugates, we aimed to further investigate the bioorthogonality of this chemistry. To do so, we explored the stability of the reagents and products in biological conditions, as well as the toxicity of the reagents towards bacterial and mammalian cells.

3.3.1 Assessing the Bioorthogonality of Diazaborine Formation of Semicarbazide

Given our reports on the slowly reversible conjugation of 2-FPBA and cysteine at low micromolar concentrations[36], we postulated that this thiazolidinoboronate (TzB) formation with 2-FPBA may interfere with the conjugation of 2-FPBA to semicarbazide. To test this hypothesis, we pre-incubated 2-FPBA with equimolar L-cysteine (0.2 mM), and then examined the diazaborine formation of 2-FPBA with semicarbazide, which yielded only 40% diazaborine after 40 minutes (**Figure 3-17a**). 2-APBA, which also conjugates with free cysteine in a rapidly reversible manner, was also pre-incubated with

equimolar L-cysteine (0.2 mM), which showed no interference with diazaborine formation of 2-APBA (**Figure 3-17b**), suggesting superior bioorthogonality of the 2-APBA diazaborine forming reaction.

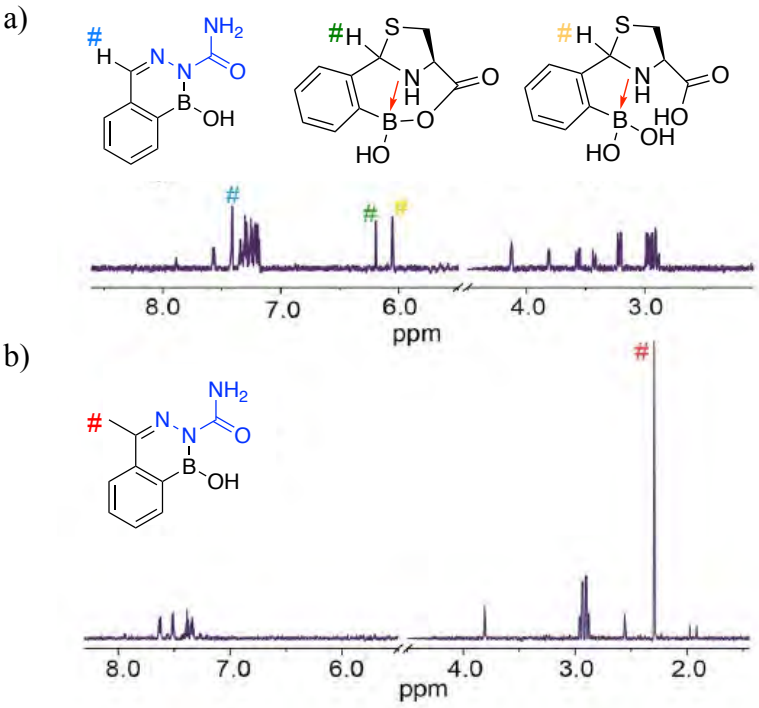

Figure 3-17. Orthogonality of diazaborine chemistry of DAB1 and DAB2 formation to cysteine-containing biological environments.[1]H NMR analysis of diazaborine formation of 0.2 mM (a) 2-FPBA or (b) 2-APBA after pre-incubation with 0.2 mM L-cysteine in PBS pH 7.4 (data collected by Dr. Anupam Bandyopadhyay).

Diazaborine formation of semicarbazide was further analyzed for bioorthogonality in the presence of fetal bovine serum (FBS), as well as bacterial and mammalian cell lysates. The presence of FBS (20%) in the reaction mixture yielded minimal interference to diazaborine formation of both 2-FPBA and 2-APBA (**Figure 3-18**), which may result from the oxidative environment of blood serum, which contains low levels of free cysteine.[37] The diazaborine formation of 2-FPBA and 2-APBA was also minimally inhibited in the presence of HEK293T mammalian cell lysates (**Figure 3-**

18). This phenomenon could be due to minimal free cysteine in the lysate as a result of dilution and oxidation during lysate preparation. *Staphylococcus aureus* lysates, however, did inhibit the conjugation of 2-FPBA to semicarbazide, which yielded only 12% diazaborine after 30 minutes (**Figure 3-18**). Beyond free cysteine, *S. aureus* is known to express high concentrations of bacillithiol, which displays an N-terminal cysteine, and thus is likely responsible for the inhibition of 2-FPBA diazaborine formation. The diazaborine product of 2-FPBA in the *S. aureus* lysate mixture was observed to increase over the course of several hours (data not shown), highlighting the reversibility of the interfering TzB reaction. In contrast to 2-FPBA, 2-APBA was observed to rapidly conjugate with semicarbazide, with little interference by *S. aureus* lysates (**Figure 3-18**).

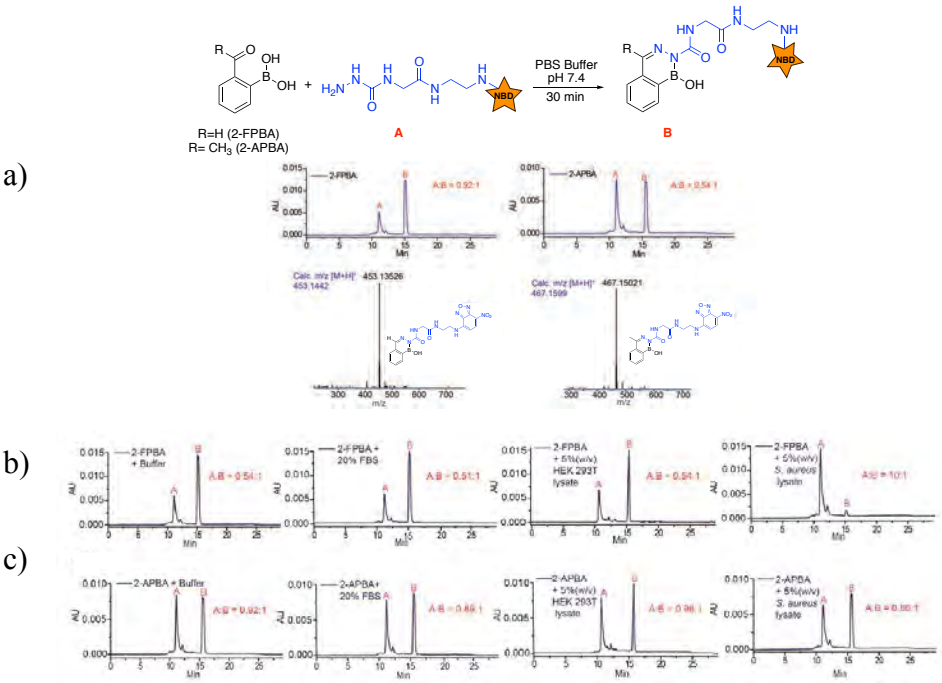

Figure 3-18. Compatibility of diazaborine chemistry to mammalian and bacterial biological systems. (a) LC-MS confirmation of the diazaborine formation of 2-FPBA/APBA with semicarbazide-NBD. (b) DAB1 and (c) DAB2 formation of 25 µM 2-FPBA/APBA and 50 µM semicarbazide-NBD in PBS buffer (pH 7.4) alone, or in the presence of FBS (20% v/v), HEK cell lysate (5 mg/mL), and *S. aureus* (5 mg/mL). (Data collected by Dr. Anupam Bandyopadhyay)

3.3.2 Assessing the Stability and Toxicity of Diazaborine Conjugation Reagents

To test the stability of the diazaborine-forming reagents in biological conditions, we incubated 2-FPBA, 2-APBA and a FITC labeled semicarbazide (Scz-FITC) with 20% FBS or HEK cell lysates for 24 hours before subjecting them to diazaborine conjugation reactions. HPLC analysis of these reactions (**Figure 3-19**) showed essentially the same yields regardless of the length of incubation (0 or 24 hours). Notably, the reactive semicarbazide molecule is quite stable in comparison to the fast degradation observed with phenylhydrazine (**Figure 3-8**). Moreover, PAGE analysis of the HEK cell lysates treated with Scz-FITC showed no significant protein labeling (**Figure 3-20**). Altogether these results confirm the stability of all three reagents in biological systems.

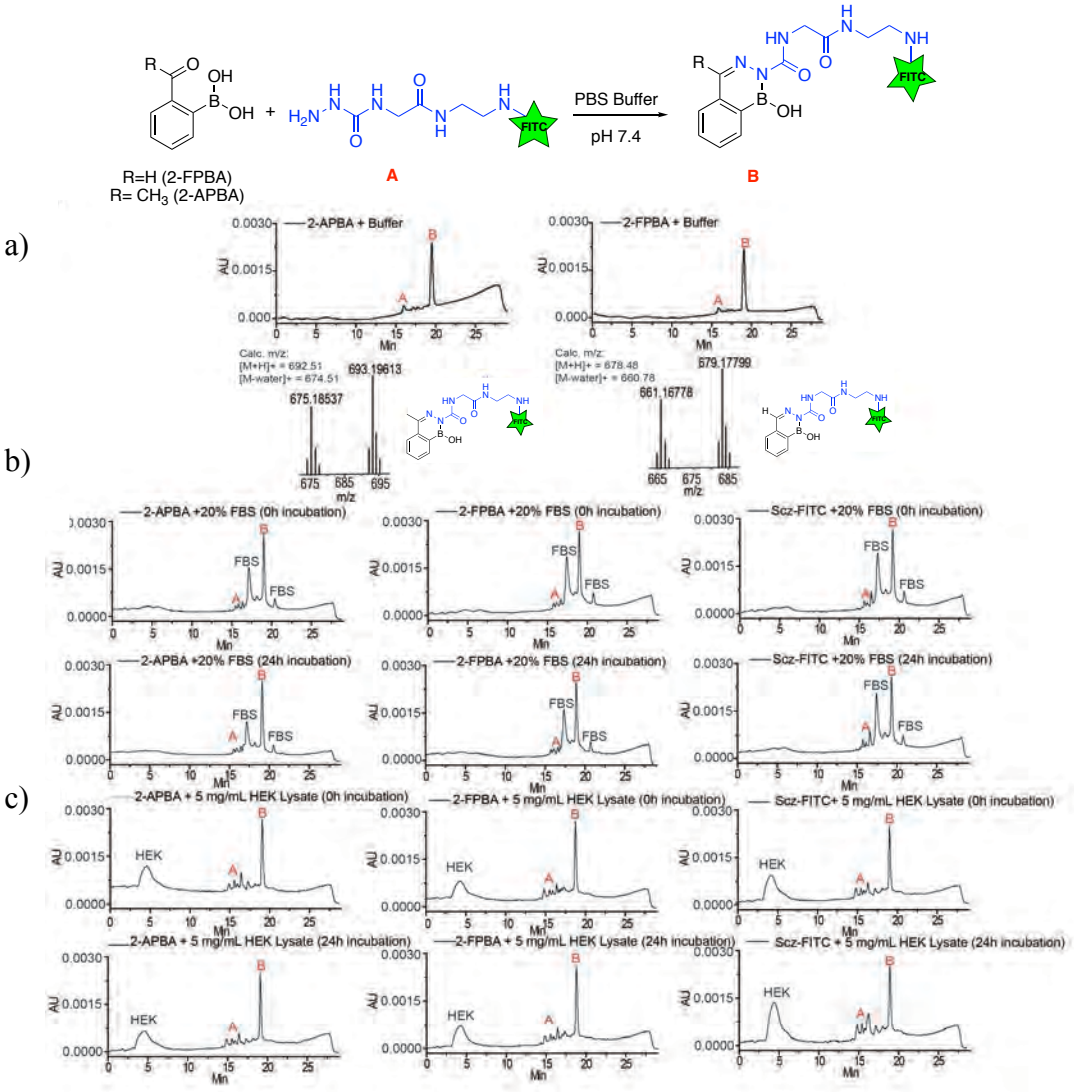

Figure 3-19. Stability of diazaborine reactants in biological conditions. (a) Analytical HPLC traces and mass spectrometry data of the conjugation of 2-FPBA (left) and 2-APBA (right) (100 μM each) with Scz-FITC (50 μM). (b) 2-FPBA (left), 2-APBA (center) and Scz-FITC (right) incubated in the presence of 20% FBS (w/v), then conjugated to either Scz-FITC or 2-APBA as in part a. (c) 2-FPBA (left), 2-APBA (center) and Scz-FITC (right) incubated in the presence of 3 mg/mL HEK 293T lysate, then conjugated to either semicarbazide-FITC or 2-APBA as in part a. Chromatograms were recorded by monitoring absorption at 480 nm.

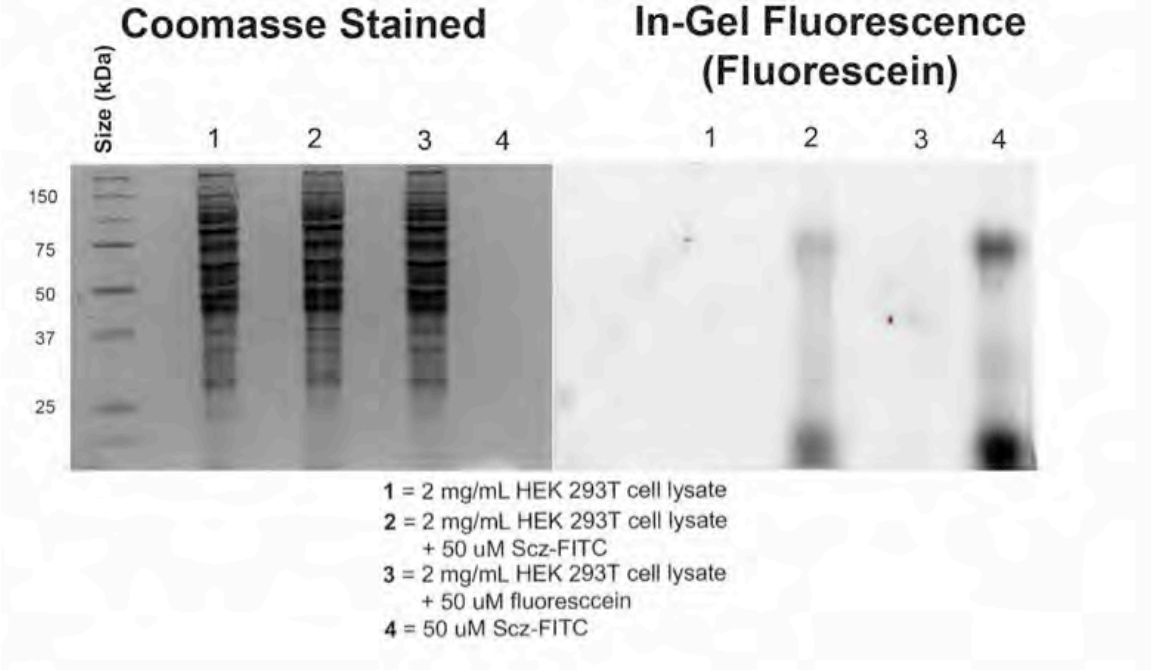

Figure 3-20. Fluorescent gel analysis of HEK293T cell lysate labeling by semicarbazide-FITC.

We also examined the potential cytotoxicity of semicarbazide alongside phenylhydrazine for comparison. Two strains of bacteria (*Escherichia coli* and *S. aureus*) and a model mammalian cell line (HEK 293T) were treated with both semicarbazide and phenylhydrazine (**Figure 3-21**). The percentage of surviving cells was determined by colony counting for the bacteria, and by MTT assay for the HEK cells. The results showed little toxicity for all three cell lines for semicarbaizde, whereas phenylhydrazine elicited 10-25% cell death for bacteria, and ~50% cell death for the HEK cells after 24 hours of incubation. We also examined the toxicity of a 2-APBA amino acid derivative, D-AB3, which elicited no measureable death for any of the cell lines. Thus, the reagents for diazaborine formation are amenable to biological systems.

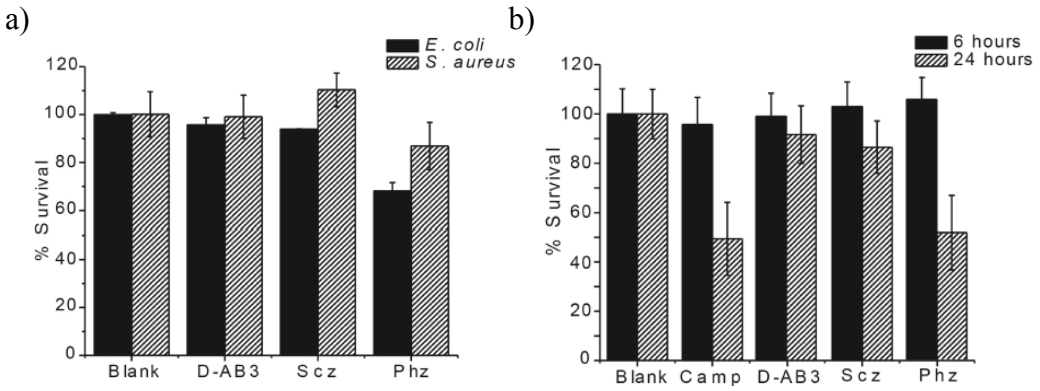

Figure 3-21. Cytotoxicity studies of the reactants for diazaborine conjugation. (a) Percentage of cell survival determined by colony counting for *E. coli* and *S. aureus*. (b) Percentage of cell survival determined by MTT assay for HEK293T cells. Phenylhydrazine (Phz) was included as a direct comparison to semicarbazide. Camptothecin (Camp) was included as a positive control in the HEK293T MTT assay. All compounds were tested at 50 μM.

3.3.3 Semicarbazide Conjugation Allows Facile Labeling of Bacterial Pathogens

Given the observed high biocompatibility of diazaborine chemistry, we applied semicarbazide conjugation chemistry to the facile detection of bacterial pathogens via peptidoglycan incorporation. Towards this end, we synthesized the amino acid D-AB3, which is a 2-APBA analogue, and analyzed its incorporation into an array of bacterial species including *S. aureus* (**Figure 3-24**), *E. coli* (**Figure 3-23**), *Klebsiella pneumonia* (*K. pneumoniae*, **Figure 3-25**), and *Pseudomonas aeruginosa* (*P. aeruginosa*, **Figure 3-26**) at varying concentrations. While *E. coli* was brightly labeled, *S. aureus* and *K. pneumoniae* were stained with lower efficiency, and *P. aeruginosa* was not significantly stained. To measure this D-AB3 incorporation, excess amino acid was washed away and the cells were subsequently stained with Scz-FITC. The semicarbazide ligation was performed with 50 μM Scz-FITC for 30 minutes, which was expected to yield 60% diazaborine. After washing, the cells were analyzed by fluorescence microscopy and flow

cytometry (**Figure 3-22**). As previously mentioned, *E. coli* exhibited bright staining in comparison to minimally fluorescent *S. aureus*. This higher efficiency of D-AB3 incorporation into *E. coli* was further validated by flow cytometry, which exhibited a median fluorescence intensity ~10X higher for *E. coli* than that for *S. aureus* and *K. pneumoniae* (**Figure 3-22c**). Importantly, the bacterial cell staining via diazaborine formation showed little interference by the presence of blood serum or cell lysates (**Figure 3-22d**). Specifically, *E. coli* cells were labeled with D-AB3, then labeled with Scz-FITC in the presence of 5 mg/mL HEK293T cell lysate or 10% (v/v) FBS. The samples were then analyzed by flow cytometry, which yielded comparable histograms of the stained cells with no FBS or HEK293T lysates.

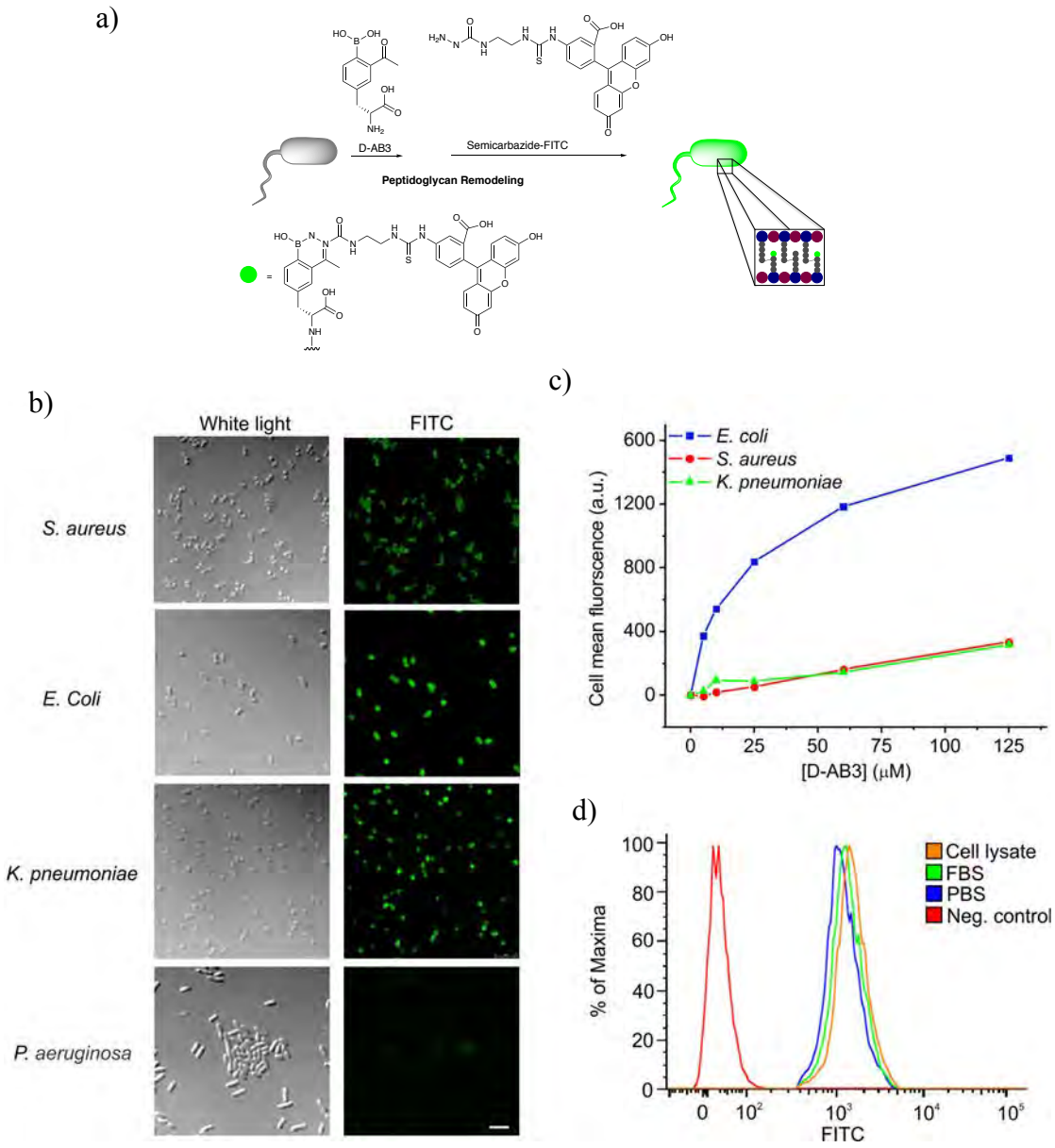

Figure 3-22. Semicarbazide conjugation to form stable diazaborines enables facile labeling of bacterial pathogens. (a) Schematic illustration of the two-step protocol for bacterial cell labeling. (b) Microscopic images and (c) flow cytometry analysis show that D-AB3 incorporation varies across bacterial species. (d) Flow cytometry histograms show that semicarbazide-enabled bacterial labeling is unaffected by blood serum or mammalian cell lysates.

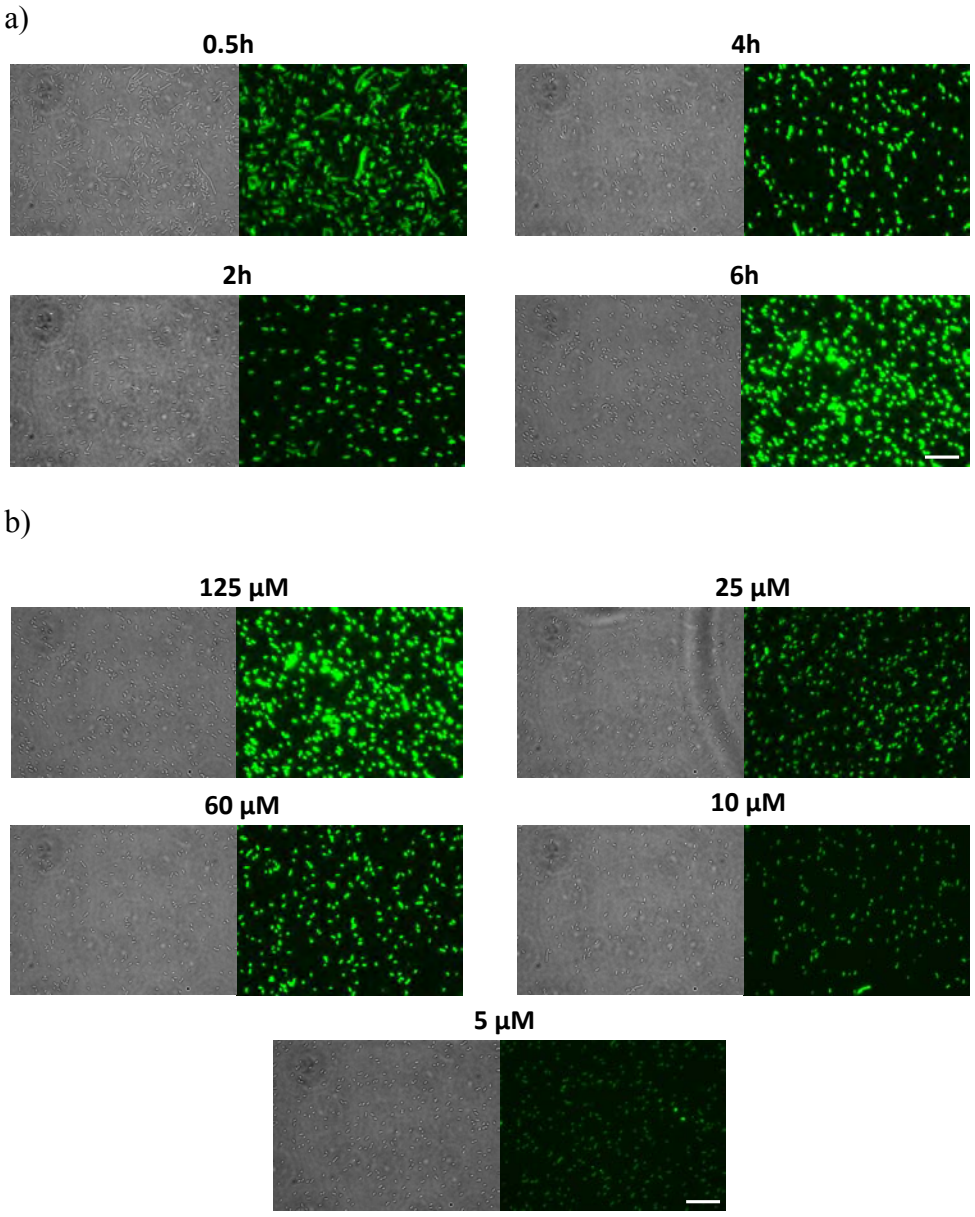

Figure 3-24. *E. coli* labeling with D-AB3 and Scz-FITC. (a) Time course of D-AB3 incubation (125 µM) at 0.5, 2, 4 and 6 hours followed by Scz-FITC incubation for 30 min. (b) D-AB3 concentration profile of labeling at 6 hours incubation (scale bar, 10 µm).

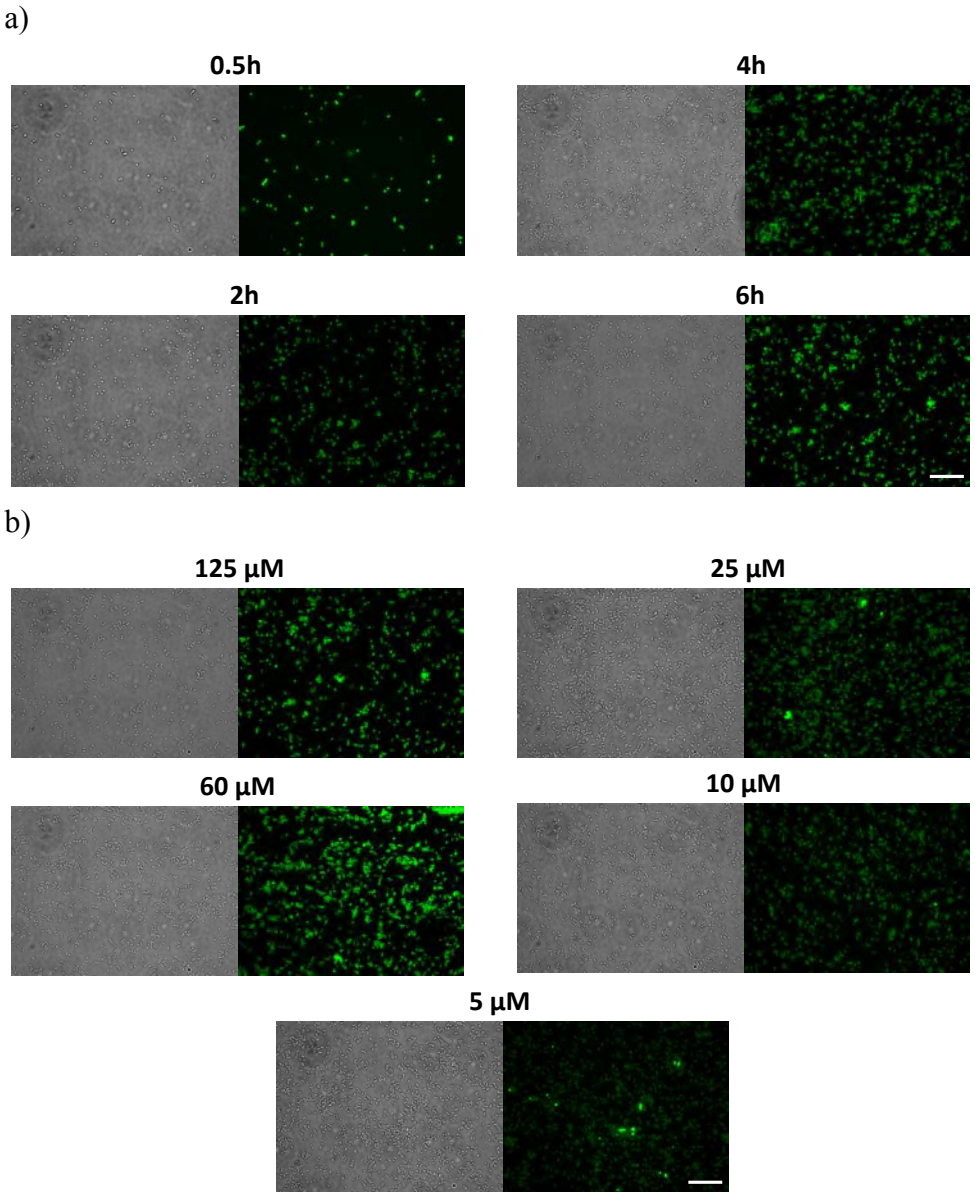

Figure 3-24. *S. aureus* labeling with D-AB3 and Scz-FITC. (a) Time course of D-AB3 incubation (125 µM) at 0.5, 2, 4 and 6 hours followed by Scz-FITC incubation for 30 min. b) D-AB3 concentration profile of labeling at 6 hours incubation (scale bar, 10 µm).

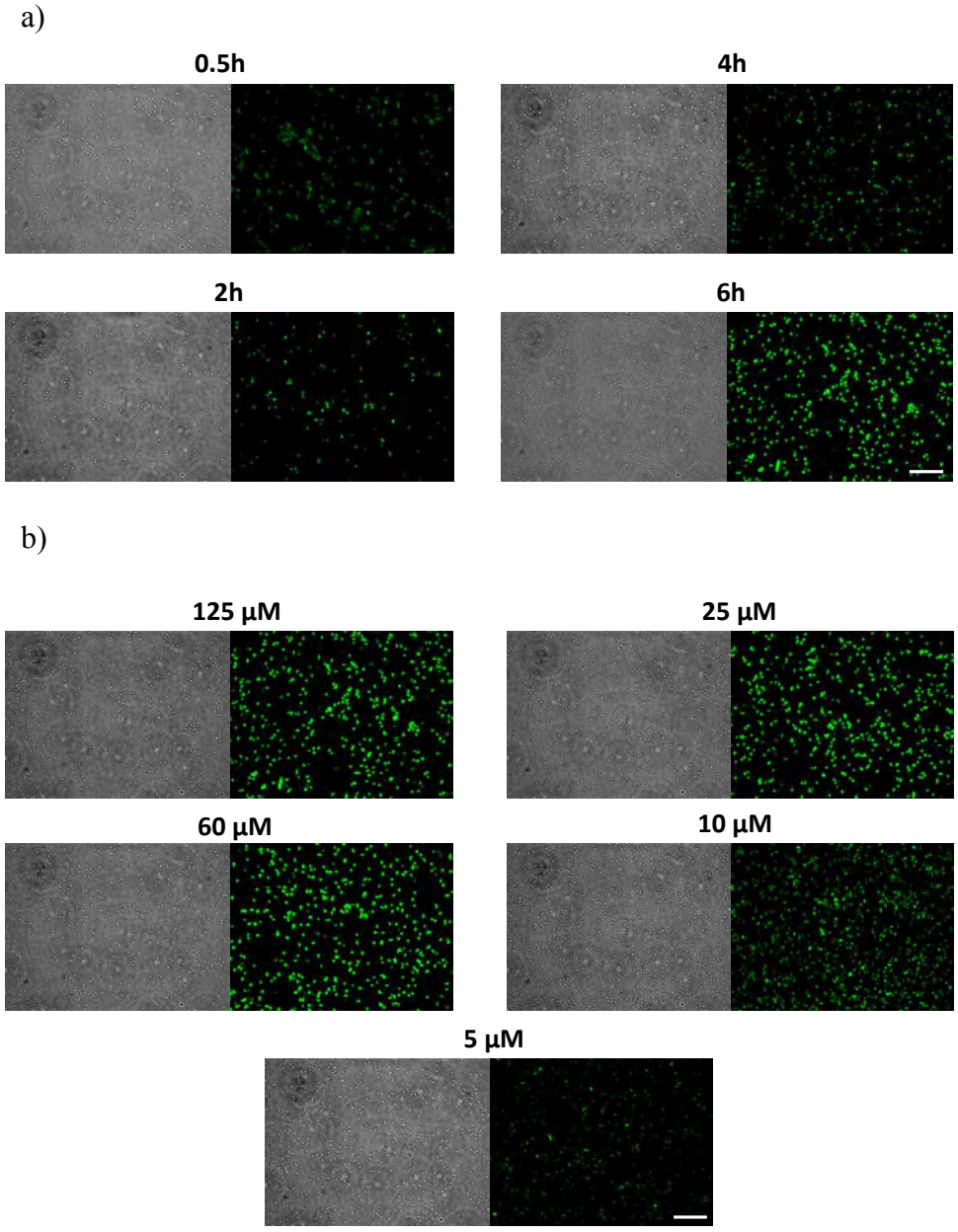

Figure 3-25. *K. pneumoniae* labeling with D-AB3 and Scz-FITC. (a) Time course of D-AB3 incubation (125 µM) at 0.5, 2, 4 and 6 hours followed by Scz-FITC incubation for 30 min. (b) D-AB3 concentration profile of labeling at 6 hours incubation (scale bar, 10 µm).

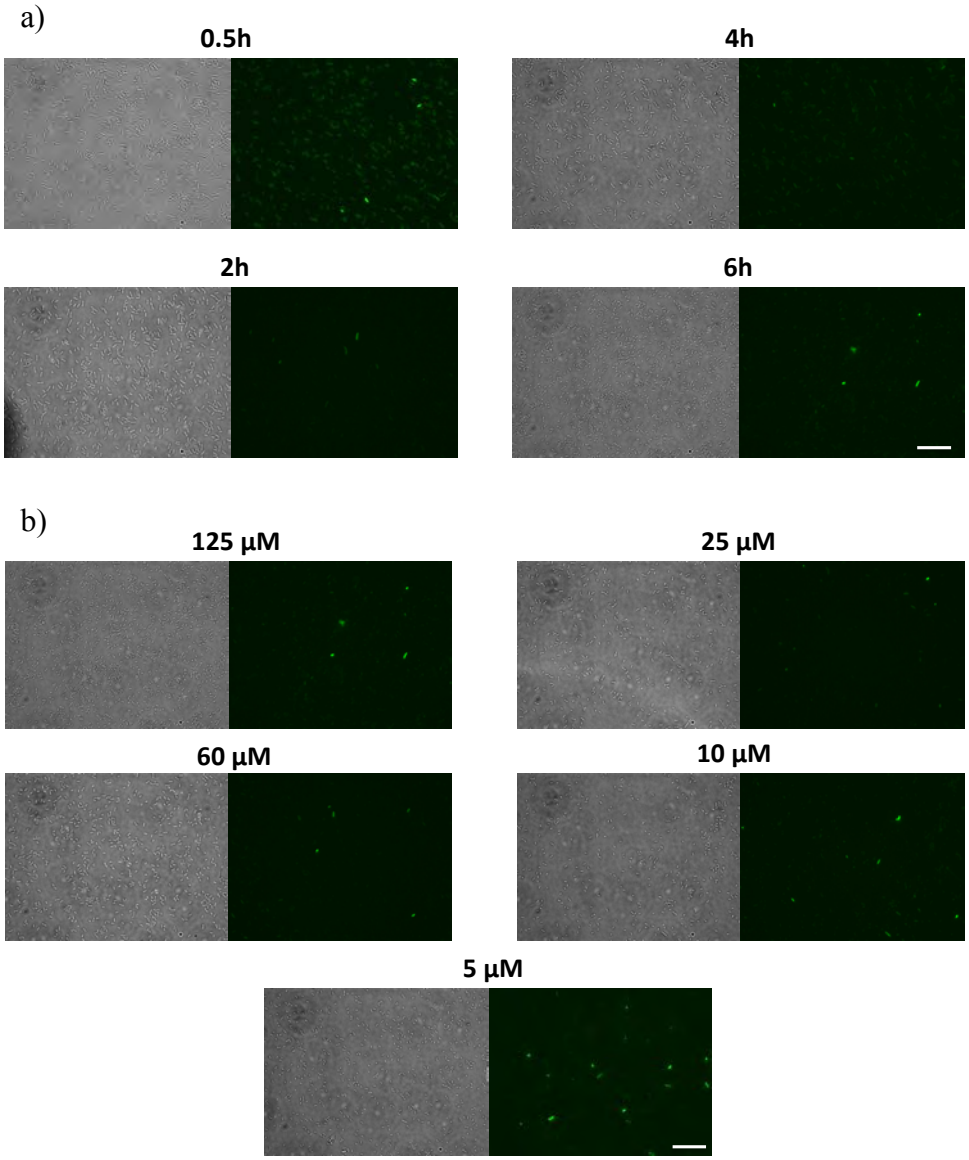

Figure 3-26. *P. aeruginosa* labeling with D-AB3 and Scz-FITC. (a) Time course of D-AB3 incubation (125 µM) at 0.5, 2, 4 and 6 hours followed by Scz-FITC incubation for 30 min. (b) D-AB3 concentration profile of labeling at 6 hours incubation (scale bar, 10 µm).

The preferential labeling of *E. coli* by D-AB3 was further validated by a co-culture experiment, for which the D-AB3 treated *E. coli* and *S. aureus* cells were mixed and then labeled with Scz-FITC (**Figure 3-27**). Microscopy of the co-culture demonstrates the selective labeling of *E. coli*, which displays strong fluorescence while *S. aureus* cells appear dimly fluorescent. This more efficient incorporation of D-AB3 into *E. coli* was further validated by flow cytometry analysis, which displays a mean cell fluorescence intensity ~10X greater than *S. aureus* and *K. pneumoniae* (**Figure 3-22c**).

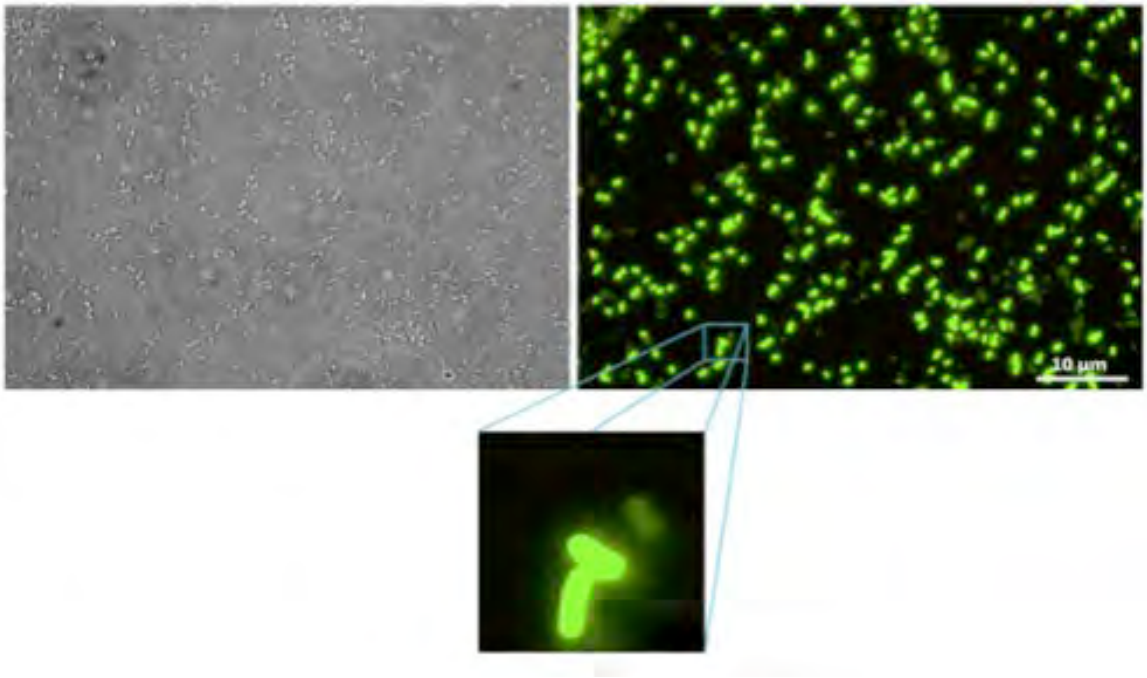

Figure 3-27. Fluorescence microscopy image of an *E. coli* and *S. aureus* co-culture showing preferential staining of *E. coli* by D-AB3.

Treating the bacterial cells with L-AB3 through the same protocol yielded minimal fluorescence staining regardless of the strain of bacteria used (**Figure 3-28**), indicating that D-AB3 can be incorporated into the PG whereas L-AB3 cannot be accepted by the transpeptidases responsible for PG remodeling as expected.[15] Confocal

microscopy images also confirmed the cellular envelope localization of fluorescence (**Figure 3-29**). Given the high specificity of Scz-FITC for D-AB3, the fluorescence of the labeled cells should directly reflect the amount of D-AB3 incorporated into peptidoglycan. Quantitative analysis of D-AB3 uptake by *E. coli* was carried out by plotting the cell mean fluorescence against D-AB3 concentration, which displays a saturating profile, as expected for an enzyme catalyzed reaction (**Figure 3-30**). Fitting the data according to a Michaelis-Menten mechanism yields a K_M value of 23 μM. This K_M value is about an order of magnitude lower than that of a D-Lysine derivative used for *S. aureus* labeling, suggesting that D-AB3 uptake by *E. coli* is highly efficient. Alternatively, the concentration profile of D-AB3 for *S. aureus* staining data displays a linear relationship (**Figure 3-31**), suggesting the K_M value is well above the highest concentration tested (125 μM). While a precise K_M value cannot be obtained for *S. aureus*, the slope of the linear fit should be roughly proportional to the catalytic efficiency of the relevant enzyme (V_{max}/K_M). Comparison of the catalytic efficiencies shows that D-AB3 is more efficiently incorporated into *E. coli* by 26 folds.

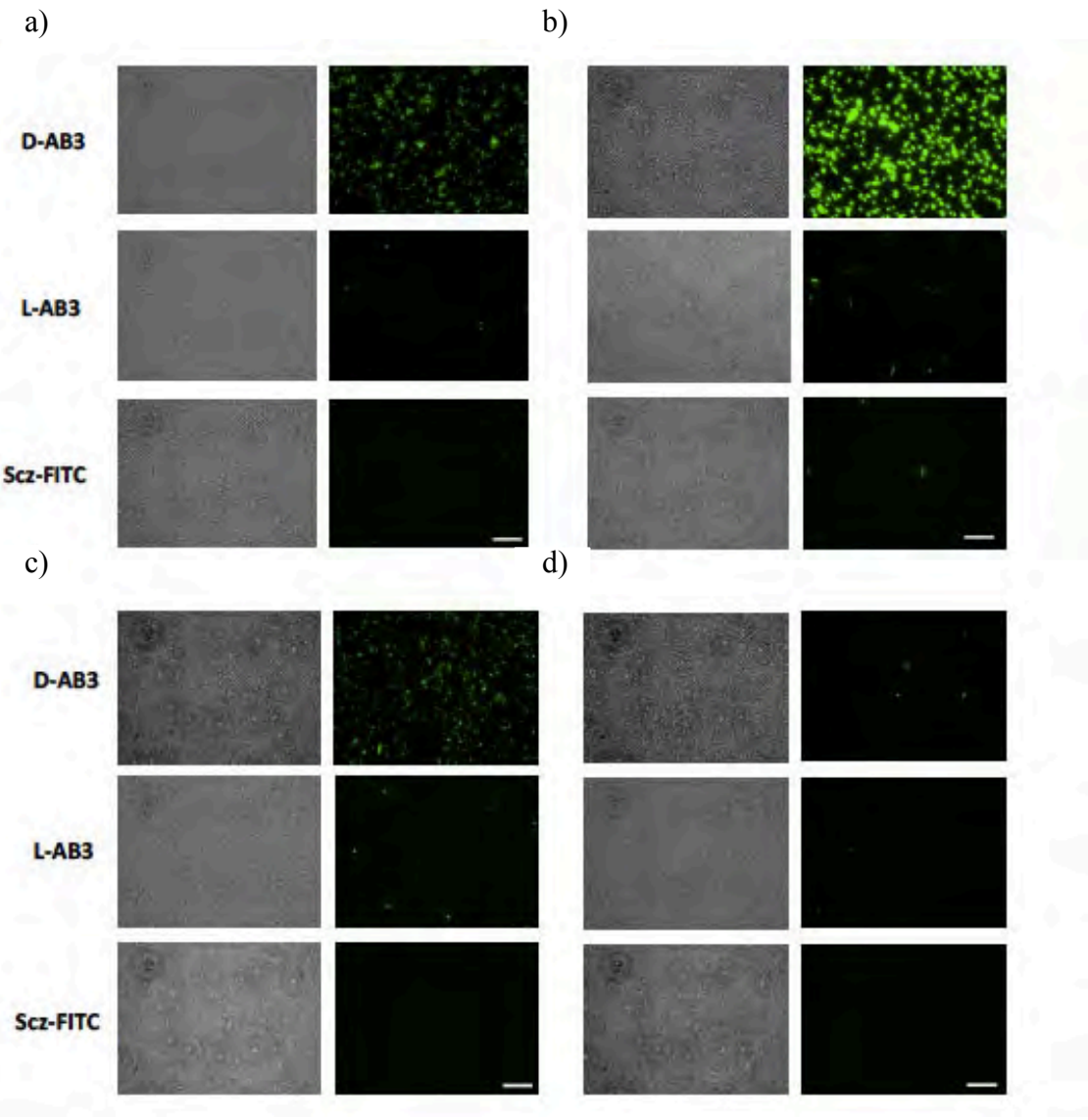

Figure 3-28. Comparison of D-AB3, L-AB3 and no treatment (Scz-FITC) in bacterial cell staining. (a) *S. aureus*, (b) *E. coli*, (c) *K. pneumoniae* and (d) *P. aeruginosa* were all incubated with 125 μM D-AB3, L-AB3 or neither for 6 hours, followed by 30 minutes of 50 μM Scz-FITC (scale bar, 10 μm).

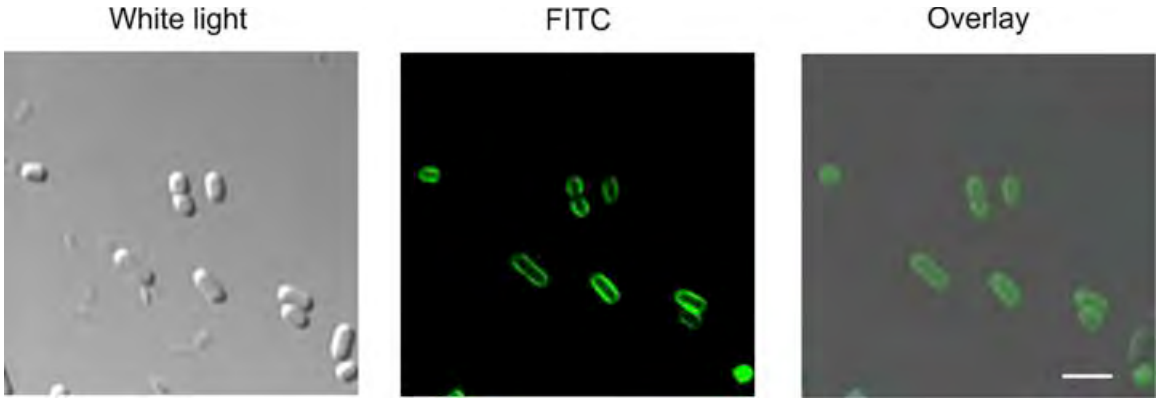

Figure 3-29. D-AB3-Scz-FITC labels the bacterial membrane. Confocal microscope images of *E. coli* display the specific bacterial cell envelope location of fluorescence (scale bar, 2.5 μm).

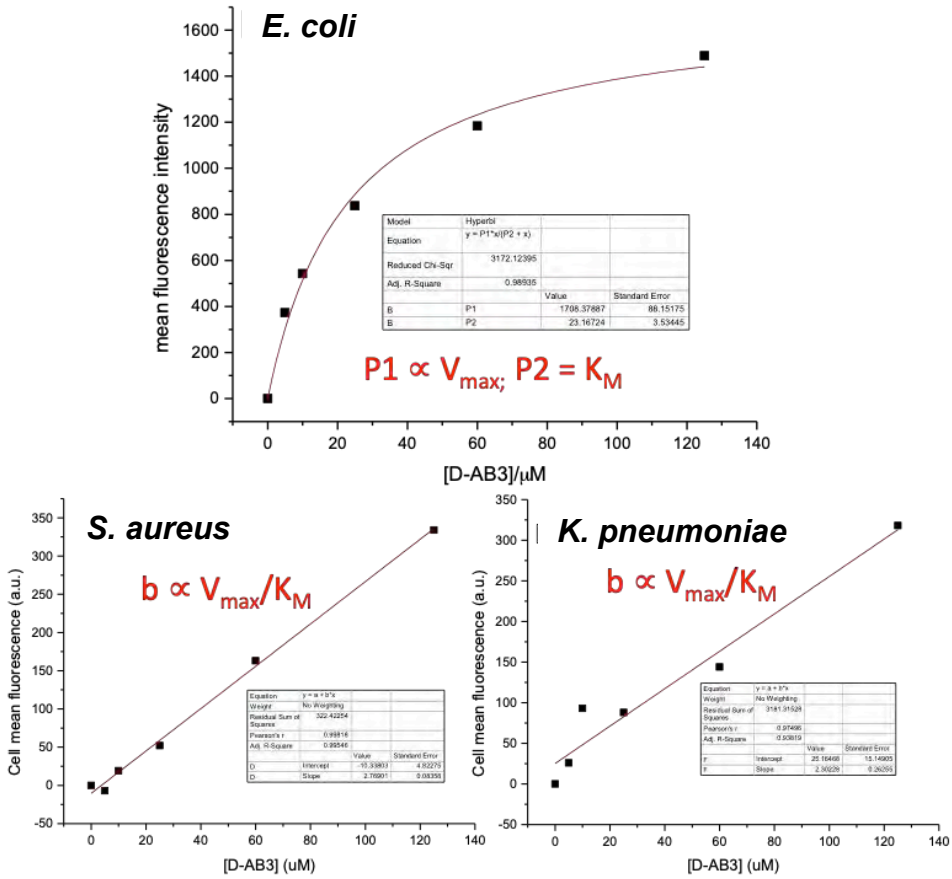

Figure 3-30. Concentration profiles of D-AB3 incorporation into *E. coli* (top) *S. aureus* (bottom left) and *K. pneumoniae* (bottom right). The flow cytometry data were fit to a hyperbolic curve for *E. coli* and a linear fit for *S. aureus* and *K. pneumoniae* according to Michaelis-Menten kinetics.

The preferential incorporation of D-AB3 into *E. coli* is interesting given the documented favorability of Gram-positive bacteria incorporation over Gram-negative bacteria incorporation of many published amino acids, likely due to outer membrane impermeability.[16,20,21] To confirm this phenomenon, we synthesized a previously reported amino acid, D-Lys-FITC, which showed 50x better staining of *S. aureus* in comparison to *E. coli* (**Figure 3-31**).[21]

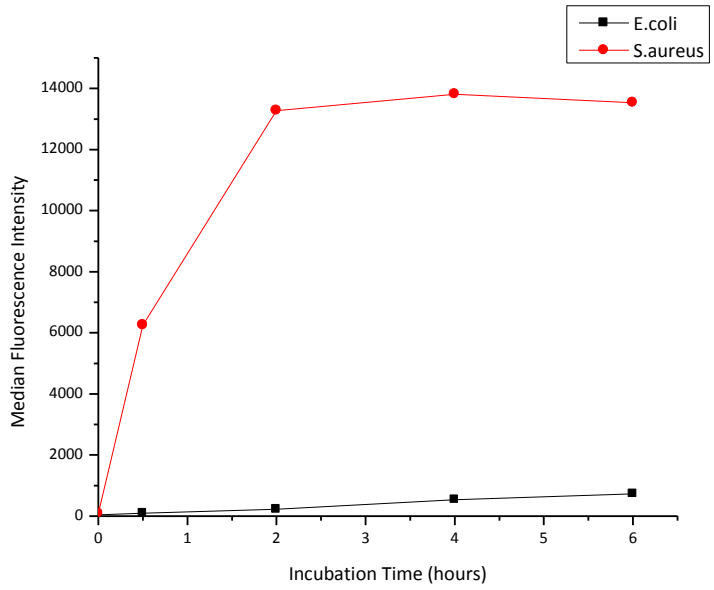

Figure 3-31. Flow cytometry analysis of *S. aureus* and *E. coli* stained with D-Lys-FITC (125 µM) reveals that D-Lys-FITC stains *S. aureus* much greater than it does *E. coli.*

Overall, the D-AB3 conjugation chemistry enables facile labeling of *E. coli* cell walls in complex biological settings via diazaborine formation with semicarbazide. While D-AB3 does not exhibit complete selectivity for *E. coli* detection, the clear saturation of incorporation is in stark contrast to that of *S. aureus* and *K. pneumoniae*, which exhibit no saturation at any concentration tested.

3.4 Turn-On Fluorescent APBA Diazaborine Formation Facilitates "No Wash" Labeling of Bacterial Pathogens

Towards our goal of achieving bioorthogonal, no wash labeling of biomolceules, we expanded the diazaborine chemistry with turn-on fluorescent APBA-presenting molecules that become fluorescent upon conjugation to semicarbazide.

3.4.1 Synthesis of APBA Coumarin Analogues

To create fluorogenic, diazaborine-forming probes, we synthesized several coumarin derivatives (AB21-24) that present either a 2-APBA motif, or one of its structural analogues at the C3 position (**Scheme 3-1**). While AB21 and AB22 are expected to conjugate with semicarbazide to form diazaborines, AB23 and AB24 are designed to serve as negative controls. The coumarin core structure has been widely used in the design of fluorescent molecules as its fluorescence can be easily tuned with electron donating and withdrawing groups.[38–41]

Scheme 3-1. Structures of the coumarin derivatives AB21, AB22, AB23 and AB24

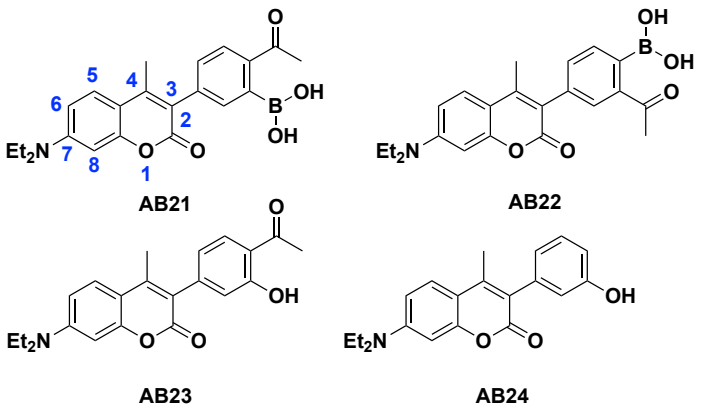

We first characterized the absorption and fluorescence properties of the coumarin analogues (**Figure 3-32**). All four coumarin derivatives display similar absorption profiles, with absorption maxima around 395 nm; the fluorescence properties, however,

dramatically differ. While AB24 exhibits strong fluorescence, AB21 and AB22 give minimal fluorescence, whereas AB23 displays slightly higher fluorescence than AB21/22. The varying fluorescence intensities correlate well with the electron withdrawing capabilities of the C3 substituents: the 2-APBA motif of AB21 and AB22 is the most electron deficient, and the phenol substituent of AB24 is the most electron rich.

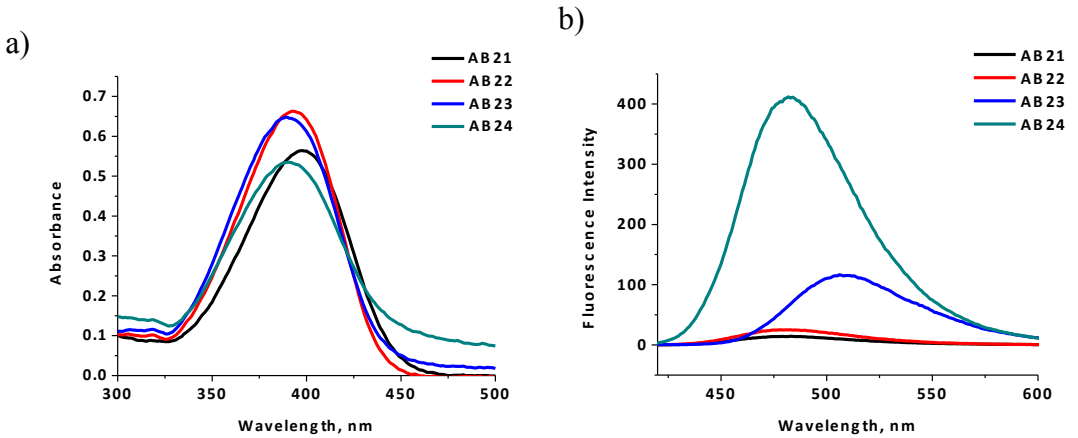

Figure 3-32. Absorption and fluorescence properties of the coumarin analogues. (a) Coumarin derivatives exhibit similar absorption properties (50 μM, 1 cm cuvette, PBS buffer pH 7.4). (b) Fluorescence emission of the coumarin derivatives show quenched fluorescence of AB21/22 (10 μM, PBS buffer pH 7.4, λ_{ex}=392 nm (AB22/24), 397 nm (AB21) and 402 nm (AB23).

3.4.2 Analysis of Diazaborine Formation of APBA Courmarin Analogues

The quenching effect of 2-APBA suggests that AB21 and AB22 are capable of exhibiting turn-on fluorescence upon conjugation, such as diazaborine formation with semicarbazide. To test this hypothesis, the APBA coumarin analogs were first examined for their ability to conjugate with semicarbazide. As shown by LC-MS, AB21 or AB22 (200 μM) mixed with semicarbazide (200 μM) for 30 minutes yielded quantitative conversion to the corresponding diazaborine (**Figure 3-33a**). Additionally, the conjugation of AB21/22 to semicarbazide is minimally inhibited in the presence of 20%

blood serum (**Figure 3-34**). To assess the possible turn-on fluorogenic property of AB21/22, the conjugation products were diluted to 10 μM for fluorescence measurement (**Figure 3-33b**). Both coumarin derivatives displayed significant fluorescence increase; while semicarbazide conjugation to AB21 elicited a 5-fold increase in fluorescence emission, AB22 gave a 7-fold enhancement. Comparatively, AB23 and AB24 showed no change in fluorescence emission when mixed with semicarbazide, which is consistent with their inability to react with semicarbazide (**Figure 3-35**).

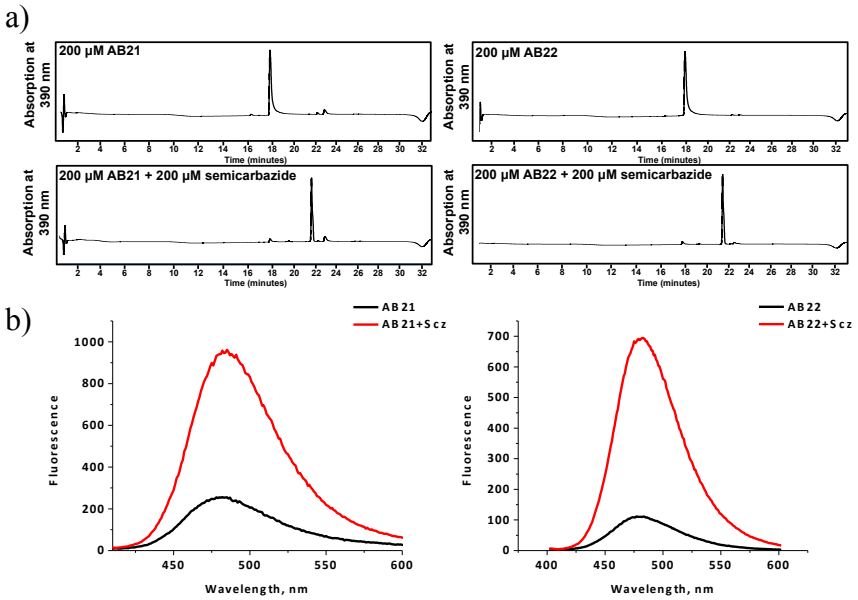

Figure 3-33. Diazaborine formation of AB21/22 with semicarbazide induces an increase in fluorescence. (a) LC traces showing clean and complete conjugation of AB21/22 (200 μM) to semicarbazide (200 μM) in 30 minutes. The identities of the peaks were confirmed with MS data. (b) Conjugation to semicarbazide leading to much enhanced fluorescence of AB21 and AB22 (10 μM, 1x PBS Buffer, pH 7.4, λ_{ex}= 392 nm (AB22) and 397 nm (AB21)).

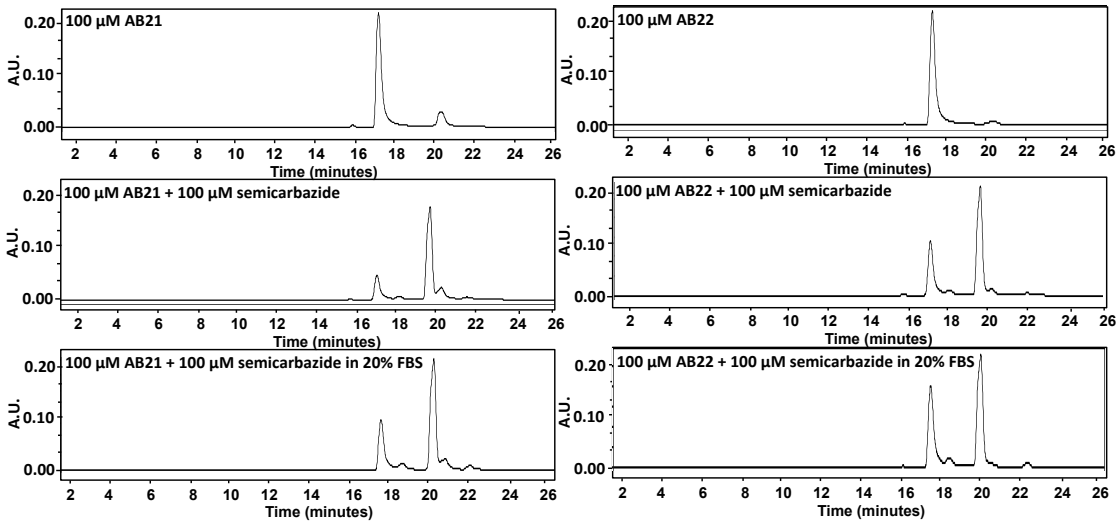

Figure 3-34. Analytical HPLC analysis of AB21 and AB22 conjugation to semicarbazide in the presence of 20% fetal bovine serum.

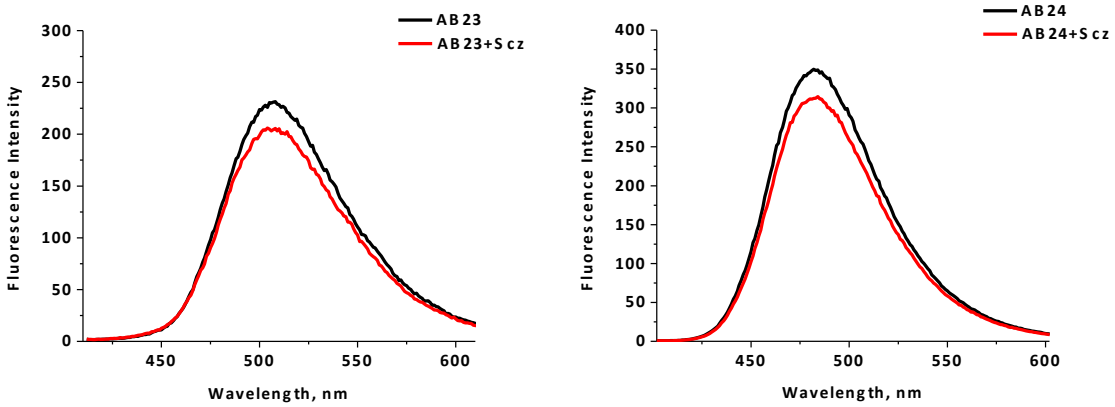

Figure 3-35. Addition of semicarbazide to AB23 and 24 generates no increase in fluorescence due to lack of conjugation (Voltage = 800 (AB21), 700 (AB22/23), 600 (AB24/25)).

The fluorogenic properties of AB21 and AB22 enabled facile quantification of the conjugation kinetics, yielding rate constants of 144 $M^{-1}s^{-1}$ and 177 $M^{-1}s^{-1}$ for AB21 and AB22, respectively (**Figure 3-36**). Although the kinetics of AB21/22 are slower than that of simple 2-APBA, the diazaborine formation of AB21/22 is still remarkably fast, with the reaction reaching completion in just a few minutes with low micromolar concentrations of reactants.

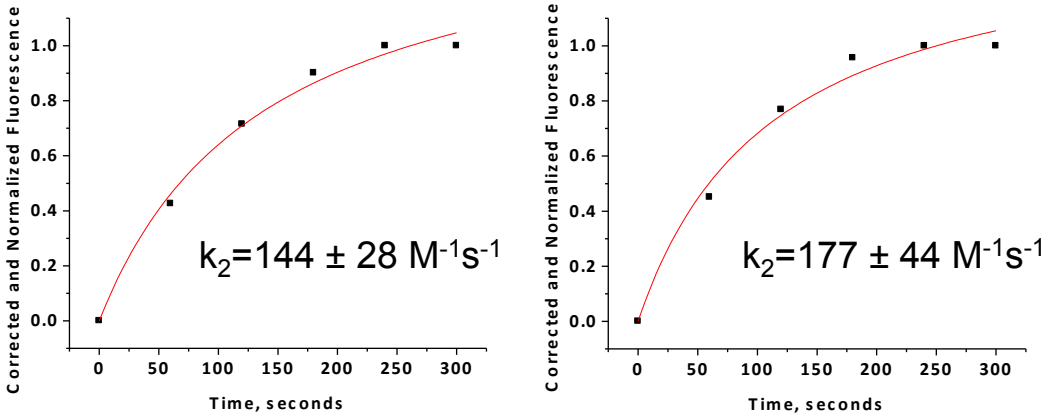

Figure 3-36. Kinetics of AB21 (left) and AB22 (right) conjugation to semicarbazide as determined by fluorescence titration.

We also obtained quantum yield data for the coumarin analogues themselves, as well as when conjugated to semicarbazide (**Table 3-2**).[42] From this data, we observed a dramatic increase in quantum yield of AB21/22 upon semicarbazide conjugation, whereas the control compounds (AB23/24) displayed no such increase, as expected, due to lack of conjugation.

Table 3-2. Summary of AB21-24 quantum yield data obtained from comparison to the quantum yield of the standard, fluorescein.[1]

	Voltage	Integrated Area	Absorbance	Quantum Yield
AB21	700 V	4,032	0.066	0.014
AB21+Scz	700 V	16,862	0.066	0.060
AB22	700 V	8,311	0.096	0.020
AB22+Scz	700 V	41,877	0.096	0.102
AB23	700 V	20,518	0.033	0.145
AB23+Scz	700 V	14,524	0.033	0.103
AB24	600 V	28,737	0.063	0.455
AB24+Scz	600 V	19,932	0.063	0.315
Fluorescein	600 V	6,768	0.071	0.950
Fluorescein	700 V	28,905	0.071	0.950

3.4.3 No Wash Labeling of Bacterial Pathogens via D-Dap-Scz Peptidoglycan Incorporation

The fast and fluorogenic conjugation of AB21/22 with semicarbazide makes these molecules appealing for biological applications. With our interest in developing novel solutions to the antibiotic crisis and our success in PG remodeling incorporation of unnatural amino acids, we envisioned that fluorogenic diazaborine formation of AB21/AB22 could be implemented for bacterial cell labeling via a semicarbazide-presenting D-amino acid (**Figure 3-37**). Towards this end, we synthesized the unnatural amino acid D-Dap-Scz, which was obtained by conjugating a semicarbazide derivative to Boc-D-Dap-OH through amide bond formation (**Figure 3-38**). With the amino acid in hand, we tested the conjugation of D-Dap-Scz to AB21 and AB22, as well as the fluorescence upon conjugation, both of which agreed with the results obtained for simple semicarbazide (**Figure 3-39**).

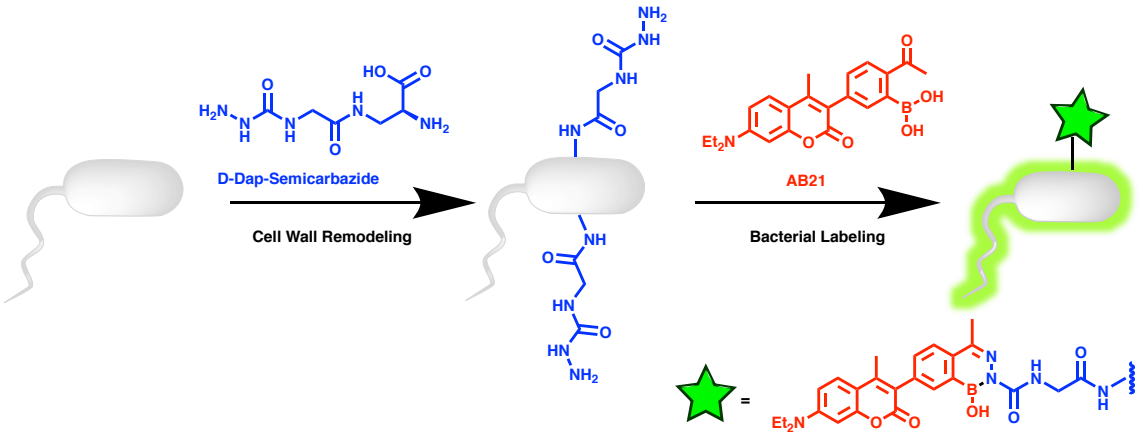

Figure 3-37. Schematic two-step labeling process involving D-Dap-Scz incorporation into peptidoglycan followed by APBA coumarin conjugation to form a stable diazaborine.

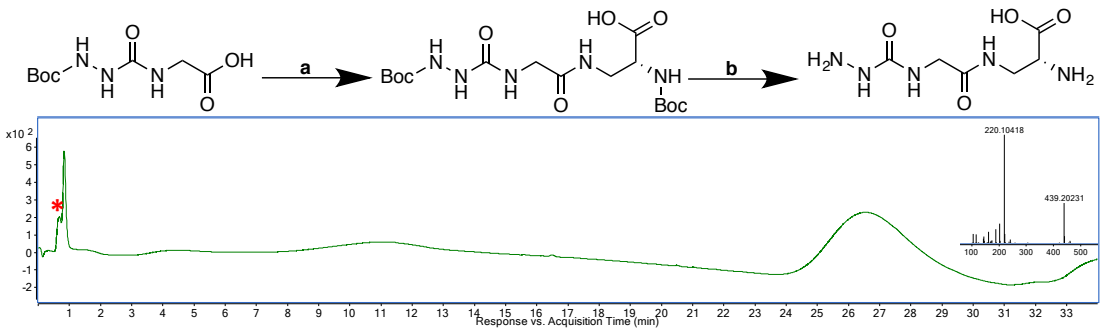

Figure 3-38. Synthetic scheme and LC-MS characterization of D-Dap-Scz (* indicates injection peak).

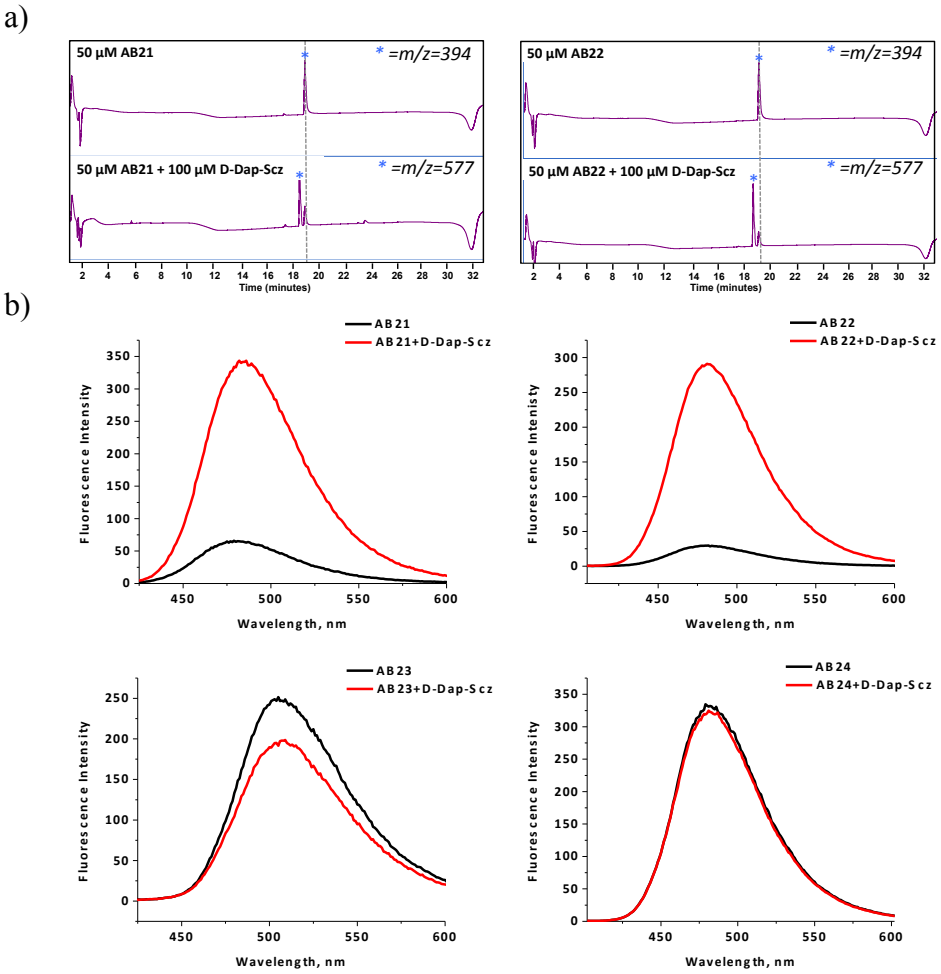

Figure 3-39. Conjugation of D-Dap-Scz to AB21 and AB22. (a) LC-MS analysis of the conjugation of AB21 and AB22 (indicated by gray dashed lines) to D-Dap-Scz. (b) Fluorescence change of AB21-24 when conjugated to D-Dap-Scz (Voltage= 700 (AB21/22), 600 (AB22/24)).

We then examined the ability of D-Dap-Scz to incorporate into the cell wall of *S. aureus*, which is a prevalent bacterial pathogen. Specifically, we incubated the bacteria with various concentrations of D-Dap-Scz (5-500 μM) for various times (0.5-4 hours). The amount of D-Dap-Scz incorporated into peptidoglycan was assessed via a fluorophore-labeled 2-formylphenylboronic acid (FPBA-FITC, **Figure 3-40**), which is expected to give quantitative diazaborine yield. The FPBA-FITC treated cells were then analyzed by flow cytometry, which showed that the extent of bacterial incorporation of D-Dap-Scz depends on both the concentration and incubation time. Efficient D-Dap-Scz incorporation was observed after 4 hours of incubation with D-Dap-Scz at 100 μM concentration or higher (**Figure 3-41**). Specifically, with 4 hours of incubation, FPBA-FITC afforded proportionally strong fluorescence staining of the cells treated with D-Dap-Scz at 100 and 500 μM, respectively.

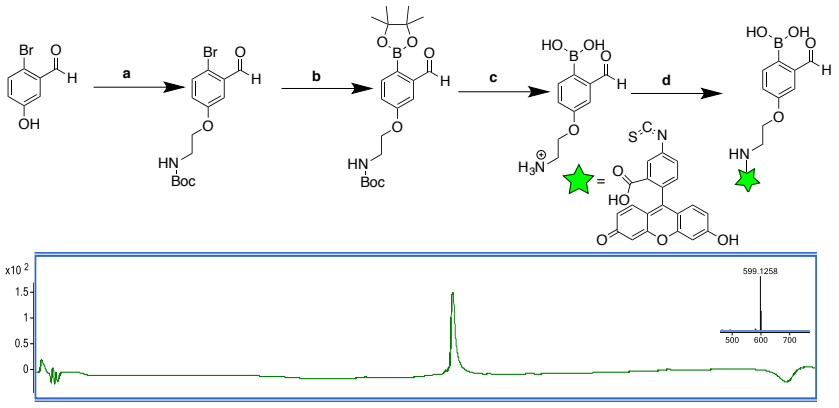

Figure 3-40. Synthetic scheme and LC-MS analysis of the conjugation of FPBA-FITC to D-Dap-Scz.

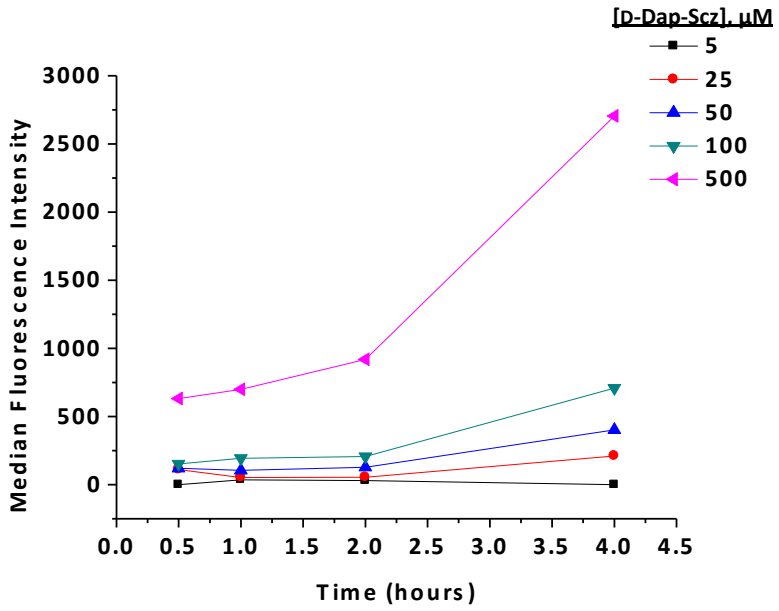

Figure 3-41. Flow cytometry of *S. aureus* metabolically labeled with D-Dap-Scz and stained with FPBA-FITC to determine the optimal concentration and incubation times for D-Dap-Scz incorporation.

These conditions were then adopted to examine the fluorogenic conjugation of the coumarin derivatives on live bacterial cell surfaces. Towards this end, *S. aureus* cells were treated with 0, 100 and 500 μM of D-Dap-Scz in LB media for 4 hours, then the cells were washed to eliminate any excess D-Dap-Scz, and finally directly stained with AB21 and AB22. FPBA-FITC and AB24 were examined in parallel as non-fluorogenic controls (**Figure 3-42**). While washing after FPBA-FITC enabled facile visualization of D-Dap-Scz treated cells (**Figure 3-41**), strong background fluorescence was observed without the washing step. Importantly, FPBA-FITC afforded significant straining of the cells without D-Dap-Scz treatment. Similarly, background fluorescence and non-specific cell staining was observed for AB24 under no-wash conditions, although AB24 is not as bright as FPBA-FITC. In sharp contrast, little background fluorescence was observed with the AB21/22 stained cells under the same settings. Comparing *S. aureus* incubated

with no D-Dap-Scz (0 μM) versus 100 μM and 500 μM D-Dap-Scz, it is apparent that AB21 and AB22 elicited bright fluorescence staining only in the presence of D-Dap-Scz. The D-Dap-Scz-dependent bacterial staining by AB21 and AB22 is presumably due to their fluorogenic conjugation with D-Dap-Scz to form diazaborines. Although it is difficult to determine whether AB21 and AB22 afford non-specific bacterial binding, their quenched fluorescence allows them to only fluorescently reveal bacterial cells that incorporate semicarbazide functionalities.

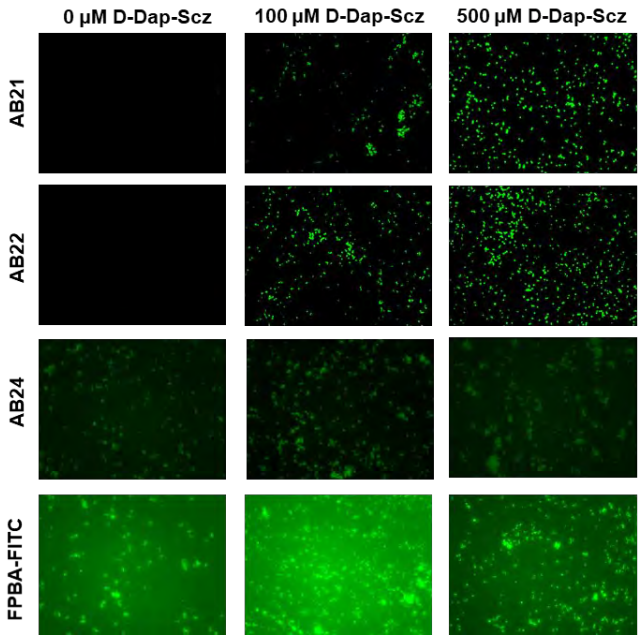

Figure 3-42. No wash *S. aureus* cell labeling by AB21/AB22 conjugation to PG-incorporated D-Dap-Scz. *S. aureus* was incubated with 0 μM, 100 μM or 500 μM D-Dap-Scz for four hours followed by 100 μM AB21, AB22, AB24 or FPBA-FITC incubation for 2 hours.

3.4.4 Development of D-Phe-Scz for E. coli Incorporation

After examining the application of D-Dap-Scz in *S. aureus* labeling experiments, we were interested in developing an unnatural amino acid with an aromatic structure (D-Phe-Scz), which, based on our results with D-AB3, we hypothesized would experience facile incorporation into *E. coli*. After synthesizing D-Phe-Scz, we applied it for bacterial labeling by incubating *S. aureus* and *E. coli* with D-Phe-Scz at 5-500 μM for 0.5-4 hours, washing the bacteria, then incubating with 50 μM FPBA-FITC for 30 minutes, again washing the bacteria, and subjecting to both fluorescence imaging and flow cytometry. These experiments were conducted alongside D-Dap-Scz for comparison, and showed that while D-Dap-Scz more efficiently incorporated into the *S. aureus* cell walls, D-Phe-Scz did not incorporate more efficiently into the *E. coli* cell wall as we had anticipated (**Figure 3-43**). While the origin of this difference in the anticipated and observed results is not certain, it is possible that the semicarbazide moiety has some effect on either incorporation efficiency or remodeling that my render its retention in the cell wall to be minimized.

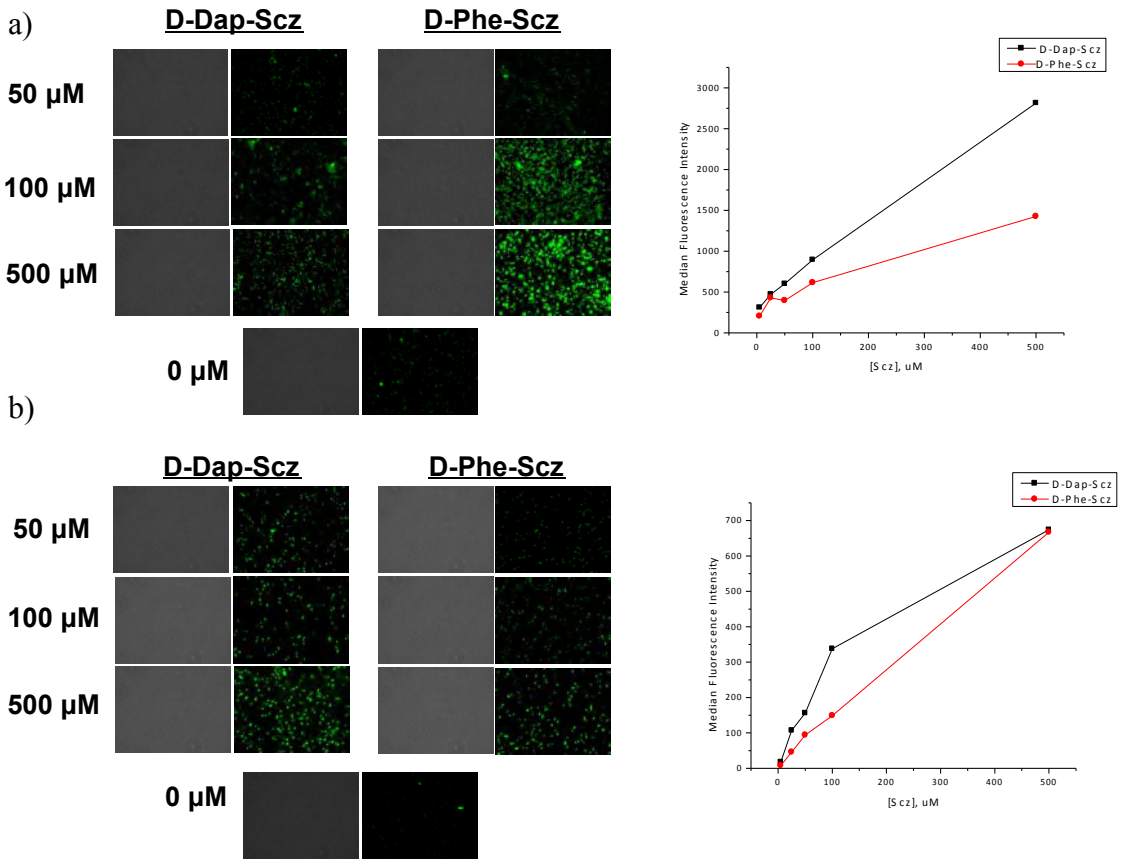

Figure 3-43. Analysis of D-Phe-Scz peptidoglycan incorporation into bacterial cell walls. (a) *S. aureus* and (b) *E. coli* were analyzed for D-Phe-Scz incorporation via FPBA-FITC conjugation by microscopy and flow cytometry analysis.

3.5 Conclusions

Through these efforts we have discovered that semicarbazide conjugation to boronic acid substituted aryl ketones and aldehydes enables stable diazaborine formation in a bioorthogonal manner. These conjugation reactions proceed with rate constants over 10^3 $M^{-1}s^{-1}$ in aqueous physiologic buffer, with no need for catalysts. Notably, the reaction rate of diazaborine formation is 2-3 orders of magnitude greater than the widely used azide-alkyne chemistry.[43] Given the degradation and toxicity observed with phenylhydrazine, as well as the lack of stability of conjugates for acethydrazide,

semicarbazide appears to reside in the "sweet spot" of reactivity, being high enough to afford diazaborines and low enough to avoid degradation. Other than the cysteine adduct formation with 2-FPBA, this diazaborine forming chemistry exhibited little interference from biological media with blood serum and cell lysates, thus indicating the high level of biocompatibility afforded by diazarborine chemistry.

To demonstrate the utility of the conjugation chemistry, we have explored the facile labeling of bacterial pathogens by diazaborine formation of semicarbazide. A synthetic amino acid, D-AB3, which displays a 2-APBA moiety, was shown to be taken up by bacterial cells through metabolic peptidoglycan remodeling. The cells with D-AB3 incorporated were visualized though conjugation with a fluorophore labeled semicarbazide. While a number of synthetic D-amino acids have been shown to covalently modify bacterial peptidoglycans with a variety of bioorthogonal reactive partners (eg. azide-alkyne click chemistry, tetrazine ligation, alkyne-nitrone cycloaddition motifs), the diazaborine formation chemistry is much faster than most of these alternative chemistries.

We observed that D-AB3 preferentially labeled *E. coli* over several other bacterial species including *S. aureus*, a Gram-positive bacterium. This is interesting given that several amino acids, including D-Lys-FITC, have been shown to preferentially label Gram-positive bacteria over Gram-negative strains, likely due to the outer membrane of Gram-negative bacteria acting as a barrier. Since D-AB3 incorporates into the *E. coli* peptidoglycan with high efficiency, it must also display high penetration of the cell wall. Work from the Kahne and Walker labs shows that the *E. coli* transpeptidase preferentially incorporates aromatic amino acids over aliphatic ones.[44] Given that nearly all synthetic

amino acids known to modify peptidoglycans are aliphatic, the aromatic structure of D-AB3 might be the underlying reason for its efficient uptake. Conversely, D-Phe-Scz was shown to give similar incorporation into *E. coli* in comparison to a similar aliphatic amino acid. Thus, there may be some caveats underlying this hypothesis.

In addition to D-AB3 incorporation, we also explored the incorporation of a semicarbazide presenting unnatural amino acid, D-Dap-Scz, to use for turn-on fluorescent detection of bacterial pathogens via diazaborine formation with the APBA coumarin analogues AB21/22. Specifically, the D-Dap-Scz amino acid was incorporated into *S. aureus* peptidoglycan, and subsequently detected with the turn-on fluorescence elicited by diazaborine formation of AB21/22 with minimal background fluorescence. Altogether, these bioorthogonal probes enable efficient bacterial pathogen detection to further our efforts towards developing solutions to the antibiotic resistance crisis.

3.6 Experimental Procedures

3.6.1 General Methods

Triflic anhydride, tert-Butyl 2,2,2-trichloroacetimidate, 1,1′-Bis(diphenylphosphino)ferrocene (dppf), sodium chloride (NaCl), tyrosine, fluorescein isothiocyanate isomer I (FITC), N-Boc-Bromoethylamine, potassium carbonate, 2-bromo hydroxybenzaldehyde, potassium acetate and triethylamine were purchased from Sigma Aldrich Trifluoroacetic acid, dry DCM, dry dioxane, DMF, tetrahydrofuran, N-hydroxysuccinimide, ethyl isocyanoacetate, tert-butyl carbazate, N-boc-ethylenediamine, 2-acetylphenyl boronic acid, 2-formylphenyl boronic acid, 4-chloro 7-nitrobenzofurazan (NBD-Cl), semicarbazide, fetal bovine serum (FBS) and B-per were purchased from Fischer Scientific. $Pd(dppf)Cl_2$ was purchased from Strem Chemicals. B_2pin_2 was

purchased from Frontier Scientific. Boc-D-Dap-OH and dicyclohexylcarboiimide were purchased from Chem Impex International. Diethanolamine was purchased from Alfa Aesar. D-AB3 was synthesized according to a published procedure.[45] *Klebsiella pneumoniae* (ATCC 4352), *Pseudomonas aeruginosa* (ATCC 27853), and *Staphylococcus aureus* (ATCC 6538) were purchased from ATCC as a lyophilized cell pellet. *Escherichia coli* (BL 21) was a gift from the lab of Professor Mary F. Roberts at Boston College. HEK293T cells were a gift from the lab of Professor Eranthie Weerapana at Boston College. All the ligation experiments were performed in PBS (1X, 7.4) buffer unless noted otherwise.

UV-vis spectra were collected on a Nanodrop UV-Vis spectrometer (Thermo Scientific, Waltham, MA, USA). NMR data were collected on a Varian 600 MHz NMR spectrometer. LC-MS data were generated using an Agilent 6230 LC-TOF mass spectrometer with an Agilent Extend C18 column with acetonitrile/water (0.1% formic acid) eluent. HPLC purification and analysis was performed using a Waters Alliance 2695 system with a Jupiter C18 column (Phenomenex) with acetonitrile/water (0.1% TFA) eluent. Analytical HPLC data was obtained on a Waters Alliance 2695 HPLC with a Phenomenex C18 column with acetonitrile/water (0.1% TFA) eluent. Fluorescence images were taken on a Zeiss Axio Observer A1 inverted microscope. Confocal images were taken on the Leixa SP5 confocal fluorescence microscope housed in the Biology Department at Boston College. Flow cytometry analyses were carried out on a BD FACSAria cell sorter also housed in the Biology Department of Boston College. NMR spectra were recorded in the presence of 10% D_2O using the water suppression PRESAT parameter, 160 scans, and a line broadening value of 0.5 on a Varian 600 MHz NMR

spectrometer. All NMR data processing was performed in MestReNova 10. Fluorescence data were collected on a Cary Eclipse fluorescence spectrophotometer with slit width set to 5 nm. Voltages varied, as noted in the designated fluorescence sections. 96 well plate absorbances were obtained with a SpectraMax M5 plate reader (Molecular Devices). The concentration of all fluorescently labeled samples was determined by measuring their absorbance at 495 nm (ε=72,000 $M^{-1}cm^{-1}$) for FITC or 493 nm (ε=24,000 $M^{-1}cm^{-1}$) for NBD with a Nanodrop 2000c UV-Vis spectrometer.

3.6.2 Synthesis of Semicarbazide-FITC, Semicarbazide-NBD, and Phenylhydrazine-FITC

Synthesis of Semicarbazide-FITC (3-I-f)

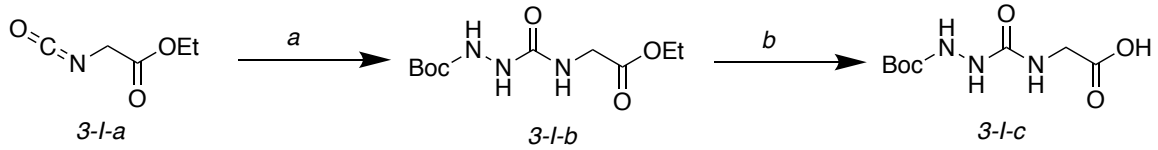

(a) Synthesis of **3-I-b**: **3-I-b** was synthesized following a previously reported protocol.[46] Ethyl isocyanatoacetate (0.56 mL, 5 mmol) was dissolved in dry dichloromethane (5 mL) by stirring. Tert-butyl carbazate (650 mg, 5 mmol) was dissolved in dichloromethane (5 mL) and added into the stirring mixture, followed by the addition of N-Methylmorpholine (800 µL, 5.5 mmol). The reaction mixture was then refluxed at 50 ^{o}C for 2 hours. Upon completion, the reaction mixture was cooled to room temperature and diluted into 250 mL ethyl acetate. The resulting solution was then washed with sodium carbonate (1x150 mL), 1N HCl (1x150 mL), and brine (1x150 mL). The organic layer was then dried over sodium sulfate and evaporated to yield a thick solid (1.3g ,73%). The compound identity was confirmed by ^{1}H-NMR, which agrees with the earlier reported spectrum.

Compound **3-I-b** was directly used for the next step without purification.

(b) Synthesis of **3-I-c**: **3-I-b** (500 mg, 1.92 mmol) was dissolved in 5 mL methanol and the solution was treated with 2.5 mL of 2N NaOH with stirring condition for 0.5 hours. The solvent was then evaporated and the resulting residue was acidified with 1N HCl (~5 mL) and subsequently extracted with ethyl acetate (3x25 mL). The combined organic layer was dried over sodium sulfate and concentrated to afford a white solid pure product (323 mg, 72%).

^{1}H NMR (MeOH d_4) δ: 3.88 (s, 2H), 1.47 (s, 9H).

^{13}C NMR (MeOH d_4) δ: 172.29, 159.88, 156.84, 80.41, 40.85, 27.20.

MS-ESI^{+} (m/z): Calculated for $C_8H_{15}N_3O_5$ $[M+H]^{+}$ 234.1090, observed 234.1084.

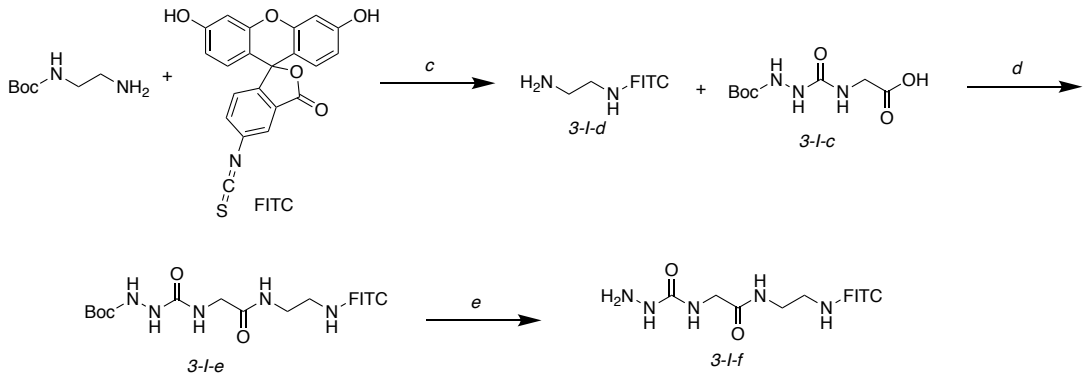

(c) Synthesis of **3-I-d**: N-Boc-ethylenediamine (6 mg, 0.0375 mmol) was stirred with fluorescein isothiocyanate (FITC) (15 mg, 0.0375 mmol) and triethylamine (10 μL, 0.0075 mmol) in DMF (1.5 mL). The reaction was allowed to proceed for 1 hour and the product formation was confirmed by LC-MS. The reaction mixture was then purified using reverse phase HPLC using semi-prep column to obtain the Boc protected intermediate as an orange powder after lyophilization. Further, the Boc protected intermediate (15 mg, 0.0309 mmol) was Boc-deprotected using 2:1

dichloromethane:trifluoroacetic Acid (DCM/TFA: 400 μL/ 200 μL) on ice for 0.5 hours. The solvent was then evaporated from the reaction mixture, and the product was purified via reverse phase HPLC using a semi-prep column to yield an orange powder after lyophilization. The product identity was confirmed by LC-MS and NMR, which agrees with the data previously reported.[47]

(d) Synthesis of **3-I-e**: **3-I-c** (6 mg, 0.024 mmol), **3-I-d** (11 mg, 0.024 mmol) and HBTU (9 mg, 0.024 mmol) were dissolved together in DMF (500 μL). Then, N-methylmorpholine (11 μL, 0.096 mmol) was added to the reaction mixture and stirred at room temperature for 3 hours. The reaction mixture was then acidified with 1N HCl (20 mL) and extracted with ethyl acetate (3 × 20 mL). The combined organic layers were dried over sodium sulfate and concentrated. Then, the crude product was purified via reverse phase HPLC to yield an orange powder after lyophilization. The identity and purity of FITC labeled Boc-semicarbazide (**3-I-e**) was confirmed by LC-MS analysis.

MS-ESI$^+$ (m/z): Calculated for $C_{31}H_{32}N_6O_9S$ $[M+H]^+$ 665.20, observed 665.2044.

(e) Synthesis of **3-I-f**: **3-I-e** (2 mg, 0.0030 mmol) was Boc-deprotected in 2:1 Dichloromethane:Trifluoroacetic acid (200 μL/100 μL) on ice for 0.5 hours. The resulting crude mixture was then purified via reverse phase HPLC to yield an orange powder after lyophilization. The product purity and identity was confirmed by LC-MS.

MS-ESI$^+$ (m/z): Calculated for $C_{26}H_{24}N_6O_7S$ $[M+H]^+$ 565.14, observed 565.1507.

Synthesis of Semicarbazide-NBD (3-II-c)

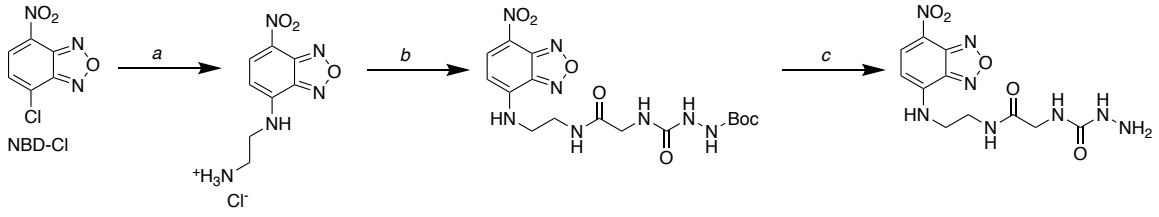

3-II-a *3-II-b* *3-II-c*

(a) Synthesis of **3-II-a**: Synthesis of **3-II-a** was carried out following the previously reported protocol by Palomo et al.[48] The method was slightly changed due to reagent availability and synthetic convenience. NBD-Cl (1 mmol, 200 mg) was dissolved in DCM (5 mL) and the solution was cooled in an ice bath under argon. Then, a solution of N-Boc ethylenediamine (1.1 mmol, 176 mg) and NMM (1.1 mmol, 0.2 mL) in DCM (2 mL) was added slowly using a syringe. The reaction mixture was stirred for 2 hours at room temperature. The reaction progress was monitored by TLC. DCM was evaporated from the reaction mixture after completion and the residue was dissolved in ethyl acetate (100 mL). The organic layer was washed with 0.1 N HCl (2 × 70 mL). The organic layer was then washed with brine and dried over Na_2SO_4. The organic layer was evaporated under vacuum and the product was purified through silica gel using hexane/EOAc as eluent to yield an orange solid product. The product formation was confirmed by LC-MS. The intermediate compound was then subjected for Boc-deprotection using 4N HCl in dioxane (2 mL) for 1 hour at room temperature. Dioxane was evaporated from the reaction mixture and the oily residue was dissolved in EtOAC (1 mL) and 9 mL ether was added into the solution to precipitate out the product **3-II-a** as a brown solid. The overall yield over two steps was 82%. NMR

and mass spectrum suggested that the product was pure enough to use for the next step.

^{1}H NMR (Acetone-d_6) δ 2.54 – 2.60 (quin, J = 6.2 Hz, 2H), 4.92 (b, 4H), 6.67–6.68 (d, J = 7.2 Hz, 1H), 8.54 – 8.56 (d, J = 8.4 Hz, 1H).

^{13}C NMR (DMSO-d_6) δ: 150.02, 143.83, 132.95, 130.95, 129.23, 66.78, 37.69.

MS-ESI$^+$ (m/z): Calculated for $C_8H_{10}N_5O_3$ $[M+H]^+$ 224.0784, observed 224.0786.

(b) Synthesis of **3-II-b**: **3-I-c** (0.02 mmol, 6.2 mg), **3-II-a** (0.021 mmol, 2.5 mg) and HBTU (0.02 mmol, 8 mg) were dissolved together in DMF (0.1 mL). NMM (0.1 mmol, 9 μL) was the added to the reaction mixture, which was stirred for 3 hours at room temperature. The reaction mixture was then diluted with 30 mL ethyl acetate and washed with 1N HCl (2x20 mL), followed by 10% sodium carbonate solution in water (1x20 mL). The organic layer was then washed with brine (20 mL) and dried over anhydrous Na_2SO_4. The organic layer was evaporated under reduced pressure to give a dark orange solid product, which was purified through silica gel using ethyl acetate/hexane to yield an orange solid product. The product identity was confirmed by LC-MS.

MS-ESI$^+$ (m/z): Calculated for $C_{16}H_{22}N_8O_7$ $[M+H]^+$ 461.15, observed 461.1491.

(c) Synthesis of **3-II-c**: **3-II-b** (5mg) was dissolved in 0.5 mL of DCM:trifluoroacetic acid (1:1) and stirred for 30 minutes. Finally, the mixture was evaporated under reduced pressure, dissolved in 1 mL deionized water, and the product was purified via reverse phase HPLC using acetonitrile/water (1% TFA) mixture as eluent to get an orange yellow powder after lyophilization. The compound identity and purity were confirmed by LC-MS.

MS-ESI$^+$ (m/z): Calculated for $C_{11}H_{14}N_8O_5$ $[M+H]^+$ 339.12, observed 339.1169.

Synthesis of Phenylhydrazine-FITC (3-III-b)

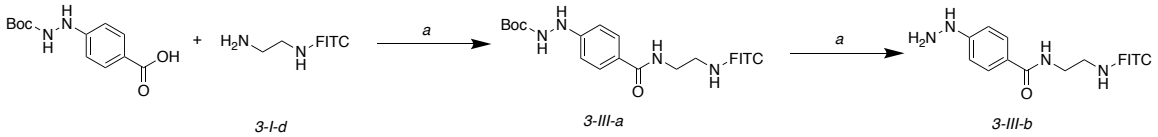

(a) Synthesis of **3-III-a**: 4-(2'-N-Boc-hydrazino)benzoic acid (6 mg, 0.024 mmol), **3-I-d** (11 mg, 0.024 mmol) and HBTU (9 mg, 0.024 mmol) were dissolved together in DMF (500 μL). Then, N-Methylmorpholine (11 μL, 0.096 mmol) was added to the reaction mixture and stirred at room temperature for 3 hours. The reaction mixture was then acidified with 1N HCl (20 mL) and extracted with ethyl acetate (3 × 20 mL). The combined organic layers were dried over sodium sulfate and concentrated. Then the crude product was purified via reverse phase HPLC to yield an orange powder after lyophilization. The identity and purity of FITC labeled Boc-phenylhydrazine (**3-III-a**) was confirmed by LC-MS analysis.

MS-ESI$^+$ (m/z): Calculated for $C_{35}H_{33}N_5O_8S$ $[M+H]^+$ 684.20, observed 684.2076.

(b) Synthesis of **3-III-b**: **3-III-a** (2 mg, 0.0030 mmol) was Boc-deprotected in 2:1 Dichloromethane:Trifluoroacetic Acid (200 μL/100 μL) on ice for 0.5 hours. The resulting crude mixture was then purified via reverse phase HPLC to yield an orange powder after lyohpilization. The product purity and identity was confirmed by LC-MS.

MS-ESI$^+$ (m/z): Calculated for $C_{30}H_{25}N_5O_6S$ $[M+H]^+$ 584.1604, observed 584.1606.

3.6.3 Stability of Phenylhydrazine and Semicarbazide in Neutral Buffer

100 μM solutions of the FITC derivatives of phenylhydrazine and semicarbazide were prepared in PBS (1X, pH 7.4). The stability of the reagents was monitored by analytical HPLC over time. Additionally, the stability of unlabeled phenylhydrazine and semicarbazide were examined via ^{1}H NMR. A 1 mM solution of each was prepared in PBS (1X, pH 7.4). Aliquots were taken at 0, 24, 48 and 240 hours, and conjugated to an equimolar concentration of 2-APBA for 10 minutes at room temperature. Then the NMR spectra were recorded in the presence of 10% D_2O

3.6.4 NMR and LC-MS Analysis of DAB1 and DAB2 Formation

NMR analysis of the conjugation reactions was performed in PBS buffer (1X, pH 7.4) in the presence of 10% D_2O. 300 μM of 2-FPBA or 2-APBA was mixed with 300 μM of semicarbazide and incubated at room temperature for 10 min. NMR analysis revealed complete conjugation with 2-FPBA and ~90% product formation with 2-APBA. The reaction mixtures were further analyzed with LC-MS, which confirmed clean conversion without any formation of side product.

3.6.5 Assessing the Hydrolytic Stability of DAB1 and DAB2

Semicarbazide (6 mg, 0.5 mmol) was dissolved in 1 mL PBS buffer (1X, pH 7.4) and then mixed with 2-FPBA (7.5 mg, 0.5 mmol) or 2-APBA (8.2 mg, 0.5 mmol) dissolved in 1 mL PBS:MeOH (1:4). The reaction mixture was vortexed for 2 min, during which the product precipitated out as a white solid. The product was isolated after centrifugation and then washed with water (2 × 0.5 mL) to yield essentially pure DAB1 and DAB2. The product identity was confirmed by LC-MS and NMR:

- DAB1: Isolated yield (91%), ^{1}H-NMR (1 ×PBS pH 7.4, 10% D_2O): 7.56-7.55 (d, *J* = 8.3, 1H), 7.40 (s, 1H), 7.35-7.32 (t, *J* = 7.9), 7.28-7.23 (m, 2H).
- DAB2: Isolated yield (90%), ^{1}H-NMR (1 ×PBS pH 7.4, 10% D_2O): 7.60-7.59 (d, *J* = 7.6, 1H), 7.49-7.48 (d, *J* = 7.8, 1H), 7.38-7.35 (t, *J* = 8.2, 1H), 7.32-7.29 (t, *J* = 8.0, 1H).

100 μM DAB1 and DAB2 solutions were prepared in PBS (2X, pH 7.4) with 50% D_2O. The final pH was again tuned to 7.4 using 0.1N HCl and 0.1 N NaOH. NMR spectra were recorded over time (160 scans with line broadening value of 0.3) to assess their hydrolytic stability. The aromatic signatures of DAB1 and DAB2 were compared to their parent compounds, 2-FPBA and 2-APBA, to assess the stability.

3.6.6 Assessing the Efficiency of Semicarbazide Ligation

The efficiency of semicarbazide in diazaborine formation was initially determined through LC-MS analysis. 2-FPBA and semicarbazide were mixed in PBS buffer (2X, pH 7.4, 10 μM final concentration for both reactants). LC-MS analysis was performed after 10 minutes of incubation. The efficiency of 2-APBA conjugation with semicarbazide was analyzed through both LC-MS and NMR. For NMR analysis, mixtures of 2-APBA (50 μM) and semicarbazide (50, 100, 150, 250, 400 μM) in PBS (2X, 7.4) with 50% D_2O were incubated for 10 minutes. Then, the NMR spectra were. Percentage of product formation was calculated using the ratio of the integrated area between the acetyl -CH_3 peak of 2-APBA and the acetyl –CH_3 peak of the ligated product (diazaborine). For LC-MS, 10 μM 2-APBA was mixed with semicarbazide at 100, 200, 300 and 400 μM respectively.

3.6.7 Probing the Source of Sub-Quantitative DAB2 Formation

To examine the origin of the sub-quantitative yield of DAB2 formation, 1 mM of L-AB3, an unnatural amino acid bearing a 2-APBA motif on its side chain, was conjugated to an equimolar concentration of semicarbazide in 1X PBS buffer (pH 7.4). After incubating for 5 minutes, either 1 mM excess of L-AB3 or semicarbazide was added to the conjugate in 1X PBS buffer (pH 7.4). ^{1}H NMR spectra were obtained in 10% D_2O using water suppression PRESAT parameter, 160 scans, and line broadening value of 0.5.

3.6.8 Kinetics of DAB1 and DAB2 Formation

The kinetics of the conjugation reaction between semicarbazide and 2-FPBA were studied by recording UV-vis absorption with a Nanodrop UV-vis spectrometer. The data were collected after blank subtraction using PBS buffer (1X, 7.4). The reaction was performed in a quartz cuvette (10 mm path length; total volume ~ 2 mL) at room temperature. 1 mL PBS buffer was pipetted into the cuvette, followed by addition of 1 µL of 2-FPBA stock (10 mM in PBS), and then the spectrum of 2-FPBA was recorded. Subsequently, 1 µL of the semicarbazide stock (10 mM in PBS) was added into the 2-FPBA solution in the cuvette. After quick mixing (~ 5 sec), UV-vis spectra of the reaction mixture were collected on 10 second intervals. A quick shift of the absorption maxima from ~254 nm to ~ 290 nm was observed upon DAB1 formation. The experiment was repeated three times and consistent results were obtained. The kinetic data were fitted according to a second order mechanism with the two reactants at equal concentrations. Kinetics of DAB2 formation were examined via UV-vis by mixing 20 µM of 2-APBA and 50 µM of semicarbazide, which gave 60% product formation

according to NMR results. The change of the absorption maxima at ~290 nm was collected on 4 second intervals. The experiment was repeated three times and consistent results were obtained. The kinetic data were fitted according to the equations shown below to obtain the rate constant. All kinetic data were plotted with Origin 8.

Kinetics of DAB1 Formation

$$\frac{dP}{dt} = k_2(C_0 - P)(C_0 - P) \quad \textbf{(1)}$$

in which **P** is the product concentration, $\mathbf{C_0}$ is the starting material concentration, which is 10 μM for both reactants, and $\mathbf{k_2}$ is the rate constant.

$$\frac{d(C_0-P)}{dt} = -k_2(C_0 - P)^2 \quad \textbf{(2)}$$

$$\frac{d(C_0-P)}{(C_0-P)^2} = -k_2 dt \quad \textbf{(3)}$$

Integrate both sides of the equation to obtain:

$$\frac{1}{C_0-P} - \frac{1}{C_0} = k_2 t \quad \textbf{(4)}$$

Solving the equation for P gives:

$$P = \frac{C_0 t}{t+\frac{1}{C_0 k_2}} \quad \textbf{(5)}$$

Fitting the Kinetic Data to a Hyperbolic Equation:

$$y = \frac{P_1 x}{x+P_2} \quad \textbf{(6)}$$

k_2 can be determined by:

$$P_2 = \frac{1}{C_0 k_2} \rightarrow k_2 = \frac{1}{C_0 P_2} \quad \textbf{(7)}$$

Kinetics of DAB2 Formation

$$\frac{dP}{dt} = k_2(C_1 - P)(C_2 - P) \quad \textbf{(1)}$$

in which **P** is the product concentration and $\mathbf{C_1}$ and $\mathbf{C_2}$ are the initial starting materials' concentration respectively (C_1=20 μM and C_2=50 μM). Given that C_2 is significantly larger than C_1, to simplify kinetics fitting, the reaction is treated as a pseudo-first order reaction. C_2 is set to 40 μM (C_2^*), which falls in between the initial and ending concentrations of semicarbazde. We acknowledge this treatment may introduce some error; however, if we do not carry out the approximation, the order of magnitude of the rate constant will be affected.

$$\frac{dP}{dt} = k_2 C_2^* (C_1 - P) \quad \textbf{(2)}$$

$$\frac{dP}{C_1 - P} = k_2 C_2^* dt \quad \textbf{(3)}$$

$$\frac{d(P - C_1)}{P - C_1} = -k_2 C_2^* dt \quad \textbf{(4)}$$

$$ln \frac{P - C_1}{-C_1} = -k_2 C_2^* t \quad \textbf{(5)}$$

$$P = C_1 - C_1 \exp(-k_2 C_2^* t) \quad \textbf{(6)}$$

Fitting the kinetic data according to the equation gives the k_2 value.

3.6.9 Assessing the Biocompatibility of Semicarbazide Ligation

Reversibility of 2-APBA and Cysteine Conjugation

2-APBA and L-cysteine were mixed in 1 mL PBS (1X, pH 7.4, 1 mL) in 10% D_2O at a final concentration of 2 mM each and the mixture was incubated for 30 min at room temperature. Formation of thiozolidinoboronate (~ 80% completion) was analyzed using NMR by identifying the chemical shift of the acetyl $–CH_3$ group. Then the mixture was diluted 10x and the NMR spectrum was taken immediately. The results showed 20% of the product remaining and the rest of product was hydrolyzed back to the starting

material. The experiment clearly establishes the quick equilibrium between the thiazolidinoboronate conjugate and reactants (2-APBA and cysteine).

Inhibitory Effect of Cysteine to Semicarbazide Ligation

A mixture of 2-FPBA (or 2-APBA) and L-cysteine was prepared at 200 μM (1 mL) in PBS (1X, pH 7.4) in 10% D_2O. The mixture was incubated for 30 min at room temperature. Then, 10 μL semicarbazide stock (20 mM in 1X PBS, pH 7.4) was added to the mixture, which was monitored by LC-MS analysis.

Inhibitory Effect of Bacterial Cell Lysate to Semicarbazide Ligation

The inhibitory effect of cell lysate in semicarbazide ligation was examined using HPLC analysis. To assess the extent of inhibition, control experiments were first performed in 1X PBS buffer (pH 7.4). 25 μM 2-FPBA and 2-APBA were separately incubated with 50 μM semicarbazide-NBD (Scz-NBD) in 1X PBS buffer (pH 7.4) for 30 min, and then the mixtures were analyzed using HPLC. Product formation was confirmed by LC-MS.

For *S. aureus* cell lysate, 5 mL of *S. aureus* culture in LB-broth was spun down and the pellet was washed with 5 mL PBS buffer (1X, pH 7.4). The pellet (~ 50 mg) was then lysed by the addition of 1 mL of B-per (Thermo Scientific) following the suggested protocol (https://www.thermofisher.com/order/catalog/product/78248). Then the clear supernatant was collected to give a 5 mg/mL cell lysate, as determined by standard Bradford assay. Then 475 μL cell lysate was mixed with 1.25 μL 2-FPBA or 2-APBA stock (10 mM in 1X PBS, pH 7.4). The mixture was incubated for 10 min at room temperature, and then mixed with 25 μL of Scz-NBD stock (1 mM in 1X PBS, pH 7.4). The final mixture was incubated for 30 min at room temperature and analyzed using

HPLC. Scz-NBD ligation to 2-FPBA in the presence of cell lysate was further analyzed over time by incubation at room temperature. The chromatograms were blank subtracted and plotted with Origin 8.

Inhibitory Effect of FBS to Semicarbazide Ligation

The inhibitory effect of FBS on semicarbazide ligation was studied using HPLC analysis. To assess the extent of inhibition, a mixture of 20% FBS and 25 μM 2-FPBA or 2-APBA was prepared in PBS (1X, pH 7.4). Then the mixture was incubated with 50 μM Scz-NBD for 30 min at room temperature. The mixtures were analyzed using HPLC. The chromatograms were blank subtracted and plotted with Origin 8.

Inhibitory Effect of HEK293T Cell Lysate to Semicarbazide Ligation

The inhibitory effect of HEK 293T lysate on semicarbazide ligation was studied using HPLC analysis. To assess the extent of inhibition, a mixture of 5 mg/mL HEK 293T lysate and 25 μM 2-FPBA or 2-APBA was prepared in PBS (1X, pH 7.4). Then the mixture was incubated with 50 μM Scz-NBD for 30 min at room temperature. The mixtures were analyzed using HPLC. The chromatograms were blank subtracted and plotted with Origin 8.

Stability of semicarbazide ligation reagents in FBS and HEK 293T cell lysate

To assess the stability of 2-APBA, 2-FPBA and Scz-FITC in the presence of FBS and HEK 293T cell lysates, 100 μM 2-APBA or 2-FPBA (500 μM stock in 1X PBS, pH 7.4), or 50 μM Scz-FITC (4.87 mM stock in 1X PBS (pH 7.4, 1% DMSO) were incubated in either 20% (w/v) FBS (200μL) or 5% (w/v) HEK 293T cell lysate (200 μL, 5 mg/mL) prepared in PBS for 0 or 17 hours at RT. Then, each was mixed with either 50

μM Scz-FITC or 100 μM 2-APBA. The conjugation reaction was first confirmed by LC-MS analysis, then monitored by analytical HPLC.

HEK 293T cell lysate labeling via in gel fluorescence

HEK 293T soluble protein lysates (50 μL, 2 mg/mL) were treated with Scz-FITC (50 μM, 3 mM stock in 1X PBS Buffer (pH 7.4, 1% DMSO) or fluorescein (50 μM, 3 mM stock in 1X PBS Buffer, pH 7.4, 1% DMSO) at room temperature for 0.5 hr. A sample containing 50 μM Scz-FITC (3 mM stock in 1X PBS Buffer, pH 7.4, 1% DMSO) incubated at room temperature for 0.5 hr was included as a control for non-specific interactions with the SDS-PAGE gel. SDS-PAGE loading buffer (2X, reducing, 50 μL) was added to the samples, and 25 μL of each sample was separated by SDS-PAGE at 100V for 120 minutes on a 10% polyacrylamide gel. Gels were visualized on a Hitachi FMBO II multiview flatbed laser-induced fluorescent scanner. HEK 293T protein lysates were then visualized by standard Coomassie staining and destaining protocols via a Stratgene Eagle Eye apparatus by COHU high performance CCD camera.

Evaluating bacteria cell killing by semicarbazide, phenylhydrazine and D-AB3

S. aureus and *E. coli* were grown from a single colony overnight in LB broth via incubation at 37^{o}C with agitation. A small aliquot was then taken and diluted (1:100) in fresh broth and cultured for another ~2.5 hours until the cells reached the beginning of logarithmic phase (OD_{600}~0.3). Then, the bacteria were serially diluted to a pre-determined factor (10^5 for *S. aureus* and $3x10^6$ for *E. coli*) to allow for accurate colony counting. Semicarbazide (1 mM stock), phenylhydrazine (1 mM stock) and D-AB3 (12.5 mM stock) were then added to triplicate aliquots of the bacteria dilution to reach a final concentration of 50 μM, 50 μM and 125 μM, respectively. The aliquots were incubated at

37°C for 1 hour with agitation. Then, 100 μL of the aliquots were spread on LB agar plates, and the plates were allowed to incubate at 37°C overnight. Individual colonies were counted on each plate and the average and standard deviation for triplicate plating were obtained.

MTT cytotoxicity assay

HEK 293T cells (grown in complete DMEM media with 10% fetal bovine serum, 2 mM glutamine, and 1% Pen/Strep) were grown to about 80% confluency before removal from the surface of a 20 cm petri-dish with 25% Trypsin with EDTA (5 minutes, 37°C, 5% CO_2). Cells were pelleted (3,500 rpm, 5 minutes, 4°C), diluted in 10 mL fresh complete DMEM media to generate aliquots of 30,000 cells per well (100 μL), then incubated for 24 hours before addition of semicarbazide (50 μM), phenylhydrazine (50 μM), D-AB3 (125 μM) or camptothecin (50 μM). Stock solutions of semicarbazide and phenylhydrazine were prepared fresh in DMSO, and diluted to the working concentration as listed above in DMEM so that the total volume of DMSO added was kept constant at 1% (v/v). For each reagent, samples were set up as three replicates with two timepoints (6 and 24 hours). Control wells were loaded with 1 μL DMSO or 1 μL of camptothecin (5 mM stock in DMSO for a final concentration of 50 μM, used as positive control for cytotoxicity). After incubation for 6 or 24 hours, cells were washed once with 1X PBS (pH 7.4) before being incubated for 4 hours with 110 μL of 12 mM 3-(4,5-Dimethylthiazol-2-yl)-2,5-diphenyltetrazolium bromide (MTT) dissolved in RPMI media. The MTT assay was quenched with 100 μL of 10% SDS in 0.01 M HCl and allowed to incubate overnight before absorbance at 570 nm was recorded with a

SpectraMax M5 plate reader (Molecular Devices). The results of the averages and standard deviations of the wells determined after normalization to the DMSO control.

3.6.10 Bacterial Cell Culture and Labeling Experiments for D-AB3

For each strain, bacterial cells from a single colony were grown overnight in LB broth at 37 ^{o}C with agitation. An aliquot was taken and diluted (1:100) in fresh broth and cultured for another ~ 2.5 hours until the cells reached the beginning of logarithmic phase (OD_{600} ~ 0.3). Then, the unnatural D-amino acids (4 mM stock in 1X PBS, 7.4) were added to the bacterial cell cultures (final concentration 0-125 μM) and the cultures were allowed to continue growth before 1 mL aliquots were taken at 0.5, 2, 4 and 6 hour time points. The aliquots were spun down at 5000 rcf, washed once with 1 mL PBS (1X, pH 7.4), spun down again, and the cell pellet was then incubated with 100 μL of 50 μM semicarbazide-FITC (Scz-FITC) at 37 ^{o}C for 30 minutes. The cells were then spun down and washed twice with PBS (1X, pH 7.4) before the final dilution of the cells in PBS for microscopic or flow cytometry analysis (~1 × 10^6 cells).

For bacteria labeling in the presence of 10% FBS and mammalian cell lysate, overnight cultured bacteria were diluted (1:100) and grown to OD_{600} ~ 0.3 in LB broth. 60 μM D-AB3 was added to the cultures which were continued to grow until OD_{600} ~ 1. Then cells were spun down at 5000 rcf, washed once with 1 mL PBS (1X, pH 7.4) and resuspended in either 10% FBS (95 μL) or 5 mg/mL HEK 293T cell lysate (95 μL) for 10 min. Additionally, 5 μL (1 mM stock) of Scz-FITC solution in PBS (1X, pH 7.4) was added to the mixture, which was then incubated at 37 ^{o}C for 30 minutes. The cells were spun down and washed twice with 1X PBS (pH 7.4) before a final dilution in phosphate buffer for microscopic or flow cytometry analysis (~1 × 10^6 cells).

3.6.11 Bacterial Co-Culture Preparation for D-AB3

For the co-culture staining experiment, *E. coli* (500 μL) and *S. aureus* (500 μL) were separately diluted (1:100) from overnight culture, and then treated with D-AB3 (25 μM). The cultures were then grown until OD_{600} ~1.0, spun down at 5000 rcf, washed once with PBS buffer (1X, pH 7.4, 1 mL), and resuspended in PBS (1X, pH 7.4, 1 mL). Then the bacteria were mixed together in a new microcentrifuge tube, combining 500 μL of each of the resuspended cells, which was then spun down at 5000 rcf. The combined cell pellet was treated with 100 μL semicarbazide-FITC (50 μM), and was incubated at 37 ^{o}C for 30 minutes. Cells were then spun down and washed twice with PBS buffer (1X, pH 7.4), before a final dilution of the cells in 100 μL PBS buffer (1X, pH 7.4) for microscopic analysis.

3.6.12 Microscopic Analysis of D-AB3 Labeled Bacteria

For epi-fluorescence microscopy, 2 μL of the bacterial cell suspension was placed on a glass slide (Fisherfinest premium, 75 × 25 × 1 mm^3). A coverslip (Fisherbrand, 22 × 22 × 0.15 mm^3) was pressed down on the cell droplet to give a single layer of cells on the glass slides. White light and fluorescence images were taken on a Zeiss Axio Observer A1 inverted microscope equipped with a filter cube (488 nm excitation, 515-520 nm emission) suitable for detection of FITC fluorescence. A Plan-NeoFluar × 100 oil objective from Zeiss was used to visualize the bacterial cells. All images were captured with the exposure time of 1000 ms for all D-AB3 concentrations and time points. All fluorescence images were processed following a fixed protocol with the software Fiji ImageJ.

For confocal analysis, 2 μL of cells were placed on a glass slide and a coverslip was placed on top. Images were taken on a Leica SP5 confocal fluorescence microscope with filters that allowed the detection of FITC (492 nm excitation, 518 emission). A × 63 oil objective was used with an Argon laser at 10% laser power. Gain was adjusted to between 900 HV and 1,100 HV with an offset of -0.5%. The images were captured with the software LAS 2.6 and then processed with Fiji ImageJ.

3.6.13 Bacterial Flow Cytometry Analysis for D-AB3 Labeled Bacteria

The samples were prepared and stained following the same protocol described for microscopy. 300 μL aliquots were filtered through a 35 μm filter (Nalgene) before analysis. The samples were analyzed on a BD FACSAria cell sorter (BS Biosciences). Data analysis was performed with FlowJo (Tree Star, Inc.), from which the median fluorescence intensities of the stained cells were extracted.

3.6.14 *Extraction of HEK293T Cell Lysates*

HEK 293T cells were grown at 37°C under 5% CO_2 atmosphere in DMEM media supplemented with 10% fetal bovine serum (FBS), 2 mM glutamine and 1% Pen/Strep. The plates were allowed to grow to ~100% confluency, then the cells were harvested by scraping. The cells were washed 3 times with PBS and resuspended in PBS (1X, pH 7.4, 600 μL). Cells were then sonicated for lysis to form whole cell lysates, which were centrifuged at 4°C for 30 minutes (45,000 rpm). The supernatant was collected as the soluble fraction and the pellet was discarded. The protein concentration of the supernatant was determined via standard Bradford assay.

3.6.15 X-Ray Crystallographic Data for DAB1 and DAB3

DAB1**:** DAB1 (5 mg) was dissolved in 2 mL of EtOH:water (1:1) mixture. The solution was then subjected to slow evaporation in a 5 mL glass test tube. After a week, very thin fiber shaped crystal growth was observed. The crystals were carefully taken out by spatula, and placed on glass slide in a drop of glycerol and a single crystal was selected under a Leica MDG-30 microscope. The details of structure analysis and parameters are shown below in Table S1 and CIF can be found in The Cambridge Crystallographic Data Centre (CCDC, 1478626).

Table S1. Crystal data and structure refinement for $C_8H_8BN_3O_2$.

Identification code	$C_8H_8BN_3O_2$	
Empirical formula	$C_8H_8BN_3O_2$	
Formula weight	188.98	
Temperature	100(2) K	
Wavelength	1.54178 Å	
Crystal system	Monoclinic	
Space group	$P2_1/n$	
Unit cell dimensions	a = 6.7872(3) Å	a= 90°.
	b = 11.6855(5) Å	b= 102.759(2)°.
	c = 10.8557(5) Å	g = 90°.
Volume	839.73(6) $Å^3$	
Z	4	
Density (calculated)	1.495 Mg/m^3	
Absorption coefficient	0.902 mm^{-1}	
F(000)	392	
Crystal size	0.370 x 0.080 x 0.060 mm^3	
Theta range for data collection	5.638 to 69.967°.	
Index ranges	-8<=h<=8, -14<=k<=14, -13<=l<=12	
Reflections collected	7508	
Independent reflections	1570 [R(int) = 0.0236]	
Completeness to theta = 67.679°	99.7 %	
Absorption correction	Semi-empirical from equivalents	
Max. and min. transmission	0.7533 and 0.6605	
Refinement method	Full-matrix least-squares on F^2	

Data / restraints / parameters	1570 / 3 / 136
Goodness-of-fit on F^2	1.047
Final R indices [I>2sigma(I)]	R1 = 0.0328, wR2 = 0.0930
R indices (all data)	R1 = 0.0337, wR2 = 0.0943
Extinction coefficient	na
Largest diff. peak and hole	0.267 and -0.202 e.Å^{-3}

Boc-AB3-O^{t}Bu-semicarbazide (DAB3): Boc-AB3(pin)-O^{t}Bu (25 mg) was dissolved in ethanol (1 mL) and was mixed with semicarbazide solution (5 mg in 1 mL PBS, pH 7.4). Immediate white precipitation was observed from the reaction mixture, which was isolated by centrifugation. The product was washed twice with water (2 × 1 mL) and finally with 1:1 MeOH/Water mixture (1 mL). The white powder product was lyophilized to dryness and then 5 mg of the product was dissolved in 2 mL of MeOH:water (1:1) mixture. The solution was then subjected to slow evaporation in a 5 mL glass test tube. After a week, very thin fiber shaped crystal growth was observed. The crystals were carefully taken out by spatula and placed on glass slide in a drop of glycerol, and a single crystal was selected under a Leica MDG-30 microscope. The details of structure analysis and parameters are shown below in Table S2 and CIF can be found in The Cambridge Crystallographic Data Centre (CCDC, 1478627).

Table S2. Crystal data and structure refinement for $C_{21}H_{31}BN_4O_6$

Identification code	C21H31BN4O6	
Empirical formula	C21.38 H32.50 B N4 O6.38	
Formula weight	458.32	
Temperature	100(2) K	
Wavelength	1.54178 Å	
Crystal system	Triclinic	
Space group	P1	
Unit cell dimensions	a = 11.1773(5) Å	a= 100.992(4)°.
	b = 12.6727(6) Å	b= 97.611(4)°.
	c = 18.2164(11) Å	g = 91.693(3)°.
Volume	2506.7(2) Å^3	

Z	4
Density (calculated)	1.214 Mg/m^3
Absorption coefficient	0.736 mm^{-1}
F(000)	979
Crystal size	0.300 x 0.050 x 0.030 mm^3
Theta range for data collection	2.496 to 67.150°.
Index ranges	-13<=h<=13, -12<=k<=14, -21<=l<=21
Reflections collected	8844
Independent reflections	8844 [R(int) = 0.0836]
Completeness to theta = 67.150°	98.6 %
Absorption correction	Semi-empirical from equivalents
Max. and min. transmission	0.7528 and 0.5078
Refinement method	Full-matrix least-squares on F^2
Data / restraints / parameters	8844 / 1005 / 1222
Goodness-of-fit on F^2	0.976
Final R indices [I>2sigma(I)]	R1 = 0.0905, wR2 = 0.2294
R indices (all data)	R1 = 0.1250, wR2 = 0.2604
Absolute structure parameter	0.1(4)
Extinction coefficient	n/a
Largest diff. peak and hole	0.449 and -0.357 $e.Å^{-3}$

3.6.16 Synthesis of APBA Coumarin Analogues

Synthesis of AB21 (3-VI-c)

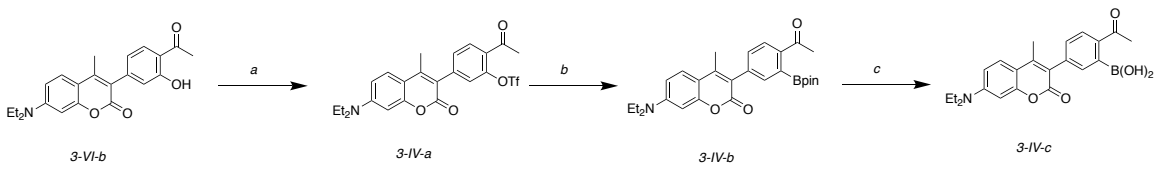

(a) Synthesis of **3-VI-a**: **3-VI-b** (100 mg, 0.274 mmol) was dissolved in anhydrous dichloromethane (1 mL) and triethylamine (160 µL, 1.15 mmol) was added while stirring. The reaction mixture was cooled to -78 ^{o}C and trifluoromethane sulfonic anhydride (102 µL, 0.6 mmol) was added slowly. The reaction mixture was allowed to stir at room temperature for 0.5 hr under an argon environment. After that, the reaction was quenched with saturated sodium bicarbonate (1 mL) and the mixture was allowed to stir for 5 min. The product was extracted with dichloromethane (3x20 mL). The combined organic layer was washed with brine (30 mL) and dried over Na_2SO_4. After removing the solvent, the crude product was purified on silica gel column using ethyl acetate:hexane (1:4) as eluent to yield a dark red gummy product (126 mg, 93%).

^{1}H NMR ($CDCl_3$): δ, 7.87-7.86, (d, J = 7.1, 1H), 7.49-7.47 (m, 2H), 7.29 (d, J = 4.2, 1H), 6.63 (d, J = 7.2, 1H), 6.53 (d, J = 3.8, 1H) 3.46-3.42 (q, J = 6.8, 4H), 2.67 (s, 3H), 2.27 (s, 3H), 1.23-1.21 (t, J = 6.5, 6H).

^{13}C NMR ($CDCl_3$): δ 196.28, 161.14, 155.36, 150.93, 149.76, 146.42, 141.71, 131.07, 130.52, 126.43, 125.20, 117.66, 108.98, 97.33, 60.36, 44.81, 29.47, 16.30, 12.43.

MS-ESI^{+} (m/z): Calculated for $C_{23}H_{22}F_3NO_6S$ $[M+H]^{+}$ 498.1196, found 498.1178.

(b) Synthesis of **3-IV-b**: **3-IV-a** (100 mg, 0.2 mmol), B_2Pin_2 (126 mg, 0.5 mmol), Pd(dppf)Cl_2 (18 mg, 0. 020 mmol, 10 mol %), and potassium acetate (60 mg, 0.6 mmol) were was dissolved in anhydrous dioxane (1.2 mL). The reaction mixture was bubbled with argon for 10 minutes and it was allowed to stir at 95 ^oC for 50 minutes. Completion of the reaction was monitored by LC-MS. Then water (30 mL) was added to the reaction and the product was extracted with ethyl acetate (3 × 30 mL). The combined organic layer was washed with brine (100 mL) and dried over Na_2SO_4. The solvent was removed under vacuum and the crude product was purified on silica gel using hexane:diethylether (11:9) as eluent. The desired product was obtained as a yellow gummy (68 mg, 72%).

^1H NMR ($CDCl_3$): δ 7.88-7.86 (d, J = 7.2, 1H), 7.43-7.41 (d, J = 6.5, 1H), 7.41-7.40 (m, 2H), 6.62-6.60 (dd, J = 7.1, J = 3.9, 1H), 6.53 (d, J = 3.8, 1H), 3.45-3.42 (q, J = 6.7, 4H), 2.61 (s, 3H), 2.20 (s, 3H), 1.46 (s, 12H), 1.22-1.20 (t, J = 6.4, 6H).

^{13}C NMR ($CDCl_3$): δ 199.52, 161.36, 155.23, 150.42, 148.73, 139.83, 134.59, 131.26, 128.24, 126.13, 120.11, 109.29, 108.61, 97.44, 83.67, 77.00, 44.74, 30.30, 25.70, 24.86, 16.38, 12.45.

MS-ESI^+ (m/z): Calculated for $C_{28}H_{33}BNO_4$ $[M-H_2O]^+$ 457.2424, found 457.2443.

(c) Synthesis of **3-IV-c**: **3-IV-b** (60 mg, 0.126 mmol) was dissolved in anhydrous THF (500 µL) and diethanolamine (150 mg, 1.25 mmol) was added into the solution at room temperature. The reaction was allowed to stir for 3 hours and then quenched with 1N HCl (30 mL). The solution was then neutralized using

$NaHCO_3$ (5%) solution in water. Then the product solution was directly purified by HPLC. The HPLC purification with acetonitrile/water (0.1% TFA) eluent, which yielded the pure product as a yellow powder after lyophilization (72%, 35 mg).

^{1}H NMR (Methanol-d_4): δ 8.11-8.10 (d, J = 6.2, 1H), 7.63-7.61 (d, J = 7.2, 1H), 7.46-7.45 (d, J = 6.4, 1H), 7.33 (s, 1H), 6.80 (dd, J = 5.7, J = 3.4, 1H), 6.58-6.57 (d, J = 4.9, 1H), 3.51-3.48 (q, J = 7.1, 4H), 2.68 (s, 3H), 2.25 (s, 3H), 1.23-1.21 (t, J = 6.3, 6H).

^{13}C NMR (Methanol-d_4): δ 200.98, 162.27, 155.07, 150.72, 150.20, 140.66, 138.60, 132.75, 130.77, 128.66, 119.16, 109.21, 96.70, 84.64, 78.76, 44.36, 23.68, 15.13, 11.30.

MS-ESI$^+$ (m/z): Calculated for $C_{22}H_{25}BNO_5$ $[M+H]^+$ 394.1826, found 394.1843.

Synthesis of AB22 (3-V-d)

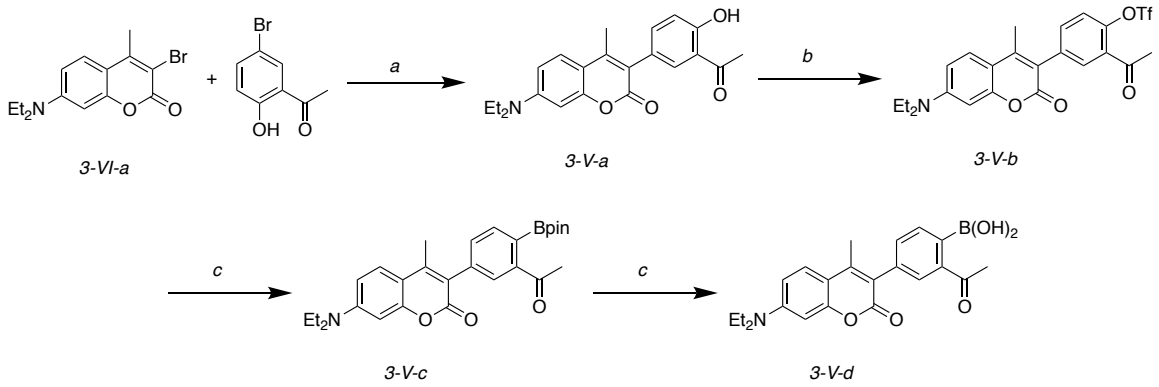

3-VI-a 3-V-a 3-V-b 3-V-c 3-V-d

(a) Synthesis of **3-V-a**: 5-bromo-2-hydroxy acetophenone (215 mg, 1 mmol), B_2Pin_2 (280 mg, 1.1 mmol), Pd(dppf)Cl_2 (22 mg, 0.03 mmol, 3 mol %) and potassium acetate (294 mg, 3 mmol) were was dissolved in anhydrous dioxane (5 mL). The

reaction mixture was bubbled with argon for 10 minutes and it was allowed to stir at 90 ^{o}C for 90 minutes. Completion of the reaction was monitored by LC-MS. The reaction mixture was cooled to room temperature, and then **3-VI-a** (216 mg, 0.7 mmol), Pd(dppf)Cl_2 (22 mg, 0.03 mmol, 3 mol %), K_3PO_4 (445 mg, 2.1 mmol) and water (1mL) were added subsequently in the same pot. Further, reaction mixture was heated to 85 ^{o}C for overnight. The reaction mixture was filtered through sintered funnel and digested in water (100 mL). The product was extracted with ethyl acetate (3x100 mL). The combined organic layer was washed with brine (100 mL) and dried over Na_2SO_4. The solvent was removed under vacuum and the crude product was purified on silica gel using hexane:ethyl acetate (4:1) as eluent. The desired product was obtained as a yellow solid (182 mg, 67%).

^{1}H NMR ($CDCl_3$): δ 12.31 (s, 1H), 7.71 (b, 1H), 7.46-7.45 (d, J = 6.9, 1H), 7.40-7.39 (d, J = 7, 1H), 7.04-7.03 (d, J = 6.9, 1H), 6.63-6.62 (dd, J = 7.0, J = 4, 1H), 6.55 (d, J = 4, 1H), 3.45-3.42 (q, J = 6.8, 4H), 2.63 (s, 3H), 2.26 (s, 3H), 1.24-1.21 (t, J = 7.5, 6H).

^{13}C NMR ($CDCl_3$): δ 204.51, 162.19, 161.77, 155.07, 150.38, 148.68, 138.80, 132.88, 126.12, 125.91, 119.53, 118.30, 109.32, 108.70, 97.44, 77.21, 77.00, 76.79, 44.76, 26.69, 16.39, 15.26, 12.45.

MS-ESI^{+}: *m/z* calculated for $C_{22}H_{23}NO_4$ $[M+H]^{+}$ 366.1707, found 366.1723.

(b) Synthesis of **3-V-b**: **3-V-a** (100 mg, 0.274 mmol) was dissolved in anhydrous dichloromethane (1 mL) and triethylamine (160 µL, 1.15 mmol) was added while stirring. The reaction mixture was cooled to -78 ^{o}C and trifluoromethane sulfonic

anhydride (102 µL, 0.6 mmol) was added slowly during 5 min. The reaction mixture was allowed to stir at room temperature for 0.5 hr under an argon environment. After that, the reaction was quenched with saturated sodium bicarbonate (1 mL) and the mixture was allowed to stir for 5 min. The product was extracted with dichloromethane (3x20 mL). The combined organic layer was washed with brine (30 mL) and dried over Na_2SO_4. After removing the solvent, the crude product was purified on silica gel column using ethyl acetate:hexane (1:4) as eluent to yield a dark red gummy product (120 mg, 91%).

^{1}H NMR ($CDCl_3$): δ, 7.76, (d, J = 5.9, 1H), 7.55-7.53 (dd, J = 6.4, J = 3.7, 1H), 7.48-7.47 (d, J = 6.5, 1H), 6.65-6.63 (dd, J = 6.7, J = 3.8, 1H), 6.55-6.54 (d, J = 6.3, 1H), 3.46-3.42 (q, J = 6.8, 4H), 2.65 (s, 3H), 2.25 (s, 3H), 1.24-1.22 (t, J = 6.3, 6H).

^{13}C NMR ($CDCl_3$): δ 196.50, 155.28, 150.80, 149.52, 145.89, 133.25, 126.35, 122.48, 119.67, 117.95, 117.54, 108.91, 97.36, 44.80, 29.55, 16.47, 12.43.

MS-ESI$^+$ (m/z): Calculated for $C_{23}H_{22}F_3NO_6S$ $[M+H]^+$ 498.1196, found 497.1182.

(c) Synthesis of **3-V-c**: **3-V-b** (100 mg, 0.2 mmol), B_2Pin_2 (126 mg, 0.5 mmol), $Pd(dppf)Cl_2$ (18 mg, 0. 020 mmol, 10 mol %), and potassium acetate (60 mg, 0.6 mmol) were was dissolved in anhydrous dioxane (1.2 mL). The reaction mixture was bubbled with argon for 10 minutes and it was allowed to stir at 95 ^{o}C for 50 minutes. Completion of the reaction was monitored by LC-MS. Then water (30 mL) was added to the reaction and the product was extracted with ethyl acetate (3x30 mL). The combined organic layer was washed with brine (100 mL) and dried over Na_2SO_4. The solvent was removed under vacuum and the crude

product was purified on silica gel using hexane:diethylether (11:9) as eluent. The desired product was obtained as a yellow gummy (62 mg, 70%).

^{1}H NMR ($CDCl_3$): δ 7.78 (b, 1H), 7.58-7.57 (d, J = 6.8, 1H), 7.47-7.43 (m, 2H), 6.63-6.61 (dd, J = 7.3, J = 3.7, 1H), 6.54 (d, J = 3.5, 1H), 3.45-3.41 (q, J = 6.6, 4H), 2.60 (s, 3H), 2.18 (s, 3H), 1.44 (s, 12H), 1.22-1.21 (t, J = 5.9, 6H).

^{13}C NMR ($CDCl_3$): δ 199.72, 161.64, 155.20, 150.42, 148.76, 140.82, 136.24, 134.56, 132.18, 130.73, 126.13, 125.48, 119.94, 109.27, 108.65, 97.43, 44.74, 30.30, 24.87, 16.21, 12.46.

MS-ESI$^+$ (m/z): Calculated for $C_{26}H_{34}BNO_5$ $[M-H_2O]^+$ 457.2424, found 457.2415.

(d) Synthesis of **3-V-d**: **3-V-c** (50 mg, 0.105 mmol) was dissolved in anhydrous THF (500 μL) and diethanolamine (150 mg, 1.25 mmol) was added into the solution at room temperature. The reaction was allowed to stir for 3 hours and then quenched with 1N HCl (30 mL). Further, the solution was neutralized using $NaHCO_3$ (5%) solution in water. Then the product solution was directly purified through HPLC. The HPLC purification with acetonitrile/water (0.1% TFA) (Gradient: 5% ACN to 95% ACN during 50 min) mixture yielded the pure product as a yellow powder after lyophilization (74%, 28 mg).

^{1}H NMR (Methanol-d_4): δ 7.98 (b, 1H), 7.66-7.64 (d, J = 7.8, 1H), 7.56-7.55 (d, J = 6.7, 1H), 7.50-7.49 (d, J = 6.9, 1H), 6.84-6.82 (d, J = 7.8, 1H), 6.63 (b, 1H), 3.53-3.50 (q, J =7, 4H), 2.65 (s, 3H), 2.28 (s, 3H), 1.24-1.21 (t, J = 6.9, 6H).

^{13}C NMR (Methanol-d_4): δ 203.88, 165.25, 161.81, 161.55, 157.64, 152.97, 142.37, 138.50, 137.87, 133.78, 132.94, 129.16, 121.94, 112.26, 99.89, 47.35, 26.39, 17.84, 13.91.

MS-ESI$^+$ (m/z): Calculated for $C_{22}H_{25}BNO_5$ $[M+H]^+$ 394.1826, found 394.1838.

Synthesis of AB23 (3-IV-b)

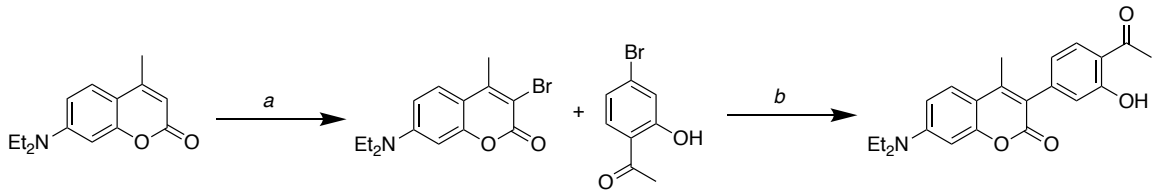

(a) Synthesis of **3-IV-a**: A mixture of 7-(diethylamino)-4-methyl-2H-chromen-2-one (**1**) (2.5 g, 13.5 mmol) and N-bromosuccinimide (3.75 g, 19.5 mmol, 1.5 eq) was added in chloroform (150 mL). Then, a catalytic amount of benzoyl peroxide (175 mg, 0.67 mmol, 0.05 eq) was added to the reaction mixture and refluxed for 12 h. The solvent was removed under a vacuum and the residue was digested in water and ethyl acetate (1:1; total volume 400 mL). Product was extracted in ethyl acetate (200 mL × 2). The combined organic layer was washed with brine (200 mL) and dried over sodium sulfate. After removing the solvent, the crude product was purified on silica gel column using ethyl acetate:hexane (1:9) as eluent to yield a yellow solid product (3.09 g, 74%). The product formation was confirmed by NMR and LC-MS.

^{1}H NMR ($CDCl_3$): δ 7.57 (d, 1H, J = 8.8 Hz), 6.92 (dd, 1 H, J = 2.5, J = 8.9 Hz), 6.85(d, 1 H, J = 2.5 Hz), 3.91 (s, 3 H), 2.63 (s, 3 H).

^{13}C NMR ($CDCl_3$): δ 158.08, 154.41, 151.45, 150.61, 128.20, 126.03, 108.99, 105.58, 97.22, 44.77, 19.08, 12.42.

MS-ESI$^+$ (m/z): Calculated for $C_{14}H_{16}BrNO_2$ $[M+H]^+$ 310.0443, found 310.0425.

(b) Synthesis of **3-IV-b**: 4-bromo-2-hydroxy acetophenone (215 mg, 1 mmol), B_2Pin_2 (280 mg, 1.1 mmol), Pd(dppf)Cl_2 (22 mg, 0.03 mmol, 3 mol %) and

potassium acetate (294 mg, 3 mmol) were dissolved in anhydrous dioxane (5 mL). The reaction mixture was bubbled with argon for 10 minutes and it was allowed to stir at 90 ^{o}C for 90 minutes. Completion of the reaction was monitored by LC-MS. The reaction mixture was cooled to room temperature, and then 2 (216 mg, 0.7 mmol), Pd(dppf)Cl_2 (22 mg, 0.03 mmol, 3 mol %), K_3PO_4 (445 mg, 2.1 mmol) and water (1mL) were added subsequently in the same pot. Further, reaction mixture was heated to 85 ^{o}C for overnight. The reaction mixture was filtered through sintered funnel and digested in water (100 mL). The product was extracted with ethyl acetate (3x100 mL). The combined organic layer was washed with brine (100 mL) and dried over Na_2SO_4. The solvent was removed under vacuum and the crude product was purified on silica gel using hexane:ethyl acetate (4:1) as eluent. The desired product was obtained as a yellow solid (170 mg, 62%).

^{1}H NMR ($CDCl_3$): δ 12.30 (s, 1H), 7.80-7.78 (d, J = 7, 1H), 7.47-7.45 (d, J = 7.4, 1H), 6.91-6.89 (m, 2H), 6.64-6.62 (dd, J = 7.2, J = 4, 1H), 6.54 (d, J = 3.8, 1H), 3.46-3.41 (q, J = 6.8, 4H), 2.65 (s, 3H), 2.26 (s, 3H), 1.24-1.21 (t, J = 6.1, 6H).

^{13}C NMR ($CDCl_3$): δ 204.13, 162.13, 161.24, 155.22, 150.57, 148.87, 144.17, 130.53, 126.25, 121.51, 120.44, 118.79, 108.77, 97.37, 44.77, 26.65, 24.83, 16.25, 12.44.

MS-ESI^{+} (m/z): Calculated for $C_{22}H_{23}NO_4$ $[M+H]^{+}$ 366.1707, found 366.1679.

Synthesis of AB24 (3-VII-a)

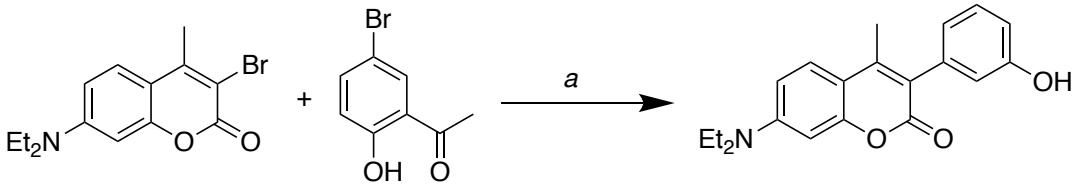

3-VI-a *3-VII-a*

(a) Synthesis of **3-VII-a**: 3-bromophenol (173 mg, 1 mmol), B_2Pin_2 (280 mg, 1.1 mmol), $Pd(dppf)Cl_2$ (22 mg, 0.03 mmol, 3 mol %) and potassium acetate (294 mg, 3 mmol) were was dissolved in anhydrous dioxane (5 mL). The reaction mixture was bubbled with argon for 10 minutes and it was allowed to stir at 90 ^oC for 90 minutes. Completion of the reaction was monitored by LC-MS. The reaction mixture was cooled to room temperature, and then **3-VI-a** (216 mg, 0.7 mmol), $Pd(dppf)Cl_2$ (22 mg, 0.03 mmol, 3 mol %), K_3PO_4 (445 mg, 2.1 mmol) and water (1mL) were added subsequently in the same pot. Further, reaction mixture was heated to 85 ^oC for overnight. The reaction mixture was filtered through sintered funnel and digested in water (100 mL). The product was extracted with ethyl acetate (3x100 mL). The combined organic layer was washed with brine (100 mL) and dried over Na_2SO_4. The solvent was removed under vacuum and the crude product was purified on silica gel using hexane:ethyl acetate (4:1) as eluent. The desired product was obtained as a yellow solid (163 mg, 67%).

^1H NMR ($CDCl_3$): δ 7.45-7.44, (d, J = 7.9, 1H), 7.26-7.22 (m, 1H), 6.77-6.74 (m, 2H), 6.72 (m, 1H), 6.63-6.61(dd, J = 8.1, J = 4,1H) , 6.53 (d, J = 7.4, 1H), 6.34 (b, 1H), 3.44-3.40 (d, J = 7.2, 1H), 2.20 (s, 3H), 1.22-1.20 (t, J = 6.8, 6H).

^{13}C NMR ($CDCl_3$): δ 162.79, 156.33, 154.95, 150.29, 149.30, 136.11, 129.40, 126.14, 122.02, 120.83, 117.58, 115.12, 109.51, 108.81, 97.41, 44.74, 16.28, 12.45.

MS-ESI$^+$ (m/z): Calculated for $C_{20}H_{21}NO_3$ $[M+H]^+$ 324.1597, found 324.1587.

3.6.17 UV-Vis Analysis of the Coumarin Analogues

The UV-Vis profiles of the coumarin analogues were obtained by diluting a DMSO stock of each analog (AB21= 1 mM, AB22=2 mM, AB23=3 mM, AB24= 2.6 mM) to 50 μM in PBS (1x, pH 7.4).

3.6.18 Fluorescence Analysis of the Coumarin Analogues

Fluorescence profiles of the coumarin analogues were obtained by diluting a DMSO stock of each analog (AB21= 1 mM, AB22=2 mM, AB23=3 mM, AB24= 2.6 mM) to 10 μM in PBS (1X, pH 7.4). Voltages applied to obtain a spectrum for each analog varied (AB21/22=800, AB23=700, AB24/25=600).

3.6.19 LC-MS Analysis of the Conjugation of Coumarin Analogues to Semicarbazide

DMSO stocks of the coumarin analogues (AB21= 1 mM, AB22=2 mM) were diluted to 200 μM in PBS (1x, pH 7.4) and incubated with 200 μM semicarbazide (18 mM stock in PBS) for 30 minutes, then analyzed by LC-MS.

3.6.20 Conjugation of the Coumarin Analogues to Semicarbazide in the Presence of Serum

DMSO stocks of the coumarin analogues (AB21= 1 mM, AB22=2 mM, AB23=3 mM, AB24= 2.6 mM) were diluted to 100 μM in 1X PBS buffer with or without 20% fetal bovine serum (FBS). Then semicarbazide was added to these solutions from a stock

solution to a final concentration of 100 μM. The reactions were incubated for 30 minutes before analysis via analytical HPLC.

3.6.21 Fluorescence Analysis of the Conjugation of Coumarin Analogues to Semicarbazide

Fluorescence profiles of the coumarin analogues conjugated to semicarbazide were obtained by diluting a DMSO stock of each analogue (AB21= 1 mM, AB22=2 mM, AB23=3 mM, AB24= 2.6 mM, AB25=5.3 mM) to 200 μM in PBS (1X, pH 7.4), adding 200 μM semicarbazide (18 mM stock in PBS), and incubating for 30 minutes. Fluorescence spectra were then obtained immediately after diluting the conjugation mixture 20X in PBS (1X, pH 7.4). Voltages applied to obtain a spectrum for each analog varied.

3.6.22 Quantum Yield of Coumarin Analogs and Diazaborine Conjugates[42]

To measure the quantum yield, the UV-Vis spectra of 10 μM AB21-24 were obtained (all around absorbance of 0.1). The concentration of fluorescein necessary to obtain the same absorbance was estimated to be 2 μM (ε=50,358 $M^{-1}cm^{-1}$ in 1M NaOH). The UV-Vis spectrum of this concentration of fluorescein was obtained in 0.1M NaOH. Fluorescence readings were then obtained for AB21-24, as well as for diazaborine conjugates as outlined. The integrations of the fluorescence peak areas were then obtained. For fluorescein, a 10x dilution of the estimated concentration to produce the same absorbance as AB21-24 was necessary to obtain a readable fluorescence peak area within the range of fluorescence detection. The fluorescence readings for fluorescein were obtained in 0.1M NaOH at 0.2 μM. Integration of the fluorescence peak area was

also obtained. To account for this dilution factor, the integrated area of fluorescein was multiplied by 10 for the quantum yield calculation.

3.6.23 Kinetics of AB21 and AB22 Conjugation to Semicarbazide

The kinetics of conjugation of AB21 and AB22 conjugating to semicarbazide were measured at 50 μM AB21/22 and 50 μM semicarbazide. Measurements were taken at 30 second intervals at a voltage of 600V until no further increase in fluorescence was observed. The reaction kinetics were fit according to a hyperbolic equation, as described below:

$\frac{dP}{dt} = k_2(C_0 - P)(C_0 - P)$ **(1)**

in which **P** is the product concentration, $\mathbf{C_0}$ is the starting material concentration, which is 50 μM for both reactants, and $\mathbf{k_2}$ is the rate constant.

$\frac{d(C_0-P)}{dt} = -k_2(C_0 - P)^2$ **(2)**

$\frac{d(C_0-P)}{(C_0-P)^2} = -k_2 dt$ **(3)**

Integrate both sides of the equation to obtain:

$\frac{1}{C_0-P} - \frac{1}{C_0} = k_2 t$ **(4)**

Solving the equation for P gives:

$P = \frac{C_0 t}{t+\frac{1}{C_0 k_2}}$ **(5)**

Fitting the kinetic data of Figure S3 to a hyperbolic equation:

$y = \frac{P_1 x}{x+P_2}$ **(6)**

k_2 can be determined by:

$P_2 = \frac{1}{C_0 k_2} \rightarrow k_2 = \frac{1}{C_0 P_2}$

3.6.24 Synthesis of D-Dap-Scz (3-VIII-c)

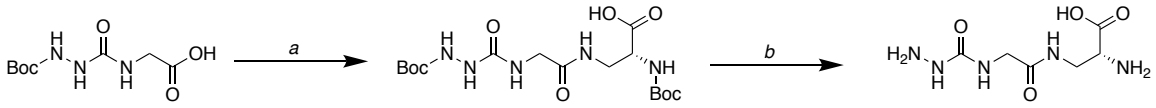

3VIII-a *3VIII-b* *3VIII-c*

(a) Synthesis of **3-VIII-b**: **3-VIII-a** (0.11 mmol) was dissolved in dimethylformamide (200 µL) on ice for 5 minutes to dissolve. N-Hydroxysuccinimide (NHS, 0.16 mmol) and dicyclohexylcarboiimide (0.10 mmol) were added, and the mixture was allowed to stir on ice for an additional 5 minutes. The reaction mixture was then stirred at room temperature for 2 hours after which all of the starting material was consumed (note: the reaction mixture turns opaque due to the formation of dicyclohexyl urea). Boc-D-Dap-OH (0.16 mmol) was then dissolved in 1:1 10% sodium carbonate: tetrahydrofuran (400 µL) and added to the stirring reaction mixture, which was then stirred for 14 hours at room temperature. The reaction mixture was then acidified with 6N HCl and extracted with ethyl acetate (3x30 mL). The combined organic layers were washed with brine and dried over sodium sulfate. The solvent was then evaporated from the reaction mixture, and the product was purified via reverse phase HPLC using a semiprep column to yield a white powder after lyophilization (24 mg, 52%).

^{1}H NMR (DMSO-d_6) δ: 1.37 (18H), 3.55-3.62 (3H), 4.00 (2H), 6.36 (1H), 6.95 (1H), 7.85 (1H), 8.54 (1H), 12.61 (1H).

MS-ESI (m/z): Calculated for $C_{16}H_{29}N_5O_8$ $[M+H]^+$ 420.40, Observed 420.21.

(b) Synthesis of **3-VIII-c**: **3-VIII-b** (24 mg, 0.057 mmol) was treated with 50% TFA in DCM (2 mL) for 1 hour. The solvent was evaporated, and the product was washed with DCM (3x10 mL). The product was then dissolved in 5 mL water and lyophilized to yield a white powder (12 mg, 100%).

^{1}H NMR (DMSO-d_6) δ: 3.45 (1H), 3.60 (1H), 2.69 (2H), 3.90-3.97 (1H), 6.55 (2H), 6.91 (2H), 7.41 (1H), 8.18 (1H), 9.13 (1H).

MS-ESI (m/z): Calculated for $C_{11}H_{21}N_5O_6$ $[M+H]^+$ 220.10, Observed 220.10.

3.6.25 Synthesis of D-Dap-Phe (3-IX-a)

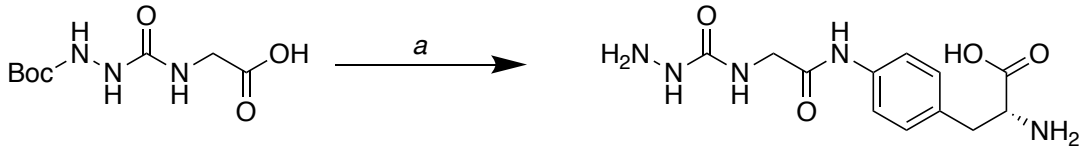

3VIII-a *3-IX-a*

(a) Synthesis of **3-IX-b**: **3-VIII-a** (0.11 mmol) was dissolved in dimethylformamide (200 μL) on ice for 5 minutes to dissolve. N-Hydroxysuccinimide (NHS, 0.16 mmol) and dicyclohexylcarboiimide (0.10 mmol) were added, and the mixture was allowed to stir on ice for an additional 5 minutes. The reaction mixture was then stirred at room temperature for 2 hours after which all of the starting material was consumed (note: the reaction mixture turns opaque due to the formation of dicyclohexyl urea). Boc-D-Phe-OH (0.16 mmol) was then dissolved in 1:1 10% sodium carbonate: tetrahydrofuran (400 μL) and added to the stirring reaction mixture, which was then stirred for 14 hours at room temperature. The reaction mixture was then acidified with 6N HCl and extracted with ethyl acetate (3x30 mL). The combined organic layers were washed with brine and dried over sodium sulfate. The solvent was then evaporated from the reaction mixture, and the

product was directly treated with 50% TFA in DCM (2 mL) for 1 hour. The solvent was evaporated, and the product was washed with DCM (3x10 mL). The product was then dissolved in 5 mL water and purified by reverse phase HPLC with water/acetonitrile (1% TFA) as eluent

MS-ESI (m/z): Calculated for $C_{12}H_{17}N_5O_4$ $[M+H]^+$ 296.13, Observed 296.10.

3.6.26 LC-MS Analysis of D-Dap-Scz for Conjugation with AB21/22

DMSO stocks of the coumarin analogs (AB21= 1 mM, AB22=2 mM, AB23=3 mM, AB24= 2.6 mM) were diluted to 50 μM in PBS (1X, pH 7.4) and incubated with 100 μM D-Dap-Scz (9 mM stock in PBS) for 30 minutes, then analyzed by LC-MS.

3.6.27 Fluorescence of Coumarin Analogues Conjugating to D-Dap-Scz

Fluorescence profiles of the coumarin analogs conjugated to D-Dap-semicarbazide were obtained by diluting a DMSO stock of each analog (AB21= 1 mM, AB22=2 mM, AB23=3 mM, AB24= 2.6 mM, AB25=5.3 mM) to 50 μM in PBS (1X, pH 7.4), adding 100 μM D-Dap-semicarbazide (9 mM stock in PBS), and incubating for 30 minutes. Fluorescence spectra were then obtained immediately after diluting the conjugation mixture 5x in PBS (1X, pH 7.4). Voltages applied to obtain a spectrum for each analog varied.

3.6.28 Synthesis of FPBA-FITC (3-X-d)

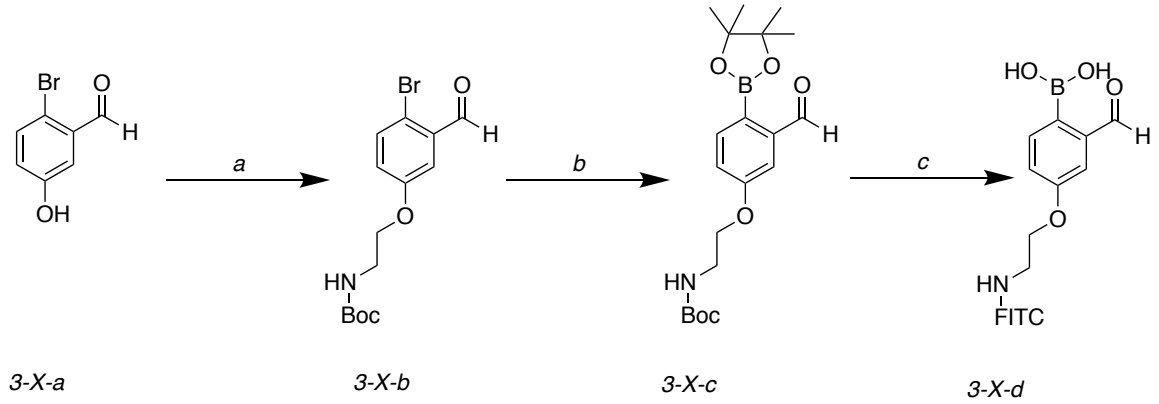

3-X-a *3-X-b* *3-X-c* *3-X-d*

(a) Synthesis of **3-X-b**: **3-X-a** (1.00 g, 0.0050 mol) was refluxed with N-Boc-bromoethylamine (1.30 g, 0.0055 mol) and potassium carbonate (2.10g, 0.015 mol) in DMF (5 mL) at 80^{o}C for 15 hours. The crude product was dissolved in 50 mL water, and extracted with ethyl acetate (3x50 mL). The combined organic layers were washed with brine, then dried over sodium sulfate and concentrated under reduced pressure. The crude material was then purified by silica gel chromatorgraphy with 1:10 ethyl acetate:hexane (550 mg, 32% yield).

^{1}H NMR (Chloroform-d_6) δ : 1.44 (s, 9H), 3.54 (q, J=5.5 Hz, 2H) 4.03-4.05 (q, J=5.3 Hz, 2H), 4.97 (s, 1H), 7.01-7.03 (dd, J=8.8, 3.2 Hz, 1H), 7.38 (d, J=3.2 Hz, 1H), 7.52 (d, J=8.8 Hz, 1H), 10.28 (s, 1H).

^{13}C NMR (Chloroform-d_6) δ: 31.02, 42.53, 63.04, 82.37, 116.38, 120.82, 125.65, 136.65, 137.30, 158.47, 160.86, 194.24.

MS-ESI (m/z): Calculated for $C_{14}H_{18}BrNO_4$ $[M+H\text{-}Boc]^+$ 244.21, Observed 244.99.

(b) Synthesis of **3-X-c**: **3-X-b** (550 mg, 0.0016 mol), B_2pin_2 (1.02g, 0.0040 mol), $Pd(dppf)Cl_2$ (65 mg, 0.000080 mol) and potassium acetate (490 mg, 0.0048 mol) were combined in dry dioxane (10 mL), and purged with argon for 15 minutes. The reaction was then allowed to stir under argon at 85°C for 1 hour. The crude product was dissolved in 50 mL water, then extracted with ethyl acetate (3x50 mL). The combined organic layers were washed with brine and dried over sodium sulfate before being concentrated under reduced pressure. The crude mixture was purified via silica gel chromatography with 3:20 ethyl acetate:hexane (439 mg, 70% yield).

^{1}H NMR (Chloroform-d_6) δ: 1.35 (s, 12H), 1.43 (s, 9H), 3.54 (q, J=5.4 Hz, 2H), 4.07 (q, J=5.7 Hz, 2H), 5.00 (s, 1H), 7.09-7.11 (d, J=8.3 Hz, 1H), 7.36 (s, 1H), 7.84-7.86 (d, J=8.3 Hz, 1H), 10.64 (s, 1H).

^{13}C NMR (Chloroform-d_6) δ: 24.83, 28.35, 39.93, 60.35, 67.30, 84.16, 111.25, 119.86, 130.11, 138.00, 143.54, 155.80, 160.86, 194.60.

MS-ESI (m/z): Calculated for $C_{20}H_{30}BNO_6$ $[M+H\text{-}Boc\text{-}4xCH_3]^+$ 391.27, Observed 236.07.

(c) Synthesis of **3-X-d**: **3-X-c** (100 mg, 0.26 mmol) was stirred with diethanolamine (270 mg, 2.6 mmol) in tetrahydrofuran (1 mL) overnight at room temperature. The mixture was then acidified with 1 N HCl, and stirred in 5 mL ethyl acetate for 30 minutes. The crude product was then extracted with ethyl acetate (3x10 mL), and the combined organic layers were washed with brine, dried over sodium sulfate, and concentrated under reduced pressure. The crude product was then

directly dissolved in 2 mL dry dichloromethane and 2 mL TFA (50% TFA in DCM), and stirred for 30 minutes. The mixture was then evaporated under reduced pressure, and crude **3-VII-d** (10 mg, 0.062 mmol) was directly stirred with fluorescein isothiocyanate (24 mg, 0.062 mmol) for 1 hour in triethylamine (18 μL, 0.124 mmol) and 2 mL DMF. The reaction mixture was then diluted in 10 mL 2:1 Water:Acetonitrile and purified via reverse phase HPLC using a semiprep column to yield a orange powder after lyophilization (9 mg, 25%).

MS-ESI (m/z): Calculated for $C_{30}H_{23}BN_2O_9S$ $[M+H]^+$ 599.39, Observed 599.13

3.6.29 Flow Cytometry Analysis of S. aureus Labeling with D-Dap-Scz/D-Phe-Scz and FPBA-FITC

S. aureus or *E. coli* from a single colony was grown overnight in LB broth at 37 ^oC with agitation. An aliquot was taken and diluted (1:100) in fresh broth and cultured for another 2 hours until the cells reached the beginning of logarithmic phase (OD_{600} ~ 0.2). Then, D-Dap-Scz or D-Phe-Scz(9 mM stock in 1X PBS, 7.4) was added to the bacterial cell culture (final concentration 0 μM, 5 μM, 25 μM, 50 μM, 100 μM, or 500 μM) and the cultures were allowed to continue to grow before 400 μL/200 μL aliquots were taken at 0.5, 1, 2 and 4 hours. The aliquots were spun down at 5000 rcf, washed once with 1 mL PBS (1X, pH 7.4), spun down again, and the cell pellet was then incubated with 50 μL of 50 μM FPBA-FITC at 37^oC for 30 minutes. The cells were spun down and washed two additional times, then diluted in 1 mL PBS (1X, pH 7.4). The cells were further diluted in PBS (1X, pH 7.4) to reach a cell density of ~$3x10^6$ cells/mL, and 300 μL aliquots were filtered through a 35 μm filter (Nalgene) before analysis on a BD FACSAria cell sorter

(BS Biosciences). Data analysis was performed with FlowJo (Tree Star, Inc.), from which the median fluorescence intensities of the stained cells were extracted.

3.6.30 Microscopy Analysis of S. aureus Cell Labeling via Fluorogenic Conjugation

S. aureus from a single colony was grown overnight in LB broth at 37 ^{o}C with agitation. An aliquot was taken and diluted (1:100) in fresh broth and cultured for another 2 hours until the cells reached the beginning of logarithmic phase (OD_{600} ~ 0.2). Then, D-Dap-Scz or D-Phe-Scz (9 mM stock in 1× PBS, 7.4) was added to the bacterial cell culture (final concentration 0 μM, 100 μM, or 500 μM) and the cultures were allowed to continue growth before 500 μL aliquots were taken at 4 hours. The aliquots were spun down at 5000 rcf, washed once with 1 mL PBS (1X, pH 7.4), spun down again, and the cell pellet was then incubated with 100 μL of 100 μM AB21/22 at 37^{o}C for 30 minutes. Parallel experiments were performed with AB24 and FPBA-FITC as controls.

For epi-fluorescence microscopy, 2 μL of the bacterial cell suspension was placed on a glass slide (Fisherfinest premium, 75 × 25 × 1 mm^3). A coverslip (Fisherbrand, 22 × 22 × 0.15 mm^3) was pressed down on the cell droplet to give a single layer of cells on the glass slides. White light and fluorescence images were taken on a Zeiss Axio Observer A1 inverted microscope equipped with a filter cube (358 nm excitation, 417-477 nm emission) suitable for detection of DAPI fluorescence. A Plan-NeoFluar × 100 oil objective from Zeiss was used to visualize the bacterial cells. All images were captured with the exposure time of 1000 ms for all D-AB3 concentrations and time points.

3.7 References

1. Kolmel, D. K. & Kool, E. T. Oximes and Hydrazones in Bioconjugation : Mechanism and Catalysis. *Chem. Rev.* **117,** 10358–10376 (2017).
2. Dirksen, A. & Dawson, P. E. Rapid Oxime and Hydrazone Ligations with Aromatic Aldehydes for Biomolecular Labeling. *Bioconjugate Chem* **19,** 2543–2548 (2008).
3. Reilly, T. P., Bellevue, F. H., Woster, P. M. & Svensson, C. K. Comparison of the In Vitro Cytotoxicity of Hydroxylamine Metabolites of Sulfamethoxazole and Dapsone. *Biochem. Pharmacol.* **55,** 803–810 (1998).
4. Schmidt, P., Stress, C. & Gillingham, D. Boronic acids facilitate rapid oxime condensations at neutral pH. *Chem. Sci.* **6,** 3329–3333 (2015).
5. Bandyopadhyay, A. & Gao, J. Iminoboronate Formation Leads to Fast and Reversible Conjugation Chemistry of α-Nucleophiles at Neutral pH. *Chem. Eur. J.* **21,** 14748–14752 (2015).
6. Dilek, O., Lei, Z., Mukherjee, K. & Bane, S. Rapid formation of a stable boron-nitrogen heterocycle in dilute, neutral aqueous solution for bioorthogonal coupling reactions. *ChemComm* **51,** 16992–16995 (2015).
7. Stress, C. J., Schmidt, P. J. & Gillingham, D. G. Comparison of boron-assisted oxime and hydrazone formations leads to the discovery of a fluorogenic variant. *Org. Biomol. Chem.* **14,** 5529–5533 (2016).
8. Wang, L., Dai, C., Burroughs, S. K., Wang, S. L. & Wang, B. Arylboronic Acid Chemistry under Electrospray Conditions. *Chem. Eur. J.* **19,** 7587–7594 (2013).
9. Bandyopadhyay, A., Cambray, S. & Gao, J. Fast Diazaborine Formation of

Semicarbazide Enables Facile Labeling of Bacterial Pathogens. *J. Am. Chem. Soc.* **139,** 871–878 (2017).

10. Cambray, S., Bandyopadhyay, A. & Gao, J. Fluorogenic diazaborine formation of semicarbazide with designed coumarin derivatives. *Chem. Comm.* **53,** 12532–12535 (2017).
11. Vollmer, W., Blanot, D. & De Pedro, M. A. Peptidoglycan structure and architecture. *FEMS Microbiol. Rev.* **32,** 149–167 (2008).
12. Vollmer, W. Bacterial outer membrane evolution via sporulation? *Nat. Chem. Biol.* **8,** 14–18 (2012).
13. Lam, H. *et al.* D-Amino Acids Govern Stationary Phase Cell Wall Remodeling in Bacteria. *Science* **325,** 1552–1556 (2009).
14. Lupoli, T. J. *et al.* Transpeptidase-Mediated Incorporation of D-Amino Acids into Bacterial Peptidoglycan. *J. Am. Chem. Soc.* **133,** 10748–10751 (2011).
15. Kuru, E. *et al.* In Situ Probing of Newly Synthesized Peptidoglycan in Live Bacteria with Fluorescent D-Amino Acids. *Angew. Chemie Int. Ed.* **51,** 12519–12523 (2012).
16. Liechti, G. W. *et al.* A new metabolic cell-wall labelling method reveals peptidoglycan in Chlamydia trachomatis. *Nature* **506,** 507–510 (2014).
17. Siegrist, M. S. *et al.* D-Amino Acid Chemical Reporters Reveal Peptidoglycan Dynamics of an Intracellular Pathogen. *ACS Chem. Biol.* **8,** 500–505 (2013).
18. Shieh, P., Siegrist, M. S., Cullen, A. J. & Bertozzi, C. R. Imaging bacterial peptidoglycan with near-infrared fluorogenic azide probes. *Proc. Natl. Acad. Sci.* **111,** 5456–5461 (2014).

19. Fura, J. M., Sabulski, M. J. & Pires, M. M. D-Amino Acid Mediated Recruitment of Endogenous Antibodies to Bacterial Surfaces. *ACS Chem. Biol.* **9,** 1480–1489 (2014).

20. Pidgeon, S. E. *et al.* Metabolic Profiling of Bacteria by Unnatural C-terminated D-Amino Acids Angewandte. *Angew. Chemie Int. Ed.* **54,** 6158–6162 (2015).

21. Sherratt, A. R. *et al.* Dual Strain-Promoted Alkyne − Nitrone Cycloadditions for Simultaneous Labeling of Bacterial Peptidoglycans. *Bioconjugate Chem* **27,** 1222–1226 (2016).

22. Fura, J. M., Kearns, D. & Pires, M. M. D -Amino Acid Probes for Penicillin Binding Protein-based Bacterial Surface Labeling. *J. Biol. Chem.* **290,** 30540–30550 (2015).

23. Chan, J., Dodani, S. C. & Chang, C. J. Reaction-based small-molecule fluorescent probes for chemoselective bioimaging. *Nat. Chem.* **4,** 973–984 (2012).

24. Jun, M. E., Roy, B. & Ahn, K. H. 'Turn-on' fluorescent sensing with 'reactive' probes. *ChemComm* **47,** 7583–7601 (2011).

25. Aron, A. T., Ramos-torres, K. M., Cotruvo, J. A. & Chang, C. J. Recognition- and Reactivity-Based Fluorescent Probes for Studying Transition Metal Signaling in Living Systems. *Acc. Chem. Res.* **48,** 2434–2442 (2015).

26. Devaraj, N. K., Hilderbrand, S., Upadhyay, R., Mazitschek, R. & Weissleder, R. Bioorthogonal Turn-On Probes for Imaging Small Molecules inside Living Cells. *Angew. Chemie Int. Ed.* **49,** 2869–2872 (2010).

27. Pitter, D. R. G. *et al.* Turn-On, Fluorescent Nuclear Stains with Live Cell Compatibility. *Org. Lett.* **15,** 1330–1333 (2013).

28. Liu, Y. *et al.* The Cation − π Interaction Enables a Halo-Tag Fluorogenic Probe for Fast No-Wash Live Cell Imaging and Gel-Free Protein Quantification. *Biochemistry* **56,** 1585–1595 (2017).

29. Razgulin, A., Rao, J. & Ma, N. Strategies for in vivo imaging of enzyme activity: an overview and recent advances. *Chem. Soc. Rev.* **40,** 4186–4216 (2011).

30. Bertozzi, C. R. A Decade of Bioorthogonal Chemistry. *Acc. Chem. Res.* **44,** 651–653 (2011).

31. Mahdavi, A. *et al.* Identification of secreted bacterial proteins by noncanonical amino acid tagging. *Proc. Natl. Acad. Sci.* **111,** 433–438 (2014).

32. Du, S. *et al.* Cell type-selective imaging and profiling of newly analogues. 8443–8446 (2017). doi:10.1039/c7cc04536k

33. Prescher, J. A. & Bertozzi, C. R. Chemistry in living systems. *Nat. Chem. Biol.* **1,** 13–21 (2005).

34. Shieh, P. & Bertozzi, C. R. Design strategies for bioorthogonal smart probes. *Org. Biomol. Chem.* **12,** 9307–9320 (2014).

35. Bandyopadhyay, A. & Gao, J. Iminoboronate-Based Peptide Cyclization That Responds to pH, Oxidation, and Small Molecule Modulators. *J. Am. Chem. Soc.* **138,** 2098–2101 (2016).

36. Bandyopadhyay, A., Cambray, S. & Gao, J. Fast and selective labeling of N-terminal cysteines at neutral pH via thiazolidino boronate formation. *Chem. Sci.* **7,** 4589–4593 (2016).

37. Jones, D. P. Radical-free biology of oxidative stress. *Am. J. Physiol. Cell Physiol.* **295,** C849–C868 (2008).

38. Sivakumar, K. *et al.* A Fluorogenic 1,3-Dipolar Cycloaddition Reaction of 3-Azidocoumarins and Acetylenes. *Org. Lett.* **6,** 4603–4606 (2004).

39. Li, J., Zhang, C., Yang, S., Yang, W. & Yang, G. A Coumarin-Based Fluorescent Probe for Selective and Sensitive Detection of Thiophenols and Its Application. *Anal. Chem.* **86,** 3037–3042 (2014).

40. Tran, T. M., Alan, Y. & Glass, T. E. A highly selective fluorescent sensor for glucosamine. *Chem. Commun.* **51,** 7915–7918 (2015).

41. Jiang, X. *et al.* Quantitative Imaging of Glutathione in Live Cells Using a Reversible Reaction-Based Ratiometric Fluorescent Probe. *ACS Chem. Biol.* **10,** 864–874 (2015).

42. Würth, C., Grabolle, M., Pauli, J., Spieles, M. & Resch-Genger, U. Relative and absolute determination of fluorescence quantum yields of transparent samples. *Nat. Protoc.* **8,** 1535 (2013).

43. Mckay, C. S. & Finn, M. G. Review Click Chemistry in Complex Mixtures: Bioorthogonal Bioconjugation. *Chem. Biol.* **21,** 1075–1101 (2014).

44. Lebar, M. D. *et al.* Reconstitution of Peptidoglycan Cross-Linking Leads to Improved Fluorescent Probes of Cell Wall Synthesis. *J. Am. Chem. Soc.* **136,** 10874–10877 (2014).

45. Bandyopadhyay, A. & Gao, J. Iminoboronate-Based Peptide Cyclization That Responds to pH, Oxidation, and Small Molecule Modulators. *J. Am. Chem. Soc.* **138,** 2098–2101 (2016).

46. Rabong, C. *et al.* NXO beta structure mimicry: an ultrashort turn/hairpin mimic that folds in water. *RSC Adv.* **4,** 21351–21360 (2014).

47. Gentsch, R. *et al.* Modular Approach toward Bioactive Fiber Meshes Carrying Oligosaccharides. *Macromolecules* **43,** 9239–9247 (2010).

48. Filice, M., Romero, O., Guisan, J. M. & Palomo, J. M. trans,trans-2,4-Hexadiene incorporation on enzymes for site-specific immobilization and fluorescent labeling. *Org. Biomol. Chem.* **9,** 5535–5540 (2011).

CHAPTER 4

Discovery of Novel APBA Dimer Peptide Sensors of Colistin Resistant Bacteria

**The work in this chapter was carried out in collaboration with Dr. Kelly A. McCarthy*

4.1 Introduction

The ESKAPE pathogens (*Enterococcus faecium*, *Staphylococcus aureus*, *Klebsiella pneumoniae*, *Acinetobacter baumannii*, *Psuedomonas aeruginosa*, *Enterobacter*) represent bacterial species with high levels of antibiotic resistance in clinical settings.[1] The gram-negative pathogens on this list have recently begun to exhibit wide ranging resistance to multiple antibiotics, making treatment of these infections extremely challenging, and causing physicians to turn to previously rejected antibiotics that show high levels of toxicity for treatment.[2]

5.1.1 Polymyxin Antibiotics

Given the current challenges associated with widespread antibiotic resistance, bacterial membranes are an attractive target for development of novel therapeutics due to their conserved structures, as well as the lack of permeability needed for these drugs since their targets reside on the exterior of the cell wall. While only a few notable membrane-targeting antibiotics exist in the clinic (eg. vancomycin, daptomycin), nature widely utilizes cationic antimicrobial peptides (CAMPs), such as the aforementioned defensins, to combat bacterial infections.[3] CAMPs generally consist of 20-50 amino acids with a net positive charge of +2 to +7 in physiological conditions, and are oftentimes amphiphilic, with over 50% of amino acids usually containing hydrophobic side chains.[4] This amphiphilic characteristic of CAMPs allows them to make crucial interactions with bacterial membranes.[5]

Cationic lipopeptide antibiotics are one subset of CAMPs that exert their bactericidal activity by selectively binding to lipopolysaccharides (LPS), which is a major lipid component of the outer membrane of Gram-negative bacteria.[6] The lipopeptides

polymyxin B and polymyxin E (eg. colistin) were isolated from the Gram-positive bacteria *Bacillus polymyxa*, and consist of a hepta-peptide ring and a tripeptide side chain with a fatty acid tail (**Figure 4-1**).[2] These polymyxins exert their bactericidal activity by specifically binding to the lipid A core of LPS with >3 times higher affinity than the natural calcium and magnesium cations that normally stabilize the LPS molecules.[7] Specifically, the short fatty acid side chain of the polymyxins interacts with the lipid region of LPS to anchor these antibiotics to the outer membrane lipid bilayer Additionally, the positively charged diaminobutyric acid (Dab) side chains of polymyxins interact with the two phosphate groups of lipid A via ionic interactions.[8,9] By binding to these LPS molecules, polymyxins are able to disrupt LPS assembly in the outer membrane of Gram-negative bacteria.

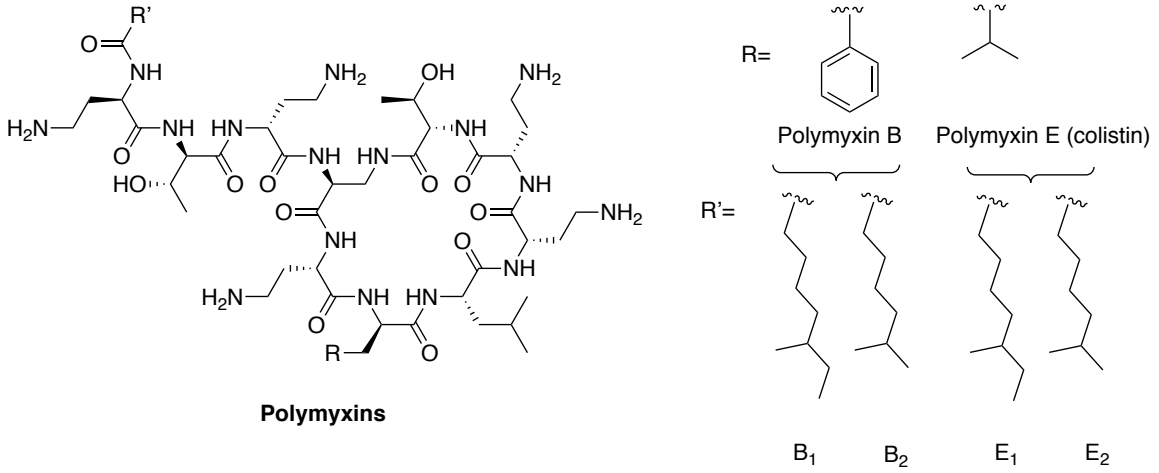

Figure 4-1. Structure of polymyxin cationic antimicrobial peptides.

Despite the effectiveness of these CAMPs, bacteria have developed mechanisms of resistance to evade killing by these membrane targeting peptide antibiotics. Since the peptides utilize electrostatic interactions driven by their cationic charge to achieve

binding and activity, Gram-negative bacteria have evolved cell surface modification strategies to increase electrostatic repulsion by enabling the addition of cationic primary amines to LPS (**Figure 4-2** and **Figure 4-3**).[6] These modifications include the addition of phosphatidylethanolamine (PE) and/or 4-aminoarabinose (Ara4N), both of which are LPS modifications implicated in the resistance of *Acinetobacter baumannii* (*A. baumannii*), as well as several other Gram-negative bacterial species, to colistin.[10] As an alternative resistance mechanism, Gram-negative colistin resistant bacteria can shut down their LOS biosynthesis and replace the outer leaflet of the outer bacterial membrane with amine-presenting lipoproteins, which eliminates the capacity for polymyxins to bind Lipid A altogether (**Figure 4-3**).[11,12]

Importantly, polymyxin antibiotics are used as antibiotics of last resort due to high levels of neuro- and renal toxicity.[13] However, the recent discovery of widespread resistance indicates that these therapeutics are not immune to development of resistance, which demands development of novel diagnostics and further identification of novel therapeutics to avoid complications as a result of the continued spread of resistance.

4.1.2 Mechanisms of Colistin Resistance

As noted, Gram-negative bacteria are capable of acquiring resistance to polymyxin antibiotics, and colistin specifically, through several different mechanisms: addition of PE to LPS, addition of Ara4N to LPS, or LOS depletion. The PE and Ara4N modifications can originate from either a plasmid-mediated mechanism via mobilized colistin resistance determinant (*mcr*-1), or via mutations in the PmrAB two-component regulatory system.

The *mcr-1* plasmid-borne gene has been detected in nearly 40 countries worldwide, with over 11 species of Enterobacteriaceae carrying this gene (eg. *E. coli*, *K. pneumoniae*, *Salmonella enterica*).[13,14] The *mcr-1* gene enables colistin resistance by encoding PE-Lipid A transferases that specifically append PE to the 1(4')-phosphate position of glucosamine on Lipid A (**Figure 4-2**). Based on the widespread nature of the gene across various bacterial species, *mcr*-1 appears to be highly transferrable. Additionally, several genetic variants (eg. *mcr*-2, *mcr*-3, *cr*-4), have been recently identified, which further highlights the threat posed by this highly transferrable mechanism of colistin resistance.

Amine-presenting modifications to LPS can also occur as a result of mutations in the PmrAB regulatory system, which lead to its constitutive activation and subsequent expression of PmrC.[15] In *A. baumannii* specifically, polymyxin resistance is controlled at the chromosomal level by the PmrA/B two-component regulatory system, in which PmrB is a membrane-localized sensor kinase that phosphorylates and activates PmrA, the cytosolic DNA-binding response regulator. Importantly, PmrA/B regulates the enzyme PmrC, which encodes the PE/Ara4N transferases that are responsible for attaching the PE group to the 4'-phosphate of Lipid A, as well as Ara4N to the 1'-phosphate. Thus, mutations that up-regulate the expression of PmrA/B also influence the expression of PmrC. Reports have elucidated that *A baumannii* with PmrB gene mutations contain Lipid A modified with both PE and Ara4N (**Figure 4-2**).[16,17] Bacterial species in which the locations of the Ara4N and PE groups (1' and 4' phosphate), are reversed, or in which both phosphates are modified with the same substituent also exist at low occurence.

Additionally, depending on the species of colistin resistant *A. baumannii*, either the PE modification alone, or both the PE and Ara4N modification may exist.

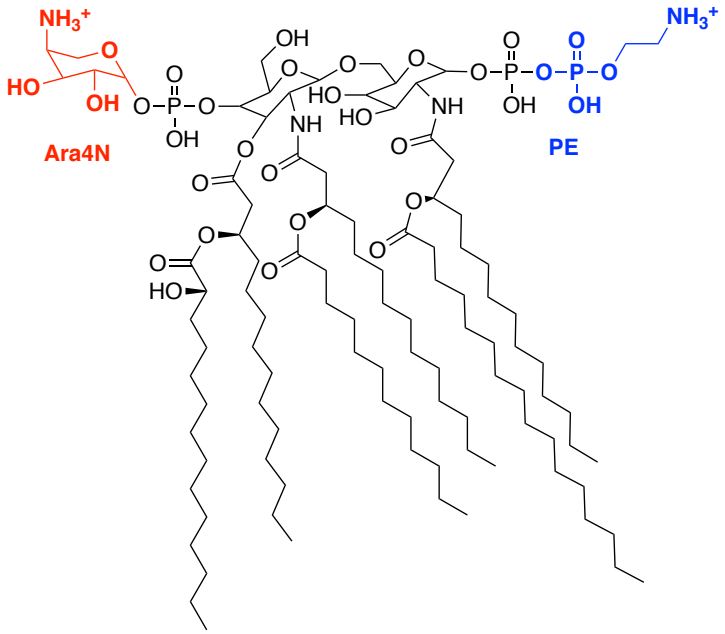

Figure 4-2. Amine presenting PE (blue) and Ara4N (red) modifications on Lipid A resulting from PmrAB mutants and *mcr-1*.

Unlike *mc-r1* and pmrAB mediated amine-presenting modifications, LOS depleted colistin resistant Gram-negative bacterial variants entirely inactivate the lipid A biosynthetic pathway to mediate resistance to polymyxins (**Figure 4-3**).[18] *A. baumannii* are one of only three (*Neisseria meningitides* and *Moraxella catarrhalis*) known Gram-negative bacteria that survive after inactivation of lipid A biosynthesis.[19] Importantly, LOS-deficient *A. baumannii* have been isolated following colistin treatment of a patient in South Korea, highlighting the potential clinical relevance of this type of bacterial cell wall modification.[20] Examination of LOS deficient *A. baumannii* strains indicates that the lack of LOS in the cell wall is compensated for by increasing the transcription of genes that encode cell-envelope biogenesis of lipoproteins and their associated transport

proteins (eg. *mla* retrograde phospholipid transporter, *lol* lipoprotein transport) to maintain an outer membrane barrier. Interestingly, the expression of PBP1 in *A. baumnnii* mitigated the development of colistin resistance in LOS deficient strains. Although LipidA biogenesis and peptidoglycan synthesis are not linked, previous analysis has shown that mutations can result in convergence of the two distinct pathways.

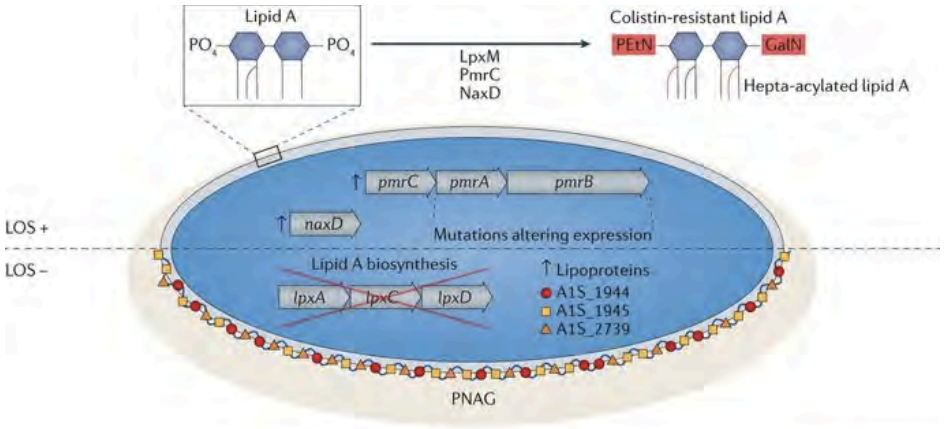

Figure 4-3. LOS deficient Gram-negative bacteria upregulate lipoprotein expression to maintain an outer membrane barrier (image from Ref.18).

These three different pathways to achieve colistin resistance that involve variations in alterations made to the outer membrane of Gram-negative bacterial species, and especially *A. baumannii*, were of interest to our group in our efforts to develop targeted peptide probes of antibiotic resistant bacterial species and strains (**Figure 4-4**).

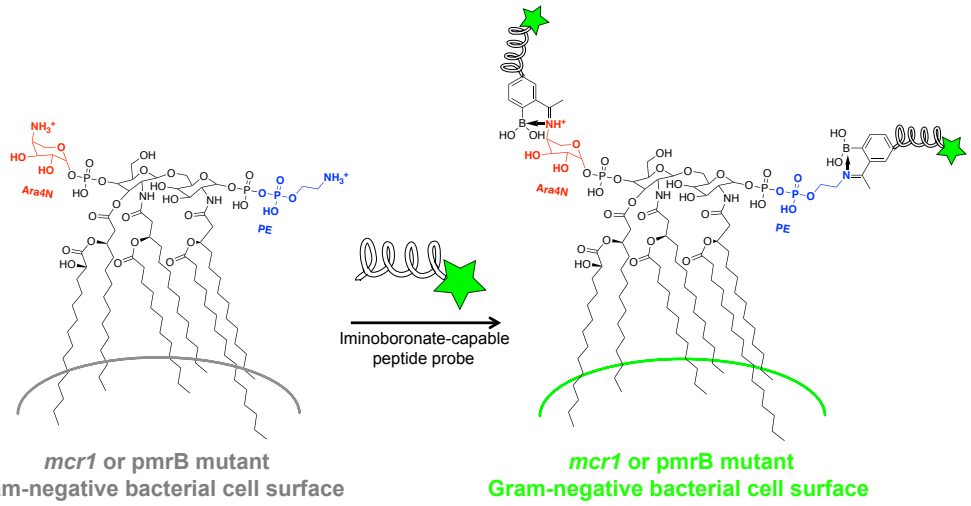

Figure 4-4. Schematic of APBA dimer peptide binding of amine-modified Gram-negative bacterial cell surfaces via pmrB and *mcr-1* mediated pathways.

4.1.3 Whole Cell Phage Screening Approach to Identify Targeted Peptide Probes of Colistin Resistance

Our group has applied an APBA dimer phage library screening approach to identify species-, as well as strain-specific peptide binders to *S. aureus* and LOS- *A. baumannii*, respectively.[21] The bacterial species *A. baumannii* is of particular interest to our research efforts as it has become increasingly more common in hospital settings, concurrent with new reported cases of colistin resistance, making it particularly relevant to clinical applications.[22] Previous work carried out by Dr. Kelly A. McCarthy led to the discovery of novel peptides (KAM20 and KAM21, **Table 4-1**) that specifically detect a strain of *A. baumannii* carrying a pmrB mutation (EGA-408) in relation to its wild type counterpart (**Figure 4-5**). Further investigation of these peptides revealed that while they efficiently differentiate between EGA-408 and the non-mutant *A. baumannii* (17978), these peptides also bind to LOS deficient *A. baumannii* (LOS-), indicating that they are not colistin resistance mechanism-specific peptide probes (**Figure 4-6**). Thus, this work

aimed to identify peptides that would act as resistance mechanism-specific probes to provide facile identification of the mechanism of colistin resistance for any bacterial sample in question.

Table 4-1. Sequences of KAM20 and KAM21 EGA-408 peptides (peptides synthesized by Dr. Kelly A. McCarthy).

Name	Peptide Sequence
KAM20	AC$_m$TNANHYFC$_m$GGGDap*
KAM21	AC$_m$YSSPSHFC$_m$GGGDap*

C$_m$= APBA-IA modified Cys; Dap*= fluorophore (FAM/TAMRA) modified Dap

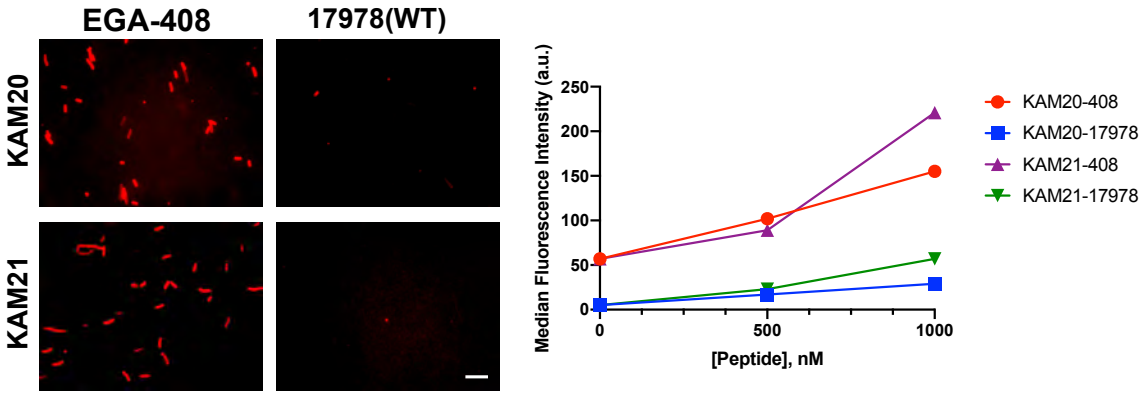

Figure 4-5. KAM20 and KAM21 are selective peptide probes for EGA-408 compared to the 17978 WT strain. Fluorescence microscopy (left) and flow cytometry (right) analysis of KAM20 and KAM21 binding to EGA-408 and 17978 (WT) *A. baumannii* (microscopy images with 2 μM peptide in presence of 1 mg/mL BSA, flow data obtained in presence of 1 mg/mL BSA, scale bar = 10 μm).

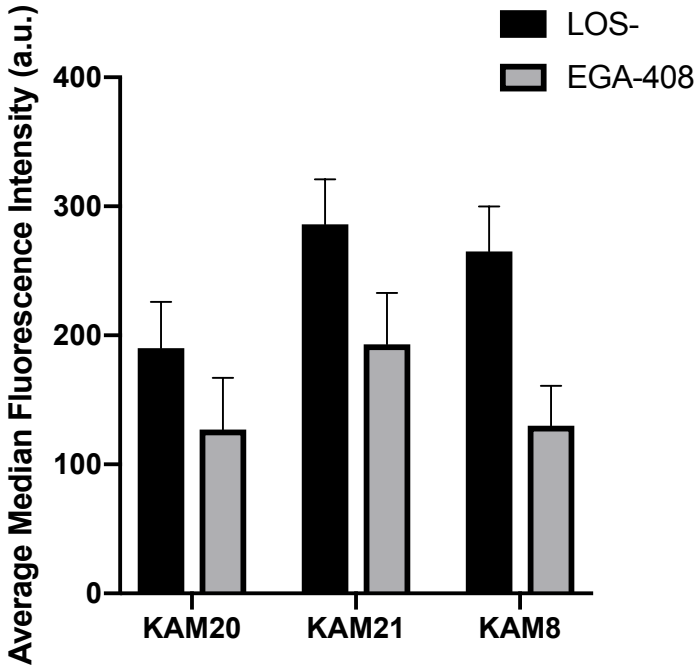

Figure 4-6. EGA-408 binding peptides KAM20 and KAM21 also bind to LOS- *A. baumannii*, as depicted by replicate flow cytometry analysis (data collected by Dr. Kelly A. McCarthy, 1000 nM peptide in presence of 1 mg/mL BSA). Error bars represent standard deviation of triplicate measurements.

Additionally, we acquired several *mcr-1* carrying Gram-negative strains of bacteria, which display amine-presenting PE modifications, similar to those of the EGA-408 strain. Thus, we also aimed to determine if pmrAB mutant detecting peptide probes would also act as probes of *mcr-1* mediated colistin resistance, given the similarities in cell surface modifications conferred by each mechanism. The strains of bacteria referenced throughout are summarized in **Table 4-2**.

Table 4-2. Summary of colistin resistant Gram-negative bacterial strains.

Strain	Species	Genotype
EGA-408	*A. baumannii*	pmrB
17978	*A. baumannii*	WT
LOS-	*A. baumannii*	LOS-
AR497	*K. pneumoniae*	mcr-1
AR496	*S. enteritiditis*	mcr-1

4.2 Negative Screen APBA Dimer Phage Library Selection of EGA-408 and LOS- Peptide Probes

4.2.1 APBA Dimer Phage Library Negative Screen Selection for Identification of EGA-408 and LOS- Specific Binders

In order to identify iminoboronate capable peptide probes that selectively bind to the EGA-408 *pmrB* mutant *A. baumannii* strain or alternatively to the LOS- *A. baumannii* strain, we devised a negative selection APBA dimer phage library screening scheme that aimed to eliminate any phage binders to the non-target strain (**Figure 4-7**).

We carried out two individual screens with the APBA dimer phage library: 1) EGA-408 positive selection with an LOS- negative selection, and 2) LOS- positive selection with an EGA-408 negative selection. Unique peptide hits from each screen were synthesized and fluorophore/APBA labeled (**Table 4-3**).

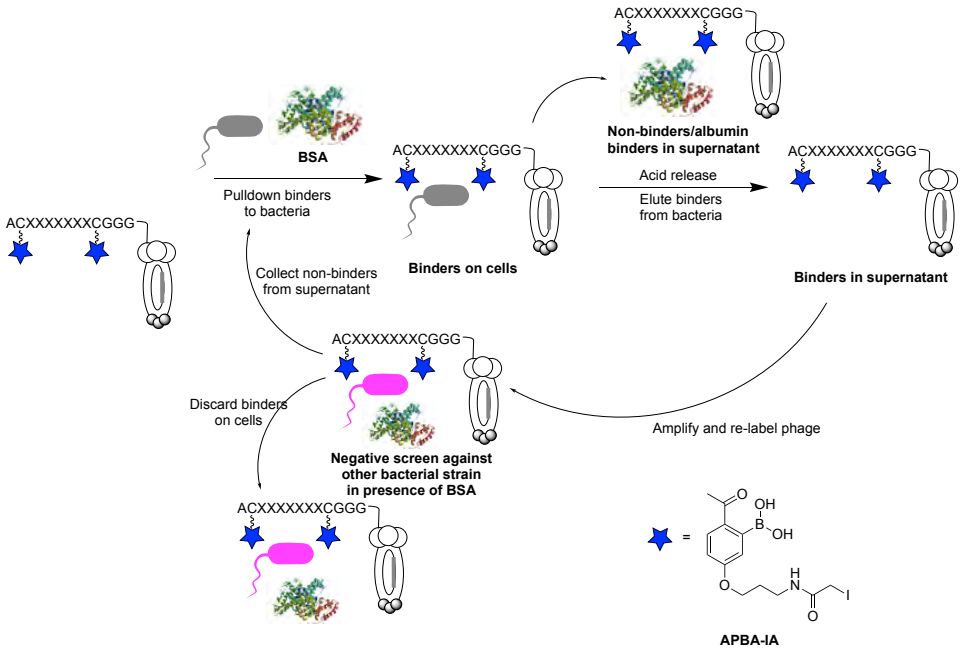

Figure 4-7. Negative screen APBA dimer phage library selection scheme.

Table 4-3. Sequences of EGA-408, LOS- and control peptides.

Peptide	Sequence	Screen
SEC5	$AC_mKPLHSRSC_mGGGDap^*$	EGA-408
SEC6	$AC_mFLEYAPTC_mGGGDap^*$	EGA-408
SEC8	$AC_mSIIPEKYC_mGGGDap^*$	LOS-
SEC9	$AC_mGSFWSLTC_mGGGDap^*$	LOS-
SEC14	$AC_mPLTAVISC_mGGGDap^*$	Naïve Library

C_m= APBA-IA modified Cys; Dap*= fluorophore (FAM/TAMRA) modified Dap

4.2.2 Analysis of EGA-408 and LOS- Binding of Peptide Hits

To analyze the specificity of *A. baumannii* binding for each of the peptide hits, the peptides were assessed by both microscopy and flow cytometry. Fluorescence microscopy studies first showed that while SEC8 and SEC9, the peptides extracted from the LOS- specific screen, were indeed selective for LOS- binding in comparison to EGA-408, the EGA-408 peptides, SEC5 and SEC6, exhibited binding to both strains, and thus lacked the desired strain selectivity (**Figure 4-8**).

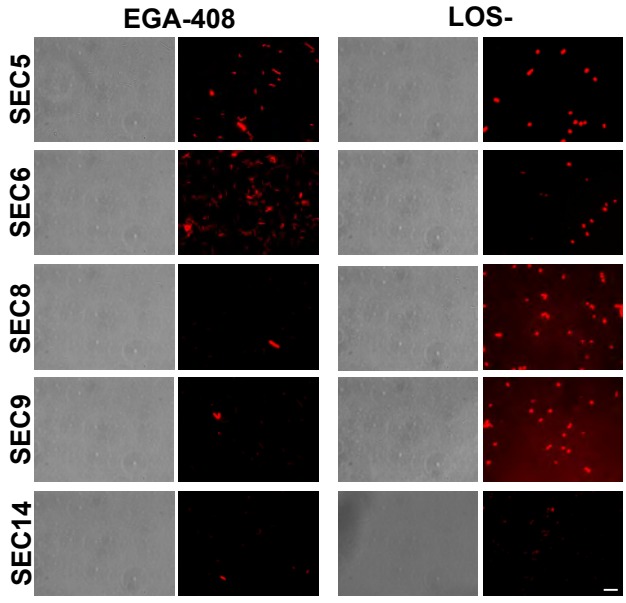

Figure 4-8. Fluorescence microscopy analysis of EGA-408 and LOS- binding of SEC5, SEC6, SEC8, SEC9 and SEC14 (2 μM peptide, 1 mg/mL BSA, scale bar = 10 μm).

The selectivity of the LOS- peptides, and lack thereof of the EGA-408 peptides was confirmed by flow cytometry (**Figure 4-9**). In comparison to a negative control peptide (SEC14) extracted from a naïve phage library, the EGA-408 and LOS- peptides display clear binding to the *A. baumannii* colistin resistant strains. Also compared to KAM8, a peptide previously extracted from a screen directly against LOS-[21], the SEC8 and SEC9 peptides display a marked improvement in LOS- specific binding.

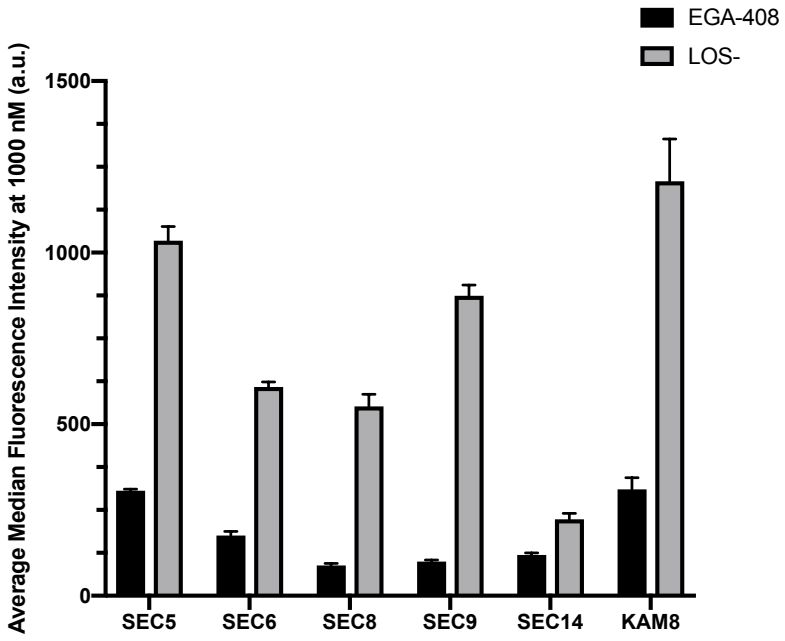

Figure 4-9. Flow cytometry analysis of EGA-408 and LOS- binding of SEC5, SEC6, SEC8, SEC9, SEC14 and KAM8 (1 μM peptide, 1 mg/mL BSA). Error bars represent standard deviation of triplicate measurements.

4.2.3 Selectivity of SEC5 for Binding EGA-408 in Comparison to WT (17978) A. baumannii

Intrigued by the lack of specificity of SEC5 for binding to EGA-408 in comparison to the LOS- *A. baumannii* strain, we aimed to assess the selectivity of this

peptide in comparison to WT strain binding. The WT strain from which EGA-408 was derived does not carry the *pmrB* mutation, and thus is not anticipated to display either of the amine presenting cell surface modifications to which the SEC5 peptide should be selectively binding. Consistent with our hypothesis, SEC5 displays selective binding to EGA-408 over the WT strain, as assessed by fluorescence microscopy and flow cytometry (**Figure 4-10**). Additionally, a co-culture experiment carried out with an increasing ratio of the EGA-408 strain relative to 17978 (WT) exhibited an increase in the proportion of cells fluorescently labeled consistent with the proportion of EGA-408 cells in the mixture in the presence of human serum (**Figure 4-11**).

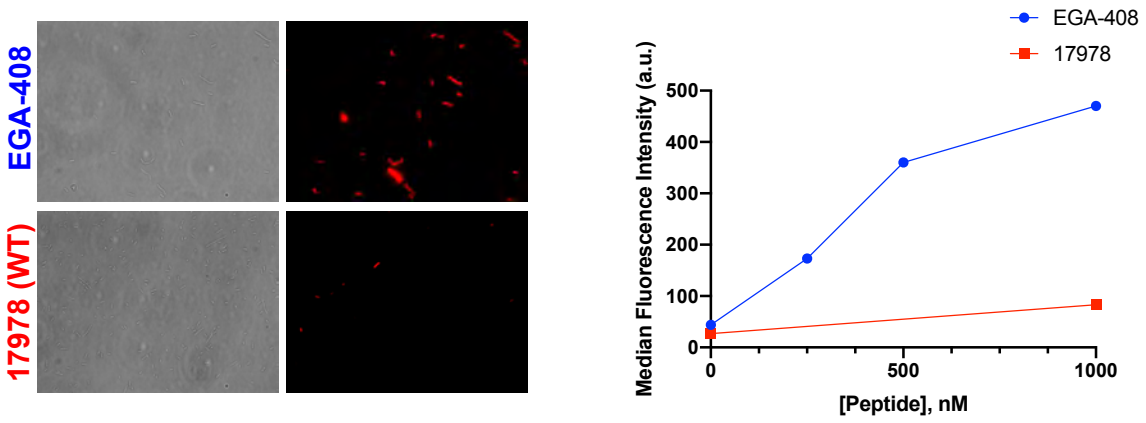

Figure 4-10. SEC5 displays selective binding to EGA-408 over 17978. Fluorescence microscopy (left) and flow cytometry (right) analysis of SEC5 binding to EGA-408 and 17978 (2 μM peptide for microscopy, 1 mg/mL BSA for microscopy and flow cytometry).

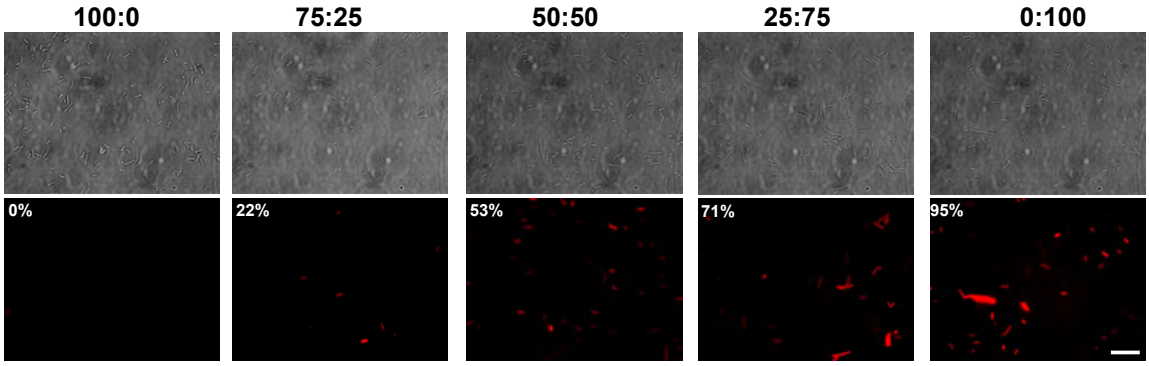

Figure 4-11. Varying ratios of 17978:EGA-408 co-cultures labeled with SEC5-TAMRA. Percentage of stained cells shown in left corner of fluorescence images (2 μM peptide, 20% human serum, scale bar = 10 μm).

Together, the fluorescence microscopy and flow cytometry data show that while SEC5 is specific for EGA-408 binding in comparison to the wild type *A. baumannii* strain, identification of peptides that do not bind to the LOS- strain of *A. baumannii* is much more challenging. Given the overexpression of lipoproteins on the surface of these bacteria, it is possible that the lipoproteins may present a sticky surface for the non-specific binding of our APBA handles, which may prohibit the identification of binding selectivity conferred by unique peptide sequences. Nonetheless, implementation of a negative screen selection was successful in development of peptides that display weakened binding to an alternative *A. baumannii* strain, EGA-408.

4.3 mcr-1 AR497 Phage APBA Dimer Screening Selection

As an alternative to the pmrB and LOS- mechanisms of colistin resistance, we acquired several alternative Gram-negative colistin resistant bacterial strains that carry the *mcr-1* gene, which upregulates PE Lipid A modifications in the bacterial cell walls (**Table 4-2**). Given our knowledge with the screening of EGA-408 and LOS- towards development of strain specific peptide binders, we were interested to determine if a

peptide selected to bind to one of the *mcr-1* carrying strains would display similar binding affinity to the other *mcr-1* strains given the similarities in cell surface modifications.

4.3.1 APBA Dimer Phage Library Screening Against AR497

The APBA dimer phage library was screened directly against the AR497 *K. pneumoniae* strain, which yielded several repeating peptide hits that were subsequently synthesized and labeled with FAM/TAMRA and APBA (**Table 4-4**). This screen differed from the EGA-408/LOS- screen in that no negative selections were carried out, as the aim of this experiment was to determine if peptides that bind to one *mcr-1* carrying Gram-negative bacterial strain are capable of binding to alternative *mcr-1* carrying strains.

Table 4-4. Sequences of AR497 peptides.

Peptide	Sequence
SEC18	$AC_mSERQHLQC_mGGGDap*$
SEC19	$AC_mRSHDSAMC_mGGGDap*$
SEC20	$AC_mLATKGSIC_mGGGDap*$

C_m= APBA-IA modified Cys; Dap*= fluorophore (FAM/TAMRA) modified Dap

4.3.2 Analysis of SEC18-20 Binding to mcr-1 Carrying Gram-Negative Bacterial Strains

Fluorescence microscopy of the TAMRA labeled peptides revealed that while SEC18-20 exhibit strong binding to the AR497 *K. pneumoniae* strain as expected, their binding to the alternative *mcr-1* carrying strains is diminished (**Figure 4-12**). These results were confirmed by replicate flow cytometry analysis, whereby the SEC18 and SEC19 peptides exhibit concentration-dependent binding up to ~1000 a.u. at 1000 nM, whereas the median fluorescence intensity values for AR493 (*E. coli*) and AR496

(*Salmonella enteritiditis*) were ~3-4x less at the same concentrations (**Figure 4-13**, **Figure 4-14**). Thus, while the peptides do exhibit binding to the varying *mcr-1* carrying bacterial strains, there is a significant difference in fluorescence intensity imparted by the variations on the species level.

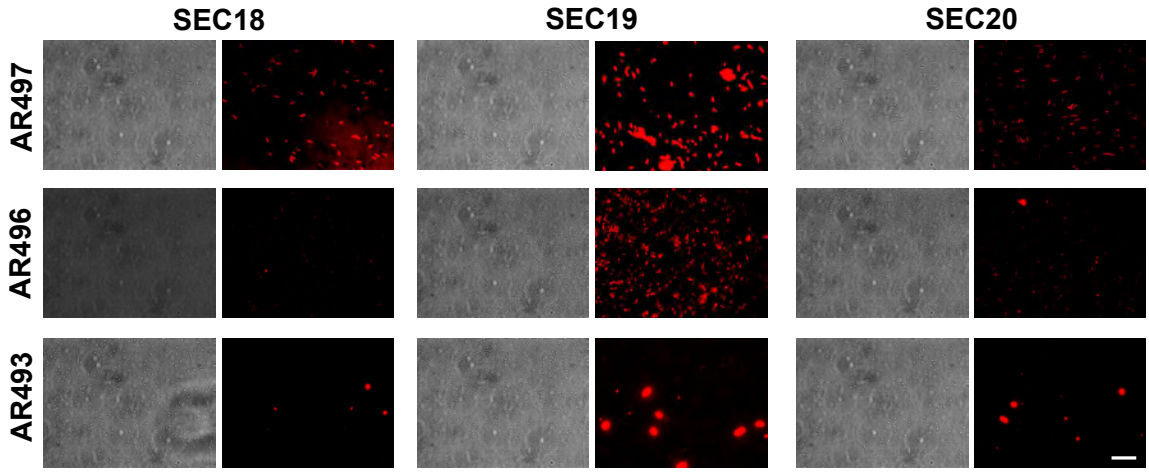

Figure 4-12. Fluorescence microscopy analysis of the binding of SEC18, SEC19 and SEC20 to AR493, AR496 and AR497 (2 μM peptide, 1 mg/mL BSA, scale bar = 10 μm).

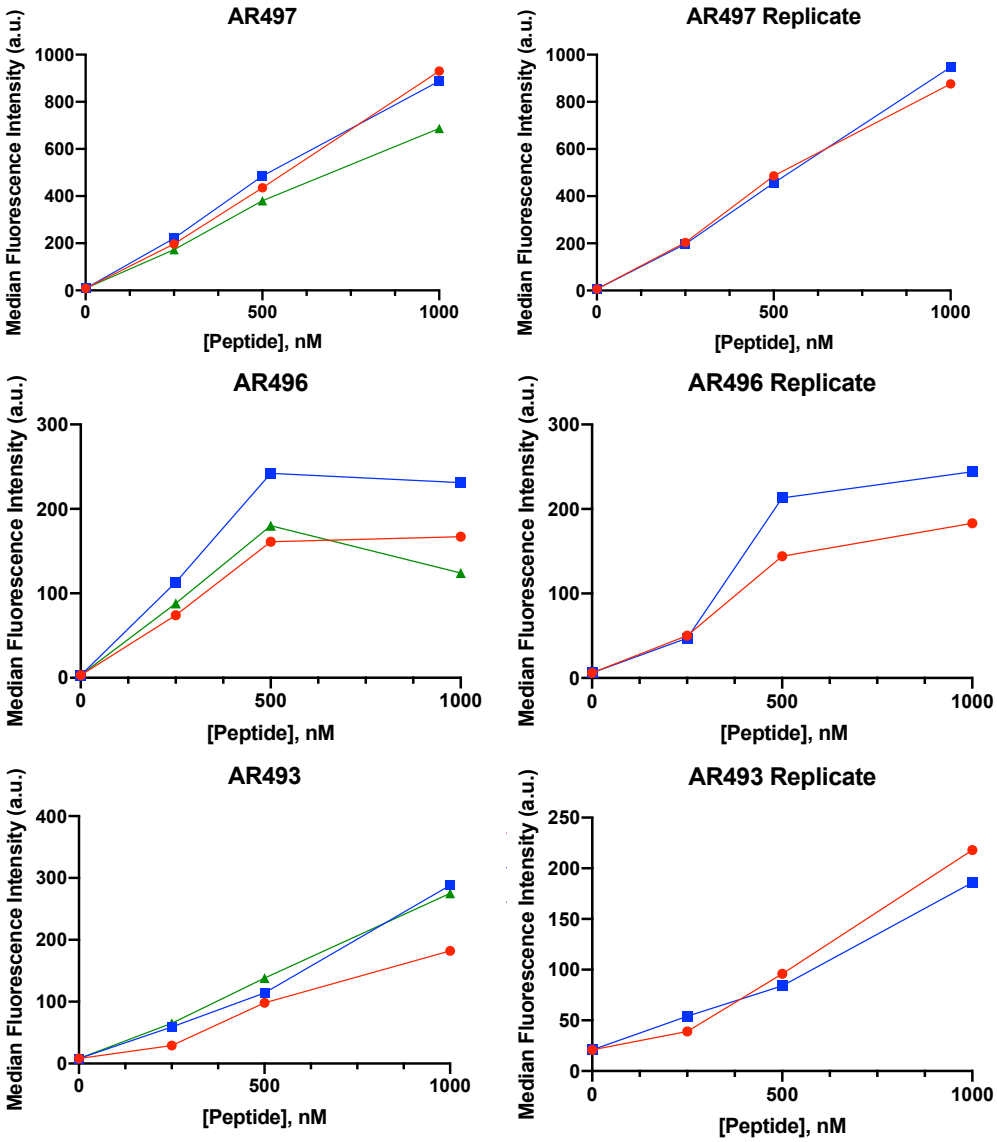

Figure 4-13. Flow cytometry analysis of the binding of SEC18 (red), SEC19 (blue) and SEC20 (green) to AR493, AR496 and AR497. All samples contain 1 mg/mL BSA. Replicates of SEC18 and SEC19 were obtained.

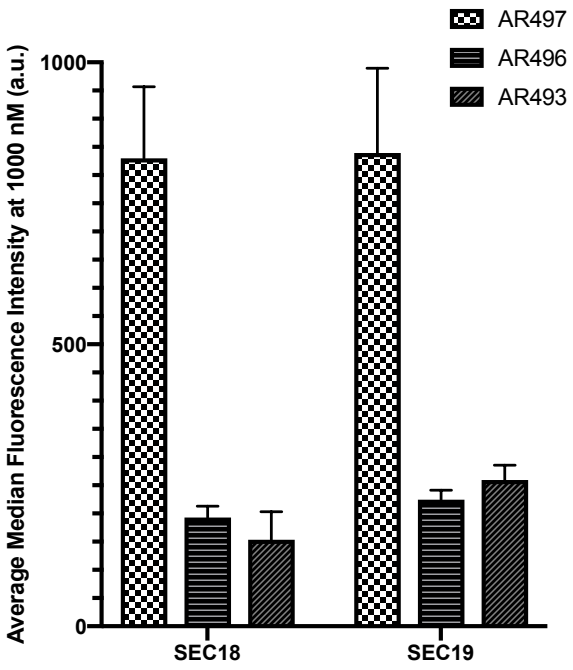

Figure 4-14. Average median fluorescence intensity of 1000 nM SEC18 and SEC19 binding to AR493, AR496 and AR497. Error bars represent standard deviation of triplicate readings. Measurements carried out in the presence of 1 mg/mL BSA.

4.4 Cross Analysis of mcr-1 and pmrB Peptide Binders

Intrigued by the lack of cross-species peptide binding exhibited by the *mcr-1* selected peptides, we aimed to determine if the EGA-408 and *mcr-1* peptides would display any cross-strain binding capabilities given the overlap in modifications enabled by the *mcr-1* gene and *pmrB* gene mutations, respectively.

5.4.1 Flow Cytometry Analysis of SEC5 and SEC18-29 Binding to EGA-408, AR497, AR496 and AR493

Flow cytometry analysis of the binding of SEC5, a peptide selected for EGA-408 binding, and the SEC18/19, peptides selected for AR497 binding display the cross-reactivity of peptides for binding to strains carrying plasmids or mutations that up-regulate amine presenting cell surface modifications, such as phosphatidylethanolamine

(**Figure 4-15**). Interestingly, all peptides show strongest binding to the AR497 strain, which may indicate either a greater presence of these amine-presenting modifications on the cell surface, or alternative cell surface features that promote binding of these amine-targeting peptides. SEC5, the peptide selected for EGA-408 binding, also displays significant binding to the *mcr-1* carrying strains, especially in comparison to the *A. baumannii* WT strain 17978. SEC18 and SEC19 also display binding to the EGA-408 strain. Importantly, the control peptide, SEC14, displays no significant binding to any of the strains. Thus, it appears that the peptides identified are general sensors of similar mechanisms of colistin resistance that append amine presenting groups to Lipid A in the cell wall of a variety of Gram-negative bacterial species.

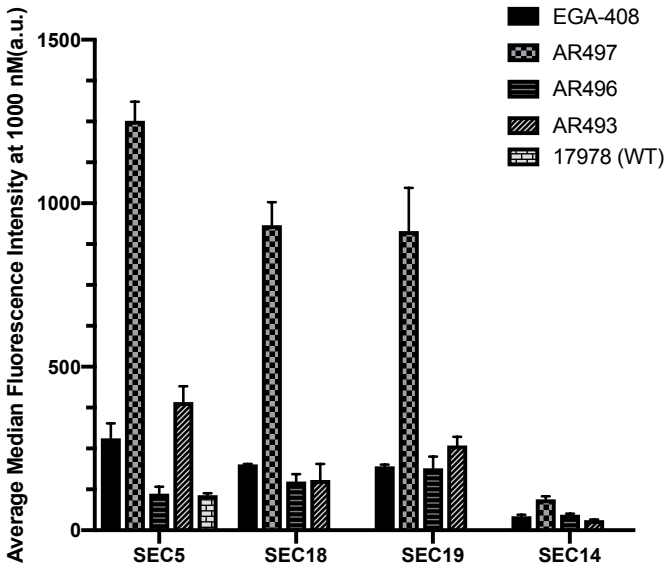

Figure 4-15. Average median fluorescence intensity of 1000 nM SEC5, SEC18, SEC19 and SEC14 binding to EGA-408, AR493, AR496, AR497 and 17978 (*A. baumannii* WT). Error bars represent standard deviation of triplicate readings. Measurements carried out in the presence of 1 mg/mL BSA.

To assess the significance of the median fluorescence intensity readouts for the *mcr-1* carrying strains AR496 and AR493, two *K. pneumoniae* strains that do not have

any amine-presenting modifications on their surfaces were used as controls to assess peptide binding readouts relative to background fluorescence. Fluorescence microscopy analysis (**Figure 4-16**) shows a distinct difference in binding of the SEC5, SEC18 and SEC19 peptides to the mutant amine-presenting modification containing strain, AR497, and a strain that contains no such mutation (AR347), as well as a wild-type *K. pneumoniae* strain. Assessing the binding by flow cytometry shows that while SEC5, SEC18 and SEC19 exhibit diminished binding in comparison to AR497, the fluorescence intensity readout is higher than that of these other strains, indicating that the peptides do bind, although at lower affinity (**Figure 4-17**). This could be a result in a differing number of PE modifications on the cell surfaces, or alternative cell surface features that contribute to peptide binding. Nonetheless, these peptides remain selective for binding colistin-resistant strains of bacteria, as desired.

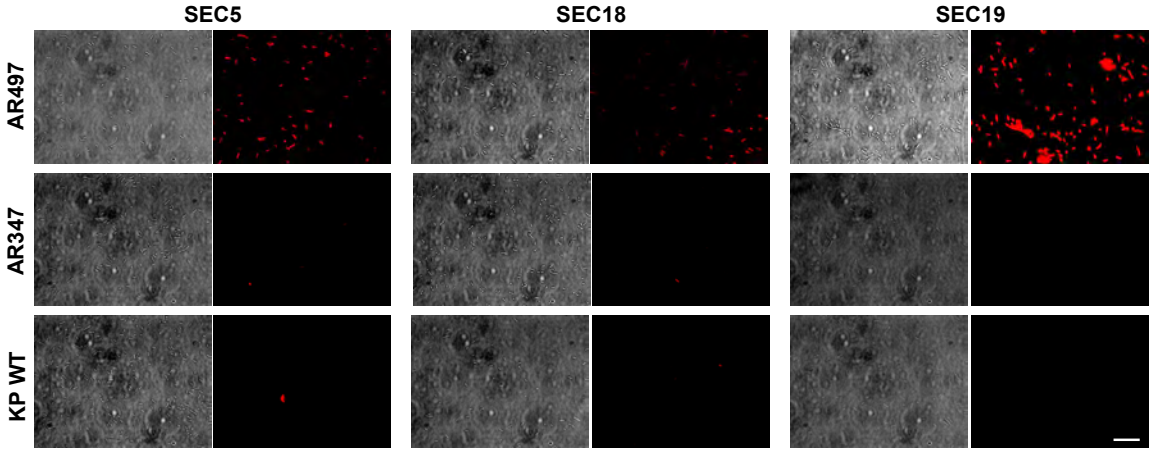

Figure 4-16. Fluorescence microscopy analysis of the binding of SEC5, SEC18 and SEC19 to AR497, AR347 and WT *K. pneumoniae* (2 μM peptide, 1 mg/mL BSA, scale bar = 10 μm).

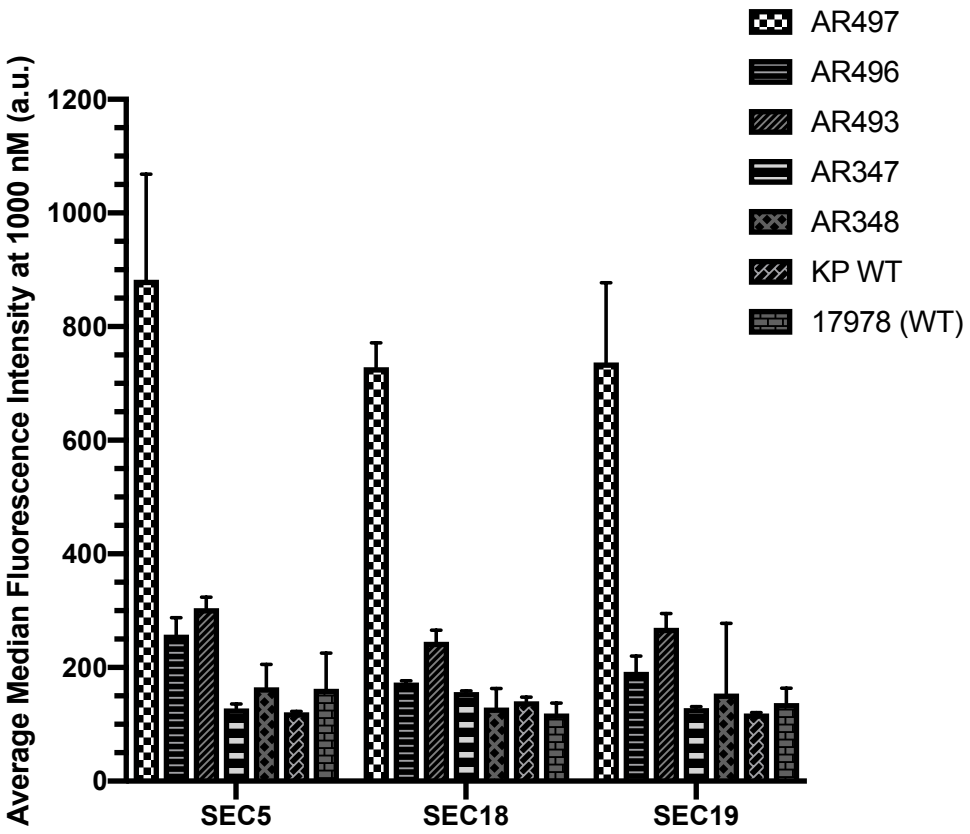

Figure 4-17. Average median fluorescence intensity of 1000 nM SEC5, SEC18, SEC19 and SEC14 binding to AR497, AR493, AR496, AR347, AR348, WT *K. pneumoniae* and 17978 (*A. baumannii* WT). Error bars represent standard deviation of triplicate readings. Measurements carried out in the presence of 1 mg/mL BSA.

4.5 Conclusions

The APBA dimer library phage display screening platform was successful in identifying peptides that selectively bind to Gram-negative bacterial strains of interest that harness mutations or genes which cause the expression of amine-presenting Lipid A modifications on the cell surface. For example, the peptide SEC5, which was initially selected for EGA-408 binding, displays robust binding to the *A. baumannii* strain EGA-408, but no binding to the WT *A. baumannii* strain, which displays no amine-presenting Lipid A modifications.

The LOS- *A. baumannii* strain presented a challenge for the development of strain selective peptide probes of EGA-408 in that all the EGA-408 selected peptides also showed significant binding to the LOS- strain, even with negative selection against the LOS- strain during phage library screening. On the other hand, selection of LOS- selective peptides was successful, as SEC8 and SEC9 display targeted LOS- binding in comparison to EGA-408. Therefore, the overexpression of lipoproteins on the surface of the LOS- strain may make the cells capable of binding strongly to APBA dimer peptides that were selected for *A. baumannii* binding in general.

We also explored the identification of peptide probes for alternative mechanisms of colistin resistance, such as *mcr-1*. Screening of a *K. pneumoniae* strain carrying *mcr-1* revealed several peptides that also exhibited binding to alternative *mcr-1* carrying strains, although at lower fluorescence intensity. Interestingly, SEC5, an EGA-408 derived peptide, also exhibited strong binding to AR497, which may indicate the presence of a larger proportion of Lipid A PE modifications relative to the other species of *mcr-1* carrying Gram-negative bacteria, AR493 and AR496. Nonetheless, these results imply a capacity for cross-reactivity of these peptides for detecting PE Lipid A modifications presented by a variety of colistin resistant Gram-negative bacteria. Thus, while the phage screening platform enables isolation of peptides that are selective for identification of colistin-resistant versus colistin-sensitive strains of bacteria, these peptides may also be able to be extended to alternative species and mechanisms of resistance that cause the same types of modifications to be made to the bacterial surfaces.

4.6 Experimental Procedures

4.6.1 General Methods

The Ph.D.™-C7C Phage Display Peptide Library Kit and the *E. coli* K12 ER2738 strain were purchased from New England Biolabs. The *E. coli* K12 ER2738 used for amplification and titering steps was grown on LB+Tetracycline plates prior to culturing in LB media. All reagents used for panning were made and used in accordance with the NEB Ph.D.™ Phage Display Libraries Instruction Manual. The *A. baumannii* EGA-408, *A. baumannii* LOS-, *A. baumannii* 17978, *K. pneumoniae* AR497, *E. coli* AR493 and *S. enteritiditis* AR493, *E. coli* AR348 and *K. pneumoniae* AR347 strains were provided by the laboratory of Prof. Tim van Opijnen at Boston College. The *K. pneumoniae* WT strain (ATCC 4352) was purchased from ATCC as a lyophilized cell pellet. All strains were grown in LB media, while the EGA-408 strain was additionally grown in the presence of 8 μg/mL colistin.

All amino acids and Rink-Amide resin were purchased from Creosalus, Chem Impex International and EMD Millipore. All reagents for peptide synthesis, including dimethylformamide, dichloromethane N-methylmorpholine, triisopropylsilane and piperidine were purchased from Fisher Scientific. Trifluoroacetic acid was purchased from Protein Technologies. Peptide synthesis was carried out on a Tribute peptide synthesizer, and peptides were purified via RP-HPLC on a Waters Prep LC with a Jupiter C18 column (Phenomenex) with water/acetonitrile and 0.1% TFA as eluent (Buffer A=95% water, 5% acetonitrile, 0.1% TFA; Buffer B= 95% acetonitrile, 5% water, 0.1% TFA) with a gradient to 60% Buffer B. The peptide concentration of all fluorescent peptide stocks (made in DMSO) was determined by measuring their absorbance at 495

nm for fluorescein (E=75,000 $M^{-1}cm^{-1}$) or 556 nm for TAMRA (E=89,000 $M^{-1}cm^{-1}$) on a Nanodrop 2000c UV-Vis spectrometer.

Fluorescence images were obtained on a Zeiss Axio Observer A1 inverted microscope with rhodamine filter. Flow cytometry analysis was performed on a BD FACSAria cell sorter by Dr. Patrick Autissier in the Biology department at Boston College.

4.6.2 APBA Dimer Phage Library Screening Against EGA-408, LOS- and AR497

For all phage display panning experiments, 3 μL (~$1x10^{10}$ pfu) of the C7C library was diluted into 172 μL of 1X PBS pH 9.0 with 25 μL iTCEP and stirred for 48 hours at 4°C. The reduced C7C library was then labeled with 2 mM APBA-IA (synthesized as previously reported, stored at 200 mM in DMSO)[23] and stirred at room temperature for 2 hours. The iTCEP mixture was then centrifuged, and the APBA-IA labeled phage-containing supernatant was collected. The phage precipitated with 1/5 volume of 20% PEG8000/2.5M NaCl on ice for 5 hours. The mixture was centrifuged at 14,000 rpm at 4°C for 30 minutes. The APBA-IA labeled phage was then dissolved in 100 μL of PBS pH 7.4 and used for phage panning experiments.

For the negative screens against EGA-408 and LOS-, EGA-408 and LOS- were grown to an OD_{600}≈1.0 (~$1x10^9$ cfu/mL) in LB media. For the first round, a 1 mL aliquot of cells (aliquoted into a 10 mg/mL BSA in 1X PBS pH 7.4 in a pre-blocked eppendorf tube) was washed twice with chilled PBST (0.05%), then re-suspended in 1X PBS pH 7.4 with 10 mg/mL BSA (950 μL) and incubated on ice for 0.5 hours. 50 μL of the APBA-labeled phage library was added to the cell suspension, which was incubated on ice for 1 hour. The cells were then washed 3 times with PBST (0.05%) and 3 times with PBS to

remove unbound phage. Cell-bound phage were incubated with 200 μL elution buffer (glycine-HCl, pH 2.2, 1 mg/mL BSA) for 15 minutes, followed by cell centrifugation at 5000 rcf for 5 minutes. The supernatant containing the eluted phage was then removed and neutralized with 150 μL Tris-HCl (pH 9.1). The eluted phage solution was added to early log phase ER2738 and amplified 5 hours, followed by precipitation to isolate the amplified phage, which was again subjected to APBA-IA labeling protocols. In the second and third rounds, the APBA labeled phage library was first incubated with the negative screen species of bacteria for 1 hour on ice as described above. The cells were then centrifuged at 5000 rcf for 5 minutes, and the phage-containing supernatant was then directly removed and added to a washed cell pellet of the positive screen bacterial species. The remainder of the panning protocol was kept consistent. The phage titer was calculated before and after each round of panning with LB/IPTG/Xgal plating to determine input and output populations. Individual phage colonies from the third round of panning were amplified in ER2738, then phage DNA was isolated using a GeneJet MiniPrep kit and sent for sequencing analysis to Eton Bioscience, Inc. The screen against AR497 was carried out similarly, except with no negative selection step.

Table 4-5. Sequencing analysis of EGA-408 positive/LOS- negative selection (sequences chosen for peptide synthesis shown in bold).

Hit #	DNA Sequence	Peptide Sequence
1	GCTTGTGATCAGCGGGATGATAGGTTTTGC	ACDQRDDRFC
2	n/a	Blank
3	n/a	Blank
4	n/a	Blank
5	n/a	Blank
6	n/a	Blank
7	GCTTGTGGGTGGATGAATGGTCATCATTGC	ACGWMNGHHC
8	n/a	Blank
9	n/a	Blank
10	n/a	Blank
11	GCTTGTATGCGGGCTGGTTCTCATAATTGC	ACMRAGSHNC
12	n/a	Blank
13	n/a	Blank
14	GCTTGTAAGCCGCTGCATTCGAGGTCGTGC	**ACKPLHSRSC**
15	n/a	Blank
16	n/a	Blank
17	GCTTGTCCGGCGCTTGAGAAGGCTAATTGC	ACPALEKANC
18	n/a	Blank
19	n/a	Blank
20	GCTTGTCCTCAGAGTAATTTTAAGTCTTGC	ACPQSNFKSC
21	n/a	Blank
22	GCTTGTAGTGCTGGGCCGACGTTGAATTGC	ACSAGPTLNC
23	GCTTGTTTTCTTGAGTATGCTCCGACTTGC	**ACFLEYAPTC**
24	GCTTGTACTAAGGATCTTACGATGCGTTGC	ACTKDLTMRC
25	n/a	Blank

26	n/a	Blank
27	GCTTGTCTGGATAGTCCTATTACTTCTTGC	ACLDSPITSC
28	GCTTGTAAGCCGCTGCATTCGAGGTCGTGC	**ACKPLHSRSC**
29	GCTTGTGATCAGCGGGATGATAGGTTTTGC	ACDQRDDRFC
30	GCTTGTCAGAGTGAGATGCGTGAGTCGTGC	ACQSEMRESC
31	GCTTGTGATCAGCGGGATGATAGGTTTTGC	ACDQRDDRFC
32	GCTTGTGTTGATCCGCATCCGAGGACTTGC	ACVDPHPRTC
33	GCTTGTTGGGGTGGGGGTTTTAGTAGTTGC	ACWGGGFSSC
34	GCTTGTCTGAATACTAATGTTAATCATTGC	ACLNTNNVNHC
35	GCTTGTGATCTTTGGGGTGCTCGTACGTGC	ACDLWGARTC
36	GCTTGTATGCGGGCTGGTTCTCATAATTGC	ACMRAGSHNC
37	GCTTGTGCTCCGAATAATCGTCTTCAGTGC	ACAPNNRLQC
38	GCTTGTGATCTGACGAGTTATGAGTGGTGC	ACDLTSYEWC
39	GCTTGTTCGTATAGTCGGGATTTGACTTGC	ACSYSRDLTC
40	n/a	Blank

Table 4-6. Sequencing analysis of LOS- positive/EGA-408 negative selection (sequences chosen for peptide synthesis shown in bold).

Hit #	DNA Sequence	Peptide Sequence
1	GCTTGTGCTCCGAATTCGCATAAGGATTGC	ACAPNSHKDC
2	n/a	Blank
3	n/a	Blank
4	GCTTGTGAGGGTGCGGTGGGTCCTGCGTGC	ACEGAVGPAC
5	n/a	Blank
6	GCTTGTTATCCTTATTCTCTTTCTCAGTGC	ACYPYSLSQC
7	GCTTGTACGAATCTGGTTTATCAGCAGTGC	ACTNLVYQQC
8	GCTTGTCATCTTCCGCCTTCGCATTATTGC	ACHLPPSHYC
9	GCTTGTTCGAATCCGCAGTCTTATAAGTGC	ACSNPQSYKC
10	GCTTGTGGTCCGTATCCGGGGAGGGTTTGC	ACGPYPGRVC
11	n/a	Blank
12	GCTTGTTCGAAGTATCCTCGTGAGATGTGC	ACSKYPREMC
13	GCTTGTGGTCCGCGGGCTGCTACTTCTTGC	ACGPRAATSC
14	n/a	Blank
15	GCTTGTGTGCGTACGCTGTCGCCGTTTTGC	ACVRTLSPFC
16	GCTTGTGTTGATCCGCATCCGAGGACTTGC	ACVDPHRPTC
17	GCTTGTGCTCCGAATAATCGTCTTCAGTGC	ACAPNNRLQC
18	n/a	Blank
19	GCTTGTAATCAGTGGTTGACGCAGAATTGC	ACNQWLTQNC
20	n/a	Blank
21	GCTTGTATGCGGGCTGGTTCTCATAATTGC	ACMRAGSHNC
22	GCTTGTAATAAGAAGGTGGGTAAGCATTGC	ACNKKVGKHC
23	GCTTGTGATCAGCGGGATGATAGGTTTTGC	ACDQRDDRFC
24	GCTTGTACGTCTCCGGAGCGGTATTCGTGC	ACTSPERYSC
25	GCTTGTTCGATTATTCCGGAGAAGTATTGC	**ACSIIPEKYC**

26	GCTTGTGATCAGCGGGATGATAGGTTTTGC	ACDQRDDRFC
27	GCTTGTGCTCCGAATAATCGTCTTCAGTGC	ACAPNNRLQC
28	n/a	Blank
29	GCTTGTGCTCCGAATAATCGTCTTCAGTGC	ACSSTGLSKC
30	n/a	Blank
31	GCTTGTAATACGAAGATGGGTAAGACTTGC	ACNTKMGKTC
32	GCTTGTGATCAGCGGGATGATAGGTTTTGC	ACDQRDDRFC
33	GCTTGTGGGTCTTTTTGGTCGCTGACGTGC	**ACGSFWSLTC**
34	n/a	Blank
35	GCTTGTGTTGATCCGCATCCGAGGACTTGC	ACVDPHPRTC
36	GCTTGTGTTGATCCGCATCCGAGGACTTGC	ACVDPHPRTC
37	n/a	Blank
38	GCTTGTAAGATTAGTTCGTTTACTCAGTGC	ACKISSFTQC
39	GCTTGTCCTTTGGCTCCGATGCCGGCGTGC	ACPLAPMPAC
40	n/a	Blank

Table 4-7. Sequencing analysis of the naïve C7C library (sequences chosen for peptide synthesis shown in bold).

Hit #	DNA Sequence	Peptide Sequence
1	GCTTGTGTGCGTGCGTATGATGGTATTTGC	ACVRAYDGIC
2	n/a	Blank
3	GCTTGTGATGGTAAGTATATTCAGAATTGC	ACDGKYIQNC
4	GCTTGTCCGAAGAGTATGTTGCCTTGGTGC	ACKSMLPWC
5	GCTTGTTAGGTGGATGGTTCTCCTCGGTGC	ACQVDGSPRC
6	GCTTGTGTTTCGACTTGGCTGACTTCTTGC	ACVSTWLTSC
7	GCTTGTACTATTCCTGGTATTGATACGTGC	ACTIPGIDTC
8	GCTTGTCCGCTTACGGCGGTTATTTCTTGC	**ACPLTAVISC**
9	GCTTGTAGTCATGGTCATTAGGCTCAGTGC	ACSHGHQAQC
10	GCTTGTACGAATCCGCCTACGGCGTCTTGC	ACTNPPTASC
11	GCTTGTCAGATGGCTCCGACGGATGGTTGC	ACQMAPTDGC
12	GCTTGTCTGGCGACTAAGACTGCTGGTTGC	**ACLATKTAGC**
13	GCTTGTCCTGCTTATACGTCTCATGCGTGC	ACPAYTSHAC
14	GCTTGTAATCTGTCTACGGCGCATGCTTGC	ACNLSTAHAC
15	GCTTGTCAGATTACTGGGTTTTTGAGGTGC	ACQITGFLRC
16	n/a	Blank
17	GCTTGTCTGCCTCTGCCTACTGTGGGGTGC	ACLPLPTVGC
18	GCTTGTGATGTTCGTGATTCGACTGCTTGC	ACDVDRSTAC
19	GCTTGTTCGAATCCTTCGACGGAGTGTTGC	ACSNPSTECC
20	GCTTGTCATGGTGCTCCGGGGCCTTCTTGC	ACHGAPGPSC

Table 4-8. Sequencing analysis of the AR497 selection (sequences chosen for peptide synthesis shown in bold).

Hit #	DNA Sequence	Peptide Sequence
1	GCTTGTACGCCGACGGCTCGTGGTACTTGC	ACTPTARGTC
2	GCTTGTCATTATGGGGATTCTCGTACTTGC	ACHYGDSRTC
3	GCTTGTTTGGCTACTAAGGGGTCGATTTGC	**ACLATKGSIC**
4	GCTTGTGGGGTGGGTATGAATATTATGTGC	ACGVGMNIMC
5	n/a	Blank
6	n/a	Blank
7	GCTTGTTTGGCTACTAAGGGGTCGATTTGC	**ACLATKGSIC**
8	GCTTGTACGCCGACGGCTCGTGGTACTTGC	ACTPTARGTC
9	GCTTGTTCTGAGCGGCAGCATCTTCAGTGC	**ACSERQHLQC**
10	GCTTGTCGTTCTCATGATTCGGCGATGTGC	**ACRSHDSAMC**
11	GCTTGTCGTTCTCATGATTCGGCGATGTGC	**ACRSHDSAMC**
12	n/a	Blank
13	n/a	Blank
14	n/a	Blank
15	GCTTGTCATGTTTCTAATCATAAGACTTGC	**ACHVSNHKTC**
16	n/a	Blank
17	n/a	Blank
18	n/a	Blank
19	GCTTGTCGTTCTCATGATTCGGCGATGTGC	**ACRSHDSAMC**
20	n/a	Blank
21	n/a	Blank
22	GCTTGTCGTTCTCATGATTCGGCGATGTGC	**ACRSHDSAMC**
23	n/a	Blank
24	n/a	Blank
25	n/a	Blank

26	n/a	Blank
27	n/a	Blank
28	n/a	Blank
29	GCTTGTTCTACTTCTCAGGTTCGGTGGTGC	ACSTSQVRWC
30	n/a	Blank
31	GCTTGTCATTATGGGGATTCTCGTACTTGC	ACHYGDSRTC
32	n/a	Blank
33	n/a	Blank
34	n/a	Blank
35	n/a	Blank
36	n/a	Blank
37	GCTTGTTCTGAGCGGCAGCATCTTCAGTGC	**ACSERQHLQC**
38	GCTTGTTCTGAGCGGCAGCATCTTCAGTGC	**ACSERQHLQC**
39	GCTTGTCAGCATGAGGAGTATCGGACGTGC	ACQHEEEYRTC
40	n/a	Blank
41	GCTTGTTCTGAGCGGCAGCATCTTCAGTGC	**ACSERQHLQC**
42	n/a	Blank
43	n/a	Blank
44	GCTTGTTTGGCTACTAAGGGGTCGATTTGC	**ACLATKGSIC**
45	n/a	Blank
46	n/a	Blank
47	GCTTGTGGGAATTGGTCGATGAATCAGTGC	**ACGNWSMNQC**
48	GCTTGTTCTGAGCGGCAGCATCTTCAGTGC	**ACSERQHLQC**
49	GCTTGTCATTATGGGGATTCTCGTACTTGC	ACHYGDSRTC
50	n/a	Blank

4.6.3 Synthesis of APBA Dimer Peptides

SPPS was carried out on Rink Amide MBHA resin with Fmoc/Tbu chemistry on a 0.05 mmol scale. Five equivalents of commercially available amino acids and 4.9 equivalents of HBTU were used for each coupling reaction. An Alloc-protected Dap residue was installed at the C-terminus for on-resin coupling of the 5(6)-FAM/5(6)-TAMRA fluorophores, followed by a triple glycine linker and the peptide hit sequence at the N-terminus. 5(6)-FAM or 5(6)-TAMRA were conjugated to the peptide on resin after removal of the Alloc protecting group, as described in 4.6.5, followed by HBTU-mediated amide bond coupling of the fluorophore in 0.4M NMM in DMF. The peptides were cleaved off resin and globally deprotected with 95% TFA, 2.5% water and 2.5% TIS. Crude peptides were obtained by ether precipitation and purified by RP-HPLC. For APBA-IA cysteine labeling, each peptide hit was treated with 3 equivalents of APBA-IA in the presence of TCEP (2 equivalents) in 2M NMM in DMF for 3 hours and directly purified by RP-HPLC. All peptides were assessed for purity by LC-MS.

Table 4-9. LC-MS analysis of EGA-408, LOS- and AR497 peptide hits (C_m: APBA-IA modified Cys, C_I: IA modified Cys, Dap*: FAM-labeled Dap, Dap*: TAMRA-labeled Dap)

Peptide	Peptide Sequence	Calculated m/z	Observed m/z
SEC5	AC$_m$KPLHSRSC$_m$GGGDap*	1126.46 $[M-H_2O+2H]^{2+}$	1126.95 $[M-H_2O+2H]^{2+}$
	AC$_m$KPLHSRSC$_m$GGGDap*	1141.51 $[M-2H_2O+2H]^{2+}$	1141.94 $[M-2H_2O+2H]^{2+}$
SEC6	AC$_m$FLEYAPTC$_m$GGGDap*	1125.43 $[M-2H_2O+2H]^{2+}$	1125.91 $[M-2H_2O+2H]^{2+}$
	AC$_m$FLEYAPTC$_m$GGGDap*	1152.98 $[M-2H_2O+2H]^{2+}$	1152.93 $[M-2H_2O+2H]^{2+}$
SEC8	AC$_m$SIIPEKYC$_m$GGGDap*	1130.55 $[M-2H_2O+2H]^{2+}$	1130.45 $[M-2H_2O+2H]^{2+}$
	AC$_m$SIIPEKYC$_m$GGGDap*	1157.51 $[M-2H_2O+2H]^{2+}$	1157.45 $[M-2H_2O+2H]^{2+}$
SEC9	AC$_m$GSFWSLTC$_m$GGGDap*	1113.93 $[M-H_2O+2H]^{2+}$	1113.41 $[M-2H_2O+2H]^{2+}$
	AC$_m$GSFWSLTC$_m$GGGDap*	1140.46 $[M-H_2O+2H]^{2+}$	1140.45 $[M-H_2O+2H]^{2+}$
SEC14	AC$_m$PLTAVISC$_m$GGGDap*	1063.93 $[M-H_2O+2H]^{2+}$	1064.43 $[M-H_2O+2H]^{2+}$
	AC$_m$PLTAVISC$_m$GGGDap*	1091.48 $[M+2H]^{2+}$	1091.97 $[M+2H]^{2+}$
SEC18	AC$_m$SERQHLQC$_m$GGGDap*	1162.96 $[M-H_2O+2H]^{2+}$	1163.43 $[M-H_2O+2H]^{2+}$
	AC$_m$SERQHLQC$_m$GGGDap*	1181.51 $[M-2H_2O+2H]^{2+}$	1181.46 $[M-2H_2O+2H]^{2+}$
SEC19	AC$_m$RSHDSAMC$_m$GGGDap*	1108.08 $[M-6H_2O+2H]^{2+}$	1107.37 $[M-6H_2O+2H]^{2+}$
	AC$_m$RSHDSAMC$_m$GGGDap*	112.51 $[M-2H_2O+2H]^{2+}$	1125.41 $[M-2H_2O+2H]^{2+}$
SEC20	AC$_m$LATKGSIC$_m$GGGDap*	1058.99 $[M-2H_2O+2H]^{2+}$	1058.91 $[M-2H_2O+2H]^{2+}$
	AC$_m$LATKGSIC$_m$GGGDap*	1077.56 $[M-4H_2O+2H]^{2+}$	1077.45 $[M-4H_2O+2H]^{2+}$

4.6.4 Fluorescence Microscopy Analysis of TAMRA/APBA Labeled Peptide Hits

Each bacterial strain was grown to an OD_{600}≈1.0 (~1x10^9 cfu/mL), washed and diluted with 1X PBS pH 7.4. The cells were incubated with 2 μM of TAMRA-labeled peptide in 1 mg/mL BSA in 1X PBS pH 7.4 for 1 hour. White light and fluorescent images were obtained on a Zeiss microscope equipped with filter set 20 HE (excitation=BP 546/12, emission=BP 607/80) suitable for detection of TAMRA fluorescence. Images were captured using the 100X oil immersion objective with 1000 ms exposure time. All images were processed consistently using ImageJ software.

4.6.5 Flow Cytometry Analysis of FAM/APBA Labeled Peptide Hits

Each bacterial strain was grown to an OD_{600}≈1.0 (~1x10^9 cfu/mL), washed and diluted to ~1x10^7 cfu/mL with 1X PBS pH 7.4. The cells were incubated with various concentrations (250, 500 or 1000 nM) of FAM-labeled peptide in 1 mg/mL BSA in 1X PBS pH 7.4. After incubation for 1 hour at room temperature, the samples were filtered through Corning 0.35 μm cell strainer filter caps, and subjected to flow cytometric analysis. Data obtained was analyzed with BD FACSDiva software, and median fluorescent values were computed from the generated histograms. All flow cytometry experiments were repeated and generated consistent results.

4.6.6 Microscopy Analysis of EGA-408 and 17978 Co-Cultures

Each bacterial strain was grown to an OD_{600}≈1.0 (~1x10^9 cfu/mL), washed and diluted with 1X PBS pH 7.4. The cells were combined at varying ratios as indicated, and incubated with 2 μM of TAMRA-labeled peptide in 25% human serum in 1X PBS pH 7.4 for 1 hour. White light and fluorescent images were obtained on a Zeiss microscope equipped with filter set 20 HE (excitation=BP 546/12, emission=BP 607/80) suitable for

detection of TAMRA fluorescence. Images were captured using the 100X oil immersion objective with 1000 ms exposure time. All images were processed consistently using ImageJ software.

4.7 References

1. Boucher, H. W. *et al.* Bad Bugs, No Drugs: No ESKAPE! An Update from the Infectious Diseases Society of America. *Clin. Infect. Dis.* **48,** 1–12 (2009).
2. Falagas, M. E., Kasiakou, S. K. & Saravolatz, L. D. Colistin: The Revival of Polymyxins for the Management of Multidrug-Resistant Gram-Negative Bacterial Infections. *Clin. Infect. Dis.* **40,** 1333–1341 (2005).
3. Hancock, R. E. W. & Sahl, H.-G. Antimicrobial and host-defense peptides as new anti-infective therapeutic strategies. *Nat. Biotechnol.* **24,** 1551 (2006).
4. Hancock, R. E. W. & Diamond, G. The role of cationic antimicrobial peptides in innate host defences. *Trends Microbiol.* **8,** 402–410 (2000).
5. Yin, L. M., Edwards, M. A., Li, J., Yip, C. M. & Deber, C. M. Roles of Hydrophobicity and Charge Distribution of Cationic Antimicrobial Peptides in Peptide-Membrane Interactions. *J. Biol. Chem.* **287,** 7738–7745 (2012).
6. Hwang-Soo, J., Chih-Iung, F. & Michael, O. Bacterial strategies of resistance to antimicrobial peptides. *Philos. Trans. R. Soc. B Biol. Sci.* **371,** 20150292 (2016).
7. Hancock, R. E. W. Peptide antibiotics. *Lancet* **349,** 418–422 (1997).
8. Pristovšek, P. & Kidrič, J. Solution Structure of Polymyxins B and E and Effect of Binding to Lipopolysaccharide: An NMR and Molecular Modeling Study. *J. Med. Chem.* **42,** 4604–4613 (1999).
9. Tsubery, H., Ofek, I., Cohen, S., Eisenstein, M. & Fridkin, M. Modulation of the Hydrophobic Domain of Polymyxin B Nonapeptide: Effect on Outer-Membrane Permeabilization and Lipopolysaccharide Neutralization. *Mol. Pharmacol.* **62,** 1036 LP-1042 (2002).

10. Steinbuch, K. B. & Fridman, M. Mechanisms of resistance to membrane-disrupting antibiotics in Gram-positive and Gram-negative bacteria. *Medchemcomm* **7,** 86–102 (2016).

11. Boll, J. M. *et al.* A penicillin-binding protein inhibits selection of colistin-resistant, lipooligosaccharide-deficient Acinetobacter baumannii. *Proc. Natl. Acad. Sci.* **113,** E6228–E6237 (2016).

12. Powers, M. J. & Trent, M. S. Expanding the paradigm for the outer membrane: Acinetobacter baumannii in the absence of endotoxin. *Mol. Microbiol.* **107,** 47–56 (2018).

13. Paterson, D. L. & Harris, P. N. A. Colistin resistance: a major breach in our last line of defence. *Lancet Infect. Dis.* **16,** 132–133 (2016).

14. Liu, Y. *et al.* Emergence of plasmid-mediated colistin resistance mechanism MCR-1 in animals and human beings in China : a microbiological and molecular biological study. *Lancet Infect. Dis.* **16,** 161–168

15. Dortet, L. *et al.* Rapid detection of colistin resistance in Acinetobacter baumannii using MALDI-TOF-based lipidomics on intact bacteria. *Sci. Rep.* **8,** 16910 (2018).

16. Peltier, J. *et al.* Clostridium difficile has an original peptidoglycan structure with a high level of N-acetylglucosamine deacetylation and mainly 3-3 cross-links. *J. Biol. Chem.* **286,** 29053–29062 (2011).

17. Arroyo, L. A. *et al.* The pmrCAB Operon Mediates Polymyxin Resistance in Acinetobacter baumannii ATCC 17978 and Clinical Isolates through Phosphoethanolamine Modification of Lipid A. *Antimicrob. Agents Chemother.* **55,** 3743–3751 (2011).

18. Harding, C. M., Hennon, S. W. & Feldman, M. F. Uncovering the mechanisms of Acinetobacter baumannii virulence. *Nat. Rev. Microbiol.* **16,** 91–102 (2017).

19. Raetz, C. R. H., Reynolds, C. M., Trent, M. S. & Bishop, R. E. Lipid A Modification Systems in Gram-Negative Bacteria. *Annu. Rev. Biochem.* **76,** 295–329 (2007).

20. Park, Y. K. *et al.* Independent emergence of colistin-resistant Acinetobacter spp. isolates from Korea. *Diagn. Microbiol. Infect. Dis.* **64,** 43–51 (2009).

21. McCarthy, K. A. *et al.* Phage Display of Dynamic Covalent Binding Motifs Enables Facile Development of Targeted Antibiotics. *J. Am. Chem. Soc.* **140,** 6137–6145 (2018).

22. Peleg, A. Y., Seifert, H. & Paterson, D. L. Acinetobacter baumannii: Emergence of a Successful Pathogen. *Clin. Microbiol. Rev.* **21,** 538–582 (2008).

23. Bandyopadhyay, A., McCarthy, K. A., Kelly, M. A. & Gao, J. Targeting bacteria via iminoboronate chemistry of amine-presenting lipids. *Nat. Commun.* **6,** 6561–6569 (2015).

CHAPTER 5

Selection of Targeted APBA Dimer Peptide Binders for the Chemotactic Innate Immune Peptide Human Beta Defensin 3 (hBD3)

5.1 Introduction

Towards our goal of developing novel solutions to the antibiotic crisis, recent work in our group has focused on the application of APBA-presenting phage libraries for identification of peptides that selectively bind defined strains of bacteria with varying amine presenting modifications on their cell walls.[1] This approach has been successful in identifying peptides capable of distinguishing *S. aureus* as well as several colistin resistant strains of bacteria as will be discussed in Chapter 5. We envisioned that this iminoboronate-capable high throughput peptide screening platform could be applied to identifying selective binders of proteins in addition to the aforementioned whole bacterial cell application. With our targeted protein binding in mind, we came across the protein human beta defensin 3 (hBD3), which is an innate immune peptide that exerts both antimicrobial as well as chemotactic activities, and plays an important role in aggressive head and neck cancers. Thus, we sought to identify selective binders to this protein through our phage display screening approach.

5.1.1 Classification of Defensins

Defensins are a group of small cationic peptides, which are classified by their disulfide bonding patterns, and exert both antimicrobial and immunomodulatory effects.[2] Human defensins are separated into two distinct families, α and β, depending on their sequence homology and disulfide pairing (**Figure 5-1**). Humans have six known α-defensins, and four known β-defensins, all of which display markedly distinct functions despite striking structural similarity (**Table 5-1**). The human α-defensins were initially discovered as natural peptide antibiotics, which are released from neutrophils and Paneth cells to kill ingested foreign microbes during phagocytosis.[3,4] Alternatively, human β-

defensins (hBDs) are found predominantly in epithelial cells and tissues,[5] and display varying antimicrobial potency towards different species of bacteria. For example, hBD1 and 2 are only potent against gram-negative species, such as *E. coli*, whereas hBD3 displays potent broad-spectrum activity. Notably, the antimicrobial activity of most defensins is dependent upon salt concentrations, thus highlighting the importance of electrostatic interactions between the cationic peptides and the negatively charged bacterial membranes in the activity of these peptides.

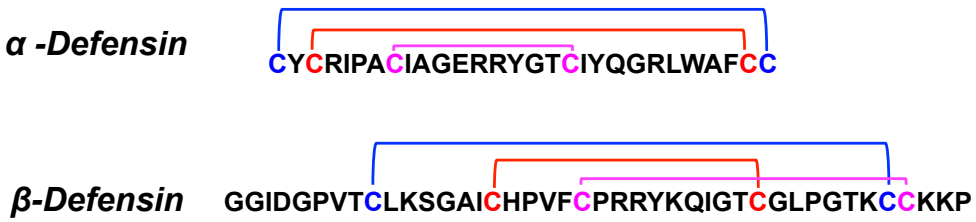

Figure 5-1. Structural differences between α and β defensins.

Table 5-1. Sample of defensin sequences and their disulfide connectivities.

Class	Name	Sequence	Disulfides
α	HNP1	ACY**C**RIPA**C**IAGERRYGT**C**IYQGRLWAF**CC**	1-6, 2-4, 3-5
	HNP2	**C**Y**C**RIPA**C**IAGERRYGT**C**IYQGRLWAF**CC**	
	HNP3	DCY**C**RIPA**C**IAGERRYGT**C**IYQGRLWAF**CC**	
	HNP4	V**C**S**C**RLVF**C**RRTELRVGN**C**LIGGVSFTY**CC**TRV	
	HD5	AT**C**Y**C**RHGR**C**ATRESLSGV**C**EISGRLYRL**CC**R	
	HD6	AFT**C**H**C**RRS**C**YSTEYSYGT**C**TMGINHRF**CC**L	
β	HBD1	DHYN**C**VSSGGQ**C**LYSA**C**PIFTKIQGT**C**YRGKAK**CC**K	1-5, 2-4, 3-6
	HBD2	GGIDGPVT**C**LKSGAI**C**HPVF**C**PRRYKQIGT**C**GLPGTK**CC**KKP	
	HBD3	GIINTLQKYY**C**RVRGGR**C**AVLS**C**LPKEEQIGK**C**STRGRK**CC**RRKK	

5.1.2 Human β-defensin 3 and its Antimicrobial Activity

Human β-defensin 3 (hBD3) is a 45 residue cationic peptide that displays uneven C-terminal clustering of its positively charged residues. Initially isolated from psoriatic scales, hBD3 forms amphipathic symmetrical dimers through one of its three β strands (β2), which affords the peptide unique characteristics including broad-spectrum and salt-insensitive activity, with low micromolar activity towards *P. aeruginosa*, *S. aureus*, *Enterococcus faecalis* and *Streptococcus pyogenes* (**Figure 5-2**).[6,7] Further mechanistic investigation has also revealed that hBD3 does not preferentially fold into its native disulfide configuration *in vivo*; however, hBD3's bactericidal activity has been shown to be independent of the arrangement of disulfide connectivity, indicating that the structure of hBD3 is less important for antimicrobial activity than the arrangement of amino acids (**Table 5-2**).[7,8]

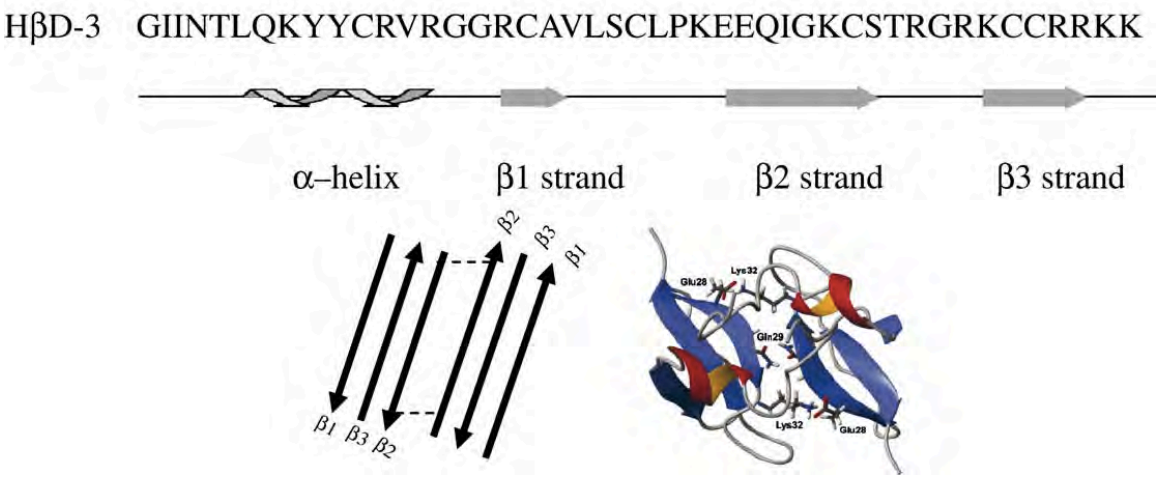

Figure 5-2. Structural features of hBD3, including the interaction between the two β2 strands, which are stabilized by salt bridge formation between Glu28 and Lys32 in an anti-parallel manner (Image from Ref. 6).

Table 5-2. Bactericidal and chemotactic activity of hBD3 and structural analogues (adapted from Ref. 7)

Peptide	Disulfide Connectivity	LD_{50} *E. coli*, ug/mL	Concentration for Chemotaxis, ng/mL
hBD3 (1)*	1-5, 2-4, 3-6	0.08	10
hBD3 (2)	1-5, 2-4, 3-6	0.06	100
hBD3 (3)	1-5, 2-3, 4-6	0.03	1,000
hBD3 (4)	1-6, 2-4, 3-5	0.08	1,000
hBD3 (5)	1-6, 2-3, 4-5	0.05	100
hBD3 (6)	1-6, 2-5, 3-4	0.02	100
Abu-hBD3	None	0.04	>10,000

*=natively folded peptide; Abu=α-aminobutyric acid capped cysteine (eg. no disulfide bonds)

5.1.3 Chemotactic Activity of Human β-defensin 3 and its Implication in Cancer

In addition to their wide-ranging antimicrobial activity, defensins have also been shown to possess important functions in the modulation of adaptive immunity by selectively chemoattracting different subsets of T lymphocytes and immature dendritic cells.[9] In contrast to antimicrobial activity, the arrangement of disulfide bonds, as well as the presence of cysteine, do affect the chemotactic activity of hBD3 (**Table 5-2**).[8] In general, defensins are considered to be pro-inflammatory since their expression increases in response to toll-like receptor (TLR) ligands, such as TNF- α, IL-1 β, IFN-γ and PMA under infection conditions. Additionally, defensins have been shown to chemoattract CD4 T cells and immature dendritic cells through chemokine receptors to induce chemotaxis.[10] hBD3 specifically chemoattracts monocytes and myeloid dendritic cells and activates them through TLR-1/2 by inducing expression of co-stimulatory molecules and NF-κB.[11]

A number of studies have been carried out to dissect the interaction of hBD3 with the adaptive immune system. *In vivo* studies have shown that hBD3 functions as a

chemoattractant to recruit macrophages via C-C chemokine receptor 2 (CCR2), as the monocytic cell migration was inhibited by the cross-desensitization with monocyte chemoattractant protein 1 (MCP-1), a tumor cell associated chemokine and a CCR2-specific inhibitor (**Figure 5-3**).[11] Additionally, hBD3 expressing tumorogenic cells have been shown to induce massive tumor infiltration of host macrophages, as well as induce expression of a wide variety of tumor promoting cytokines (IL-1α, IL-6/8, TNF- α).[11]

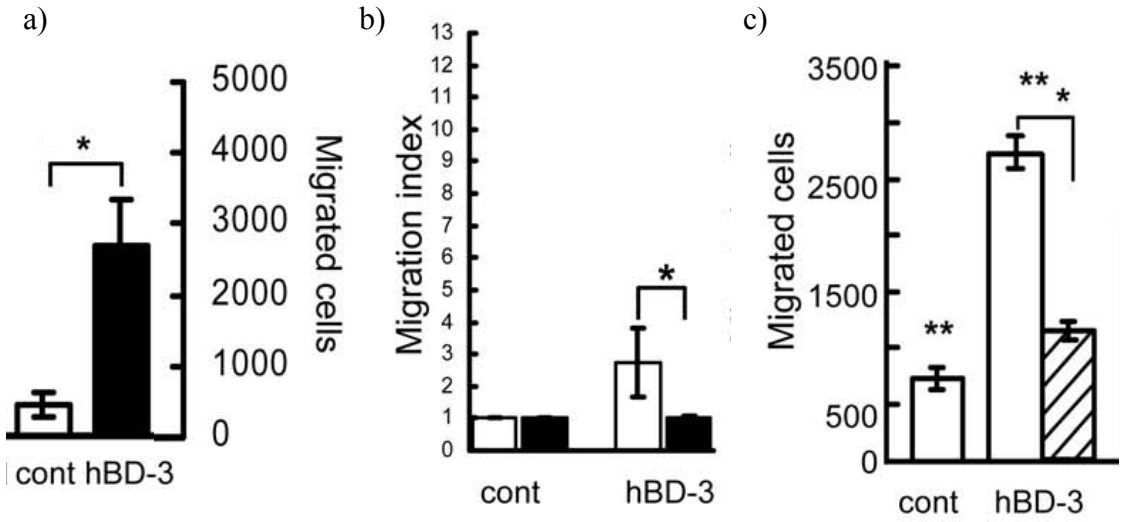

Figure 5-3. hBD3 induces CCR2-mediated monocytic cell migration. (a) Migration of Mono-Mac (CCR2-expressing) cells in response to hBD3. (b) Migration of Mono-mac and (c) monocytic (also express CCR2) cells in the absence (white bars) and presence (black/striped bars) of CCR2 inhibitors (Images from Ref. 11).

Importantly, head and neck cancers overexpress hBD3, which stimulates human macrophages to express tumor-promoting chemokines. This may result in a positive feedback loop to drive tumor progression (**Figure 5-4**). hBD3 expression was found to be induced by the activation of epidermal growth factor (EGFR)[12] and the inactivation of p53[13], and also correlates with increased levels of myeloid-derived suppressor cells, which are immune cells that are up-regulated in cancer disease states.[14] Thus, it appears that hBD3 functions as an immunomodulator to recruit and activate tumor-assisted

macrophages and myeloid-derived suppressor cells to promote progression of tumors using CCR2 to regulate monocyte/macrophage trafficking.

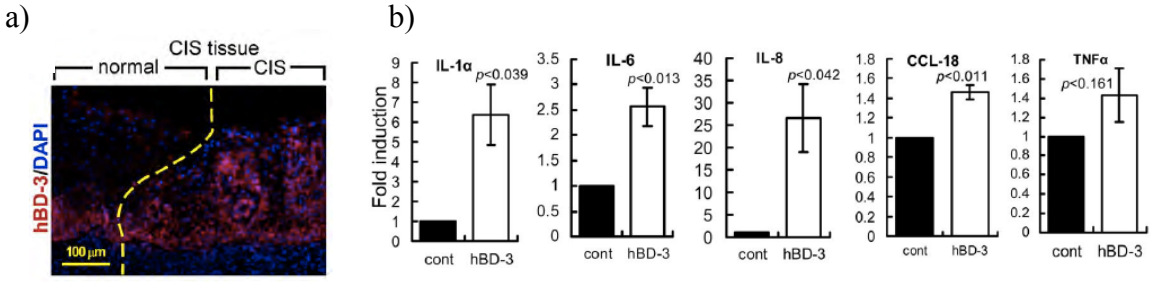

Figure 5-4. Overexpression of hBD3 in head and neck cancers induces expression of chemokines. (a) Immunofluorescent staining of *in situ* cancer biopsy shows extensive hBD3 expression (red) in comparison to normal tissue. (b) RT-PCR quantification of cytokines/chemokines expressed from hBD-3 induced macrophages (Images from Ref. 11).

5.1.4 Application of Phage Display Technology to Identify Protein Binders

The implication of the innate immune defensin hBD3 in aggressive head and neck cancers makes it an interesting therapeutic target. While literature indicates substantial proof of CCR2-mediated cheomattraction of hBD3[15], no structural studies have been conducted to elucidate the nature of the interaction between hBD3 and CCR2. Although rational design of an hBD3-binding peptide that would disrupt the interaction between hBD3 and CCR2 is not possible, we envisioned that phage display selection of hBD3 binders could provide a suitable starting point to generate peptide sequences that bind to the defensin.

Phage display has been applied to generate high affinity peptide binders and inhibitors for a wide variety of small molecule and protein targets including proteases, viruses, bacteria and tumor cells. Our group has carried out extensive investigation on identifying whole bacterial cell peptide binders using an iminoboronate-capable phage

library.[1] These CX_7C phage are reduced in order to cap the cysteines with APBA-IA, which enables them to form stabilized iminoboronate linkages with amines presented by the target (**Figure 5-5**). Since hBD3 carries several lysine residues throughout its sequence, we envisioned that the APBA warheads presented on the phage library would provide greater stabilization to the peptide-hBD3 interaction. Thus, we aimed to screen streptavidin-immobilized hBD3 with our APBA modified phage library in order to identify potent hBD3 binding peptides.

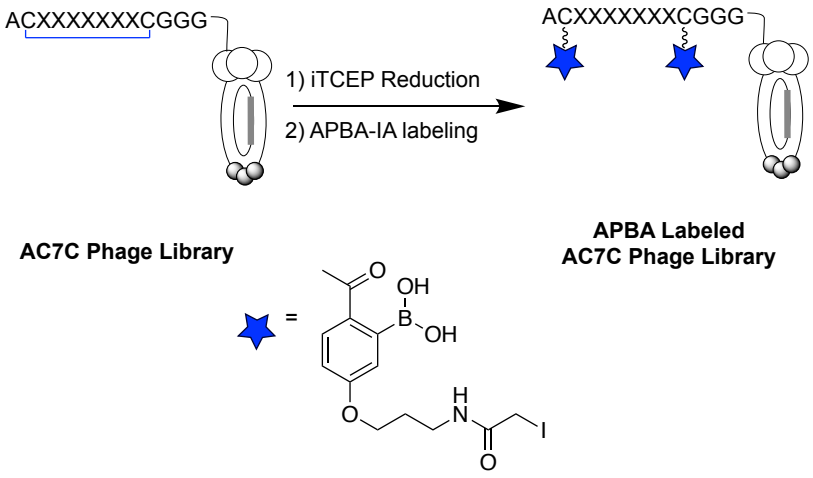

Figure 5-5. Schematic of APBA-IA labeling of CX_7C phage to generate an iminoboronate capable randomized peptide library on the surface of M13 phage.

5.2 Synthesis of Biotin-hBD3 and Biotin-hBD2

For our phage display panning against hBD3, we envisioned that we could biotin tag the hBD3 protein in order to immobilize it on streptavidin beads for phage panning. Given that isolation of overexpressed hBD3 protein in bacteria has lead to isolation of not only the native form, but also alternatively folded hBD3[8], we envisioned that solid phase peptide synthesis (SPPS) would enable us to control the folding of hBD3 to into the desired conformation for CCR2 binding and immune modulation, as well as allow us to

easily biotin tag the protein. However, given the long length (45 residues) of hBD3, straightforward SPPS of the protein in its entirety was unlikely to yield substantial amounts of full-length peptide.

5.2.1 Native Chemical Ligation

Recent interest in the chemical synthesis of proteins has uncovered the power of native chemical ligation towards generating longer peptides than previously enabled. While peptides of lengths up to 50 residues have been successfully synthesized by SPPS, these findings are generally sequence dependent and do not speak to the totality of peptides due to sequence-specific aggregation and diminished coupling efficiency of certain residues and residue combinations.[16] To work around these issues, native chemical ligation (NCL) has emerged as an efficient, tag-free approach to generating long peptides through the fusing of two shorter peptides.[17] To do so, one peptide must be synthesized on Dawson Dbz resin, which undergoes N-acylurea formation at the C-terminus by acylation with nitrophenylchloroformate, and is then subjected to intramolecular cyclization when treated with base to obtain the N-acyl-benzimidazolinone (Nbz) peptide fragment. Nbz can then undergo rapid thiolysis in neutral conditions, and ligate to an N-terminal cysteine containing peptide to yield the native, full-length peptide (**Figure 5-6**).

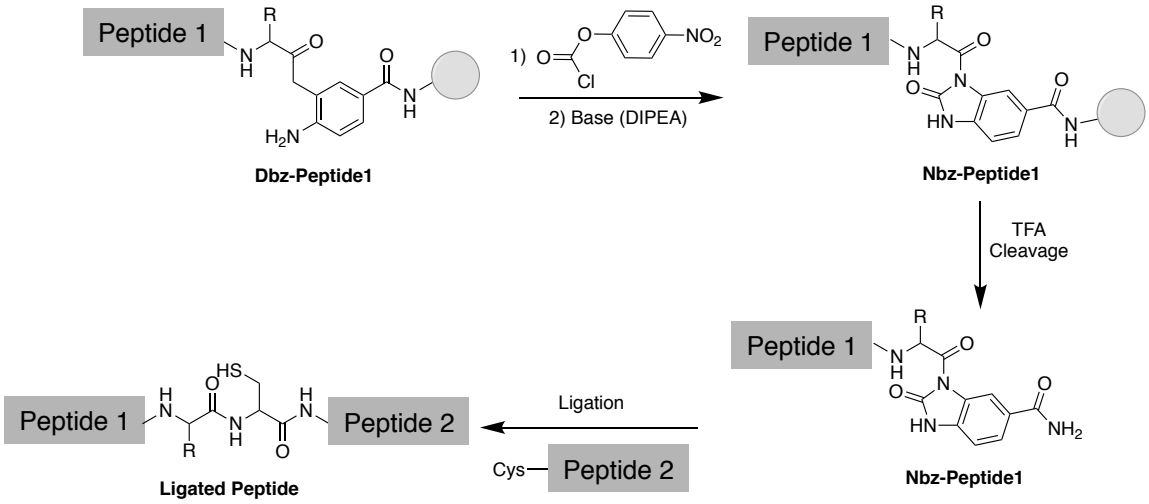

Figure 5-6. Schematic of native chemical ligation via formation of C-terminal N-acylurea followed by thioester formation and a final S-N acyl transfer to yield the native peptide (adapted from Ref. 17).

Towards this end, we synthesized two hBD3 fragments (hBD3a and hBD3b for hBD3, or hBD2a and hBD2b for hBD2) that could undergo native chemical ligation (**Figure 5-7**). The hBD2/3a fragment, which constitutes the N-terminus of full-length hBD2/3, was synthesized on Dawson-Dbz resin. The hBD2/3b fragment was synthesized on Wang resin, with cysteine as the N-terminal residue to enable facile conjugation to the Nbz modified hBD3a. One challenge encountered in the synthesis of hBD2/3a was coupling of the first residue. Instead of standard HBTU coupling with NMM, HATU with DIPEA was used instead to improve coupling efficiency. Additionally, we observed that peptides were not synthesized in pure form due to peptide elongation at the free, non-Fmoc protected amine on the Dawson Dbz resin, despite reduced activation of that amine. To eliminate this problem, the Fmoc protected resin was first alloc protected to ensure elongation at only the desired amine residue.

a)

Biotin-Aha-GIINTLQKYYC^1RVRGGRC^2AVLSC^3LPKEEQIGKC^4STRGRKC^5C^6RRKK

1/5: Tbu

2/4: Trt

3/6: Acm

hBD3-a: Dawson Dbz-RGGRVRCYYKQLTNIIG-Aha-Biotin-NH_2

hBD3-b: Wang-KKRRCCKRGRTSCKGIQEEKPLCSLAVC-NH_2

b)

Biotin-Aha-GIGDPVTC^1LKSGAIC^2HPVFC^3PRRYKQIGTC^4GLPGTKC^5C^6KKP

1/5: Acm

2/4: Tbu

3/6: Trt

hBD2-a: Dawson Dbz-FVPHCIAGSKLCTVPDGIG-Aha-Biotin-NH_2

hBD2-b: Wang-PKKCCKTGPLGCTGIQKYRRP-NH_2

Figure 5-7. Peptide fragments of hBD3 and hBD2 synthesized for efficient NCL. The synthetic strategy of orthogonal cysteine protecting groups and peptide fragments for (a) hBD3 and (b) hBD2 enabled facile synthesis of the full length, natively folded peptide.

Once the two peptide fragments were synthesized, a native chemical ligation approach was taken to carry out their ligation. A pH screen (pH 6, 7 and 8) of the NCL conditions was carried out to determine the optimal pH of the ligation reaction to minimize hydrolysis of the Nbz modified peptide and maximize the yield of the ligated product. pH 8 was found to be most optimal for maximum yield of the ligated hBD3-biotin or hBD2-biotin peptides (**Table 5-1**). Using this condition, the peptides were successfully ligated and purified to yield pure peptide.

Table 5-3. Results of pH screen of NCL to determine optimal ligation conditions.

pH	% Hydrolyzed Nbz	% Ligated Peptide
6	90	10
7	25	75
8	65	35

5.2.2 Stepwise Oxidative Folding of hBD2 and hBD3

An orthogonal cysteine protection strategy was implemented in the design of hBD3-biotin and hBD2-biotin to afford selective disulfide bond formation (**Figure 5-8**). Firstly, the trityl protecting groups were removed following peptide cleavage from resin with TFA/EDT/water. After purification of the ligated peptide, oxidation of the trityl deprotected cysteines was carried out by stirring the peptide in 10% DMSO in water. The peptides were directly lyophilized and used without purification for the next deprotection/oxidation step. The Acm protecting groups were then removed and concomitantly the disulfide bond was formed with iodine in acetic acid and 0.1M HCl before the peptides were purified. Finally, the Tbu protecting groups were removed and the disulfide bonds were formed with TFA/DMSO/anisole prior to final peptide purification.

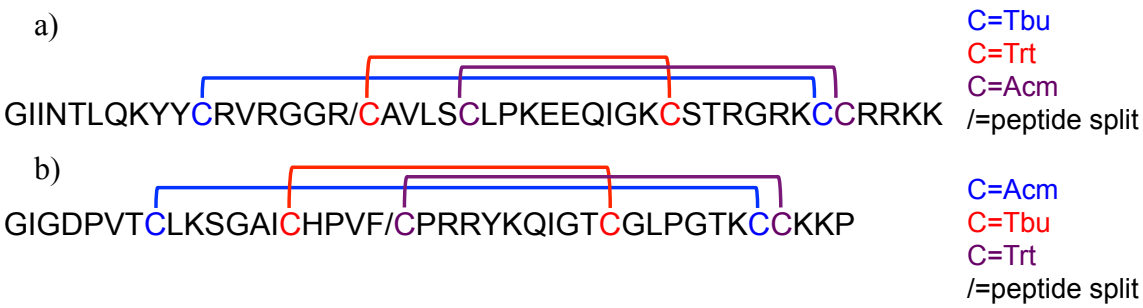

Figure 5-8. Orthogonal cysteine protection strategy to enable native disulfide formation of hBD3 and hBD2. Selective protection of cysteine residues on (a) hBD3 and (b) hBD2 enables sequential deprotection and oxidation of cysteines.

5.3 APBA Dimer Phage Library Screening Against Biotin-hBD3

5.3.1 Confirmation of Dimerization of Synthetic Biotin-hBD3

Upon successful synthesis of biotin-hBD3, the properties of the synthetic peptide were tested. It was previously noted that natively folded hBD3 forms dimers in solution

as a result of a Lys^{32}-Glu^{28} interaction[6,18], whereas reduced hBD3 does not. To confirm that our synthetic biotin-hBD3 also forms dimers in the oxidized state, we analyzed the peptide by Tricine gel electrophoresis. Our analysis revealed that indeed synthetic biotin-hBD3 (5.49 kDa) does form dimers under oxidized conditions, but this property is abolished when the peptide is reduced with 0.1M DTT (**Figure 5-9**). This suggests that the structural integrity and folding of hBD3 is not significantly impacted by our synthetic approach and modification with biotin, and confirms that our synthetic peptide should provide a closely native structure to biologically synthesized hBD3 in the process of phage panning.

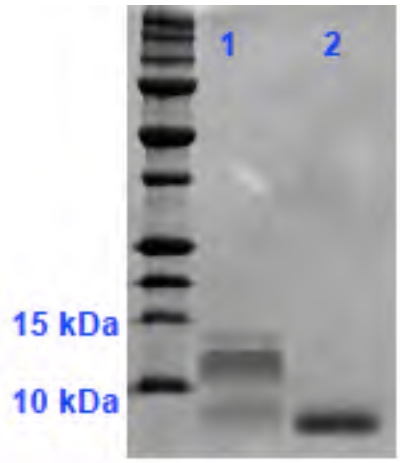

Figure 5-9. 16% tricine gel analysis of hBD3 dimerization (Lane 1= 10 µg hBD3-biotin non-reduced, Lane 2= 10 µg hBD3-biotin reduced with DTT, stained with coomassie, PrecisionPlus Ladder used as standard).

4.3.2 Phage Screening of Biotin-hBD3

For phage panning, a few key elements were introduced to the screening workflow to ensure stringency of selection, as well as to avoid isolation of binders to the affinity beads (**Figure 5-10**). Firstly, the beads were alternated between streptavidin and

neutravidin between panning rounds. Secondly, albumin was included in the wash steps to eliminate any peptides that would exhibit strong albumin binding. Finally, the phage library was pre-incubated with biotin to eliminate any biotin specific binders from the pool. Throughout the panning process, stringent washing steps were applied, with the concentration of Tween increasing from 0.1% in the first round to 0.2% in the second, and 0.3% in the third round. The phage titer results from each round (**Table 5-2**) show that the washes did increase stringency by decreasing the output population by several folds, thus enriching tight binding phage.

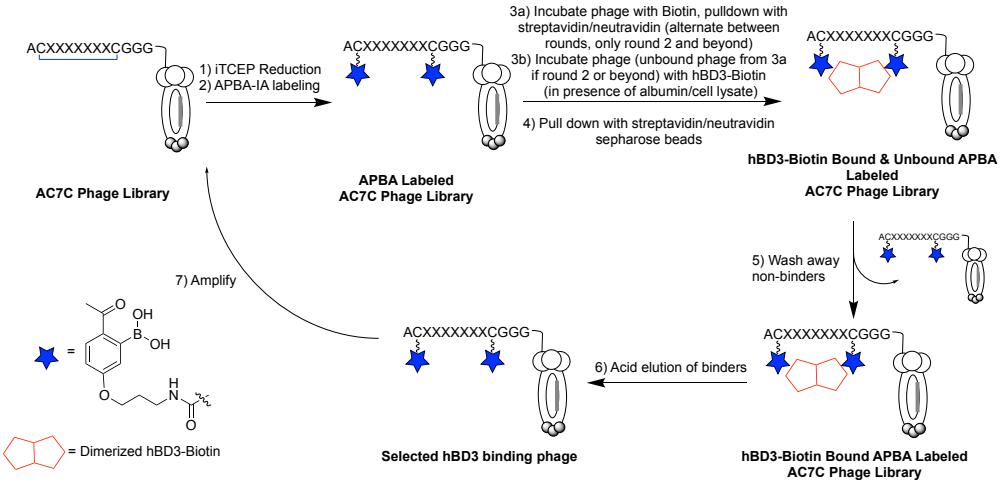

Figure 5-10. Schematic of hBD3 phage panning designed to achieve optimal selection stringency.

Table 5-4. Phage titers from each round of hBD3 panning.

Round	Input	Negative Screen Output	Positive Screen Output	Amplified
1(S)	2.60×10^{10} pfu/mL	N/A	4.65×10^{7} pfu/mL	4.90×10^{13} pfu/mL
2 (N)	4.25×10^{11} pfu/mL	6.00×10^{11} pfu/mL	6.50×10^{5} pfu/mL	2.70×10^{13} pfu/mL
3 (S)	1.00×10^{11} pfu/mL	2.60×10^{10} pfu/mL	3.00×10^{4} pfu/mL	N/A

S=streptavidin; N=neutravidin

5.4 hBD3 Peptide Hit Validation via hBD3 Binding Assays

5.4.1 Analysis of Phage Binding to hBD3 Coated Beads

Sequencing of the third round output only revealed one repeating sequence (ISL, **Table 5-5**), so a hBD3 coated bead binding phage experiment with isolated phage populations was attempted prior to carrying out any peptide synthesis. To do so, amplified phage from individual phage colonies that had been amplified for sequencing were isolated from the supernatant of the ER2738 cultures with PEG/NaCl. These isolated phage were then subjected to iTCEP reduction and APBA-IA labeling prior to bead binding experiments. For this experiment, the APBA-IA labeled phage were directly incubated with hBD3 coated beads, after which a FITC-pIII antibody was used to detect if the phage (which bear several copies of the pIII protein) were bound to the hBD3 coated beads as a measure of hBD3 binding. A negative control test of the FITC-pIII antibody's ability to bind to hBD3-coated beads was first carried out. No bead staining by the antibody alone was observed, indicating that the antibody doesn't display any non-specific binding to the hBD3 coated beads (**Figure 5-11**).

Table 5-5. Sequences of hBD3 phage panning round 3 output.

HPSNWKA	GRTPSDK	TSWSKRL	TLTAYKV	LNAGASK
NSSASKN	SLSNYHR	YKTMYGL	QPSRFVQ	NTPAMLT
TTKLPNS	VMSPGKS	RLPTSTG	GKHFQKH	LHKSVSG
KHPLYRH	MNPLYWR	DRAGLEH	MKALYWR	KIPSXGR
SSKHEAT	VHSKPGR	NSHRHGA	VNPMKRH	LWRPAAD
HRAQGTA	KNPQYRR	TDSRGQK	PAQNGWQ	
ISLTLNR*	ISLTLNR*	KEGIHMT	SAGYSRN	
SAYERPP	VSTMART	TSLTVDR	KAGHQYQ	
LVYAHHT	HGAVKNT	VSPRSHE	DIYRKGW	

*=repeating sequence

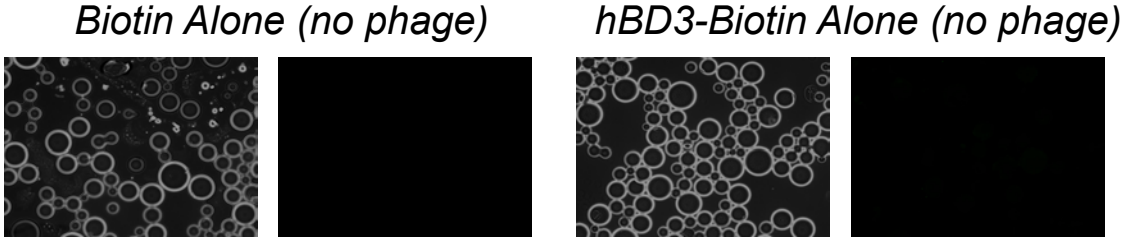

Figure 5-11. Fluorescence analysis of the binding of FITC-pIII antibody to biotin and hBD3-biotin coated streptavidin beads.

The phage bearing unique sequences were then incubated with the hBD3 coated beads to assess their binding affinity. Interestingly, all phage including the blank, insertless (eg. No CX_7C) phage displayed robust binding to the hBD3-coated beads (**Figure 5-12**). This phenomenon is likely due to electrostatic interactions between the highly positively charged hBD3 peptide (+11) and the phage's negatively charged pVIII coat protein. Attempts at washing the beads gave no decease in non-specific phage binding. This observation has also been reported by groups that have applied polylysine and related polymers as "phage wrappers" to mask the negatively charged phage surface. While it does appear that the electrostatic interaction interferes with analysis of phage binding via microscopy, the observed enrichment of the phage population between rounds indicates that this non-specific interaction likely did not play a role in the selection of strong hBD3 binders.

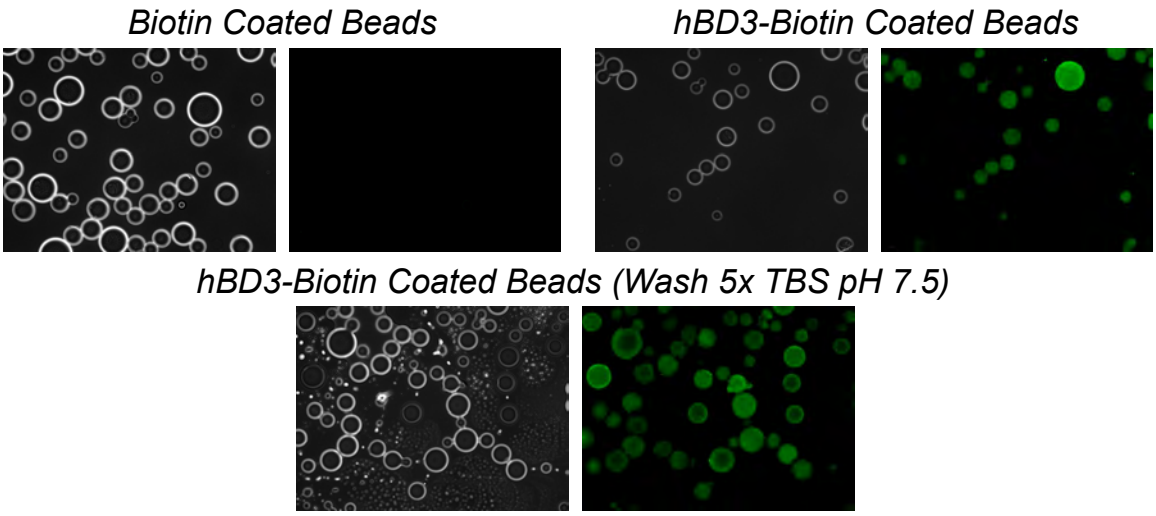

Figure 5-12. Fluorescence analysis of blank phage binding to hBD3 biotin coated beads with or without washing after phage incubation.

5.4.2 Synthesis of hBD3 Peptide Hits

Given the challenges with identifying strongly binding peptide sequences via the phage microscopy experiment, four peptide sequences from the third round output were randomly selected for SPPS (**Table 5-6**). These peptides were fluorescently labeled with TAMRA to enable facile microscopy of the hits. To enable selective TAMRA and APBA-IA labeling of the peptides, a C-terminal Alloc-protected Dap residue was included. This residue was able to be selectively deprotected on resin to enable on-resin TAMRA labeling. Following cleavage from resin and purification, the peptides were then subjected to APBA labeling to yield TAMRA and APBA labeled peptides.

Table 5-6. Sequences of CX_7C peptides selected for analysis.

Peptide	Sequence
SEC1	$AC_mISLTLNRC_mGGGDap$*
SEC2	$AC_mDRAGLEHC_m$ GGGDap*
SEC3	$AC_mVSTMARTC_m$ GGGDap*
SEC4	$AC_mKAGHQYQC_m$ GGGDap*

C_m=APBA-IA labeled; *= TAMRA

5.4.3 hBD3 Coated Streptavidin Bead Peptide Binding Analysis

To examine the binding of these peptides to hBD3, agarose beads were coated with hBD3-biotin, then incubated with each TAMRA and APBA-IA labeled peptide (10 μM), and finally analyzed by fluorescent microscopy. SEC2 and SEC4 were observed to have the most potent hBD3 binding, whereas SEC1 and SEC3 displayed minimal binding to the hBD3-coated beads (**Figure 5-13**). This experiment was also carried out in the presence of 10 mg/mL BSA and 10% human serum (HS), neither of which diminished peptide binding to hBD3-coated beads.

To quantify the hBD3 binding of the peptides, a titration experiment was carried out in which the fluorescence of the highest concentration of peptide examined was adjusted to produce maximal fluorescence. These settings were then maintained to fluorescently image the beads at lower peptide concentrations to generate a saturating binding curve. The average fluorescence of the beads was then obtained to generate a titration plot for SEC2 and SEC4 (**Figure 5-14**). These experiments indicated that the peptides bind to hBD3 with micromolar potency.

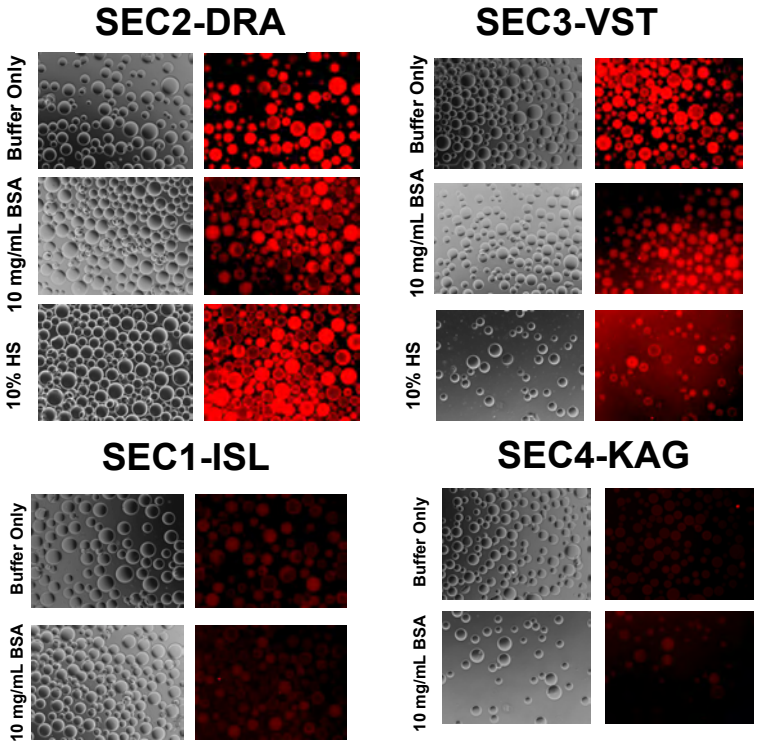

Figure 5-13. hBD3-coated bead fluorescence of APBA dimer peptide hits. Fluorescence of SEC2 (DRA), SEC3 (VST), SEC1 (ISL) and SEC4 (KAG) towards hBD3-coated beads was analyzed by fluorescence microscopy in the presence and absence of 10 mg/mL BSA and 10% human serum (HS).

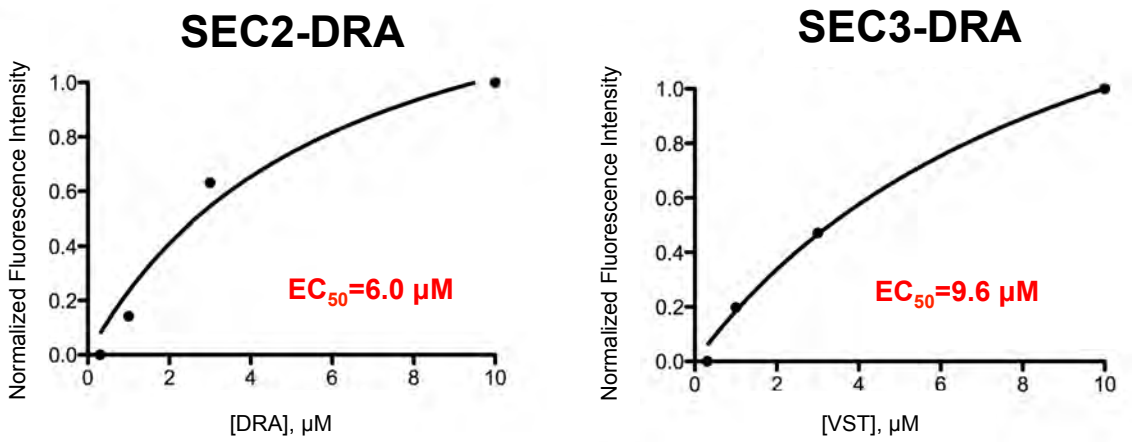

Figure 5-14. hBD3 peptide binding titration analysis. Increasing concentrations of SEC2 (left) and SEC3 (right) were titrated with hBD3-coated beads to analyze the fluorescence of the beads and determine a binding dissociation constant.

4.4.4 hBD2 Coated Streptavidin Bead Peptide Binding Analysis

To assess the hBD3 specificity of the identified peptide binders, the same agarose bead binding experiment was carried out for the closely related hBD2 protein, which displays a similar sequence and cationic charge to that of hBD3. No labeling of the hBD2-coated beads was observed for any of the peptides examined (**Figure 5-15**), indicating hBD3-specific binding of the isolated peptide hits.

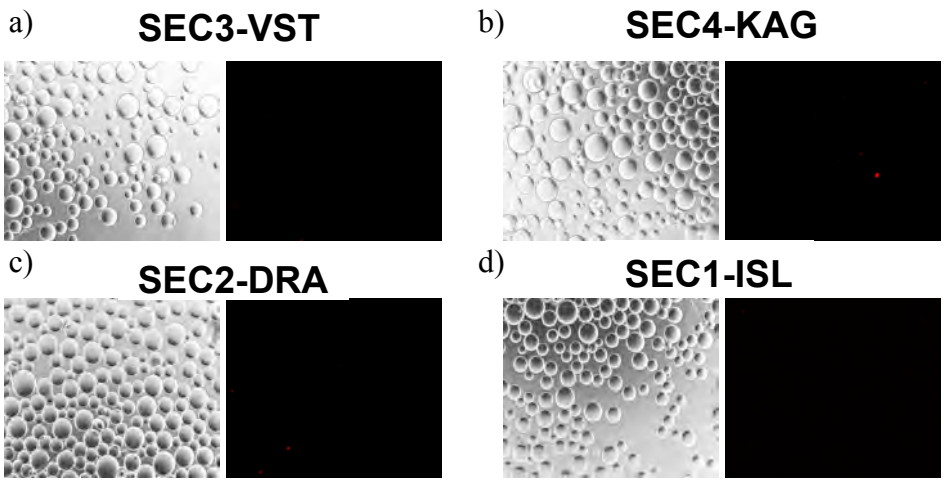

Figure 5-15. Analysis of hBD3 peptide hit binding to hBD2. The binding of (a) SEC3, (b) SEC4, (c) SEC2 and (d) SEC1 to hBD2 was analyzed by hBD2 coated agarose bead microscopy.

5.4.5 BSA Binding Anisotropy Analysis of hBD3 Binding Peptides

To assess the binding affinity of the hBD3 peptide hits towards BSA, each TAMRA labeled peptide hit was titrated with increasing concentrations of BSA. The anisotropy readings were zeroed and normalized, then plotted against BSA concentration to extract binding dissociation constants. All three peptides examined display K_d measurements around 2-4 mg/mL for binding BSA (**Figure 5-16**).

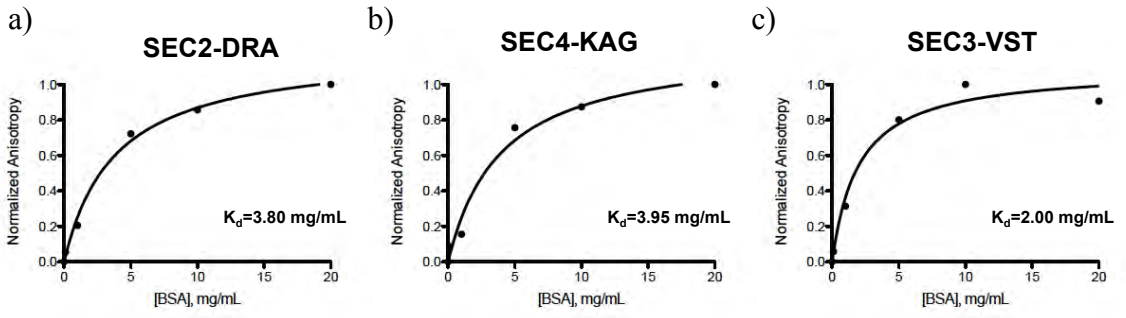

Figure 5-16. Analysis of hBD3 peptide hits BSA binding capacity. Anisotropy titrations of (a) SEC2, (b) SEC4 and (c) SEC3 with 0-20 mg/mL BSA enabled the determination of binding dissociation constants for BSA binding.

4.5 Conclusions

By chemically synthesizing hBD3-biotin through a NCL approach, we were able to successfully synthesize natively folded hBD3 with a biotin tag that retained the dimerization property of the protein. Screening of an APBA modified phage library against immobilized hBD3 yielded peptide hits that were analyzed for their capacity to bind hBD3 via fluorescent analysis of hBD3 coated beads. These experiments revealed that two of the randomly selected hits, SEC2 and SEC3, displayed potent hBD3 binding with K_d values of 6 μM and 10 μM, respectively. Notably, these peptides did not exhibit any binding towards the similar protein hBD2. Thus, our screening approach was successful in selecting for targeted peptide binders of a therapeutically relevant protein.

Further analysis of BSA binding of the peptides revealed that the peptides do indeed bind BSA; in the future, this phenomenon could be further mitigated by carrying out the screening in the presence of a higher concentration of BSA (eg. 10 mg/mL instead of 1 mg/mL). Despite the observed strong binding of our hBD3 targeting peptides, preliminary studies of the inhibition of hBD3 chemotactic activity haven't revealed any significant inhibition of hBD3 function (data not shown). Further investigation of the behavior of the peptides in biologically relevant conditions (e.g. media) may be necessary to better understand if the lack of activity inhibition is due to either a lack of binding of the peptide in these conditions (such as due to peptide degradation or aggregation), or if the peptides bind to hBD3 in a manner that is compatible with hBD3 activity. Nonetheless, our results show promise for the selection of protein binding peptides via this phage display platform.

5.6 Experimental Protocols

5.6.1 General Methods

Amino acids, HATU and HBTU were purchased from Creosalus and Chem Impex International. 5(6)-Tetramethylrhodamine was purchased from Chem Impex International. Dimethylformamide, dichloromethane, allyl chloroformate, piperidine, N-methylmorpholine, diisopropylethylamine, phenylsilane, tetrakis(triphenylphosphine)palladium(0), p-nitrophenylchloroformate, guanidinium chloride, sodium phosphate, tris(2-carboxyethyl)phosphine hydrochloride, thiophenol, DMSO, acetic acid, iodine, anisole, triisopropylsilane, ethanedithiol, biotin, bovine serum albumin and human serum albumin were purchased from Fisher Schientific. Streptavidin agarose beads, Precision Plus Ladder and immobilized TCEP were purchased from

ThermoFisher Scientific. Anti-pIII-FITC antibody was purchased from Santa Cruz Biotechnologies. Trifluoroacetic acid was purchased from Protein Technologies. The phage display C7C library was purchased from NEB. APBA-IA was synthesized according to previously reported methods[1] and used from a 200 mM DMSO stock for all phage labeling experiments, and a 10 mg/mL stock for peptide labeling. Defensins were synthesized on Dawson-Dbz (EMD Millipore) and Wang (EMD Millipore) resins using standard Fmoc chemistry procedures (0.4M NMM in DMF for amino acid couplings, 20% piperidine in DMF for fmoc removal), unless indicated otherwise. All peptide hits were synthesized on Rink Amide resin (EMD Millipore).

Peptides were synthesized on a Tribute Peptide Synthesizer from Protein Technologies. All peptides were purified via reverse phase high performance liquid chromatography (RP-HPLC) on a Waters Prep LC with a Jupiter C18 column (Phenomenex) with water/acetonitrile/0.1% TFA eluent (Buffer A= 95% water, 5% acetonitrile, 0.1% TFA, Buffer B= 95% acetonitrile, 5% water, 0.1% TFA) with a gradient from 100% Buffer A to 60% Buffer B. Mass spectrometry analysis was carried out on an Agilent 6230 LC TOF mass spectrometer. Fluorescence images were obtained on a Zeiss Axio Observer A1 inverted microscope. Fluorescence anisotropy data were generated on a SpectraMaxM5 plate reader. The concentration of TAMRA labeled peptides was determined by fluorescence readout on a Nanodrop 2000c UV/Vis spectrometer by cuvette (ε=90,000 $M^{-1}cm^{-1}$).

5.6.2 Defensin Synthesis

hBD2/3-a were synthesized on Dawson-Dbz resin. Prior to amino acid couplings, the resin was alloc protected with 350 mM allylchloroformate and 1 equivalent DIPEA in

DCM for 24 hours. The first 5 residues were then coupled by hand with 5 equivalents amino acid and 4.9 equivalents HATU in 9 equivalents DIPEA in DMF. All subsequent amino acids were coupled with 0.4M NMM in DMF using an automated peptide synthesizer. The Fmoc-aminohexanoic acid linker and biotin molecule were coupled last by hand with 0.4M NMM in DMF and 4.9 equivalents HATU. Following completion of synthesis, alloc was removed with 0.7 equivalents tetrakis(triphenylphosphine)palladium(0) and 0.1 equivalents phenylsilane in DCM. Conversion to Nbz was achieved by stirring with triphenylchloroformate in DCM for 40 minutes, then treating with 0.5M DIPEA in DMF for 30 minutes. The peptides were cleaved from resin with 95% TFA/5% water and isolated by cold ether precipitation. The peptides were then purified by RP-HPLC and their purity was confirmed by LC-MS (**Table 5-7**).

hBD2/3-b were synthesized on an automated peptide synthesizer on Wang resin with standard 0.4M NMM in DMF couplings. The completed peptides were cleaved from resin with 94% TFA, 3% EDT and 3% water, isolated via cold ether precipitation and purified by RP-HPLC with purity confirmed by LC-MS (**Table 5-7**).

To ligate the peptides, 3.8 mM hBD2/3a was stirred with 4.2 mM hBD2/3b in 2:3 DMF: ligation buffer (3M Gdn-HCl, 0.2M sodium phosphate, 20 mM TCEP, 200 mM thiophenol, pH 8) for 1 hour. The peptides were then directly purified by RP-HPLC and their purity was confirmed by LC-MS (**Table 5-7**).

The Trt deprotected peptides (1.5 mM) were then oxidized with 10% DMSO in water for 18 hours. The peptides were directly lyophilized and used for the Acm deprotection/oxidation step, in which 3 mM peptide was stirred in 20 equivalents iodine

in acetic acid with 0.1M HCl for 1.5 hours. The peptides were isolated by cold ether precipitation and purified by RP-HPLC, and the purity was confirmed by LC-MS (**Table 5-7**).

The peptides were finally Tbu deprotected and oxidized by stirring at 1 mM in TFA with 400 equivalents DMSO and 40 equivalents anisole for 5 hours. The peptides were then directly purified by RP-HPLC and their purity was confirmed by LC-MS (**Table 5-7**).

Table 5-7. hBD2/3 peptide sequences and analysis by LC-MS (see Figure 5-7 and 5-8 for sequence details).

Peptide	Expected Mass	Observed Mass
hBD3-a*	1277.04	1276.66
hBD3-b$^{\times}$	1127.59	1127.59
Ligated hBD3 $^{\theta}$	1151.42	1151.81
hBD3-1ox $^{\theta}$	1151.22	1151.61
hBD3-2ox $^{\theta}$	1122.62	1122.59
hBD3-3ox $^{\theta}$	1099.74	1099.77
hBD2-a*	1270.53	1270.62
hBD2-b*	1283.60	1283.17
Ligated hBD2 $^{\times}$	1643.60	1643.51
hBD2-1ox $^{\times}$	1643.27	1642.80
hBD2-2ox $^{\times}$	1196.11	1196.35
hBD2-3ox $^{\times}$	1167.42	1167.82

*=$[M+2H]^{2+}$; $^{\times}$=$[M+3H]^{3+}$; $^{\theta}$=$[M+5H]^{5+}$; Aha=Aminohexanoic acid

5.6.3 Phage Display Panning Protocols

5 μL (~$5x10^{10}$ pfu) of the commercial CX_7C library was stirred for 48 hours at 4^{o}C with 25 μL iTCEP in TBS pH 8.5. 2 mM APBA-IA was then added to the mixture, which was stirred for 2 hours at room temperature. The mixture was then centrifuged to isolate the phage mixture from the iTCEP beads, and the phage was precipitated from the mixture was with 1/5 volume 20% PEG/2.5M NaCl on ice for 5 hours. The precipitated

mixture was then centrifuged, and the phage pellet was re-suspended in 100 µL TBS pH 7.5. The APBA-IA labeled phage was titered to determine an input population using standard M13 titering methods indicated by NEB.

For the pulldown experiment, streptavidin beads were washed with 0.1% TBST, then blocked with blocking buffer with 5 mg/mL BSA for 1 hour at 4^{o}C. The beads were then washed with TBST. Concurrently, 12 µg hBD3-biotin was incubated with 50 µL APBA-IA labeled phage in 0.1% TBST for 30 minutes at room temperature with stirring. The phage mixture was then added to the blocked and washed streptavidin beads, which were stirred for 30 minutes at room temperature. Unbound phage was removed by washing with 0.1% TBST (5x), then TBS (5x), both with 1 mg/mL BSA. Phage binders were then eluted from the hBD3-coated beads by stirring with glycine elution buffer (0.2M glycine-HCl, pH 2.2, 1 mg/mL BSA) for 10 minutes. Eluted phage were neutralized with Tris pH 9.1. The phage output population was amplified by addition to an early-log ER2738 culture (ER2738 culture started from single colony inoculation from LB+Tet plate, grown overnight, then sub-cultured 1:100 in fresh LB media) and allowing the phage to amplify for 4.5 hours.

This panning procedure was repeated for subsequent rounds. Neutravidin beads were substituted in round 2. The washing stringency was increased with each round from 0.1% Tween in round 1 to 0.2% and 0.3% in rounds 2 and 3, respectively. The DNA from phage output population from round 3 was isolated with a GeneJet miniprep kit following 5 hours of incubation of individual phage colonies grown in 1:100 ER2738 from overnight culture in LB media. All DNA sequencing was carried out by Eton Bioscience Inc. (**Table 5-8**).

Table 5-8. DNA sequences from the round 3 hBD3 screen output.

DNA Sequence	Peptide Sequence
GCTTGTAATAGTTCGGCGTCGAAGAATTGC	ACNSSASKNC
GCTTGTACGACGAAGTTGCCTAATTCGTGC	ACTTKLPNSC
GCTTGTAAGCATCCGCTGTATAGGCATTGC	ACKHPLYRHC
GCTTGTAGTTCTAAGCATGAGGCTACTTGC	ACSSKHEATC
GCTTGTCATCGGGCTCAGGGGACTGCTTGC	ACHRAQGTAC
GCTTGTATTTCGCTTACTCTGAATCGGTGC	ACISLTLNRC
GCTTGTTCAGCGTATGAAAGGCCTCCTTGC	ACSAYERPPC
GCTTGTCTTGTTTATGCTCATCATACGTGC	ACLVYAHHTC
GCTTGTGGTCGTACGCCGTCGGATAAGTGC	ACGRTPSDKC
GCTTGTAGTTTGTCTAATTATCATCGGTGC	ACSLSNYHRC
GCTTGTGTTATGAGTCCGGGTAAGTCTTGC	ACVMSPGKSC
GCTTGTATGAATCCGCTGTATTGGCGTTGC	ACMNPLYWRC
GCTTGTGTGCATAGTAAGCCGGGGCGGTGC	ACVHSKPGRC
GCTTGTAAGAATCCTCAGTATAGGCGTTGC	ACKNPQYRRC
GCTTGTATTTCGCTTACTCTGAATCGGTGC	ACISLTLNRC
GCTTGTGTTTCGACTATGGCGCGGACGTGC	ACVSTMARTC
GCTTGTCATGGGGCGGTTAAGAATACTTGC	ACHGAVKNTC
GCTTGTACGTCTTGGTCGAAGCGGCTGTGC	ACTSWSKRLC
GCTTGTTATAAGACGATGTATGGGCTGTGC	ACYKTMYGLC
GCTTGTCGGCTTCCTACGTCTACTGGGTGC	ACRLPTSTGC
GCTTGTAATAGTCATCGTCATGGTGCTTGC	ACNSHRHGAC
GCTTGTACGGATAGTAGGGGGCAGAAGTGC	ACTDSRGQKC
GCTTGTAAGGAGGGGATTCATATGACGTGC	ACKEGIHMTC
GCTTGTACTTCGCTTACTGTGGATCGGTGC	ACTSLTVDRC
GCTTGTGTTTCTCCGAGGAGTCATGAGTGC	ACVSPRSHEC
GCTTGTACTCTGACTGCTTATAAGGTGTGC	ACTLTAYKVC
GCTTGTCAGCCTAGTCGTTTTGTTCAGTGC	ACQPSRFVQC
GCTTGTGGGAAGCATTTTCAGAAGCATTGC	ACGKHFQKHC
GCTTGTATGAAGGCGCTGTATTGGCGTTGC	ACMKALYWRC
GCTTGTCCGGCTCAGAATGGGTGGCAGTGC	ACPAQNGWQC
GCTTGTTCTGCGGGGTATAGTAGGAATTGC	ACSAGYSRNC
GCTTGTAAGGCGGGTCATCAGTATCAGTGC	ACKAGHQYQC
GCTTGTGATATTTATCGGAAGGGGTGGTGC	ACDIYRKGWC
GCTTGTCTGAATGCTGGTGCTTCGAAGTGC	ACLNAGASKC
GCTTGTAATACGCCTGCTATGTTGACTTGC	ACNTPAMLTC
GCTTGTTTGCATAAGTCTGTTTCTGGTTGC	ACLHKSVSGC
GCTTGTAAGATTCCTTCGTAGGGGCGTTGC	ACKIPSQGRC
GCTTGTCTTTGGAGGCCGGCGGCTGATTGC	ACLWRPAADC
GCTTGTGTGAATCCGATGAAGCGTCATTGC	ACVNPMKRHC
GCTTGTGATCGTGCTGGGTTGGAGCATTGC	ACDRAGLEHC
GCTTGTCATCCGTCGAATTGGAAGGCTTGC	ACHPSNWKAC

5.6.4 PAGE Confirmation of hBD3 Dimerization

hBD3 dimerization was analyzed by 16% tricine gel electrophoresis. Untreated hBD3 (10 μg) or 0.1M DTT treated hBD3 (10 μg) were boiled at 100^{o}C with non-denaturing sample buffer, then subjected to 16% tricine PAGE alongside Precision Plus Ladder for 1 hour. The gel was then stained with Coomassie, destained and imaged.

5.6.5 hBD3 Peptide Hit Synthesis

Peptide hits were synthesized by solid phase peptide synthesis on Rink Amide resin as previously detailed.[1] An alloc protected diaminopropionic acid (Dap) residue was installed at the C-terminus for facile fluorophore labeling. 5(6)-TAMRA was conjugated to the resin after removal of the alloc protecting group with 0.7 equivalents of tetrakis(triphenylphosphine)palladium (0) and 0.1 equivalents phenylsilane in DCM. The TAMRA fluorophore was then conjugated on resin with HBTU-mediated amide bond coupling with 3 equivalents 5(6)-TAMRA and 2.9 equivalents HBTU in 0.4M NMM in DMF. The peptide was then Fmoc deprotected at the N-terminus using standard Fmoc deprotection conditions, and cleaved from resin with 95% TFA, 2.5% water and 2.5% triisopropylsilane. The peptides were then isolated by cold ether precipitation and purified by RP-HPLC. The peptides were then APBA-IA labeled with 3 equivalents APBA-IA in the presence of 2 equivalents TCEP with 2M NMM in DMF, and again purified by RP-HPLC. The purity of all peptides was confirmed by LC-MS (**Table 5-9**).

Table 5-9. Sequence and LC-MS analysis of hBD3 binding peptides.

Name	Peptide Sequence	Calculated Mass	Observed Mass
SEC1	$AC_mISLTLNRC_mGGGDap$*	1150.15 $[M+2H-H_2O]^+$	1150.02 $[M+2H-H_2O]^+$
SEC2	$AC_mDRAGLEHC_mGGGDap$*	1131.51 $[M+2H-2H_2O]^+$	1131.47 $[M+2H-2H_2O]^+$
SEC3	$AC_mVSTMARTC_mGGGDap$*	1116.02 $[M+2H-2H_2O]^+$	1115.43 $[M+2H-2H_2O]^+$
SEC4	$AC_mKAGHQYQC_mGGGDap$*	1148.52 $[M+2H-2H_2O]^+$	1148.47 $[M+2H-2H_2O]^+$

C_m= APBA-IA labeled Cys; Dap*= TAMRA labeled Dap

5.6.5 Streptavidin Bead Binding Microscopy Studies

For phage bead binding experiments, 50 µL streptavidin beads were washed with TBS pH 7.5, then incubated with 2 µL hBD3-biotin (10 mg/mL) for 1 hour at room temperature with stirring in TBS pH 7.5. The beads were then washed with TBS pH 7.5, incubated with 50 µL TBS pH 7.5 and 5 µL Anti-pIII-FITC for 30 minutes, then 2 µL of beads were imaged by fluorescence microscopy (FITC channel) at 10X magnification.

For peptide bead binding experiments, the same hBD3 coating procedures were carried out. Peptides at designated concentrations were added to the bead mixtures, which were incubated for 1 hour at room temperature in TBS pH 7.5 alone, or with 10% human serum or 10 mg/mL BSA. Then, 2 µL of beads were imaged by fluorescence microscopy (rhodamine channel) at 10X magnification. The same procedure was carried out for hBD2-coated bead binding.

5.6.6 BSA Binding Anisotropy Analysis

Indicated concentrations of BSA (0-20 mg/mL) were incubated with 1 µM each TAMRA labeled peptide in PBS pH 7.4 for 1 hour at room temperature. Anisotropy readings were obtained in triplicate using TAMRA excitation and emission wavelengths (546/579 nm).

5.7 References

1. McCarthy, K. A. *et al.* Phage Display of Dynamic Covalent Binding Motifs Enables Facile Development of Targeted Antibiotics. *J. Am. Chem. Soc.* **140,** 6137–6145 (2018).
2. Ganz, T. Defensins: Antimicrobial peptides of innate immunity. *Nat. Rev. Immunol.* **3,** 710–720 (2003).
3. Ganz, T. *et al.* Defensins. Natural peptide antibiotics of human neutrophils. *J. Clin. Invest.* **76,** 1427–1435 (1985).
4. Jones, D. E. & Bevins, C. L. Paneth cells of the human small intestine express an antimicrobial peptide gene. *J. Biol. Chem.* **267,** 23216–23225 (1992).
5. Schutte, B. C. & McCray, P. B. β-Defensins in Lung Host Defense. *Annu. Rev. Physiol.* **64,** 709–748 (2002).
6. Dhople, V., Krukemeyer, A. & Ramamoorthy, A. The human beta-defensin-3, an antibacterial peptide with multiple biological functions. *Biochim. Biophys. Acta - Biomembr.* **1758,** 1499–1512 (2006).
7. Lu, W., Hoover, D. M., Lubkowski, J., Wu, Z. & Tucker, K. Antimicrobial Characterization of Human beta-Defensin 3 Derivatives. *Antimicrob. Agents Chemother.* **47,** 2804–2809 (2003).
8. Wu, Z. *et al.* Engineering disulfide bridges to dissect antimicrobial and chemotactic activities of human beta-defensin 3. *Proc. Natl. Acad. Sci.* **100,** 8880–5 (2003).
9. D. Yang *et al.* β-Defensins: Linking Innate and Adaptive Immunity Through Dendritic and T Cell CCR6. *Science* . **286,** 525–529 (1999).

10. Oppenheim, J. J., Biragyn, A., Kwak, L. W. & Yang, D. Roles of antimicrobial peptides such as defensins in innate and adaptive immunity. *Ann. Rheum. Dis.* **63,** 17–21 (2003).

11. Jin, G. *et al.* An antimicrobial peptide regulates Tumor-Associated macrophage trafficking via the chemokine receptor CCR2, a model for Tumorigenesis. *PLoS One* **5,** 1–14 (2010).

12. Steubesand, N. *et al.* The expression of the β-defensins hBD-2 and hBD-3 is differentially regulated by NF-κB and MAPK/AP-1 pathways in an in vitro model of Candida esophagitis. *BMC Immunol.* **10,** 1–16 (2009).

13. Jin, J. *et al.* Human papillomavirus oncogenic E6 protein regulates human beta-defensin 3 (hBD3) expression via the tumor suppressor protein p53. *Oncotarget* **7,** 27430–2744 (2016).

14. Gehad, A. E. *et al.* Nitric oxide-producing myeloid-derived suppressor cells inhibit vascular e-selectin expression in human squamous cell carcinomas. *J. Invest. Dermatol.* **132,** 2642–2651 (2012).

15. Rohrl, J., Yang, D., Oppenheim, J. J. & Hehlgans, T. Human Beta-Defensin 2 and 3 and Their Mouse Orthologs Induce Chemotaxis through Interaction with CCR2. *J. Immunol.* **184,** 6688–6694 (2010).

16. Kulkarni, S. S., Sayers, J., Premdjee, B. & Payne, R. J. Rapid and efficient protein synthesis through expansion of the native chemical ligation concept. *Nat. Rev. Chem.* **2,** 1–17 (2018).

17. Blanco-Canosa, J. B. & Dawson, P. E. An efficient Fmoc-SPPS approach for the generation of thioester peptide precursors for use in native chemical ligation.

Angew. Chemie Int. Ed. **47,** 6851–6855 (2008).

18. Schibli, D. J. *et al.* The solution structures of the human β-defensins lead to a better understanding of the potent bactericidal activity of HBD3 against Staphylococcus aureus. *J. Biol. Chem.* **277,** 8279–8289 (2002).

CHAPTER 6

Conclusions

6.1 Conclusions

The overarching goal of the research outlined herein was to develop novel bioorthogonal chemical tools that enable species- and strain-selective bacterial targeting for development of diagnostic approaches, and eventually therapeutic scaffolds, towards efforts to combat antibiotic resistance. Antibiotic resistance accounts for ~2 million health care cases and >23,000 deaths in the US per year, while worldwide mortality rates are around 1 million per year. Additionally, antibiotic resistance generates massive excess health care costs, totaling nearly $20 billion annually in the US alone.[1] For example, MRSA infections, of which there are about 80,000 cases annually, generate an average excess cost of ~$10,000 per incidence in comparison to MSSA infections as a result of the extra care demanded by these more challenging antibiotic resistant infections.[2] More importantly, deaths resulting from antibiotic resistance are expected to grow to 10 million by 2050 due to increasingly challenging to treat infections and a lack of novel therapeutics.

From a scientific standpoint, the challenge of antibiotic resistance stems from two key factors: 1) a lack of effective novel antibiotic therapeutics, and 2) the widespread use of antibiotics, and especially broad-spectrum antibiotics.[3] Fortunately, knowledge about the rise of antibiotic resistance has translated with some success to the clinic, as physicians have adopted more stringent practices for antibiotic prescription; however, these two key challenges remain to be seriously addressed by the scientific community.

Our research has sought to apply novel chemical tools towards identification of modalities that selectively label one species or strain of bacteria amongst all possible

species and strains of bacteria in complex biological settings. This aim has first required us to thoroughly examine the bioorthogonality of our chemical tools to ensure that they do not cause toxicity to the organism(s) of interest. This requirement for non-toxic chemical probes has also limited their working concentration in cellular contexts, which has demanded that we develop highly efficient chemical reactions that proceed with fast kinetics ($\geq 10^3$ $M^{-1}s^{-1}$) at low micromolar concentrations. Additionally, due to the physiological environments in which they are operating, these novel chemistries needed to be amenable not only to buffer conditions, but also to complicated cellular environments filled with countless proteins and metabolites. To examine this capacity, we tested the efficiency of the reactions in the presence of bovine or human serum, as well as various metabolites, including glutathione, cysteine, and fructose. Finally, the bioorthogonality requirement also demands that our probes are stable in and non-reactive towards these complex biological settings.

Our group's work initial foray into iminoboronate chemistry stemmed from the knowledge that many species of Gram-positive bacteria, including the clinically relevant *S. aureus*, display amine-presenting lipids on their cell surfaces. Iminoboronate chemistry of acetylphenyl boronic acid (APBA) enabled bacterial detection by incorporation of this chemical motif into a defined cationic peptide, H-Lys, to afford target binding synergism of electrostatic bacterial cell surface interactions and iminoboronate formation with amine-presenting lipids. Given the aforementioned requirement for bioorthogonality, we sought to determine if we could improve upon the equilibrium dissociation constant (K_d) of simple APBA binding to these amines (1-20 mM) by incorporating a variety of electron-donating and -withdrawing substituents on the APBA scaffold. Our hypothesis

for this endeavor was that analogues containing electron-withdrawing groups would increase the electron deficiency of boron in the boronic acid to promote amine conjugation. Unfortunately we did not foresee that increasing the Lewis acidity would also enhance a competing boroxole formation mechanism, which diminishes the conjugation of the APBA analogue to amines.

Although our APBA analogues did not exhibit the desired improvement in amine conjugating potency, other research groups have reported success with the incorporation of APBA into non-covalent ligand core structures, which has afforded protein inhibitors with greatly improved binding potency (IC_{50}~3 nM) in comparison to simple APBA.[4] Thus, improvement of the binding of APBA appears to be best achieved when incorporated into scaffolds designed specifically for the target of interest, rather than by substituent effects.

Towards an alternative aim of utilizing APBA for facile free and N-terminal cysteine conjugation, the APBA analogues were successful in slightly improving the binding potency towards L-cysteine in comparison to simple APBA (~3x improvement). The binding dissociation constant of thiazolidinoboronate formation of APBA and L-cysteine, however, is ~40x less than that of iminoboronate formation with 2-methoxyethylamine (0.5 mM versus 20 mM), which may mitigate the interfering effects of boroxole formation observed with iminoboronate formation. Thus, while the APBA analogues didn't prove to be successful for improving the binding potency towards forming iminoboronates, their application in thiazolidinoboronate formation did show some utility.

Considering our lack of success with discovering improved amine-binding APBA molecules, we turned to an alternative bioorthogonal chemistry, diazaborine formation, to achieve efficient bacterial labeling. Initially discovered for the conjugation of APBA and phenylhydrazine, diazaborine formation is a fast conjugation chemistry that forms stable conjugates. Phenylhydrazine, however, is neither stable in biological contexts, nor non-toxic, so we substituted semicarbazide as our nucleophile to generate a truly biocompatible chemistry.

By synthesizing D-amino acid variants of APBA and semicarbazide, we were able to efficiently incorporate these chemical motifs into the cell walls of bacteria via a cell wall remodeling mechanism that employs the transpeptidase function of PBPs. Interestingly, the APBA unnatural amino acid, D-AB3, showed significantly more efficient incorporation into *E. coli* cell walls in comparison to several other bacterial species through an unknown mechanism. While we hypothesize that the differences in incorporation efficiency could be due to differences in the PBPs and their related transpeptidases between the various species of bacteria, the actual mechanism has yet to be elucidated. This could be carried out by confirming the PBP responsible for incorporation of the amino acids by studying PBP mutants, and subsequently comparing structures of the related PBPs. Nonetheless, the diazaborine forming chemistry enables a facile method of labeling bacteria in a relatively selective manner.

We were also able to transform the diazaborine chemistry into a turn-on fluorescent bacterial labeling system, whereby we incorporated a semicarbazide containing D-unnatural amino acid into the bacterial cell wall, which underwent diazaborine formation with a non-fluorogenic APBA coumarin analog that became

fluorescent when conjugated to semicarabzide. This feature enables no-wash labeling of the bacteria at up to low millimolar concentrations, which is prohibited with fluorescent probes. Notably, the semicarbazide amino acid shows greater incorporation efficiency for *S. aureus* in comparison to *E. coli*, which is in contrast to the APBA amino acid. The species selectivity for the incorporation of APBA and semicarbazide amino acids is a serendipitous discovery, rather than a consequence of design. Thus, we sought out a platform that would enable us to develop highly selective bacterial species and strain specific chemical probes.

Over the past few years, our group has developed a method to label a randomized phage-display peptide library with APBA handles. This APBA dimer phage library has been successfully applied to identify peptides that are selective probes of several bacterial species including the clinically relevant *S. aureus* and LOS deficient (LOS-) *A. baumannii*.[5] Looking to expand upon the species-selectivity we have been able to achieve with this library, we sought to determine if we could generate strain-selective peptide probes that differentiate between different mechanisms of colistin resistance (pmrA/B and LOS-) in the same bacterial species (*A. baumannii*). Through this investigation, we discovered that the LOS- strain is capable of binding peptides that are meant to be selective for detecting the pmrA/B mechanism of colistin resistance, even if the library is first screened against the LOS- strain to eliminate any LOS- binders, which prohibits development of pmrA/B-specific peptide probes. Alternatively, we were successful in identifying probes that selectively bind to LOS- strains and not pmrA/B strains (SEC8 and SEC9). Therefore, it appears that the LOS- cell surface has features that result in some non-specific binding of the APBA dimer colistin resistance detecting peptides.

Despite a lack of resistance mechanism-specific binding of some of the hits, the peptide probes identified do selectively bind colistin resistant strains of bacteria, and do not bind colistin sensitive strains, which is important towards our efforts to create novel methods of detecting antibiotic resistant bacteria.

Furthermore, we sought to determine if we could identify peptide probes that are specific for the *mcr1* mechanism of colistin resistance in non-*A. baumannii* bacterial species. Indeed, SEC18-20 display strong binding to AR497, a *K. pneumoniae* strain, yet these peptides show diminished binding to alternative *mcr1*-carrying bacterial strains, AR493 (*E. coli*) and AR496 (*S. enteritiditis*). Interestingly, a pmrA/B *A. baumannii*-derived peptide, SEC5, also showed strong binding to the AR497 strain, indicating a potentially similar LOS- binding phenomenon, whereby the AR497 strain is sticky for colistin resistance detecting peptides. (Further investigation about other strains….)

Beyond identification of bacterial cell surface binding peptides, we also applied the APBA dimer phage library to identify peptide binders of a small protein, human beta defensin 3. Screening of the library against immobilized hBD3 resulted in peptide hits that were selective for hBD3 binding in comparison to the similar defensin, hBD2, and displayed low micromolar binding potency. This application of the phage library platform towards identification of protein binding peptides represents a new area of exploration in our lab. Identification of protein binders, and potentially protein inhibitors with this high throughput platform has many important applications in the development of novel probes and therapeutics of a wide array of proteins and disease states both within and beyond our current interests in antibiotic resistance.

Throughout all of the successes and failures of the projects explored herein, the importance of target-specific binding elements becomes apparent. The case of APBA analogues in comparison to a non-covalent ligand incorporated APBA highlights the improvement in target specificity that can be achieved by including additional specificity elements in our chemistries, including phage libraries. Towards the future, the phage screening platform presents an important opportunity to include additional specificity elements to improve targeted binding of our probes. Efforts in this area are currently being undertaken with a dual labeled phage library that can display a specificity element at the N-terminus and an APBA handle within the peptide sequence to afford additional improvements in binding potency to amine-presenting targets.

Additionally, through our library screens of many different bacterial strains, we were able to discover a variety of peptides that exhibit binding to one or more strains of interest; however, we remain uncertain about the cell wall features to which these peptides are binding. While the key difference between the antibiotic resistant strains and wild-type strains from which they were derived is the amine presenting modifications, there may be other differences between the cell surfaces that contribute to the varied binding of these peptides. Therefore, it may be helpful to better characterize the cell wall features of the strains studied, as well as which features the peptides are binding to in order to understand the mechanism of bacterial binding afforded by each peptide.

Overall, we have successfully developed several different approaches to selective detection of different bacterial strains by both serendipity as well as careful design. Our goal is that these probes can be translated to the clinic not only as diagnostic tools, but

also eventually as targeted therapeutics towards our efforts to improve the current state of antibiotic resistance.

6.2 References

1. Hampton, T. Report Reveals Scope of US Antibiotic Resistance Threat. *JAMA* **310,** 1661–1663 (2013).
2. Lees, C. H. *et al.* Excess Costs and Utilization Associated with Methicillin Resistance for Patients with Staphylococcus aureus Infection. *Infect. Control Hosp. Epidemiol.* **4,** 365–373 (2010).
3. CDC. Antibiotic Resistance Threats. 1–114 (2013). Available at: https://www.cdc.gov/drugresistance/pdf/ar-threats-2013-508.pdf.
4. Akçay, G. *et al.* Inhibition of Mcl-1 through covalent modification of a noncatalytic lysine side chain. *Nat. Chem. Biol.* **12,** 931–938 (2016).
5. McCarthy, K. A. *et al.* Phage Display of Dynamic Covalent Binding Motifs Enables Facile Development of Targeted Antibiotics. *J. Am. Chem. Soc.* **140,** 6137–6145 (2018).